Effect of Hydrogen on the Microstructure and Cold Rolling Behavior of Commercially Pure Titanium and β-metastable Titanium Alloy

Jing Wen

UNIVERSITÉ DE LORRAINE

Ecole doctorale EMMA

THÈSE

Pour l'obtention du titre de :

DOCTEUR DE L'UNIVERSITÉ DE LORRAINE

Spécialité : Science des Matériaux

Présentée par :
Jing WEN

Effet de l'Hydrogène sur la Microstructure et la Déformation en Laminage à Froid du Titane de Pureté Commerciale et d'un Alliage de Titane β Métastable

Effect of Hydrogen on the Microstructure and Cold Rolling Behavior of Commercially Pure Titanium and β-metastable Titanium Alloy

---

Thèse soutenue publiquement le 11 juillet 2017 à Metz devant le jury composé de:

Xavier Feaugas	Prof., Université de La Rochelle	Rapporteur
Frédéric Prima	Prof., Ecole Nationale Supérieure de Chimie de Paris	Rapporteur
Anne Habraken	Directrice de Recherche, FRS-FNRS, Université de Liège, Belgique	Examinatrice
Nadine Pébère	Directrice de Recherche, CIRIMAT, Université de Toulouse	Examinatrice
Nathalie Allain	Prof., Université de Lorraine	Co-directrice de thèse
Eric Fleury	Prof., Université de Lorraine	Directeur de thèse

LEM3 - Île du Saulcy 57000 METZ
Université de Lorraine – Pôle M4 : matière, matériaux, métallurgie, mécanique

Table of Contents

List of Figures

List of Tables

Abstract

Due to an attractive combination of physical, chemical and mechanical properties, titanium and titanium alloys have become promising candidates in the field of chemical industry, aerospace and biomedical materials. During manufacturing procedures and applications, components are exposed to environments that can act as sources of hydrogen. Therefore, understanding their interaction with hydrogen upon various mechanical/thermal processing is important so that their properties and performance can be controlled and reliably predicted. With the aim of enhancing the properties and performance of titanium and reducing the cost of manufacturing products, the present work is primarily focusing on the effect of hydrogen on the cold rolling behavior and the subsequent annealing of titanium and titanium alloy characterized by different crystalline structure, i.e. hexagonal and body cubic centered (bcc) structure for the commercial pure titanium Ti50A and metastable β-titanium alloy β-21S, respectively. Since the microstructure of titanium and its alloys is the governing factor that determines their properties and performance, the microstructural evolution in the presence of hydrogen upon various procedures was analyzed by combination of XRD, SEM-EBSD and TEM.

The introduction of hydrogen in Ti50A by electrolytic method induced the precipitation of two types of hydrides (δ-TiH_x, ε-TiH_2) in the α phase matrix, and it was found that the volume fraction of these hydrides increased as the charging time increased. Five orientation relationships (ORs), three of them being new orientation relationships ever reported, between the α-phase and the hydride δ-TiH_x were determined. Moreover, the correlation between the rolling texture and the hydride precipitation was also established. It was found that the existence of the rolling texture facilitated the precipitation of δ-hydride following the OR2-type orientation relationship. X-ray analyses revealed a broadening of the diffraction peaks corresponding to the α phase, indicating a increase of the dislocation density, these dislocations being necessary to accommodate the lattice misfit between hydrides and the matrix. Under compression loading, the observation of slip traces and tension twin $\{10\bar{1}2\}<\bar{1}011>$ TT1 in the α-grains containing hydrides, suggested that the hydrides had a certain ability to accommodate the imposed shear strain, depending on the orientation relationships between the matrix and the hydrides as well as on their thickness. Although no correlation between the nucleation of twinning and the hydride could be established in this study, the hydrides seemed to play an important role on the

development of twinning deformation. The effects of hydrogen on the cold rolling behavior in Ti50A showed that, the formation of TT1tension twins can be facilitated due to the increase of the c/a ratio owing to the hydrogen addition and the existence of local stresses generated by the precipitation of hydrides. The refinement of the microstructure was also observed in the hydrogenated Ti50A-H suggesting that the presence of hydrides can enhance the generation of high angle boundaries (HABs). In addition, the formation of numerous geometrically necessary dislocations (GND) allowing the accommodation of the strain incompatibility between the hydride and matrix could be worked out by SEM-EBSD, which also confirmed analyses of the X-ray traces.

In the case of β-21S alloy, with bcc structure that can accommodate a larger concentration of interstitial atoms, hydrogen was introduced by gas method. The effect of hydrogen on the microstructure was found to be closely related to the hydrogen concentration. In the range of hydrogen/metal ratio $0.052 < H/M < 0.300$, the microstructure consisting of the single β-phase showed that the dissolved hydrogen atoms expanded the bcc β-lattice and suppressed the decomposition of the β phase upon cooling. As the hydrogen/metal ratio was increased further till $H/M = 0.460$, the appearance of a considerable amount of plate-shape martensites indicated that a high content of hydrogen atoms can lead to a large shear deformation in the β-lattice inducing the martensite transformation. The influence of hydrogen on the cold rolling behavior of β-21S alloy showed that hydrogen had contradictory effects, depending on the hydrogen concentration. At lower hydrogen concentration ($H/M < 0.160$), a hydrogen-induced softening occurred, which was explained by a reduction of the formation energy of kink pairs owing to the hydrogen addition as proposed by the 'defactant' concept. In contrast, as the hydrogen concentration increased to $H/M = 0.215$, the observation of less deformed β grains and the presence of micro-cracks in the grain boundaries indicated that the hydrogen-induced solid solution strengthening mechanism became dominant. Results of tensile and compressive mechanical tests showed that hydrogen had distinct effects on the tensile and compressive properties. Additionally, the combined effect of hydrogen and cold rolling on recrystallization showed that the formation of new recrystallized strain-free grains was promoted due to the increase of dislocation density owing the presence of hydrogen upon cold rolling.

Résumé

En raison d'une combinaison de propriétés physiques, chimiques et mécaniques remarquables, les alliages de titane et de titane sont devenus des candidats prometteurs dans le domaine de l'industrie chimique, de l'aéronautique, de l'aérospatiale et des matériaux biomédicaux. Durant les procédures de fabrication ainsi qu'en service, les composants sont exposés à des environnements tels que la surface de ces composant seront exposées à l'hydrogène. Par conséquent, la compréhension de l'interaction de ces matériaux avec l'hydrogène lors de divers procédés de d'élaboration et de mise en forme est importante afin que leurs propriétés et leurs performances puissent être contrôlées et prédites de manière fiable. Dans le but d'améliorer les propriétés et les performances du titane et de réduire le coût de fabrication des produits en titane, le présent travail se concentre principalement sur les effets de l'hydrogène sur le laminage à froid et le phénomène de recristallisation de deux titanes caractérisés par une structure cristalline différente, c'est-à-dire une structure hexagonale et cubique cubique pour respectivement le titane de pureté commerciale Ti50A et l'alliage de titane β-métastable β-21S. Étant donné que la microstructure du titane et de ses alliages est le facteur contrôlant leurs propriétés et leurs performances, l'évolution microstructurale en présence d'hydrogène introduit par deux méthodes distinctes a été analysée par une combinaison de techniques expérimentales incluant DRX, SEM-EBSD et TEM.

L'introduction de l'hydrogène dans le Ti50A par une méthode électrolytique a conduit à la précipitation de deux types d'hydrures (δ-TiHx, ε-TiH_2) dans la matrice de phase α, et il a été constaté que la fraction volumique de ces hydrures augmentait avec la durée du temps de chargement électrolytique. En raison du mode de formation par précipitation à partir des joints de grains, cinq relations d'orientation (OR) entre la α-phase et l'hydrure δ-TiHx ont été déterminées par analyses des projections stéréographiques, et parmi celles-ci trois nouvelles relations d'orientation ont pu être mise en évidence. En outre, la corrélation entre la texture de laminage et la précipitation à l'hydrure a pu être établie. On a constaté que l'existence de la texture de de laminage facilitait la précipitation d'hydrure δ suivant l'orientation d'orientation de type OR2. Les analyses de rayons X révélaient un élargissement des pics de diffraction de la phase α, ce qui indiquait une augmentation de la densité de dislocation, ces dislocations étant nécessaires pour tenir compte de l'inadéquation du réseau entre les hydrures et la matrice. Sur la surface d'échantillons déformés en compression, l'observation des traces de glissement et de macle de

tension de type TT1 $\{10\bar{1}2\}\langle\bar{1}011\rangle$ dans les α-grains contenant des hydrures a suggéré que les hydrures avaient une certaine capacité à supporter une déformation de cisaillement, en fonction des relations d'orientation entre la matrice et les hydrures mais aussi de leur épaisseur. Bien qu'aucune corrélation directe entre la nucléation des macles et la présence des hydrures n'ait été établie dans cette étude, l'effet des hydrures sur le développement des macles a été constaté. En étudiant l'effet de l'hydrogène sur le comportement au laminage à froid dans Ti50A, il a été possible de montrer que la formation de macle de type TT1 peut être facilitée par l'augmentation du rapport c/a de la maille hexagonale résultant de l'addition de l'hydrogène et de l'existence de contraintes locales générées par la précipitation des hydrures. Un raffinement de la microstructure a également été observé dans le Ti50A hydrogéné, ce qui suggère que la présence d'hydrures a tendance à générer de nouveaux grains de fortes désorientations (HAB). En outre, de nombreuses dislocations géométriquement nécessaires (GND) permettant de tenir compte de l'incompatibilité de contrainte entre l'hydrure et la matrice, ont été détectées par analyses SEM-EBSD confirmant le résultat des analyses des courbes de diffraction des rayons X.

Dans le cas de l'alliage β-21S qui peut accueillir une plus grande concentration d'atomes dans des sites interstitiels, l'hydrogène a été introduit par la méthode de chargement en phase gazeuse. L'effet de l'hydrogène sur la microstructure s'est avéré être étroitement lié à la concentration d'hydrogène. Dans la gamme du rapport hydrogène/métal $0.052 < H/M < 0.300$, la microstructure consistant en l'unique phase β a montré que la dissolution des atomes d'hydrogène conduisait en une augmentation du réseau cc de la phase β. De plus, il a été constaté que le chargement en hydrogène contribué à la suppression de la décomposition de la phase β lors du refroidissement. À mesure que le rapport hydrogène/métal a été augmenté jusqu'à atteindre une valeur $H/M = 0.460$, l'apparition d'une quantité importante de phase martensite en forme de plaque a indiqué qu'une teneur élevée en atomes d'hydrogène peut conduire à un fort cisaillement de la maille β induisant la formation de la martensite. L'influence de l'hydrogène sur le comportement au laminage à froid dans l'alliage β-21S a montré que l'hydrogène en fonction de sa concentration avait des effets contradictoires sur le comportement du laminage à froid. Pour une faible concentration en hydrogène (c'est-à-dire $H/M < 0.160$), un adoucissement induit par l'hydrogène a pu être mis en évidence qui a été expliqué par le concept de défactant. D'après ce concept, l'hydrogène réduit l'énergie de formation des paires de dislocation de type kink, facilitant la déformation plastique. Pour des valeurs de concentration d'hydrogène H/M comprises entre 0.160

et 0.215, l'observation de grains β moins déformés et la présence de micro-fissures dans les joints de grains ont suggéré que le durcissement des grains α par un mécanisme de solution solide induite par l'hydrogène devenait le mécanisme dominant. Les essais de traction et de compression uniaxiale ont montré que l'hydrogène avait des effets distincts sur les propriétés de traction et de compression. Finalement, ce travail a pu démontrer l'effet positif de l'hydrogène sur la recristallisation de tôles préalablement déformées par laminage. Lors de l'application d'un traitement thermique de courte durée sur des éprouvettes de Ti50A et de 21S, les résultats des analyses EBSD ont pu clairement mettre en évidence que la formation de nouveaux grains recristallisés exempts de dislocation avait été favorisée par l'addition d'hydrogène. Cet effet notable a pu être expliquée par l'augmentation de la densité de dislocation après laminage à froid dans les échantillons préalablement chargés en hydrogène.

Acknowledgments

During my PhD study at LEM3 (Laboratoire d'Etudedes Microstructures et de Mécanique des Matériaux), Université de Lorraine, I have been so lucky to study and work with many people who helped and supported me to arrive where I am at right now. First of all and most importantly, I would like to give my hearted thanks to French Ministry of National Education, Higher Education and Research for providing the Doctoral Contract. I would like to express the most sincere gratitude and appreciation to my advisors, Prof. Eric FLEURY and Prof. Nathalie ALLAIN, for their endless support and guidance in every aspect of my PhD student life. Their foresight and suggestions towards research lead me into not only the field of titanium and hydrogen but also the whole world of materials science and research. I thank them to give me the freedom in my research to think independently and try different ideas, designing and conducting a lot of experiments using various tools to explore the effect of hydrogen in titanium and its alloys.

Secondly, I need to thank Dr. Julien GUYON for teaching me the SEM-EBSD operation and sample preparation using FIB. I wish to express special thanks to my colleague Dr. Yudong ZHANG for her kindness help in TEM characterization. I sincerely thank Dr. Fei CAO and Prof. Ravi CHANDRAN (University of Utah, U.S.A.) for their help in hydrogen charging and measuring the hydrogen concentration. I also would like to say thanks to my ‘mentors’ Prof. Laszlo TOTH, Dr. Yajun ZHAO and Dr. Cai CHEN for all their guidance in research, study and life at univeristy of lorraine.

I would like to thank all the current and previous TMP group members for such a warm and friendly environment to study and work. Special thanks to my colleagues Benoit BEAUSIRand Jean-Jacques FUNDENBERGER for their assistance with the ATOM and JTEX softwares, Laurent WEISS for his advices in sample preparation, Olivier PERROUD for his assistance on XRD work, Christophe SCHUMAN and Jean-Sébastien LECOMTE for their help in discussion on twinning and Prof. Nicolas STEIN for his suggestion on fabrication of electrolytic cell for hydrogen charging. I also would like to express my thanks to Mr. Jérôme SLOWENSKY, Ms. Auriane MANDRELLI, Ms. Jacqueline DECKER, Ms. Nathalie KASPRZAK, Ms. Anne-martine BLUM and Ms. Arlette JACQUIERRE in LEM3 for their technical and administrative help and support during my PhD work.

Thanks to all my colleagues and friends in the LEM3 Dr. Chunyang ZHANG, Ms. Meriem BEN HAJ SLAMA, Dr. Nan XU, Dr. Haile YAN, Dr. Xiaorui LIU, Dr. Jiangkun FAN, Mr. Naifu ZOU, Mr. Shun XU, Mr. Ke HUA, Ms. Chunqing LIN, Ms. Meishuai LIU, Ms. Xiaomeng LIU, , and Pengru ZHAO for sharing four years of PhD life together.

Last but not least, I would like to thank my parents in China for their tremendous support, encouragement and love, not only in the last four years but all my life. I wish what I have achieved today can make them feel proud and I will spend all my life with all my effort to bring them more honor and happiness.

General introduction

Due to an excellent combination of properties such as strength, toughness, ductility and corrosion resistance, titanium and titanium alloys are used in wide range of fields. Chemical industry is the area employing the largest amount of titanium due to its excellent corrosion resistance especially at the presence of oxidizing acids. Next areas in which titanium and its alloys are widely used are the aeronautic and aerospace those take advantage of their great strength to weight ratio for fuel saving purpose. In addition, titanium alloys are tending to replace stainless steel and Co-based alloys as metallic biomaterials due to their low Young's modulus, excellent biocompatibility, shape memory response and high fatigue strength **[BW13]**. However the relative high price of the raw materials combined with the production costs are still the major problem limiting the application of titanium alloys. Therefore, further understanding of the microstructural evolution in titanium alloys upon various mechanical/thermal processes is essential to better control the cost, due to a better choice between processing, microstructure and properties. On the other hand, with the depletion of fossil fuels, mankind is searching for other sources of energy. Hydrogen is believed to be a possible future energy source and it is very possible that a "hydrogen economy" will be realized within the next 50 years. In such a scenario, large-scale production, storage, transportation and use of hydrogen will become necessary.

Hydrogen is an unique alloying element in metallic materials such as titanium alloys because, unlike others elements, it can be easily added and removed without melting. Titanium and its alloys have a large affinity for hydrogen, being capable of absorbing up to 60 at.% hydrogen at 600 °C, and even higher contents can be achieved at lower temperatures upon proper constituent alloying [**MM87**]. Since the beginning of the titanium industry, a great deal of attention has been given to controlling the hydrogen content of α-titanium products as hydrogen levels above 0.02 ppm can lead to a degradation of the fracture-related mechanical properties [**LG54, W97**]. One particularity of hydrogen in comparison to other constitutive elements is the fact that the reaction of hydrogen with titanium at high temperature is reversible due to a positive enthalpy of solution in titanium [**W97, M51**], allowing hydrogen to be removed upon thermal treatment under vacuum. Recently progress in the understanding of the titanium metallurgy has demonstrated that, the use of hydrogen as a temporary alloying element in titanium alloys is an attractive approach for enhancing its processability including working, machining, sintering, compaction, etc., and

also for controlling the microstructure and thereby optimizing the final mechanical properties [**SG96, G94, SF99 and SZ08**].

In many of the possible manufacturing procedures, titanium and titanium alloys is unavoidably exposed to environments that can act as sources of hydrogen. Thus, a better understanding of the interaction of hydrogen with titanium and its alloys upon various mechanical/thermal processing is important so that their properties and performance can be controlled and reliably predicted. Recently, a new term "defactant" (defects acting agents) has been introduced to explain the modifications of the mechanical properties and the mechanisms behind hydrogen embrittlement [**K09, BV10, KS10**], in which the defect formation energy was reduced by hydrogen addition. Therefore, if hydrogen, initially dissolved as defactant into metallic alloys to facilitate the formation of vacancies, dislocations and stacking faults under cold rolling process, is then subsequently removed by vacuum annealing, it is known that the dislocation density will be increased and that the concomitantly properties such as hardness/strength will be enhanced. Moreover, Goltsov and co-workers [**G06**] have found that hydrogen action stimulated the initiation of the recrystallization and recovery of the mechanical properties of deformed palladium. According to these reports, it is reasonable to assume that, if perfectly controlled, the presence of hydrogen can not only enhance the properties but also reduce the cost of titanium products. Following this proposition, the present work has been undertaken with the aim of performing a thorough microstructural study of the hydrogen effect on cold rolling and the subsequent recrystallization in titanium and titanium alloys, processes the most used in manufactural procedures for titanium-sheet products.

For that purpose, two different titanium alloys were primarily selected for the current study, both being provided by TIMETAL Corporation in the form of thin sheets. The first one was the commercial pure titanium α-phase Ti50A, characterized by a hexagonal crystal structure and widely used in key engineering applications covering a variety of areas, such as chemical industrial, marine, biomaterials, etc. **[DJ00].** The other one is the metastable β-titanium alloy β-21S (*Ti-15Mo-3Nb-3Al-0.2Si*), with a body-centered-cubic structure and essentially used for high temperature application due to its excellent oxidation resistance and creep properties. To simplify this study, the β-21S was selected among several β-metastable Ti alloys since its microstructure can be composed of the single bcc phase under controlled heat-treatment. Although extensive studies on the hydrogen effect on mechanical properties have been reported in these two alloys,

especially on sheet tensile behavior under low triaxiality **[HF98, WB98, BW02 and TR01],** no work has been reported on the influence of hydrogen on the cold deformation and recrystallization of Ti alloys.

To explore how hydrogen acts upon cold rolling and the subsequent annealing treatment, hydrogen was first introduced into Ti50A and β-21S alloys by means of electrolytic charging and molecular hydrogen gas, respectively. Then the normal symmetrical rolling was immediately performed on the pre-charged specimens. Following cold rolling, annealing treatments were conducted on the hydrogenated specimens. The evolution of microstructure during these procedures was examined by the combination of XRD, SEM-EBSD and TEM measurements. The results and findings of this research study are presented in five chapters.

In chapter 1, a general introduction of the effects of hydrogen in titanium and titanium alloys is provided. At the beginning of this chapter, the physical metallurgy of titanium and its alloys is given based on the phase structure and the alloying elements. Then, the equilibrium and kinetic aspects of hydrogen in titanium is presented in the view of the interaction of hydrogen with titanium and its structural defects. Finally, the hydrogen-induced phase transformations and its effects on the mechanical properties on titanium and its alloys are introduced. The effect of hydrogen on recrystallization in titanium alloys and other metals is also introduced.

In chapter 2, a detailed description of the materials (α-titanium Ti50A and β-titanium alloy β-21S) and the experimental procedures are presented. First, the microstructure and mechanical properties of as-received specimens are thoroughly described and a detailed account of the both hydrogen charging methods i.e., electrolytic charging and molecular hydrogen gas is given. In this chapter, the mechanical tests (microhardness, nanoindentation, and tension and compression tests), cold rolling and annealing treatments are presented. Finally, the different microstructural characterization tools (XRD, SEM-EBSD and TEM) used in the current work are introduced.

In chapter 3, the microstructural evolution induced by hydrogen and its effects on the mechanical properties of Ti50A are presented. The hydrogen-induced phase transformation and microstructural evolution were analyzed using combined XRD, SEM-EBSD and TEM characterizations. Two types hydrides (δ-TiH_x, ε-TiH_2) precipitating in the α- phase matrix culd be identified, and the volume fraction of these hydrides with the charging time was investigated. A thorough analysis of the diffraction peaks from XRD enabled to extract information that would

be correlated later with EBSD analysis. We have focused the microstructural analyses on the determination of orientation relationships (ORs) between the α-phase and the hydride δ-TiH_x, which could be confirmed by both SEM-EBSD and TEM analyses. With the aim of understanding the role of hydrogen and hydrides on the deformation mechanisms of Ti50A, microhardness and nanoindentation measurements as well as compression tests were performed and the microstructural evolutions was finely study.

In chapter 4, the hydrogen-induced microstructure evolution and its effects on the mechanical properties of β-21S alloy are introduced. As for the Ti50A, the microstructural evolution was investigated by the combined analyses of XRD, SEM-EBSD and TEM. The variation of the microstructure for the β-21S alloy could be investigated in a wider range of hydrogen concentration, which was indeed till H/M = 0.460, the H/M ratio expressing the concentration ratio between hydrogen and the concentration of metallic elements. SEM and TEM analyses were employed to reveal the formation of martensite α". This hydrogen-induced microstructural evolution on the mechanical properties was investigated by means of compressive and tensile tests, revealed the variation in the mechanical properties interpreted with the concept of "defactant" concept.

In chapter 5, the effects of hydrogen on cold rolling behavior and recrystallization of Ti50A and β-21S alloys are presented. Cold rolling process was performed at two different levels of equivalent strain in order to dissociate the effect of hydrogen on the deformation mechanism. The texture evolution was also studied to reveal the effect of hydrides on grain orientation. This study was completed by applying short annealing treatments with the aim of determining the positive effect of hydrogen on the recrystallization process.

Finally, this main finding of this study on the hydrogen-induced microstructural evolution and its effects on the mechanical properties of α-titanium Ti50A and β-titanium β-21S alloys are given in the conclusion, with emphasis on the cold rolling behavior and recrystallization.

Summary of the contributions of this thesis on the effect of hydrogen on the microstructure and properties of commercially pure Ti and β-metastable titanium alloy :

- observation by SEM-EBSD of two hydrides in hydrogenated Ti50A charged by electrolytic method
- determination of 3 new orientation relationships between the δ-TiHx and the α-matrix
- increase of the TT1 twins in rolled samples owing to the increase of the hydrogen concentration
- correlation between the hydride and TT1 twin formation in deformed hydrogenated Ti50A samples
- observation of α" martensite by means of SEM-EBSD in highly hydrogenated beta metastable β-21S alloy charged by gas method
- determination of the orientation relationships between alpha" martensite and beta phase using SEM-EBSD
- evidence of the acceleration of recrystallization owing to the presence of hydrogen in rolled Ti50A and beta-21S sheets.

Chapter 1 Physical and metallurgical aspects of hydrogen in titanium and titanium alloys

1.1 Introduction

In this chapter, the general background of hydrogen effects on titanium and titanium alloys is introduced. Hydrogen is an element in titanium that stabilizes the high temperature body centered cubic (BCC) β phase, destabilizes the low temperature pseudo-hexagonal close packed (HCP) α phase, and decreases the temperature of the allotropic transformation. The addition of hydrogen also has a significant effect on the microstructure and mechanical properties, and understanding the interaction of hydrogen with titanium-based materials is important so that their properties can be controlled and reliably predicted. The chapter starts from the physical metallurgy of titanium and titanium alloys. Equilibrium and kinetic aspects of hydrogen in titanium and titanium alloys will be discussed secondly. Finally, hydrogen effects on the mechanical properties of titanium and its alloys, especially hydrogen embrittlement will be introduced in detail.

1.2 Physical metallurgy of titanium and titanium alloys

Titanium is a transition metal element with the mass number 47.867 g/mol. The electronic configuration of titanium is $1s^2 2s^2 2p^6 3s^2 3p^6 3d^2 4s^2$ **[BM07].** Compared to other pure metals presented in **Table 1. 1**, pure titanium exhibits the best strength-to-density ratio, the highest melting point and the best corrosion resistance. The density of pure titanium is 4.5 g/cm^3 and the yield strength of its alloy can be higher than 1000MPa **[LW07]**.

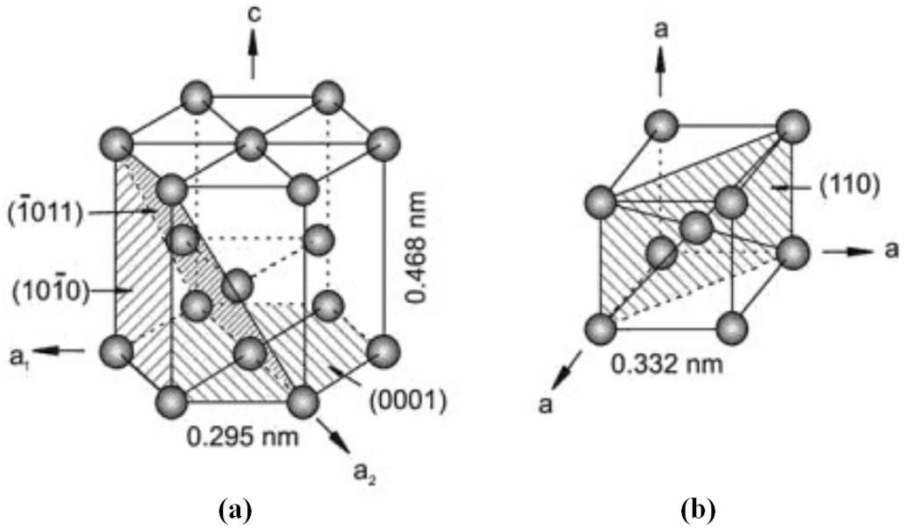

Figure 1. 1 The unit cells show the crystal structure of hcp α phase and bcc β phase, their lattice parameters and most densely packed planes and directions are also illustrated [LP03].

1.2.1 Physical metallurgy of pure titanium

In solid state, atoms forming pure titanium could be arranged in two types of crystal structure, in other words, there exist two allotropes in pure titanium, namely the α-titanium and β-titanium. Each allotrope is only stable within a particular temperature range. The temperature at which one allotrope transforms into the other is called β-transus temperature. The β-transus temperature of pure titanium is 882 ^{o}C. Above the β-transus temperature that domain is called β-titanium and below the β-transus temperature, it is referred to as α-titanium **[LW07, LP03]**.

Table 1. 1 Crucial characteristics of titanium and titanium alloys compared with other commonly used metals and alloys **[LW07]**.

	Ti	Fe	Ni	Al
Melting Temperature (°C)	1670	1538	1455	660
Allotropic Transformation (°C)	882	912	-	-
Crystal Structure	bcc→hcp	fcc→bcc	fcc	fcc
Room Temperature E (GPa)	115	215	200	72
Yield Stress Level (MPa)	1000*	1000†	1000#	500‡
Density (g/cm^3)	4.5	7.9	8.9	2.7
Comparative Corrosion Resistance	Very high	Low	Medium	High
Comparative Reactivity with Oxygen	Very high	Low	Low	High
Comparative Price of Metal	Very high	Low	High	Medium

*Ti6Al4V, †high strength steel, #superalloy, ‡heat-treatable Al alloy.

The crystal structure of pure α-titanium is hexagonal structure, as shown in **Figure 1. 1**(a). The lattice parameters of pure α-titanium are a=0.295 nm and c=0.468 nm, giving a c/a ratio of 1.587, smaller than the ideal ratio of 1.633. The addition of interstitial elements (C, N, O and H) could slightly result in an increase of the c/a ratio in the hexagonal lattice of the α-titanium. The crystal structure of pure β titanium is body centered cubic (bcc) structure. The lattice parameter of pure β-titanium at 900°C is a=0.332 nm, as presented in **Figure 1. 1**(b) **[LP03]**. The properties of pure titanium are highly dependent on the microstructure, thus on the existence of the two allotropes **[LP03].** For instance, the anisotropy in hexagonal structure leads to the elastic anisotropy in α-titanium. The Young's modulus along c-axis is 145GPa and only 100GPa along a-axis in α-titanium. Meanwhile, the elasticity anisotropy of β phase has been reported in β-Ti and its alloys, as given in **Table 1. 2.** In addition, both diffusion and plastic deformation are closely connected with the respective crystal structure. The diffusion in more densely packed pseudo-hcp structure

is much slower than in bcc structure. Therefore, compared to β-titanium, α-titanium has a superior creep performance.

Table 1. 2 Elasticity anisotropy of β phase in β-Ti and its alloys reported in the references

Referances	Elasticity Constants [GPa]			Anisotropy Coefficient	Alloy
	C_{11}	C_{12}	C_{44}	$A=2C_{44}/(C_{11}-C_{12})$	
Martin, 2012. [**M12**]	100	70	36	2.40	Ti 17, Ti5553
Petry et al., 1991.[**PH91**]	134	110	55	4.58	Pure
Herbig, 2011. [**H11**]	153	101	57	**2.19**	β21S
Ogi et al., 2004. [**OK04**]	97.7	82.7	37.5	5.00	Pure
Fréour et al., 2011. [**FF00**]	167	115	44	1.69	Ti17
Tane et al., 2008. [**TN11**]	65.1	40.5	32.4	2.63	Ti-29Nb-Ta-Zr
Raghunathan et al., 2007 [**RS07**]	140	128	50	8.33	Ti-10V-2Fe-3Al

1.2.2 Categories of titanium alloys

Depending on their influence on the β-transus temperature, the alloying elements of titanium are classified as neutral, α-stabilizers, or β-stabilizers. The elements like Al, Ga, B, Sc, La, Ce, C, O and N that extend the α phase field to higher temperatures are called α stabilizers. While alloying additions of V, Mo, Nb, Hf, Ta, Mn, Cr, Cu, Ni, Fe, Co, Au, Ag, W and H can lower the β-transus temperature and cause a stabilization of the β phase down to low temperatures, thus are regarded as β stabilizers. Elements like Zr, Hf and Sn are referred as neutral elements since they have negligible influence on the stability of α and β phase **[LW07]**. Therefore, based on the alloy composition, titanium alloys are divided into three groups, with the predominant room temperature groups being: α or near-α, α+β alloys, and β alloys.

The α-Ti alloys comprise commercially pure (cp) titanium and alloys exclusively alloyed with α-stabilizing and/or neutral elements. If minor fractions of β-stabilizing elements are added, they

are referred to as near-α alloys. α- and near α-titanium alloys are primarily used in the chemical and process engineering industry. Hence excellent corrosion behavior and deformability are of prime concern while high (specific) strength only ranks second. To reach the required strength levels of commercial pure (cp) titanium grades, only oxygen is intentionally alloyed, while other elements like carbon and iron are considered impurities brought into the alloy via the manufacturing process. Near-α titanium alloys are the classical elevated-temperature alloys. This alloy class is ideal for elevated-temperature since it combines the excellent creep behavior of α alloys with the high strength of α+β alloys.

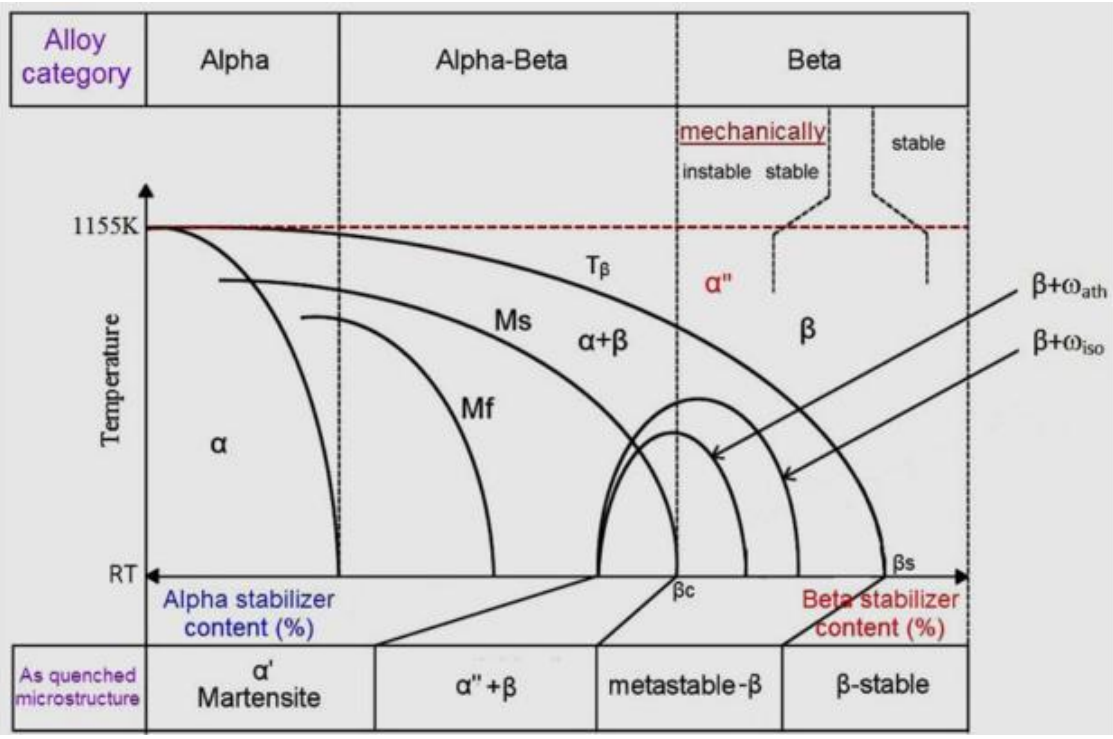

Figure 1. 2 Pseudo-binary phase diagram of Ti-alloys with the deformation products of the β-phase. Here, β_c is the critical minimum β stabilizer amounts for near β or metastable β alloys to retain β phase completely on quenching from β phase field and β_s is the minimum amounts of β stabilizer for stable β alloys; T_β, RT, M_s and M_f refer to the β-transus temperature, room temperature, martensite start and finish temperatures, respectively [ZJY2014].

Beta alloys can be further divided into stable and metastable alloys, with stable alloys having a unique β-phase microstructure after air cooling to room temperature and metastable alloys having α-precipitates in the β-matrix after air cooling or quenching and aging, as schematically shown in **Figure 1. 2 [ZJY14]**. β titanium alloys are the most versatile class of titanium alloys. They offer the high strength to weight ratio and very attractive combinations of strength, toughness, and fatigue resistance at large cross sections. Some of the disadvantages compared to the α+β alloys

are the increased density owing to the heavy addition elements such as V, Nb, Mo, W, a rather small processing window, and the higher cost. One of the materials used in the present work is the β-21S alloy, which offers the good cold formability, weldability, oxidation resistance and creep strength. It is commonly used in aerospace applications include engine exhaust plug and nozzle assemblies due to its excellent oxidation resistance with creep properties comparable to Ti-6Al-4V.

1.2.3 Phases in titanium alloys

Phase is a region of a thermodynamic system, which could be of the same crystal structure and the same composition, and exhibit uniform properties **[PE09]**. At different temperature and pressure conditions, upon addition of alloying elements, different phases can be acquired.

1.2.3.1 α phase in Ti

The crystal structure of the α-phase can be represented by two atoms at (0, 0, 0, 0) and (1/3, 1/3, -2/3, 1/2) positions in the hcp unit cell in the space group of *P6/mmm*. Compared to cubic lattice, the hexagonal structure with low symmetry has fewer available slip systems to accommodate arbitrary imposed strains in polycrystalline aggregates. Slip only occurs in the slip plane and along the slip direction. The magnitude and direction of slip are represented by the Burgers vector. The slip shear can happen in two directions with an unfixed shear strain, which is dependent on the amount of shear**.** After slip, the orientation of the whole crystal is preserved. The plastic deformation in hcp α phase primarily occurs through slip of dislocations with either <a> or <c+a> Burgers vectors, as indicated in **Figure 1. 3** **[MP07]**. At room temperature, in pure α-titanium, the prismatic slip <a>-P ($a/2<11\bar{2}0>\{10\bar{1}0\}$) is currently recognized as the easiest slip mode. <a> dislocation with Burgers vector $a/2<11\bar{2}0>$ may also glide on basal plane {0001} or on a first order pyramidal plane $\{10\bar{1}1\}$ (π1), which are defined as secondary slip systems [**C81, RF12, BD15, BDC15, CG17**]. Meanwhile, cross-slip of <a> dislocations in first-order pyramidal plane $\{10\bar{1}1\}$ was also observed [**BD15, CG17**].

However, to accommodate tensile or compression strains along the c-axis, either pyramidal <c+a> slip (with its associated higher critical resolved shear stress) or deformation twinning must be activated. Unlike slip, twinning occurs in only one direction, and the crystallography is such that elongation is generated in one direction and contraction in others. The strain produced by the

twinning shear depends on the twinning system and the value of c/a. **Figure 1. 3** gives the observed twinning systems in α-titanium. The three most common twins observed in titanium, are the $\{11\bar{2}2\}<11\bar{2}\bar{3}>$ compression twin and $\{10\bar{1}2\}<\bar{1}011>$, $\{11\bar{2}1\}<\bar{1}\bar{1}26>$ tension twins **[KK00]**. The other less observed compression twin $\{10\bar{1}1\}<\bar{1}012>$ can be activated under severe plastic deformation under compression load, e.g. strain>25% at room temperature **[PB70]**, or under low compression load along the c-axis at high temperature, above 400°C **[IO80]**. Thus, deformation twinning has an important impact on mechanical properties such as the material formability **[PE88]**, texture development **[CY05, SK03]**, strain hardening **[Y81]** and ductility **[CL10]** in α-titanium or near α-titanium alloys.

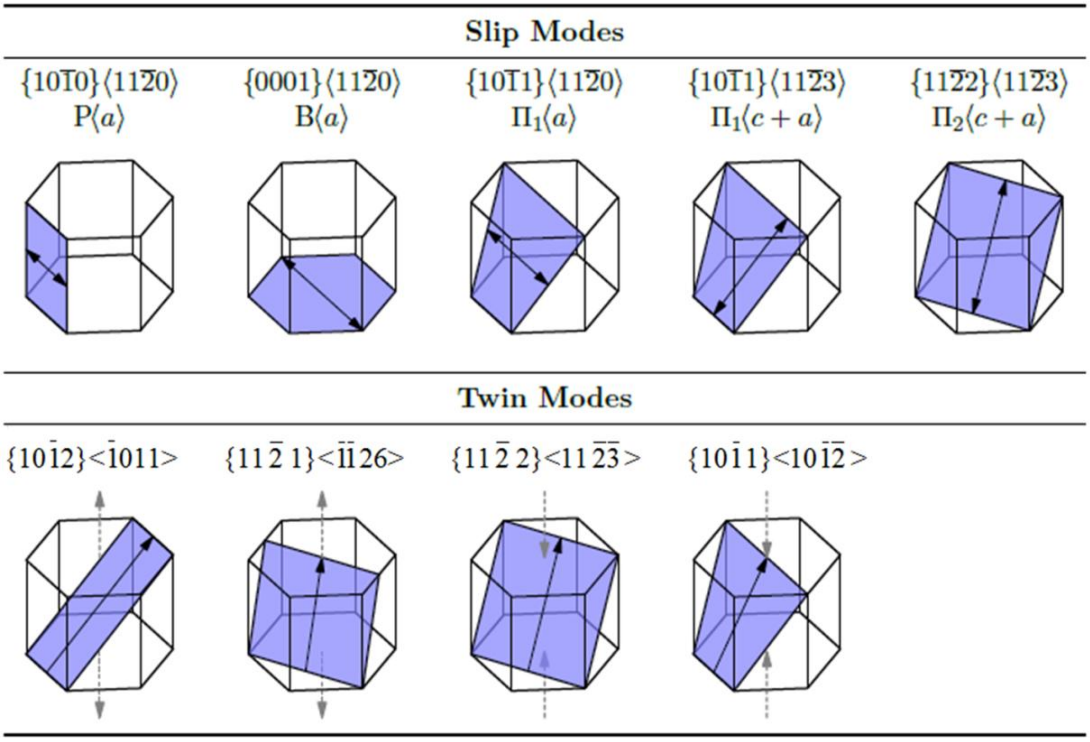

Figure 1. 3 Slip and twin modes in hcp metals. The arrow on the plane indicates the shear direction. Note that for the twin modes the shear is unidirectional, depending on the direction of stress, which is also shown by arrows.

1.2.3.2 β phase in Ti

The crystal structure of the β-phase is body centered cubic (bcc) which can be represented by two atoms at (0, 0, 0) and (1/2, 1/2, 1/2) positions in the unit cell and classified as $Im\bar{3}m$ space group. Compared to the hcp structure, the bcc structure is less densely packed, in which atoms may vibrate more severely when temperature is elevated. The β-phase is more stable than the α-phase

at higher temperature. Upon cooling from the β-phase field, the {110} planes of the bcc β-phase (most densely packed) transform into the basal planes {0001} of the hexagonal α-phase. The distance between the basal planes in α is slightly larger than the corresponding distance between the {110} planes in the β lattice. Therefore, the β/α transformation causes a slight atomic distortion, as indicated in **Figure 1. 4**. This leads to a slight contraction of the c-axis relative to the a-axis in the hcp α and reduces the c/a-ratio below the value of ideally close packed hexagonal atomic structures. Meanwhile, the corresponding β/α phase transformation can be described by an orientation relationship referred as Burgers relationship **[LW07]**: $\{0001\}_\alpha$ // $\{110\}_\beta$ and $<1120>_\alpha$ // $<111>_\beta$.

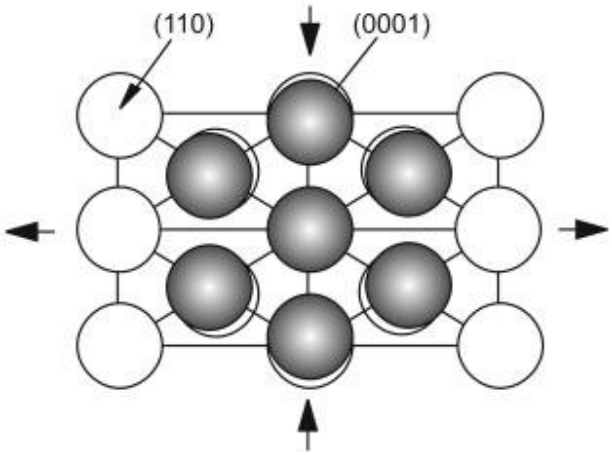

Figure 1. 4 β/α transformation according to Burgers relationship [LW07].

It is well known that in bcc structure, slip occurs in the closest packed <111> direction and the Burgers vector is a/2 <111>. However, identifying the specific planes on which slip occurs in bcc phase is less straightforward. The planes with the largest interplanar spacing are {110} followed by {112} then {123}. Therefore, the slip in pure β titanium could occur on either {110}, {112} or {123} planes, as indicated in **Figure 1. 5** **[WB13]**. In total, there exist 48 slip systems in bcc structure.

In β-titanium alloys, depending on the alloy composition, twinning deformation can also be activated. Generally, there exist two twinning systems $\{11\bar{2}\}<11\bar{1}>$ and $\{332\}<11\bar{3}>$ in metastable and/or in stable β-titanium alloys **[HL86, SL13]**. It has been reported that the deformation of $\{332\}<11\bar{3}>$ twinning in metastable β-titanium alloys caused a large elongation through the significant work hardening due to the dynamic grain refinement **[MH13]**.

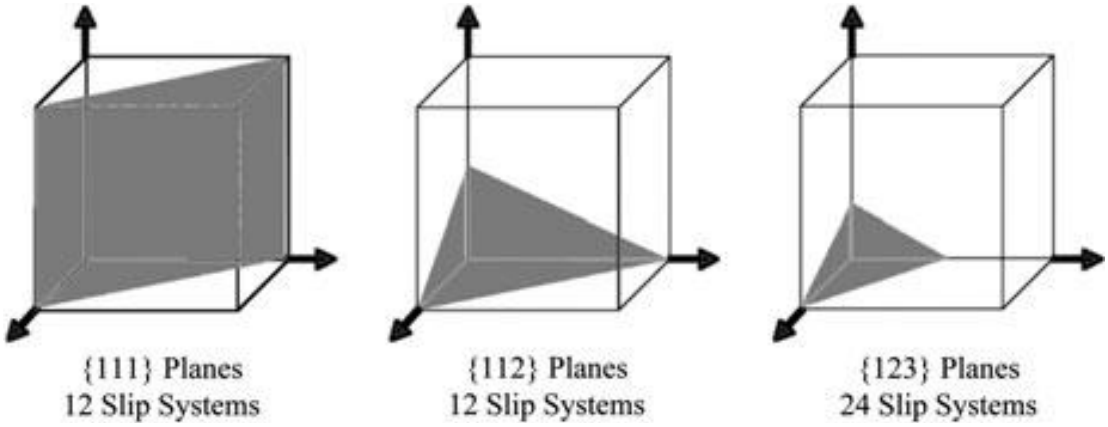

Figure 1. 5 Slip planes and number of slip systems in bcc crystals.

1.2.3.3 Metastable Phases

In addition to α and β equilibrium phases, metastable phases can be produced in titanium and titanium alloys, depending on thermo-mechanical processing. Metastable phase is the compromise of thermodynamics, the whole system is tending to the lowest Gibbs free energy state, and kinetics, i.e., how fast the system could achieve the lowest Gibbs free energy state **[PE09]**. Because only small driving force is required and no diffusion or only short range diffusion is necessary/possible, metastable phase can be formed in short time.

a) α' phase in Ti

The α' phase is a hcp type structure martensite, the metastable phase in pure α titanium, α-titanium alloys and near α-titanium alloys. α'-phase can be formed by martensite transformation upon fast cooling from the single β phase field. Actually, α' can be treated as supersaturated α phase in dilute titanium alloy. Depending on the species and content of solute element, α' phase exhibits different morphologies and contains different internal substructures **[SMK10]**, as shown in **Figure 1. 6a**.

b) α'' phase in Ti

When the amount of β phase stabilizers (alloying elements lowering the β-transus temperature) reaches a critical value, α" phase instead of α' phase is produced in the as-quenched titanium alloys. The α"-phase has a C-centered orthorhombic crystal structure **[AR96]**, usually exhibits acicular morphology and contains mainly twin substructures **[DF76]**, as shown in **Figure 1. 6b**. It is formed by martensite-type transformation. As the amount of β-phase stabilizer increased, the

martensite start temperature (Ms) deceases rapidly and therefore the α"-phase is more difficult to form. The martensite transformation is a diffusionless, shear (displacive) solid state structure transformation, which is commonly driven by a change in temperature or mechanical deformation. Indeed, though the cooling rate is the well-known parameter, mechanical deformation resulting from either applied stress or locally induced stress can also induce martensite transformation in metastable β-titanium alloys **[BM07, LW07]**.

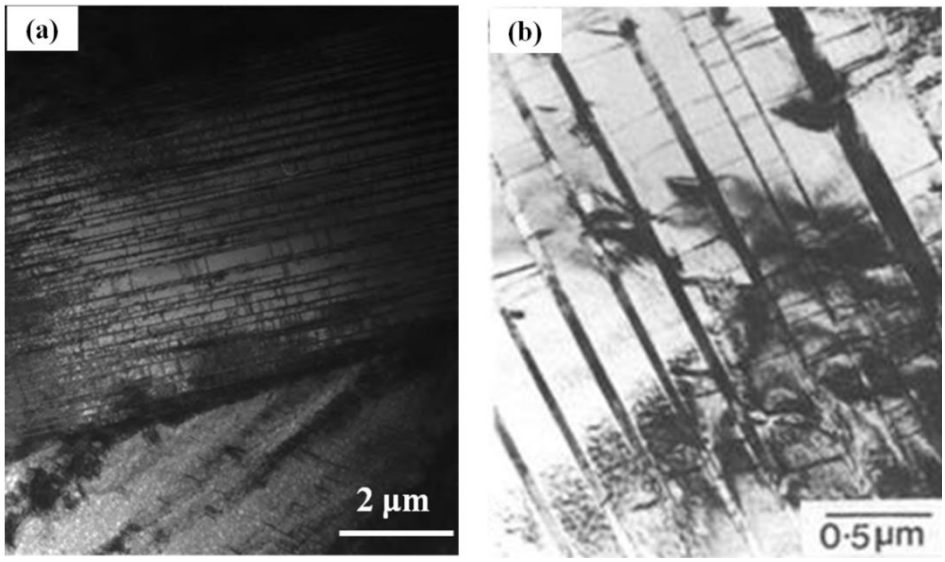

Figure 1. 6 TEM image of (a) α' martensite and (b) α'' martensite

c) ω phase in Ti

The ω-phase can be formed in titanium alloys rather than the α"-phase, on the condition that the as-quenched titanium alloy contains high concentration of β phase stabilizers [**BW13, ZS13**]. The ω-phase can be treated as a transition phase between the α- and β-phases, and it exhibits a hexagonal structure.

Generally, there exist two types of ω phase in titanium alloys, namely the athermal ω phase and the isothermal ω phase. The athermal ω phase is formed by a diffusionless transformation mechanism, and its formation cannot be avoided no matter how fast the cooling rate is. The size of athermal ω phase is always small, usually from several nanometers diameter to no more than 20 nanometers diameter **[ZS13]**, as shown in **Figure 1. 7**a. The athermal ω phase and parent β matrix obey following orientation relationships:

$$\{0001\}_{\omega} // \{111\}_{\beta} \text{ and } <11\bar{2}0>_{\omega} // <1\bar{1}0>_{\beta}$$

Compared to the athermal ω phase, the isothermal ω phase is formed during isothermally aging of the as-quenched titanium alloys. Therefore, the diffusion of solute atoms occurs during isothermal ω phase transformation. The morphology of isothermal ω phase may be cuboidal or ellipsoidal (shown in **Figure 1. 7**b and c) depending on the coherency of isothermal ω phase and parent β phase **[BW68]**. Similar to stress-induced martensite (SIM) α", plate-like ω phase can be produced in the β-stabilizer alloys upon deformation **[SZM13],** as shown in **Figure 1. 7d**.

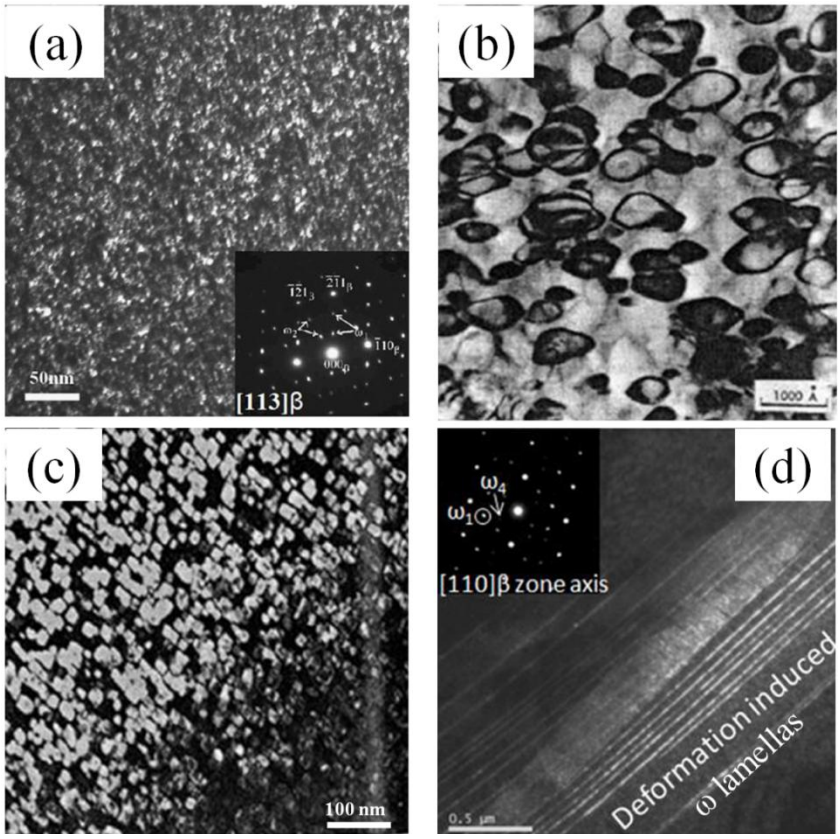

Figure 1. 7 The typical TEM micrographs and corresponding diffraction patterns of three types ω phase. (a) nano-size athermal ω particles in quenched Ti-Mo alloys; (b) ellipsoidal morphology isothermal ω phase in Ti-Mo system; (c) cuboidal morphology isothermal ω phase in Ti-V alloys; (d) plate-like deformation induced ω phase in Ti-12Mo alloy upon strain.

1.3 Physical and metallurgical aspects of hydrogen in titanium and titanium Alloys

Hydrogen is a unique alloying element in titanium alloys because, unlike other elements, it can be easily added and removed without melting. Titanium and titanium alloys have a large affinity for hydrogen, being capable of absorbing up to 60 at.% hydrogen at 600 °C, and even higher contents have been even achieved within titanium at lower temperature **[SM87].** Recently a better understanding of the titanium metallurgy has demonstrated that, hydrogen as a temporary alloying element can be used to improve the processing, microstructure and mechanical

properties of titanium alloys **[FS04, ZZ97].** The addition of hydrogen as an alloying element has a beneficial effect on hot workability **[WS99]**, because it can lead to a decrease in the strength at elevated temperatures but a significant increase in the ductility. Thus, operations involving hot processing, such as forging, hot pressing, superplastic forming, powder consolidation **[ZD10]** and composite processing are all facilitated.

1.3.1 Equilibrium aspects of dissolved hydrogen in titanium and titanium Alloys

1.3.1.1 Interstitial site occupancy of hydrogen

Hydrogen is the lightest element on the periodic table, with an atomic weight of 1.00794 g/mol. When hydrogen atoms enter into metals, they always occupy the interstitial sites of crystal lattice. Generally, there exist two types of interstitial sites in titanium, octahedral and tetrahedral sites. For example, the bcc lattice (β phase) has three octahedral interstitial sites per titanium atom (at the centers of the cube faces and of the cube edges) and six tetrahedral interstitial sites per titanium atom at (1/2, 1/4, 0) and equivalent positions. In addition, it can be noted that, in bcc structure, the tetrahedral sites are larger compared with octahedral sites. Compared with the bcc structure, the larger atom packing density leads to the smaller number of interstitial sites in hcp lattice. There are 4 tetrahedral sites and 2 octahedral sites per unit hcp cell, and the octahedral positions have the larger free volume. **Figure 1. 8** shows the octahedral and tetrahedral sites in HCP and BCC lattice, respectively.

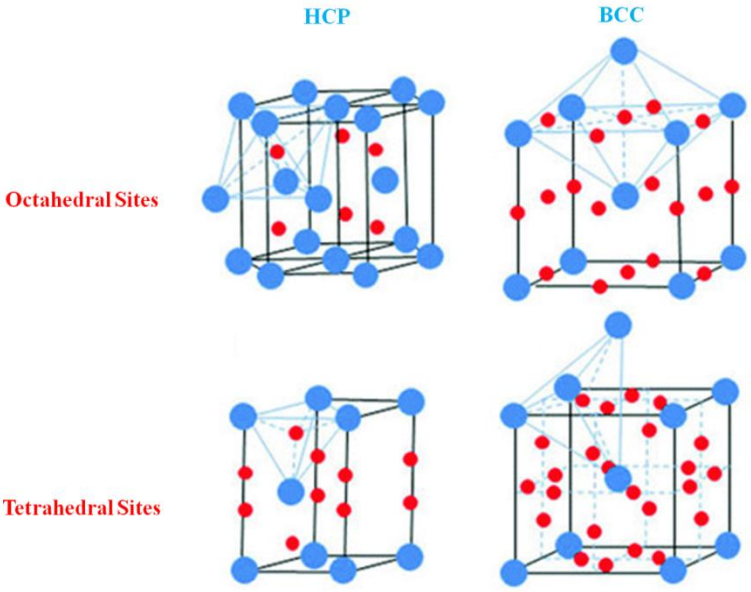

Figure 1. 8 Interstitial sites in bcc and hcp lattice. (a) tetrahedral site in bcc lattice; (b) octahedral sites in bcc lattice; (c) tetrahedral sites in hcp lattice and (d) octahedral sites in hcp lattice.

Table 1. 3 Interstitial sites for hydrogen in hcp and bcc lattice

	Phase	Size of T sites, nm	Size of O sites, nm	Number of T sites	Number of O sites	Atom packing density
α-Ti	hcp	0.034	0.062	4	2	74 %
β-Ti	bcc	0.041	0.022	12	6	68 %

*r[H] = 0.046 nm

First principle density functional theory (DFT) calculations have found that hydrogen is more stable in an octahedral site at 0 K in α-Titanium **[XV07, LG10, CH11]**. That hydrogen atoms occupy interstitial positions in titanium lattice has been demonstrated by neutron diffraction **[SC01].** Since the molar volume of a hydrogen atom is much smaller than that of a titanium atom, the observed expansion of the crystal lattice upon dissolution of hydrogen is evidence that the titanium-hydrogen solution is not substitutional. For a random distribution of hydrogen atoms in interstitial sites of a titanium lattice, the volume change due to the insertion of hydrogen atoms can be measured by the change of lattice parameter of titanium. **Table 1. 3** collects information on the location of dissolved hydrogen in titanium.

The occupation by hydrogen atoms at interstitial sites leads to a thermodynamic description of the dissolved hydrogen in terms of Fermi-Dirac statistics. Thus, the chemical potential of dissolved hydrogen μ_H is related to its thermodynamic activity a_H as expressed by eq. **1.1 [S78]**

$$\mu_H = \mu_H^0 + RTln(a_H) = RTln(\frac{\gamma\theta_l}{1-\theta_l}) \quad (1.1)$$

Here, μ_H^0 indicates the chemical potential of dissolved hydrogen under standard conditions (i.e. T=295 K and hydrogen pressure of 1 bar), a_H is the thermodynamic activity of hydrogen, γ is the activity coefficient of dissolved hydrogen, and θ_l is the interstitial sites occupancy of hydrogen in crystal lattice ($\theta_l = n_H/n_{sl}$, where n_H is the number of dissolved hydrogen atoms and n_{sl} is the number of interstitial positions that produce the lowest Gibbs free energy state). The important consequence of this is that the value of the chemical potential u_H depends on the interstitial sites occupancy of hydrogen in the crystal lattice. As presented in **Table 1. 3**, there exist a large number of interstitial sites in the β-phase, which leads to a higher solubility of hydrogen in β-titanium alloys. For example, the critical hydrogen concentration in a single β-phase titanium alloys is H/M = 0.67 (H/M indicates the hydrogen to metal ratio) **[AH94]**.

1.3.1.2 Hydrogen-Titanium interactions

As it was well documented by Oriani **[O93]**, the dissolved hydrogen atoms strongly perturbs the electronic structure of the matrix titanium. That is to say, the entry of hydrogen changes the density of states at the Fermi surface and causes shifts of the energy bands in titanium. Generally, the electron energy bands are long-range interactions between the dissolved hydrogen atoms, while there are also short-range interactions among the hydrogen atoms due to the localized heaping up of Fermi electrons around the hydrogen protons [**S78**].

Since hydrogen changes the local and the global electronic structure of the matrix titanium, and increases the mean separation between the titanium atoms, it is not surprising to find that the cohesive force between the titanium atoms is affected by the presence of hydrogen. Although, no experiment has been devised to measure this effect, several different theoretical approaches demonstrate that hydrogen reduces the cohesive forces in titanium **[MB82, DB84, ZW00]**. For example, McMullen et al. **[MS87]** used an effective-medium model to calculate the force required to rigidly separate two halves of a 3d-metal crystal, and have shown that hydrogen decreases the necessary forces for Ti, V, Mn, Fe, Cu and Ni. However there are still controversies according to the alloy composition, hydrogen-charging method and mode of characterizations used by the researchers, which explained the different mechanisms proposed in the literature that will be explicated in a following paragraph.

1.3.1.3 Interaction of hydrogen with structural defects

The interactions of hydrogen with structural defects are important and often dominant in determining the mechanism of hydrogen embrittlement. Nevertheless, in general, these interactions are far less understood at a fundamental level than the behavior of hydrogen in perfect lattices. Within the past decade, however, research in the area has been stimulated on a broad front by both technological and scientific developments **[PK06]**. **Figure 1. 9** schematically shows possible defects in pure metal and their interactions with hydrogen.

a) Point defects

Vacancy is the simplest defect in metal, consisting of an empty lattice site with modest peripheral relaxation. The interaction between hydrogen and vacancy has been investigated in depth using a combination of experimental and theoretical methods **[MM02, LK05, PA16]**. When the surface

chemisorption state of hydrogen is energetically favored over interstitial solution, hydrogen can be driven to enter the vacancy.

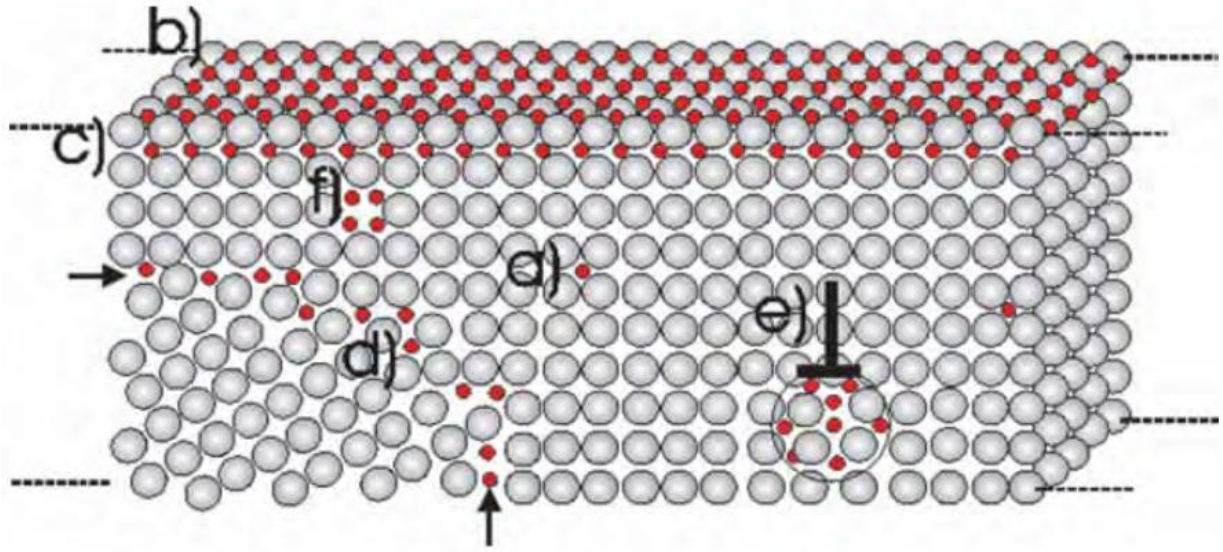

Figure 1. 9 Schematic presentation of defects in metal and accumulation of hydrogen atom in the low-concentration range. Along with the conventional hydrogen solubility in the lattice matrix (a), there are trap sites for hydrogen atoms on the surface (b) and in subsurface (c) sites. At edge dislocations (position indicated by ⊥) (e) a cylindrically shaped region of hydrogen segregation is expected. Also, grain boundaries (d) and vacancies (f) solve hydrogen differently than does the matrix [PK06].

The occurrence of hydrogen trapping at vacancies has been demonstrated in a number of metals by positron annihilation, a probe specifically sensitive to the presence of vacancies. In the absence of hydrogen, during the annealing treatment, vacancies disappear until the temperature is raised sufficiently for them to become mobile. However, in the presence of dissolved hydrogen, the equilibrium vacancies concentration is increased, proving a driving force for recovery to occur at lower temperatures **[G06]**.

Recently, researchers have found that vacancies may play a role in hydrogen embrittlement. For example, one set of experiments has established that a superabundant vacancy formation can be induced by the dissolved hydrogen in a number of metals, such as Pd, Ni, Cr, etc. **[F03, FO94]**. The estimated vacancy concentration, C_H, in these systems can reach a value as high as 23 at.% at high temperature **[F03]**. A conclusion drawn from these experiments by Fukai is that hydrogen atoms, originally at interstitial positions in the lattice, are trapped at vacancies in multiple numbers with rather high binding energies.

b) Dislocations

Dislocations can be produced in titanium and titanium alloys by plastic deformation and many other processes. An understanding of the interactions between hydrogen and dislocations is of crucial importance in titanium-based materials due to these effects on plastic flow behavior and hydrogen mobility. The interaction between hydrogen and dislocations is very complex; hydrogen can be trapped at dislocations and also be transported by mobile dislocations **[DM15].** For example, the mobility of hydrogen can be substantially reduced by its attractive interactions with dislocations. These effects are usually treated within the framework of simple trapping models, which assume a constant interaction energy **[O70]** between hydrogen and dislocations. On the other hand, hydrogen-enhanced dislocation mobility was detected in a series of transmission electron microscope (TEM) studies of several metals, including titanium, by Robertson and co-workers **[RB86, RR90, SR88]**.

Recent developments in the study of hydrogen effects on dislocation nucleation using in situ electrochemical nanoindentation **[GG10, BV10, GK14]**, have shown that hydrogen reduces the required stress for the onset of plasticity, i.e. homogeneous dislocation nucleation by reduction in the shear modulus, dislocation line energy and stacking fault energy **[BV10]**. The change in shear modulus can be related to reduction in crystal cohesion whereas the reduction in dislocation line energy and stacking fault energy are explained by the defactant **[K07]** concept, i.e. reduction in the defect formation energy in the presence of hydrogen. Thus, neither hydrogen-enhanced decohesion nor hydrogen-enhanced plasticity, but the reduction in the cohesion and defect formation energy are responsible for hydrogen embrittlement **[GK14]**.

Moreover, the effect of hydrogen on the activation volume and density of mobile dislocations has been investigated under simultaneous hydrogen cathodic charging conditions in iron **[WH13].** It was shown that, the effective activation volume decreases immediately with hydrogen charging; the density of mobile dislocations in the hydrogen-charged iron has a lower rate of exhaustion than in the hydrogen-free one; moreover the thermal activation energy decreases and the average dislocation velocity increases as a function of hydrogen concentration.

c) Grain boundaries

Grain boundaries (GBs) are the second major class of extended defects in crystalline metals, and the interaction of hydrogen with GBs are crucial to the influence of hydrogen on mechanical

properties. In annealed polycrystalline materials, grain boundaries have a crucial impact on the transport and segregation of hydrogen as well as on the fracture mechanisms.

Based on several studies **[BC95, LB87, LL86, TL82, HL91]**, it is reported that grain boundaries enable short-circuit diffusion and thus they accelerate hydrogen ingress and transport through the material. Brass et al. **[BC89]** have shown that there are cases of preferential diffusion along grain boundaries in some stable fcc structures, such as nickel or stainless steels particularly at low temperatures. Louthan et al. **[LD75]** and Tseng et al. **[TL88]** maintained that the acceleration of hydrogen diffusion along GBs is caused by the geometrically necessary dislocations (GNDs) stored at, or at the proximity of, in these interfaces. However, it was also showed that these defects represent trapping sites for hydrogen **[TM08]**, inducing a slowdown of its diffusivity **[YC91].**

Generally, both hydrogen diffusion and trapping mechanisms depend mainly on the nature of grain boundaries **[OC12, DB16]**. The high-angle random boundaries are considered as disordered phase where the hydrogen diffusion is accelerated, while the low-angle boundaries and special boundaries constitute a potential zone for hydrogen trapping due to the high density of trapping sites as dislocations and vacancies. The predominance of one phenomenon over the other depends on several parameters, such as the grain size, the probability of grain boundary connectivity, the grain boundary energy and the excess of free volume in the GBs **[YC91, TM08, OC12, DB16].**

1.3.2 Kinetics aspects of dissolved hydrogen in titanium and titanium Alloys

1.3.2.1 Entry of hydrogen into titanium and titanium Alloys

a) Entry of gaseous hydrogen

The enthalpy of solution of hydrogen from the molecular gas into the metal is composed of two aspects: the energy of dissociation of the molecule, which is, of course, independent of the nature of the metal; and the energy of interaction between the dissolved hydrogen atoms, and between the hydrogen and the metal.

The transition between the gaseous molecular H_2 state and the lattice-dissolved H atom state must follow the sequences: impingement of H_2 molecules on the surface, adsorption of the H_2 molecules, dissociation into adsorbed H atoms, and diffusion of H atoms into the lattice. The rate-determining step for the whole process was found to be the dissociation of the adsorbed H_2

molecules **[AG74].** Each of these steps strongly depends on the atomic topography of the surface i.e., atomic steps, kinks on the steps, and surface vacancies. For example, the adsorption of the H_2 molecule on titanium and its dissociation are strongly impeded by pre-adsorbed species such as oxygen, nitrogen and atomically adsorbed hydrogen. It should be noted that whereas the absorbed impurities (C, O, and N) can affect the rate of hydrogen ingress, they do not affect the equilibrium hydrogen concentration in the lattice at a given temperature and gas fugacity **[O93]**. And if there already exists a hydride phase near the input surface, the penetration of dissolved hydrogen deeper into the material is seriously impeded by the low diffusivity of hydrogen in the hydride.

For titanium and titanium alloys, hydrogenation by gas method consists of the following procedures: firstly the specimens are placed in the charging furnace; subsequently the furnace temperature is increased to a predetermined value for several minutes to dissolve any surface oxides; then H_2 gas is charged at a specific pressure, and maintained for sufficient time to reach equilibrium; finally the specimens are cooled at a specific cooling rate. In this method, by controlling the partial pressure of hydrogen and charging time, different hydrogen concentrations can be obtained. It should be mentioned that, the final hydrogen concentration in the sample is not only dependent on the pressure during charging, but also on the pressure in the furnace chamber during cooling and on the cooling rate. Experimental confirmation of this was evident in the decrease of hydrogen gas pressure during cooling under a constant flow rate **[TR01].**

Although hydrogenation by gaseous method is an efficient way to introduce hydrogen into specimens, a problem referred as hydrogen safety arises due to its ease of leaking as a gaseous fuel, low-energy ignition, wide range of combustible fuel-air mixtures, especially at high temperature. Therefore, safeguard procedures must be provided when using hydrogen gaseous as the source of hydrogen.

b) Entry of hydrogen by electrolytic method

There are many instances that metals may absorb considerable amounts of hydrogen derived from the aqueous environments. For aqueous electrolytes, the deposition reaction on the surface of the negatively charged electrode can occur by the reduction of water or of hydronium ion.The rate of hydrogen entry depends on many variables: material composition, surface conditions, electrolyte composition, cathodic current density, electrode potential, temperature, pressure, etc. **[B04]**.

The cathodic evolution of hydrogen from aqueous electrolytes is known to proceed in several successive stages **[B54, B43 and B04]**. Depending on the electrolyte, the overall hydrogen evolution reaction can be expressed by the following **equations 1.2** or **1.3**:

$$\text{(a) } 2H_3O^+ + 2e^- \rightarrow H_2 + 2H_2O \quad \text{(in acid solutions)} \qquad \textbf{(1.2)}$$

$$\text{(b) } 2H_2O + 2e^- \rightarrow H_2 + 2OH^- \quad \text{(in alkaline solutions)} \qquad \textbf{(1.3)}$$

Therefore, the influx of hydrogen into the titanium and titanium alloys consists of the following simple steps: 1) deposition of hydrogen ions onto the electrode surface; 2) consumption of one electron by each hydrogen ion to form atomic hydrogen; 3) adsorption of atomic hydrogen on the electrode surface; 4) dissolution of hydrogen at the electrode surface; 5) diffusion of atomic hydrogen into the material through the lattice. Usually only a small portion of hydrogen liberated on the cathode surface enters into the sample. To promote the entry of hydrogen into metals, a poison (e.g. thiourea) is added to the electrolyte to prevent hydrogen recombination.

According to the Fick's second law, the distribution of hydrogen in the crystal lattice changes with time. Therefore, the characteristic diffusion time to achieve equilibrium throughout the specimen volume is so long that there always exists marked hydrogen concentration gradients in the materials. The total hydrogen concentration C_H can be determined via the Faraday's law **[D15]** as expressed in **equation 1.4**:

$$\Delta C_H = It/n_{Ti}F \qquad \textbf{(1.4)}$$

where *I, t,* n_{Ti} and F indicate the current density, charging time, molar mass of Ti and Faraday's constant, respectively. To ensure uniform distribution of hydrogen throughout the volume of the specimen, annealing treatment can be undertaken following the electrochemical charging process.

It is worth noting that at the point of lattice expansion, the equal concentration of hydrogen may be injected into the metal by equilibrating with high-pressure molecular gas or by subjecting the metal to cathodic charging, the internal thermodynamic state of the dissolved hydrogen will be different in these two conditions **[O93].** In the first case, the large pressure upon the metal will decrease the expanding effect of interstitial hydrogen by compressing the metal, whereas in the latter case there will not be any decrease of the intrinsic expanding effect because of the absence of the pressure on the external surface of the metal.

1.3.2.2 Hydrogen diffusion in perfect crystal lattice

It is well known that hydrogen atoms in Ti and Zr alloys diffuse more rapidly than any other solute (e.g. C, N and O) due to its lower activation energy for diffusion **[AV78, WS99, and FS04]**. The diffusion coefficient D_H can be expressed by the Arrhenius **equation 1.5**:

$$\mathrm{D_H} = D_0 \exp\left(-\frac{Q}{RT}\right) \qquad \textbf{(1.5)}$$

where D_0 is the maximum diffusion coefficient (at infinite temperature; m^2 / s), Q is the activation energy for diffusion (J $atom^{-1}$), T is the absolute temperature (K), R is the Boltzmann constant. The diffusion behavior of hydrogen in titanium and its alloys depends on many factors, such as the alloy composition, lattice structure, grain boundaries, internal stresses, vacancy concentrations etc. **[CD00, P97, and P94].**

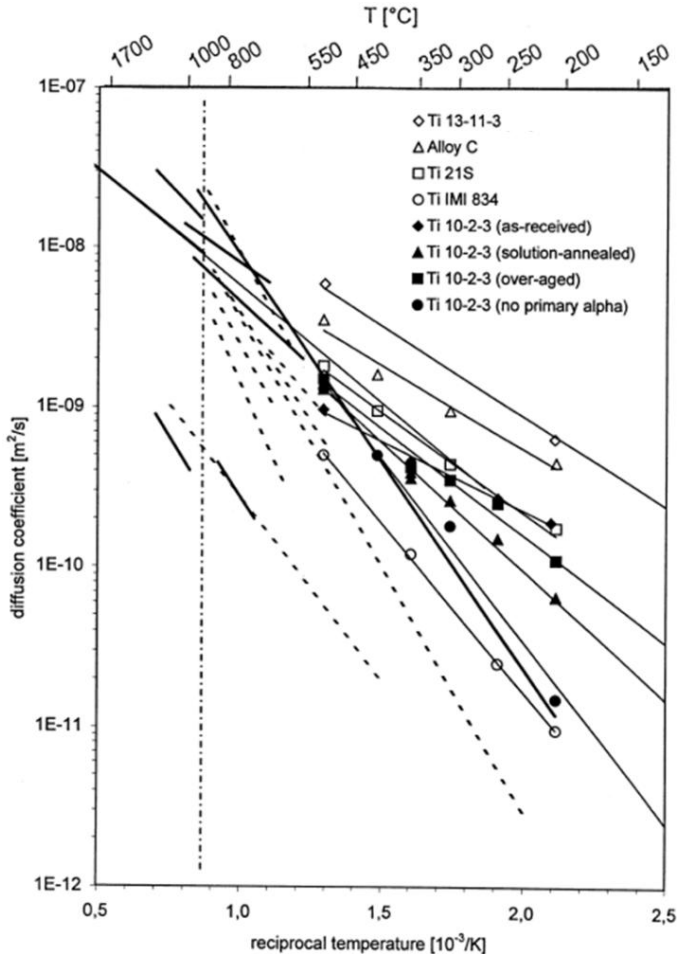

Figure 1. 10 Hydrogen diffusion coefficient in titanium and titanium alloys [CD00]. The solid lines and dashed lines represent the data for pure β titanium and pure α titanium [S00, W97]. The vertical line displays the beta-transus temperature of 882.8 °C.

Because of the densely packed atoms in hcp α-titanium, hydrogen diffusion is considerably lower than in bcc β-titanium: hydrogen diffusion coefficient in α-titanium is of the order of one magnitude smaller than that of β-titanium. **Figure 1. 10** presents the diffusion coefficient of hydrogen in titanium and its alloys collected from the literature **[W97, CD00 and S00]**. By extrapolation till room temperature, we obtained from **Figure 1. 10**, the value of hydrogen diffusion coefficient for the stable β titanium Alloy C (Ti-35V-15Cr) is $8.0 \times 10^{-9} cm^2/s$ at ambient temperature **[CD00]**, while the diffusion coefficient of hydrogen is about $2.6 \times 10^{-10} cm^2/s$ in commercial pure titanium **[W97]**.

The diffusivity of hydrogen in titanium is a function of hydrogen concentration, and it is generally decreasing with increasing the hydrogen concentration **[O93]**. This is based on the fact that, the number of vacant interstitial sites for hydrogen atoms jumping diminishes with increasing hydrogen concentration, and also the interaction between titanium and hydrogen atoms changes as the lattice expands with increasing the hydrogen concentration. It should be mentioned, the diffusion of hydrogen along grain boundaries in titanium and its alloys is much faster than the bulk diffusion. It has been reported that the values of the diffusion coefficient for grain boundary diffusion ($D_{gb} = 9.1 \times 10^{-5}\, cm^2/s$) and lattice diffusion ($D_L = 2.6 \times 10^{-10} cm^2/s$) of hydrogen in commercial pure titanium at room temperature **[HL96]**.

Owing to its different diffusivity and solubility in the α- and β-phases, hydrogen has different effects on the mechanical behavior in α and β titanium alloy. For instance, the limited volume diffusion of hydrogen in α-titanium leads to a superior creep performance of α-Ti alloys and α containing titanium alloys compared to β-titanium alloys **[HL96].** While, β-titanium and its alloys show predominant hot workability and superplasticity, because of faster diffusion rate of hydrogen in bcc lattice **[SJ96].**

1.3.2.3 Hydrogen diffusion with dislocation trapping and dragging

The concept of trapping originated in the attempt to understand the tremendous decrease of the diffusivity of hydrogen in steels as a result of plastic deformation **[DS49]**. As reported by Oriani, the mobility of hydrogen can be substantially reduced by its attractive interactions with dislocations **[O70]**. In the case of hydrogen interacting with dislocations, hydrogen atoms spend more time in their vicinity than at a normal lattice site, because the activation energy for escaping from a tight-binding site will be increased. Therefore, hydrogen diffusion in a rolled metal may

be delayed by a high-density of dislocations **[O70, KJ80, K81, BE91, KM93 and YS98]**. For example, hydrogen diffusion is retarded due to hydrogen trapping by dislocations in palladium during the process of high pressure torsion (HPT) **[IA16]**. Consequently, the amounts of lattice dissolved hydrogen in titanium decrease due to the trapping-reduced diffusivity of hydrogen.

However, hydrogen can also be faster transported by mobile dislocations. Hydrogen transported by mobile dislocations was first suggested Bastien and Azou **[BA51]** and is supported by numerous experimental observations **[WS68, KL79, HB86, FL86, IG97 and NK98]**. Models for hydrogen transport by edge dislocations have been proposed by Tien **[TK76]**. These dislocation transport models yield much faster diffusion rates than lattice diffusion and support the idea that dislocations can carry hydrogen deep into a specimen gage section or plastic zone even at ambient temperatures. Associated with these models discussed by Tien is the proposition that local hydrogen supersaturations develop through stripping of the solutes off the moving dislocations by traps.

On the other hand, theoretical analysis by Hirth and Johnson **[HJ83]** pointed out that the transport of hydrogen by dislocations in iron or steel at room temperature produces only small supersaturations at internal trap sites; larger supersaturations by dislocation transport are predicted to be possible in metals with much smaller diffusivities for hydrogen, e.g. nickel. A secondary but important consequence of the attendant hydrogen concentration associated with the dislocations is that it reduces the interaction energy between dislocations allowing them to pack more densely. It was also proposed to stabilize the microstructure preventing reorganization since an additional driving force would have to be provided to first remove hydrogen from the dislocations to permit reorganization **[FR98]**.

1.3.3 Hydrogen-induced phase transformation in titanium and titanium Alloys

According to the binary constitution phase diagram of Ti-H system in **Figure 1. 11** **[MM86]**, the terminal hydrogen solubility in the α phase is only approximately 7 at.% at 300°C and decreases rapidly with decreasing temperature. At room temperature, the terminal hydrogen solubility in α-titanium is quite negligible (~0.04 at.%) **[N96]**. Therefore, at low hydrogen concentration, the hydrogen atoms dissolved in the lattice as an eutectoid solid solution. At temperatures above the eutectoid point, the addition of hydrogen causes the α phase to transform into the β phase. The solubility of hydrogen in the β phase is much higher (i.e., 39% at 300°C) than in the α phase (i.e.,

6.7% at 300°C). In the two-phase region, the hydrogen concentrations in the α phase and β phase do not change with increasing hydrogen content at a given temperature; only the phase proportion changes.

The hydrogen in the solid solution state may diffuse easily by any perturbation and is thus defined as quasi-mobile hydrogen. At a higher hydrogen concentration, well above the expected terminal solubility limit **[N96]**, the formation of hydride occurs, then hydrogen atoms are bonded in the interstitial sites of the Ti-lattice (hydride state), and it is referred as bonded hydrogen. However, hydrogen is hardly detectable by local solid-state chemical analyses. In particularly, the distribution of hydrogen atoms in the sample cannot be directly obtained by means of the characteristic X-rays or electron energy loss spectroscopy in an electron microscope. Interstitially dissolved hydrogen is trapped preferably in areas of local stress concentrations, such as vacancies, dislocations, precipitations, phase and grain boundaries, which cause crystal lattice expansion as well as lattice distortion **[KK01, SC01]**. Therefore, the hydrogen-induced phase transformation occurred preferentially at grain and phase boundaries as a consequence of hydrogen supersaturation.

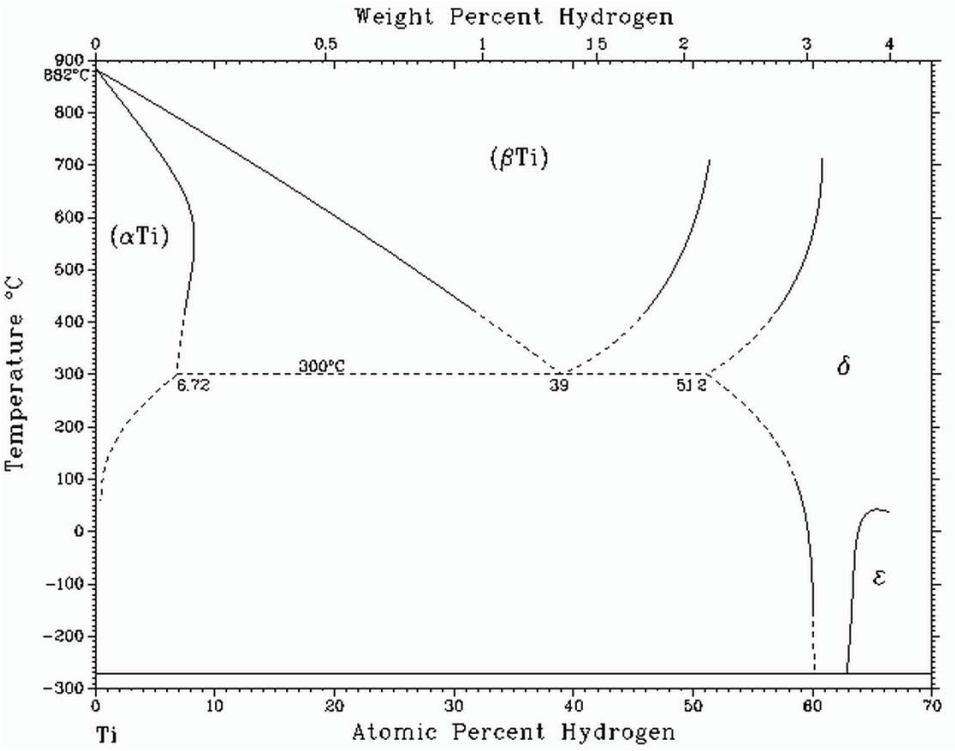

Figure 1. 11 The titanium-hydrogen phase diagram [MM86]

Table 1. 4 Crystallographic structure of three types hydrides

Hydride	Composition	Lattice Structure	Lattice parameters, nm	Volume Expansion
γ	TiH	BCT	a=0.420 c=0.470	12.5 14%
δ	TiH2-x (0<x<0.4)	FCC	a=0.445	17.2 29%
ε	TiH2	BCT	a=0.312 c=0.418	3 141%

Several hydride phases can be obtained at room temperature, corresponding to various amounts of hydrogen: tetragonal γ-TiH, fcc δ-TiH2-x (with x ranging between 0 and 0.4) and tetragonal ε-TiH_2 **[NK84, WW85, MS00 and CG17],** as shown in **Table 1. 4**. The hydride γ-TiH with an ordered arrangement of hydrogen atoms has a body centered tetragonal (bct) structure, which is formed at low hydrogen concentrations (1-3 at.% H). With the dissolved hydrogen amounts increasing, the hydride δ-TiH_{2-x} has an fcc unit cell with the hydrogen atoms occupying the tetrahedral interstitial site (CaF_2 type structure) formed. When the amounts of dissolved hydrogen atoms exceeds 60 at.%, the hydride ε-TiH_2 with a bct (c/a < 1) structure is precipitated from the matrix α phase, this ε hydride being metastable at temperature above 298 K **[YJ58]**.

Table 1. 5 Orientation relationships between Ti and Ti hydrides **[CG17]**

	Parallel plane and Parallel zone axes between two phases	Interface plane
OR1	(0001) // (001), [1-210] // [110]	(10-10) // (2-20)
OR2	(0001) // (1-11) angle of 4°, [1-210] // [110]	(10-13) // (2-20)
OR3	(10-10) // (-111), [1-210] // [110]	(0001) // (2-20)
OR4	(-1011) // (001), [1-210] // [110]	(10-11) // (-111)

The transformation of titanium into several hydride phases has been investigated by Egle Conforto and co-worker **[CC07, CG17]** using transmission electron microscopy. In their work, four different orientation relationships have been observed between hydride phases and the Ti hexagonal phase, as shown in **Table 1. 5** **[CG17]**. The hydride γ-TiH can nucleate in prismatic

planes of the hexagonal structure of Ti to form lamellae in OR1 relationship. This nucleation is favored by the excellent crystallographic coincidences that are consistent with a low-energy interface plane. It is preceded by an ordering of Ti phase when quantity of hydrogen atoms in solution amounts to Ti/H ~1.

Titanium transforms into fcc TiH_{2-x} hydride by several paths depending on the plane on which the hydride nucleates. The formation of the TiH_{2-x} phase takes place either directly (for a favorable TiH_{2-x}/Ti orientation relationship) or via the nucleation of the TiH phase (for a favorable TiH/Ti orientation relationship). In the latter case, the transformation of TiH into TiH_{2-x} takes place with the amount of hydrogen in increasing excess. The orientation relationship and the interface plane remain unchanged during this process, although the conditions for a favorable interface become much less satisfied. Therefore, misfit dislocations must be introduced at this step, to compensate for the higher crystallographic mismatch **[CG17]**.

1.4 Effects of hydrogen on mechanical properties in titanium and titanium alloys

The introduction of hydrogen into metallic systems has generally a deleterious effect on the mechanical properties, and particularly on the fracture and fracture toughness at low temperatures **[B79]**. Post-fracture evidence suggests that hydrogen embrittlement in Ti-based materials is complicated by the existence of different phases, α and β, which have different susceptibilities to hydrogen; the hcp α phase being more susceptible to embrittlement and having a lower hydrogen solubility and diffusivity than the bcc β phase **[WK54, PW74]**. It has after been reported that, alloys containing a mixture of the α and β phases often fracture at the interface of the α-β phases **[S83]**. Hence, several mechanisms appear to be the cause of hydrogen embrittlement, including the stress-induced hydride formation and cleavage mechanism **[WN72, M72, PS76, N76, DN77, SP79 and RB88]**, decohesion **[T60, OJ74, PBW75, PB76, OJ77, O87 and TRB01]**, and the hydrogen enhanced localized plasticity (HELP) mechanism **[B72, SR88, RB86, BRB87, BRB89, FRB98 and B94]**.

1.4.1 Hydrogen embrittlement in α-titanium and its alloys

Numerous experiments were performed to study the effect of hydrogen on the fracture of the α-titanium alloys **[GK85, SRB88 and LK83]**. Since the solubility of hydrogen in the α phase is very low, hydrides can form at stress concentrators at very low hydrogen concentrations and these can cause embrittlement **[WN72, M72, PS76, N76, DN77, SP79 and SR88]**.

Commercially pure titanium is very resistant to hydrogen embrittlement when tested in the form of fine-grained specimens at low-to-moderate strain rates in uniaxial tensile tests. However, it becomes susceptible to hydrogen embrittlement in the presence of a notch, at low temperatures or/and high strain rates, or large grain sizes **[LKS83 and GK85]**. The latter effect was reported to be a consequence of the enhancement of both void nucleation and void link-up at large grain sizes or biaxial stresses. **Figure 1. 12** shows the stress-strain curves for uncharged and hydrogenated grade 2 titanium (Ti-0.02C-0.008N-0.08Fe-0.14O) with different hydrogen concentrations **[BW02]**. It can be seen that the strain to failure decreases with increasing hydrogen concentration, while at the same time, the yield strength and the ultimate tensile strength increase. The hydrogen effect on the fracture surface is presented in **Figure 1. 13**. As the hydrogen concentration increased, the fracture surface changed from large microvoids coalescence in the uncharged material (**Figure 1. 13**a) to smaller microvoids in the 600 wppm charged specimen (**Figure 1. 13**b) and finally to brittle facets in the specimen that contains 3490 wppm hydrogen (**Figure 1. 13**c).

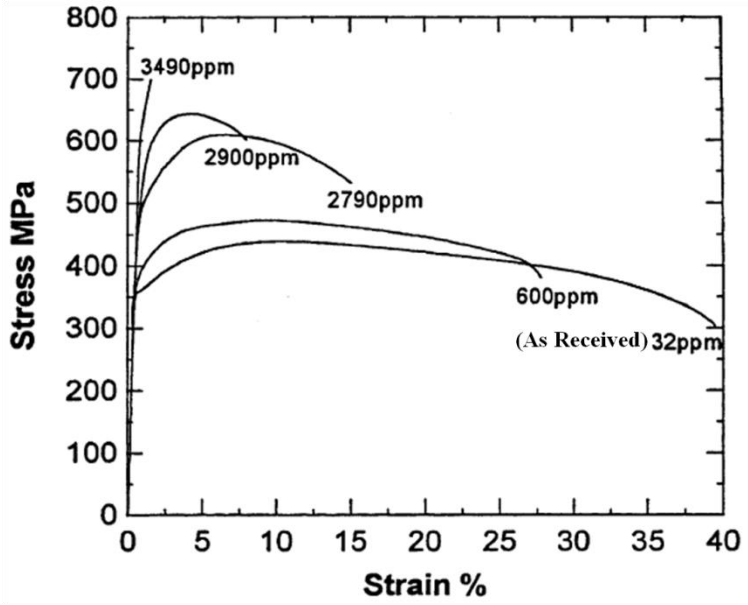

Figure 1. 12 The stress-strain curves for uncharged and hydrogenated up to different hydrogen concentrations grade 2 titanium [BW02].

On the other hand, in α-Ti alloys the main mechanism of hydrogen embrittlement was often suggested to result from the precipitation and decomposition of brittle hydride phases. At lower temperatures, the titanium hydride becomes brittle and severe degradation of the mechanical and fracture behaviors of these alloys were reported **[N83]**. For instance, by deforming the hcp phase

in α-titanium Ti-4%Al in situ TEM in a gaseous hydrogen environmental cell, two fracture mechanisms have been observed at room temperature **[SRB88]**. One mechanism emphasizes that fracture by localized plastic deformation enhanced by the presence of hydrogen, the other is attributed to a brittle fracture of the stress-induced titanium hydrides which precipitate at elastic singularities. Consequently, two fracture mechanisms could operate depending on the intensity of the local stress. For local stress having high intensities, the crack propagates by the process of hydrogen enhanced localized plasticity (HELP), while at low stress intensities titanium hydrides form in the vicinity of crack tips and crack propagation proceeds though the hydrides.

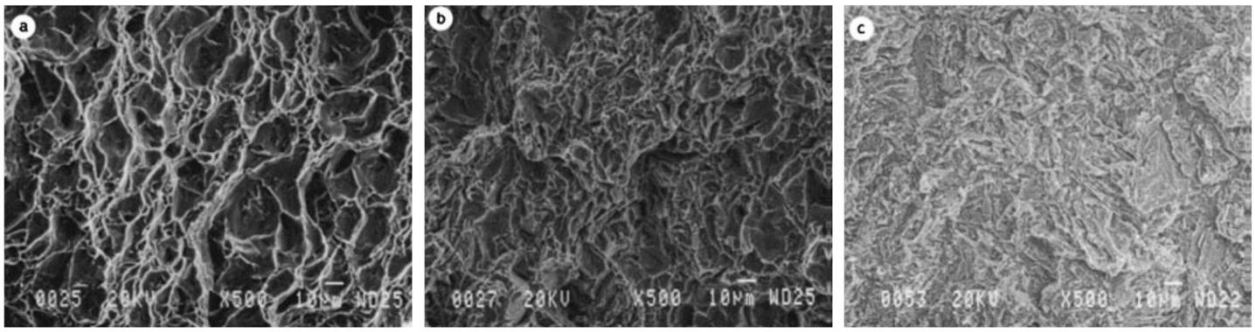

Figure 1. 13 SEM micrographs of fracture surface of uncharged and hydrogenated grade 2 titanium, failed during tensile testing: (a) uncharged specimen (b) hydrogenated up to 600 wppm, (c) hydrogenated up to 3400 wppm [BW02].

1.4.2 Hydrogen embrittlement in β-titanium and its alloys

In contrast to α phase, the solubility of hydrogen in the β phase is significantly high. In stable β titanium alloys, the hydrogen concentration can exceed 50 at.% without any hydride formation **[SB86]**. Since β-titanium alloys exhibit very high terminal hydrogen solubility and do not readily form hydrides, until lately these materials were considered to be fairly resistant to hydrogen, except possibly under very high hydrogen pressures **[PS81]**.

However, it was recently reported that the hydrogen-induced ductile-brittle transition in the bcc β-titanium alloy β-21S, occurs abruptly beyond a critical hydrogen concentration (H/M = 0.21, the hydrogen to metal atoms ratio) that decreased with decreasing tensile test temperature **[TR01].** Mechanical property tests showed that solute hydrogen reduced the yield strength of ductile specimens and decreased the fracture stress of brittle specimens, as shown in **Figure 1. 14** **[TR01]**.

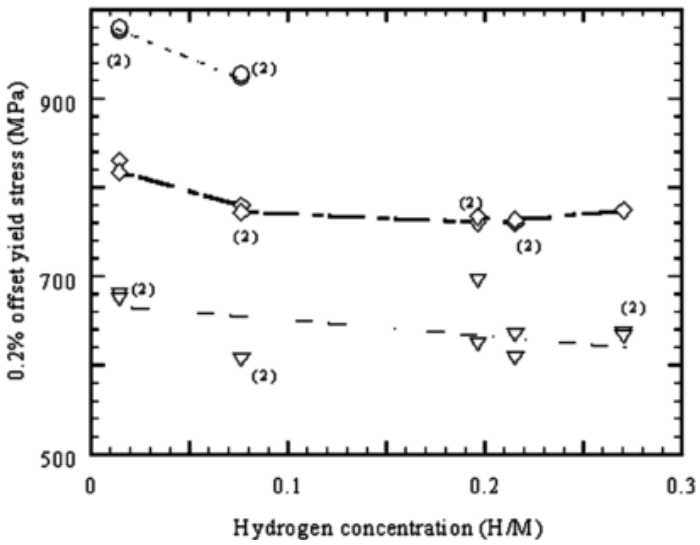

Figure 1. 14 Variation of the yield stress (0.2% offset yield) as a function of the hydrogen concentration. ○, 248 K; ◇,298 K; ▽,373 K. The number in parentheses refers to the number of tests performed.

To identify the operative mechanism, a series of experiments **[TR01]** were performed by Teter D.F. Teter and co-workers. The aim of this investigation was to test the applicability of the stress-induced hydride mechanism, the hydrogen-enhanced plasticity mechanism, and the decohesion mechanism of hydrogen embrittlement. Typical fracture surfaces for ductile (H/M = 0.014) and brittle (H/M = 0.27) samples are shown in **Figure 1. 15**. In specimens having H/M < 0.21, fracture occurred by microvoid coalescence, **Figure 1. 15**a and b. Significant plasticity, as evidenced by the slip bands on the transverse surface, accompanied the fracture, which is consistent with the higher stress intensities found in these samples. Above the ductile-brittle transition (H/M>0.21), the fracture mode was found to be cleavage-like as shown for sample (H/M = 0.27) in **Figure 1. 15**c and d. Evidence of the accompanying deformation is seen in the curved and bent edges on the cleavage steps (white arrow in **Figure 1. 15**d and e), and small voids on the cleavage facets (black arrows) in **Figure 1. 15**d and f. The experiments showed that no hydrides were associated with the fracture process, indicating that the stress-induced hydride mechanism was not responsible for the observed sharp ductile-brittle transition.

Since the hydrogen-enhanced localized plasticity mechanism for hydrogen embrittlement has been observed in many systems, including α-Ti **[SR88]**, the assumption that the mechanism occurred in β-21S alloy was investigated by deforming uncharged samples *in-situ* in a controlled environment transmission electron microscopy. It was observed that solute hydrogen increased

the mobility of dislocations, which is consistent with the decrease in offset yield strength with increased H/M. While enhancement of dislocation mobility by hydrogen was observed, fracture due to localized ductile processes was not observed and the hydrogen-enhanced localized plasticity mechanism is thus not expected to exhibit a sharp ductile-brittle fracture transition at a critical hydrogen concentration. Above the critical H/M for the fracture transition, there was little plasticity associated with the fracture. Thus, the HELP mechanism is not considered to be responsible for the abrupt loss of ductility at the critical hydrogen concentration in β-Titanium alloys. However, the sharp ductile-brittle transition and the decrease in the fracture load of the brittle specimens with increasing hydrogen concentration, are consistent with a decohesion mechanism at the observed high values of H/M ratio.

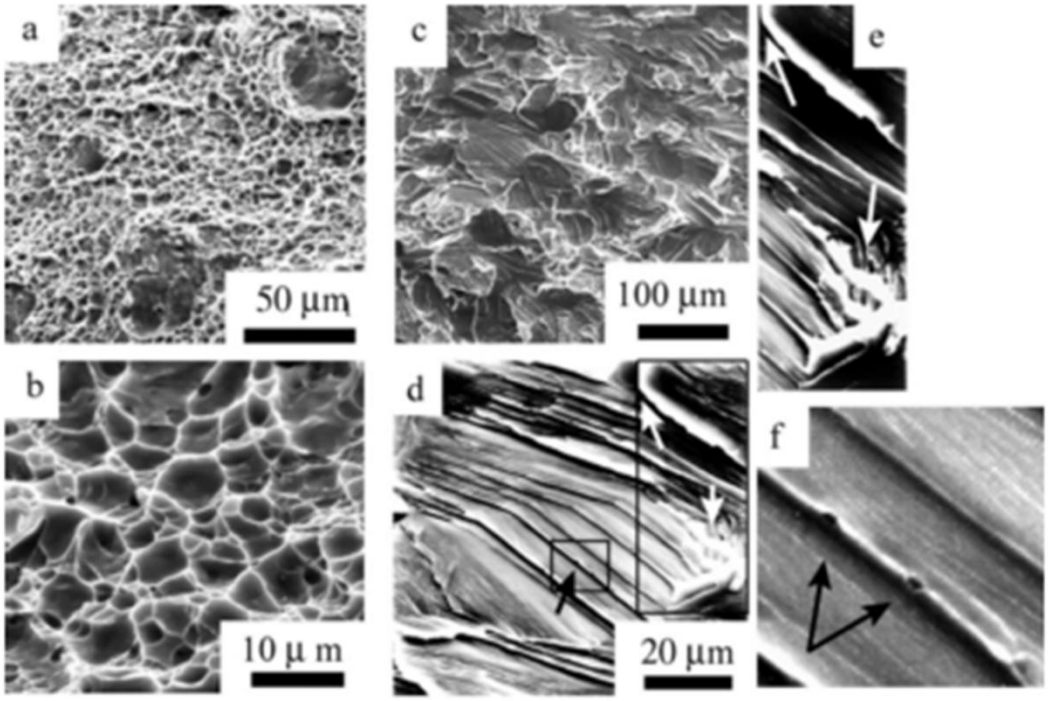

Figure 1. 15 SEM fractographs of the fracture surfaces of specimens tested at 298 K. (a, b) H/M = 0.014; (c, d) H/M = 0.27 and (e, f) higher magnifications of the regions indicated in (d). The white arrows in (d and e) indicate regions of plasticity on the fracture surface and the black arrows in (d and f) indicate a small microvoid.

1.5 Effects of hydrogen on the recrystallization behavior in titanium and other metals

As it is well known, titanium and titanium alloys are produced initially as large castings which are then further processed in the solid state by forging, rolling, extrusion, etc., to an intermediate or final products. Among these procedures, intermediate annealing treatments are often performed to relief the internal stress produced during cold or hot deformations. Recovery,

recrystallization and grain growth are core elements of annealing treatments in highly deformed alloys.

Recrystallization is one of the fundamental metallurgical and physical phenomena **[T86, G78]** whose conditions of evolution depend on the nature of the metallic alloy, the chemical and phase composition, peculiarities of the initial microstructure and degree of the initial deformation, as well as the parameters of recrystallization treatment. According to the published literatures [**SJ96**] and [**G78**], it is assumed that the interstitial impurities (C, N, B) and substitutional alloying elements impede the recrystallization evolution and, accordingly, can result in a shift of the temperature interval of a primary recrystallization to the domain of higher temperatures. However Goltsov and co-workers [**G06**] have recently found that hydrogen action stimulates the initiation of the recrystallization and recovery of mechanical properties of deformed palladium. For example, **Figure 1. 16** shows the variation of yield limit with temperature for palladium under vaccum and hydrogen atmosphere [**G06**], respectively. It can be observed, the presence of hydrogen lowered the recrystallization temperature.

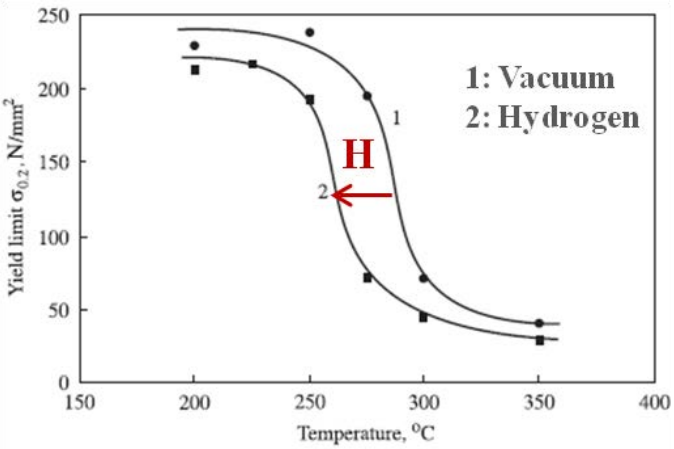

Figure 1. 16 The change of yield limit with temperature under vaccum and hydrogen atmosphere for palladium, respectively [G06].

Meanwhile, Shan and co-workers [**SZ08**], who studied the flow softening of the phase in Ti-6Al-4V-xH alloy, have reported that the hydrogen stimulated the dynamic recrystallization (DRX) occurring during mechanical loading at high temperature. The typical DRX microstructures is shown in **Figure 1. 17**. The recrystallized grain size of the unhydrogenated alloy was 500 nm (**Figure 1. 17**a). It can be seen, some DRX new grains nucleating at the existing grain boundaries (signed with A) and some deformed DRX grains containing a substructure of high density dislocations in their interiors (signed with B). In the hydrogenated alloy (**Figure 1. 17**b), DRX

took place not only in α phase but also in β phase. Moreover, the recrystallized grain size in hydrogenated alloy deformed at 973K was about 400 nm smaller than the unhydrogenated alloy. A smaller grain size indicates a higher rate of DRX that rapidly annihilates dislocations.

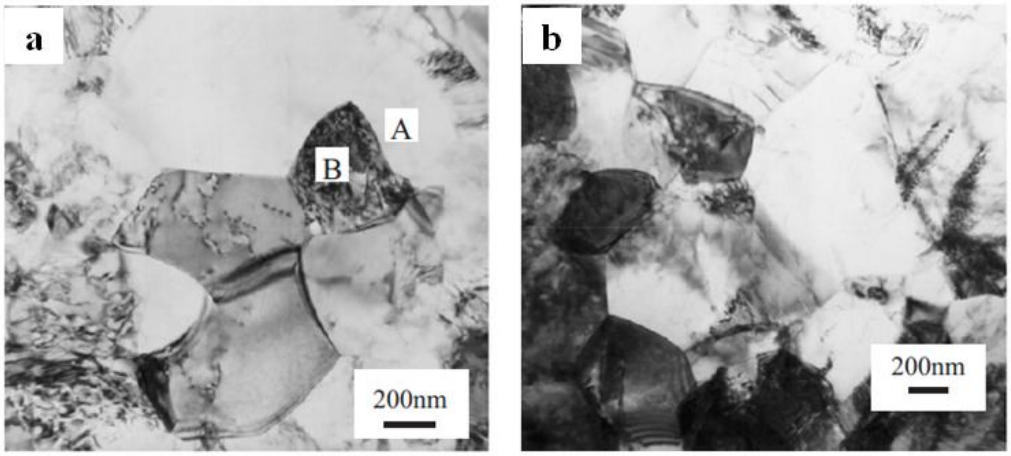

Figure 1. 17 TEM micrographs of the Ti–6Al–4V alloys deformed at 6.7×10−3s−1 at 973 K: (a) unhydrogenated and (b) 0.3 wt% H. A: DRX new grain existing at the grain boundary, B: growing DRX grain containing gradient of dislocation density.

Based on these observations, it can be drawn that hydrogen behaved totally differently on the recrystallization, as compared to the other interstitial elements (C, N, B and O). It makes the evolution of recrystallization in metal easier and characterized by a shift of the recrystallization temperature interval to the area of lower temperatures. In the view of thermodynamics**,** the dissolved hydrogen atoms forming an intersititial solution raise the level of thermodynamic level of the instability of a deformed metal. That is also the reason that has been proposed for the hydrogen-induced phase transformations in metals [**G06**]. In the view of kinetics, the dissolved hydrogen atoms can increase the dislocations mobility [**SG96, G94, SF99, SZ08**], because the interaction between the mobile dislocations and the impurities were shielded by the presence of hydrogen atmosphere. Moreover, in the framework of the defactant, the defect formation energy being reduced by the hydrogen addition **[K09, BV10 and KS10**], the formation of vacancies, dislocations and stacking faults under cold deformation can be enhanced in the presence of hydrogen.

It is well known that the stored energy of a deformed metal is a thermodynamic driving force for the recrystallization process. The greater density of dislocations leads to the higher level of stored energy of a deformed metal and, accordingly, the recrystallization evaluates at lower temperatures. Therefore, if hydrogen atoms, which are initially dissolved as defactants into

titanium to facilitate the formation of vacancies, dislocations and stacking faults under cold rolling, are then subsequently removed by vacuum annealing, it is reasonable that the recrystallization temperature will be reduced.

Reference

[AH94] S. Ankem, J.A. Hall, in Microstructure/Property Relationships in Titanium Alloys. TMS, Warrendale, PA, **1994**, p. 215.

[AG74] W. Aver and H.J. Grabke, Ber. Bunsenges, The Kinetics of Hydrogen Absorption in Palladium (α-and β-phase) and Palladium-Silver-Alloys, Phys. Chem. 78 (**1974**) 58.

[AR96] T. Ahmed, H. Rack, Martensitic transformations in Ti-(16–26 at%) Nb alloys, J. Mater. Sci. 31 (**1996**) 4267-4276.

[AV78] G. Alefeld and J. Völkl, Hydrogen in Metals, G. Alefeld and J. Volkl, eds., Springer-Verlag, Berlin, Vols. 1 and 2, **1978**.

[B43] J. Bockris, Recent developments in the study of hydrogen overpotential., Chem. Rev. 43 (**1943**) 525-577.

[B54] J. Bockris, Modern aspects of electrode kinetics, Annu. Rev. Phys. Chem. 5 (**1954**) 477-500.

[B72] C.D. Beachem, A New Model for Hydrogen Assisted Cracking (Hydrogen Embrittlement), Metall. Mater. Trans. A 3 (**1972**) 437-451.

[B79] H.K. Birnbaum, Hydrogen related failure mechanisms in metals. In: Environment-sensitive Fracture of Engineering Materials, ed. by Z.A. Foroulis, The Metallurgical Society (AIME), Warrendale, PA, **1979**, pp. 326-360.

[B94] H.K. Birnbaum, Scripta Mater. 31 (**1994**) 49.

[B04] J. Bockris, E. Potter, The mechanism of hydrogen evolution at nickel cathodes in aqueous solutions, J. Chem. Phys. 20 (**2004**) 614.

[BA51] Bastien, P. Azou, Effect of hydrogen on the deformation and fracture of iron and steel in simple tension, In: Proceedings of the First World Metallurgical Congress, Ed. by W.M Baldwin, ASM, Cleveland, OH, **1951**, pp.535-552.

[BC89] A.M. Brass, A. Chanfreau, J. Chene, Hydrogen Effects on Materials, Jackson Lake, Moran, WY, **1989**.

[BC96] A.M. Brass, A. Chanfreau, Accelerated diffusion of hydrogen along grain boundaries in nickel, Acta Mater. 44 (**1996**) 3823-3831.

[BD15] T.B. Britton, F.P. Dunne and A.J. Wilkinson, On the mechanistic basis of deformation at the microscale in hexagonal close-packed metals. Proc. R. Soc. A 471 (**2015**) 20140881.

[BDC15] B. Barkia, V. Doquet, J.P. Couzinié, I. Guillot, E. Héripré, In situ monitoring of the deformation mechanisms in titanium with different oxygen content. *Mat. Sci. Eng. A.* 636 **(2015)**, 91-102.

[BE91] R.V. Bucur, N.O. Ersson, X.Q. Tong, Solubility and diffusivity of hydrogen in palladium and $Pd_{77}Ag_{23}$ containing lattice defects, J. Less Common Met. 172-174 (**1991**) 748-758.

[BP07] M. Battaini, E.V. Pereloma, C.H. Davies, Orientation effect on mechanical properties of commercially pure titanium at room temperature. Metall. Mater. Trans. A 38 (**2007**) 276-285.

[BM07] S. Banerjee and P. Mukhopadhyay, Phase transformations examples from titanium and zirconium Alloys. **2007**: Elsevier.

[BRB87] G.M. Bond, I.M. Robertson, H.K. Birnbaum, The influence of hydrogen on deformation and fracture processes in high-strength aluminum alloys. Acta Mater. 35 (**1987**) 2289-2296.

[BRB89] G.M. Bond, I.M. Robertson, H.K. Birnbaum, on the mechanisms of hydrogen embrittlement of Ni3Al alloys, Acta Mater. 37 (**1989**) 1407-1413.

[BV10] A. Barnoush, H. Vehoff, Recent developments in the study of hydrogen embrittlement: Hydrogen effect on dislocation nucleation, Acta Mater. 58 (**2010**) 5274-5285.

[BW02] C.L. Briant, Z.F. Wang and N. Chollocoop, Hydrogen Embrittlement of Commercial Purity Titanium, Corros. Sci. 44 (**2002**) 1875-1888.

[BW68] M.J. Blackburn and J.C. Williams, Phase transformations in Ti-Mo and Ti-V alloys, Transactions of the Metallurgical Society of Aime, 242 (**1968**) 2461-2469.

[BW13] D. Banerjee, J.C. Williams, Perspectives on titanium science and technology, Acta Mater. 61 (**2013**) 844-879.

[C81] H. Conrad. Effect of interstitial solutes on the strength and ductility of titanium. Prog. Mater. Sci. 26 **(1981**) 123-403.

[CC07] E. Conforto, D. Caillard, A fast method for determining favourable orientation relationships and interface planes: Application to titanium-titanium hydrides transformations, Acta Mater. 55 (**2007**) 785-798.

[CD00] H.J. Christ, M. Decker, S. Zeitler, Hydrogen diffusion coefficients in the titanium alloys IMI 834, Ti10-2-3, Ti21 S, and alloy C, Metall. Mater. Trans. A 31 (**2000**) 1507-1517.

[CG17] E. Conforto1, E. Guillot, X. Feaugas, Solute hydrogen and hydrides phases implications on the plasticity of zirconium and titanium alloys: a review and some recent advances, Phil. Trans. R. Soc. A. **2017**.

[CL10] C. Alexis, Lewis et al., Slip systems and initiation of plasticity in a body-centered-cubic titanium alloy, Metall. Mater. Trans. A 41 (**2010**) 2522-2531.

[CY05] Y.B. Chun, S.H. Yu, S.L. Semiatin, S.K. Hwang, Effect of deformation twinning on microstructure and texture evolution during cold rolling of CP-titanium, Mater. Sci. Eng. A 398 **(2005**) 209-219.

[CH11] D. Connetable, J. Huez, E. Andrieu, C. Mijoule, First-principles study of diffusion and interactions of vacancies and hydrogen in hcp-titanium, J. Phys. Condens. Matter 23 (**2011**) 405401.

[DB15] M. Deutges, H.P. Barth, Y.Z. Chen, C. Borchers and R. Kirchheim, Hydrogen diffusivities as a measure of relative dislocation densities in palladium and increase of the density by plastic deformation in the presence of dissolved hydrogen, Acta Mater. 82 (**2015**) 266-274.

[DB16] R. Dingreville, S. Berbenni, On the interaction of solutes with grain boundaries, Acta Mater. 104 (**2016**) 237-249.

[DB84] M.S. Daw and M.I. Baskes, Phys. Rev. B, 29 (**1984**) 6443.

[DF76] R. Davis, H.M. Flower, D.R. West, Martensite Transformation in Ti-Mo Alloys. J. Mater. Sci. 14 (**1979**) 712-722.

[DM15] M. Dadfarnia, M.L. Martin, A. Nagao, P. Sofronis, I.M. Robertson, Modeling hydrogen transport by dislocations, J. Mech. Phys. Solids 78 (**2015**) 511-525.

[DN77] R. Dutton, K. Nuttall, M.P. Puls, L.A. Simpson, Metall Mater Trans A 8 (**1977**) 1553.

[DS49] L.S. Darken and R.P. Smith, Corros. Sci. 5 (**1949**) 1.

[FL86] G.S. Frankel, R.M. Latanision, Hydrogen transport during deformation in nickel: Part II. single crystal nickel, Metall. Mater. Trans. A 17 (**1986**) 869-875.

[F03] Y. Fukai, Superabundant Vacancies Formed in Metal–Hydrogen Alloys, Phys. Scripta, T103 **(2003)** 11.

[FO94] Y. Fukai and N. Okuma, Formation of superabundant vacancies in Pd hydride under high hydrogen pressures, Phys. Rev. Lett. 73 **(1994)** 1640.

[FR98] P.J. Ferreira, I.M. Robertson, H.K. Birnbaum, Hydrogen effects on the interaction between dislocations. Acta Mater. 46 (**1998**) 1749-1757.

[FS04] F.H. Froes, O.N. Senkov, J.I. Qazi, Hydrogen as a temporary alloying element in titanium alloys: thermohydrogen processing, Int. Mater. Rev. 49 (**2004**) 227.

[FF10] S. Freour, M. François, R.Guillén, Determining Ti-17 β-Phase single-crystal elasticity constants through X-Ray diffraction and inverse scale transition model, Materials Science Forum 681, June **2010,** Conference: 8th European Conference on Residual Stresses (ECRS8), At Riva del Garda, Italy.

[G94] R.M. German, Powder Metallurgy Science. Princeton, Metal Powder Industries Federation, **1994**.

[G78] S.S. Gorelick, Recrystallization of metals and alloys. The 2nd issue, Moscow: Metallurgia; **1978**, in Russian.

[G06] V.A. Goltsov, Influence of dissolved hydrogen on recrystallization and recovery of mechanical properties of deformed palladium, Int. J. Hydrogen Energy 31 (**2006**) 211-216.

[GG10] E. Gutelmacher, R. Gemma, C.A. Volkert and R. Kirchheim, Hydrogen effect on dislocation nucleation in a vanadium (100) single crystal as observed during nanoindentation, Scripta Mater. 63 (**2010**) 1032-1035.

[GK85] D.A. Gerard and D.A. Koss, The combined effect of stress state and grain size on hydrogen embrittlement of titanium, Scripta Mater. 19 (**1985**) 1521-1524.

[GK14] V. Gaspard, G. Kermouche, D. Delafosse, A. Barnoush, Hydrogen effect on dislocation nucleation in a ferritic alloy Fe–15Cr as observed per nanoindentation, Mater. Sci. Eng. A 604 (**2014**) 86-91.

[H11] M. Herbig, 3D short fatigue crack investigation in beta titanium alloys using phase and diffraction contrast tomography, PhD thesis, l'INSA de Lyon, 2011.

[HB86] C. Hwang, I.M. Bernstein, Dislocation transport of hydrogen in iron single crystals. Acta Metall. 34 (**1986**) 1001-1010.

[HJ83] J.P. Hirth, H.H. Johnson, On the transport of hydrogen by dislocations. Ed. R.M. Latanision, J.R. Pickens, Proceedings of a NATO Advanced Research Institute on Atomistics of Fracture. Plenum Press, NewYork, **1983**, pp.771-787.

[HL86] S. Hanada, O. Lzumi, Transmission electron microscopic observations of mechanical twinning in metastable beta titanium alloys, Metall. Mater. Trans. A 17 (**1986**) 1409-1420.

[HL91] T.M. Harris, R.M. Latanision. Metall. Mater. Trans. A 22 (**1991**) 351.

[HL96] A. Hamid, R.M. Latanision, et al., in Hydrogen Effects in Materials, ed. A.W. Thompson and N. R. Moody, TMS, Warrendale, PA, **1996**, p. 205.

[IO80] N. Itoh, M. Ogaya, S. Ishiyama, T. Matsushita, Y. Hayashi, M. Koike, Press Formability of Commercial Pure Titanium at Warm Working Temperatures. Titanium 80, Science and Technology, vol. 4, **1980**, pp. 2523-2529. Proceedings of the 4th International Conference on Titanium.

[IA16] H. Iwaoka, M. Arita, Z. Horita, Hydrogen diffusion in ultrafine-grained palladium: Roles of dislocations and grain boundaries, Acta Mater. 107 (**2016**) 168-177.

[IJ97] G. Itoh, T. Jinkoji, M. Kanno, K. Koyama, Effect of impurity hydrogen on the deformation and fracture in an Al-5mass Pct mg alloy, Metall. Mater. Trans. A 28 (**1997**) 2291-2295.

[K07] R. Kirchheim, Reducing grain boundary, dislocation line and vacancy formation energies by solute segregation. I. Theoretical background, Acta Mater. 55 (**2007**) 5129.

[K81] R. Kirchheim, Interaction of hydrogen with dislocations in palladium: Activity and diffusivity and their phenomenological interpretation, Acta Mater. 29 (**1981**) 835-843.

[KK00] P. Komninou, T. Kehagias, T. Karakostas, J.G. Antonopoulos, T. Braisaz, G. Nouet, A. Serra, ed. Lepinoux et al., Electron Microscopy of Defects in Hexagonal Materials, Multiscale Phenomena in Plasticity, Kluwer, **2000**, pp. 215-226.

[KK01] E. Kunze, Korrosion und Korrosionsschutz, 3th ed. Weinheim: Wiley-VCH Verlag; **2001**.

[KJ80] A.J. Kumnick, H.H. Johnson, Deep trapping states for hydrogen in deformed iron, Acta Mater. 28 (**1980**) 33-39.

[KL79] M. Kurkela, R.M. Latanision, The effect of plastic deformation on the transport of hydrogen in nickel. Scripta Mater. 13 (1**979**) 927-932.

[KM83] K. Kiuchi, R.B. McLellan, The solubility and diffusivity of hydrogen in well annealed and deformed iron, Acta Mater. 31 (**1983**) 961-984.

[LB87] B. Ladna, H.K. Birnbaum, SIMS study of hydrogen at the surface and grain boundaries of nickel bicrystals, Acta Mater. 35 (**1987**) 2537-2542.

[LD75] M.R. Louthan, J.A. Donovan, G.R. Caskey, Hydrogen diffusion and trapping in nickel, Acta Mater. 23 (**1975**) 745-749.

[LG10] C.P. Liang, H.R. Gong, Fundamental influence of hydrogen on various properties of a-titanium, Int. J. Hydrogen Energy 35 (**2010**) 3812-3816.

[LG54] G.A. Lenning, C.M. Graighead, R.I. Jaffee, Constitution and mechanical properties of titanium-hydrogen alloys, Trans. AIME 200 (**1954**) 367-376.

[LKS83] C.W. Lentz, D.A. Koss, M.G. Stout and S.S. Hecker, The effect of hydrogen on the multiaxial stress-strain behavior of titanium tubing, Metall. Mater. Trans. A 14 (**1983**) 2527-2533.

[LK05]G. Lu, E. Kaxiras, Hydrogen embrittlement of aluminum: The crucial role of vacancies, Phys. Rev. Lett. 94 (**2005**) 155501.

[LL86] S.M. Lee, J.Y Lee. Metall. Mater. Trans. A 17 (**1986**) 181.

[LP03] C. Leyens, M. Peters (Eds.), Titanium and Titanium Alloys: Fundamentals and Applications, Wiley-VCH Verlag GmbH, Weinheim, **2003**.

[LS93]R.J. Lederich, D.D. Schwartz and S.L. Sastry, in Beta Titanium Alloys in the 1990's. TMS, Warrendale, PA, **1993**, p. 159.

[LW07] G. Lütjering and J.C. Williams, Titanium (Engineering Materials and Processes), Berlin Heidelberg: Springer, **2007**.

[M51]A.D. McQuillan, An experimental and thermodynamic investigation of the hydrogen-titanium system, Proc. R. Soc. A 204 (**1951)** 309-322.

[M72] D.A. Meyn, Cleavage in Ti-8Al-1Mo-1V caused by hydrogen gas, Metall. Trans. A 3 (**1972**) 2302.

[M12] G. Martin. Numerical simulation of the mechanical behavior of the beta-titanium alloys Ti5553 and Ti17, PhD thesis, Ecole Nationale Supérieure des Mines of Paris, 2012.

[MB82] R.P. Messmer and C.L. Briant, The role of chemical bonding in grain boundary embrittlement, Acta Metall. 30 (**1982**) 457-467.

[MM02] J. Mao, R. McLellan, The thermodynamics of hydrogen-vacancy interactions in aluminum, J. Phys. Chem. Slids 63 (**2002**) 2029-2036.

[MM87] S. Martin, F.D. Manchester. The H-Ti (Hydrogen-Titanium) System, Bulletin of Alloy Phase Diagrams 8 (**1987**) 30-42.

[MM86] T.B. Massalski, J.L. Murray, L.H. Bennett and H. Baker (eds.), Binary Alloy Phase Diagrams, ASM, Metals Park, OH, **1986**, p.1283.

[MS87] T. McMullen, M.J. Stott and E. Zaremba, Phys. Rev. B, 35 (1987) 1076.

[MS00] F.D. Manchester, A.H. San Martin. In: Manchester FD, editor. Phase diagrams of binary hydrogen alloys. Materials Park, OH: ASM International; **2000**. p. 238.

[MT13] X.H. Min, K. Tsuzaki, S. Emura, T. Sawaguchi, et al., {332}< 113> Twinning system selection in a β-type Ti–15Mo–5Zr polycrystalline alloy, Mater. Sci. Eng. A 579 (**2013**) 164-169.

[N76] H.G. Nelson, A film-rupture model of hydrogen-induced, slow crack growth in acicular alpha-beta titanium, Metall. Mater. Trans. A **7** (**1976**) 621.

[N83] H.G. Nelson, Hydrogen Embrittlement-Treatise on Materials Science and Technology, Vol. 25, Embrittlement of Engineering Alloys, (Eds.: C.L. Briant, S.K. Banejri), (Academic Press, NewYork, NY, **1983**), pp. 275-359.

[N96] H.G. Nelson, Hydrogen Effects in Metals, (Eds.: A. W. Thompson, N.R. Moody), (TMS, Warrendale, PA, **1996**) pp. 699-715.

[N86] II. Novikov, Theory of a Thermal Treatment of Metals, (Moscow: Metallurgia, **1986**, in Russian).

[NK84] H. Numakura, M. Koiwa, Hydride precipitation in titanium, Acta Mater. 32 (**1984**) 1799.

[NK98] A. Nagao, S. Kuramoto, M. Kanno, Hydrogen microprint technique applied to observe impurity hydrogen in aluminum during deformation. In: Proceedings of the1998 TMS Annual Meeting, ed. B. Mishra, TMS, Warrendale, PA, **1998**, pp.867-875.

[O93] R.A. Oriani, Fourth International Conference on Cold Fusion (in ICCF4) (**1993**).

[O70] R. Oriani, The diffusion and trapping of hydrogen in steel, Acta Mater. 18 (**1970**) 147-157.

[O87] R.A. Oriani, Hydrogen-The Versatile Embrittler, Corros. Sci. 43 (**1987**) 390-397.

[OC12] A. Oudriss , J. Creus, J. Bouhattate, E. Conforto, C. Berziou, C. Savall, X. Feaugas, Grain size and grain-boundary effects on diffusion and trapping of hydrogen in pure nickel, Acta Mater. 60 (**2012**) 6814-6828.

[OJ74] R.A. Oriani, P.H. Josephic, Equilibrium aspects of hydrogen-induced cracking of steels, Acta Mater. 22 (**1974**) 1065.

[OJ77] R.A. Oriani, P.H. Josephic, Equilibrium and kinetic studies of the hydrogen-assisted cracking of steel, Acta Mater. 25 (**1977**) 979-988.

[OK04] H. Ogi, S. Kai, H. Ledbetter, R. Tarumi, M. Hirao, M and K. Takashima, Titanium's high-temperature elastic constants through the hcp-bcc phase transformation, Acta Mater. 52 (**2004**) 2075-2080.

[PH91] W. Petry, A. Heiming, J. Trampenau, M. Alba, Chr. Herzig, H.R. Schober, G. Vogl, Phonon dispersion of the bcc phase of group-IV metals. I. bcc titanium, Phys. Rev. B 43 (1991), 10933

[PA16] D.O. Poletaev, D.A. Aksyonov, Dat Duy Vo, A.G. Lipnitskii, Hydrogen solubility in hcp titanium with the account of vacancy complex and hydrides: A DFT study, Comput. Mater. Sci. 114 (2016) 199-208.

[PE09] D.A. Porter, K.E. Easterling, M. Sherif, Phase transformations in metals and alloys. **2009**: CRC.

[PE88] M.J. Philippe, C. Esling, B. Hocheid, Role of Twinning in Texture development and in plastic deformation of hexagonal materials, Textures Microstruct. **7** (**1988**) 265-301.

[PB70] N.E. Paton, W.A. Backofen, Plastic deformation of titanium at elevated temperatures, Metall. Mater. Trans. A 1 (**1970**) 2839-2847.

[P97] B.G. Pound, Hydrogen trapping in aged β-titanium alloys, Acta Mater. 45 (**1997**) 2059-2068.

[P94] B.G. Pound, Environmentally Assisted Cracking of High Strength Beta Titanium Alloys, Acta Mater. 42 (**1994**) 1551-1559.

[PW74] N.E. Paton and J.C. Williams, Hydrogen in Metals (edited by I. M. Bernstein and A. W. Thompson), pp. 409. Am. Sot. Metals, Metals Park, Ohio, **1974**.

[PBW75] N.E. Paton, O. Buck, J.C. Williams. Scripta Mater. 9 (**1975**) 687.

[PB76] N.E. Paton, O. Buck. In: Thompson AW, Bernsteing IM, editors. Effect of Hydrogen on the Behavior of Materials. 1**976**.

[PS81] N.E. Paton, R.A. Spurling and C.G. Rhodes, Hydrogen Effects in Metals, (Eds.: A.W. Thompson, I.M. Bernstein), (TMS-AIME, Warrendale, PA, **1981**) pp. 269-279.

[PK06] A. Pundt, R. Kirchheim, Hydrogen in metals: Microstructural aspects, Annu. Rev. Mater. Res. 36 (**2006**) 555-608.

[PS76] N.E. Paton, R.A. Spurling, Hydride habit planes in titanium-aluminum alloys, Metall. Mater. Trans. A 7 (**1976**) 1769-1774.

[RB86] I.M. Robertson and H.K. Birnbaum, An HVEM study of hydrogen effects on the deformation and fracture of nickel, Acta Mater. 34 (**1986**) 353-366.

[RF12] M. Rautenberg, X. Feaugas, D. Poquillon, J.M. Cloué, Microstructural characterization of creep anisotropy at 673 K in the M5 (R) alloy. Acta Mater. 60 **(2012**) 4319-4327.

[RR90] P. Rozenak, I.M. Robertson and H.K. Bimbaum, HVEM studies of the effects of hydrogen on the deformation and fracture of AISI type 316 austenitic stainless steel, Acta Metall. 38 (**1990**) 2031-2040.

[RS07] S.L. Raghunathan, A.M. Stapleton, R.J. Dashwood, M. Jackson, D. Dye, Micromechanics of Ti–10V–2Fe–3Al: In situ synchrotron characterisation and modelling, Acta Mater. 55 (**2007**) 6861-6872.

[S78] S. Schmidt, Diplomarbeti, Munster (**1978**).

[S83] D.S. Shih, Ph.D. thesis, Georgia Institute of Technology, Atlanta, Ga (**1983**).

[S00] P.A. Sundaram et al., Determination of the diffusion coefficient of hydrogen in Gamma Titanium Aluminides during electrolytic charging, Acta Mater. 48 (**2000**) 1005-1019.

[SB86] D.S. Shih, H.K. Birnbaum, Evidence of FCC titanium hydride formation in β titanium alloy: An X-ray diffraction study, Scripta Mater. 20 (**1986**) 1261-1264.

[SB90] O.N. Senkov, I.Q. Bashkin, E.G. Ponyatovsky, Peculiarities of plastic deformation of jydrogen alloyed titanium VT 20 alloy at temperatures of 823-1073 K, Fiz. Met. Metalloved. **7** (**1990**) 119-127.

[SC01] O.N. Senkova, B.C. Chakoumakos, J.J. Jonas, Effect of temperature and hydrogen concentration on the lattice parameter of beta titanium, Mater. Res. Bull. 36 (2001) 1431-1440.

[SF99] O.N. Senkov, F.H. Froes, Thermohydrogen processing of titanium alloys, Int. J. Hydrogen Energy 24 (**1999**) 565-576.

[SJ96] O.N. Senkov and J.J. Jonas, Effect of phase composition and hydrogen level on the deformation behavior of titanium-hydrogen alloys, Metall. Mater. Trans. A 27 (**1996**) 1869-1876.

[SK03] A.A. Salem, S.R. Kalidindi, R.D. Doherty, Strain hardening of titanium: role of deformation twinning, Acta Mater. 51 (**2003**) 4225-4237.

[SM87] San-Martin, F.D. Manchester, The H-Ti (Hydrogen-Titanium) System, Bulletin of Alloy Phase Diagrams, 8 (**1987**) 30-42.

[SM10] K. Sato, H. Matsumoto, K. Kodaira, T.J. Konno, A. Chiba, Phase transformation and age-hardening of hexagonal α' martensite in Ti-12mass%V-2mass%Al alloys studied by transmission electron microscopy, J. Alloys. Compd. 506 (**2010**) 607-614.

[SP79] L.A. Simpson and M.P. Puls, The effects of stress, temperature and hydrogen content on hydride-induced crack growth in Zr-2.5 pct Nb, Metall. Mater. Trans. A 10 (**1979**) 1093.

[SR88] D.S. Shih, I.M. Robertson, H.K. Birnbaum, Hydrogen embrittlement of α Titanium: In situ TEM studies, Acta Mater. 36 (**1988**) 111-124.

[SZ13] F. Sun, J.Y. Zhang, M. Marteleur, T. Gloriant, P. Vermaut, D. Laillé, P. Castany, C. Curfs, P.J. Jacques, F. Prima, Acta Mater. 61 (**2013**) 6406-6417.

[SZ08] D. Shan, Y.Y. Zong, et al., The effect o f hydrogen on the strengthening and softening of Ti-6Al-4V alloy, Scripta Mater. 58 (**2008**) 449-452.

[SZ13] F.Sun, J.Y. Zhang, M. M arteleur, T.Gloriant, P. Vermaut, D. Laille, P. Castany et al., Acta Mater. 61 (**2013**) 6406-6417.

[T60] A.R. Troiano, The role of hydrogen and other interstitials in the mechanical behavior of metals, Trans. Am. Soc. Metals. 52 (**1960**) 54.

[TK76] J.K Tien, A.W Thompson, I.M. Bernstein, R.J. Richards, Hydrogen transport by dislocations, Metall. Mater. Trans. A 7 (**1976**) 821-829.

[TL82] T. Tsuru, R.M Latanision. Scripta Mater. 16 (**1982**) 575.

[T86] I.N. Teoriya, termicheskoy obrabotky metallov (Theory of a Thermal Treatment of Metals). Moscow: Metallurgia, **(1986)** in Russian.

[TL88] D. Tseng, Q.Y. Long, K. Tangri, Detection of hydrogen permeation on the microscopic scale in nickel, Scripta Mater. 22 (**1988**).

[TM08] S. Taketomi, R. Matsumoto, N. Miyazaki, Atomistic study of hydrogen distribution and diffusion around a {112}< 111> edge dislocation in alpha iron, Acta Mater. 56 (**2008**) 3761.

[TN] M. Tane, T. Nakano, S. Kuramoto, M. Hara, M. Niinomi, N. Takesue, T. Yano, H. Nakajima, Low young's modulus in Ti–Nb–Ta–Zr–O alloys: Cold working and oxygen effects, Acta Mater. 59 (**2011**) 6975-6988.

[TR01] D.F. Teter, I.M. Robertson and H.K. Birnbaum, The effects of hydrogen on the deformation and fracture of β-titanium, Acta Mater. 49 (**2001**) 4313-4323.

[W97] H. Wipf, Hydrogen in Metals Ill, H. Wipf, ed., Springer-Verlag, New York, **1997**, PP. 51-91.

[WB13] C.R. Weinberger, B.L. Boyce and C.C. Battaile, Slip planes in bcc transition metals, Int. Mater. Rev. 58 (2013) 296-314.

[WH13] S. Wang, N. Hashimoto, Y.M. Wang, S. Ohnuki, Activation volume and density of mobile dislocations in hydrogen-charged iron, Acta Mater. 61 (**2013**) 4734-4742.

[WK54] R.J. Wasilewski and G.L. Kehl, Metullurgia 50, 225 (**1954**).

[WN72] D.P. Williams, H.G. Nelson, Gaseous hydrogen-induced cracking of Ti-5Al-2.5 Sn, Metall. Mater. Trans. A 3 (**1972**) 2107.

[WS68] A.H Windle, G.C. Smith, Effect of hydrogen on plastic deformation of nickel single crystals. J. Met. Sci. 2 (**1968**) 187-191.

[WS99] I. Weiss, S.L. Semiatin, Flow behavior and globularization kinetics during hot working of Ti–6Al–4V with a colony alpha microstructure, Mater. Sci. Eng. A 263 (**1999**) 243.

[WW85] O.T. Woo, G.C. Weatherly, C.E. Coleman, R.W. Gilbert, Acta Mater. 33 (**1985**) 1897.

[XV07] Q. Xu, A. Van der Ven, First-principles investigation of metal-hydride phase stability: The Ti-H system, Phys. Rev. B 76 (**2007**) 064207.

[YS98] G.A. Young, J.R. Scully, The diffusion and trapping of hydrogen in high purity aluminum, Acta Mater. 46 (**1998**) 6337-6349.

[YC91] J. Yao, J.R. Cahoon, Experimental studies of grain boundary diffusion of hydrogen in metals, Acta Mater. 39 (**1991**) 119-126.

[YJ58] H.L. Yakel, Jr., Thermocrystallography of higher hydrides of titanium and zirconium, Acta Cryst. 11 (**1958**) 46-51.

[Y81] M.H. Yoo, Slip, twinning and fracture in hexagonal close packed metals, Metall. Mater. Trans. A 2 (**1981**) 409-418.

[ZD10] J.W. Zhao, H. Ding, Y.R. Zhong, C.S. Lee, Effect of thermo hydrogen treatment on lattice defects and microstructure refinement of Ti6Al4V alloy, Int. J. Hydrogen Energy 35 (**2010**) 6448-6454.

[ZJ14] J.Y. Zhang, Mechanical behavior and microstructural evolution in metastable Ti-Mo based alloys with TRIP and TWIP effects, PhD thesis, Universite Pierre et Marie Curie, **2014**.

[ZS13] J.Y. Zhang, F. Sun, Y.L. Hao, N. Gozdecki, E. Lebrun, P. Vermaut, R. Portier, T. Gloriant, P. Laheurte, F. Prima, Mater. Sci. Eng. A 563 (**2013**) 78.

[ZZ97] Y. Zhang, S.Q. Zhang, C. Tao, Hydrogenation behavior of Ti25Al10Nb3V1Mo alloy and effect of hydrogen on its microstructure and hot deformability, Int. J. Hydrogen Energy 22 (**1997**) 125-135.

Chapter 2 Experimental procedures

2.1 Introduction

In this chapter, titanium alloys and the facilities used in the current study together with the experimental procedure will be introduced. The microstructure and mechanical properties of the as-received samples will be first described. Then hydrogen charging methods, cold rolling process and annealing treatments will be illustrated. All the equipments including the characterization tools, mechanical test instruments, and thermal analysis tools will be reported in details. **Figure 2. 1** shows the experimental procedures performed in the current work.

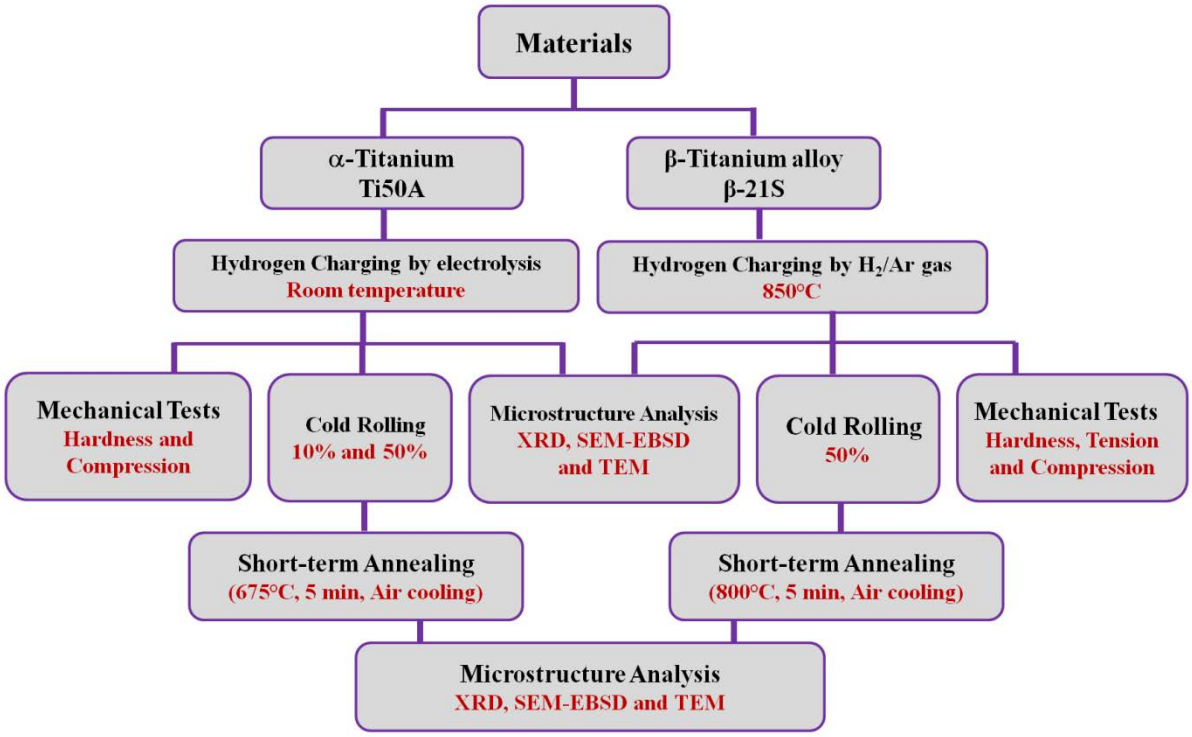

Figure 2. 1 Illustration of the experimental procedures in the current work

2.2 Materials used

Two different titanium alloys were used in this work; the commercially pure titanium (*ASTM 2*) *Ti50A* and metastable β titanium alloy *β-21S* (*Ti-15Mo-3Nb-3Al-0.2Si*). Both *Ti50A* and *β-21S* were supplied by TIMETAL Corporation in the form of thin sheets. Some of the key processes as reported in the delivered sheets include the following stages: the raw materials were prepared using standard electric-arc-melting technique, then the ingots were forged, hot rolled to achieve the desired shape, and finally, in order to improve the homogeneity of the products, annealing

treatments were performed at pre-determined temperatures in vacuum and air cooled. We will first give details for both Ti50A and β-21S alloys investigated in this study.

2.2.1 Commercially pure titanium Ti50A

The commercially pure titanium *Ti50A* is referred by the European Standard EN 3.7035, but is also designated as Ti Grade 2 by the ASTM and the UNS R50400 (Unified numbering system) in North-America. Due to its good ductility, formability and corrosion resistance, Ti50A is widely used in key engineering applications covering a variety of areas, such as chemical industrial, marine, biomaterials, etc. **[DJ00]**. The chemical composition of *Ti50A* is listed in **Table 2. 1.** It should be mentioned that the weight percent shown here is the maximum weight of each element containing in the material. In addition to its excellent mechanical properties at room temperature, *Ti50A* also has good performance at elevated temperature. For example, it is typically used in continuous service up to 425 °C and in intermittent service up to 540 °C. The typical mechanical properties of *Ti50A* is giving in **Table 2. 2**. To have a homogeneous composition and microstructure, the as-received Ti50A was annealed in vacuum at 350 °C for 6 hours. **Figure 2. 2** shows the SEM micrograph of as-annealed Ti50A. The microstructure consisted of essentially equiaxed grains with an average size of 12.0 ± 0.8 μm (data from 5 images).

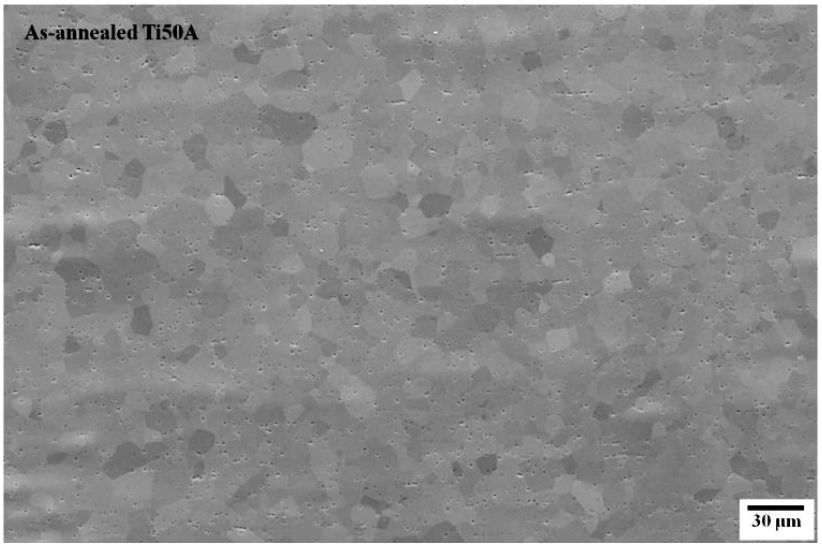

Figure 2. 2 SEM micrograph of as-annealed Ti50A

Hydrogen effects on the mechanical properties of α-Ti have been extensively investigated, especially on sheet tensile behavior under low triaxiality **[HF98, WB98 and BW02]**. However, few works have been focused on the effects of hydrogen on the cold rolling behavior in commercially pure α titanium. As it is well known, hydrogen can be readily absorbed in titanium

during melting, forging, machining, etc., and cold rolling is an essential procedure for titanium products. Therefore, understanding how hydrogen acts on cold rolling behavior in this material is an important step in order for the properties to be controlled and predicted with good reliability.

Table 2. 1 Chemical composition of commercially pure titanium Ti50A

Elements		O	N	C	Fe	H	Residual Elements	Ti
Weight (maximum)	%	0.25	0.03	0.08	0.30	0.015	0.40	Remainder

Table 2. 2 Typical mechanical properties of Ti50A at room and elevated temperature

Test Temperature °C	0.2% Yield Strength MPa	Ultimate Tensile Strength MPa	Elongation %
25	345	485	28
100	256	383	31
200	192	280	37
300	127	229	43
400	92	186	38
450	74	178	34

2.2.2 Metastable β-titanium alloy β-21S

The β-titanium alloy *β-21S* is of increasing interest for structural applications in aeronautic and aerospace due to its combination of a high strength/weight ratio, good corrosion behavior and oxidation resistance. **[N96, HU96]**. Since hydrogen has a large solubility in β-titanium alloys, hydrogen effects on the mechanical properties of *β-21S* have been extensively studied **[BH93, YS93, P97, TR01, SR03 and EG06]**. According to these studies, it can be concluded that, hydrogen in solid solution, well below the expected terminal solubility limit H/M=0.67 (H/M indicating hydrogen to metal ratio) **[SH94]** for the formation of hydride, has a significant effect on the fracture behavior.

However, there was no report related to hydrogen effects on the cold rolling behavior of *β-21S* alloy. If the amount of interstitially dissolved hydrogen is below the critical hydrogen concentration (H/M = 0.215) **[TR01]**, at which the abrupt ductile-brittle transition occurs, it is

possible or not by hydrogen action to facilitate the formation of dislocations upon cold rolling. Based on this motivation, *β-21S* alloy in solution annealed state (single β phase) was charged with hydrogen and then deformed by cold rolling.

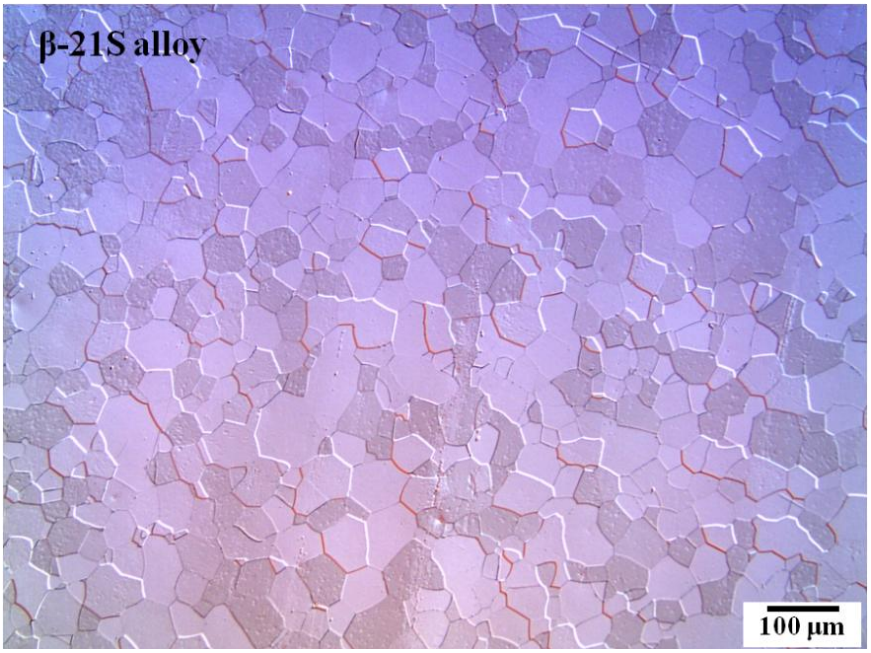

Figure 2. 3 Optical micrograph of solution-annealed β-21S alloy

Table 2. 3 Chemical composition of β-titanium alloy *β-21S*

Elements	Mo	Nb	Al	Si	Fe	O	C	N	H	Residual Elements	Ti
Weight % (maximum)	16.0	3.2	3.5	0.25	0.4	0.17	0.05	0.05	0.015	0.40	Remainder

The material used in this study is the TIMETAL®21S titanium alloy that was received in the solution annealed state in the form of 1.8 mm thick sheet. Optical micrograph (**Figure 2. 3**) revealed an equiaxed grain structure with an average grain size of approximately 35 ± 2 µm (data from 5 images). The beta transus temperature is about 807 °C. The stability of β phase can be described by the molybdenum equivalent $[Mo]_{eq}$, which combines the effects of the various β-stabilizing elements like Mo, V, Fe, Cr, Nb, etc.. A minimum value of about 10 wt. % is necessary to stabilize the β phase during quenching [**LP03 and LW07**]. As for β-21S alloy, the molybdenum equivalent $[Mo]_{eq}$ is about 13% high than the critical value for stabilizing the β phase; therefore β phase can be retained completely without α phase precipitation upon

quenching in the air. The chemical composition of *β-21S* is listed in **Table 2. 3**. The weight percent shown here is the maximum weight of each element containing in the material.

2.3 Hydrogen charging procedure

Generally, hydrogen can be introduced into metallic alloys by gaseous, electrochemical and plasma methods. Gaseous hydrogen charging is the most efficient way to hydrogenate metallic samples. Since it needs to be performed at high temperatures, safeguard procedures must be provided using hydrogen gaseous as the source of hydrogen. Compared to gaseous hydrogenation, electrochemical hydrogen charging can be performed at any temperature. **Table 2. 4** gives the advantages and disadvantages of hydrogen charging methods used in the current work.

Table 2. 4 Advantages and disadvantages of those two hydrogenation methods

	Gaseous method	Electrolytic method	Reference
Advantage	High efficiency	Temperature controllable	**[TR01]**
	Uniform hydrogen distribution	Safety	
Disadvantage	Safety problem	Slow dynamics	**[HF98], [BW02]**
	High temperature	Hydrogen concentration gradient	

2.3.1 Hydrogen charging by electrolytic technique

To investigate hydrogen-induced microstructural evolution at room temperature, hydrogen was introduced into the commercially pure titanium Ti50A by electrolytic method. In this method, the influx of hydrogen into the sample consists of the following simple steps: 1) deposition of hydrogen ions on the electrode surface; 2) consumption of one electron by each hydrogen ion to form atomic hydrogen; 3) adsorption of atomic hydrogen on the surface of sample electrode; 4) dissolution of hydrogen in the sample electrode surface; 5) diffusion of atomic hydrogen into the sample through the lattice and defects.

Prior to hydrogen charging, the samples were polished using successively SiC papers of 300, 500, 1000, 2000 and 4000 grit to remove the oxidized and contaminated layer found on the surface. Subsequently, specimens ($50 \times 15 \times 1.0$ mm^3) were charged with hydrogen in a galvanostatic mode in an electrolyte consisting of 1/3 phosphoric acid (85%) and 2/3 glycerin (85%) **[CB13]** at a current density of 2 mA/cm^2 applied during a predetermined period of time. A platinum anode of cylindrical shape was used, and specimen was located in the center of the electrolytic cell as

shown in **Figure 2. 4a**. **Table 2. 5** gives the parameters of hydrogen charging used in the present work. The hydrogen concentration C_H, which is the molar fraction of the number of hydrogen atoms to titanium atoms, can be determined via Faraday's law **(equation 1.4).** Therefore, at a constant current density, the amount of dissolved hydrogen in the sample is determined by the charging time, as shown in **Table 3. 1**. According to the Fick's second law, the distribution of hydrogen in the crystal lattice is changed with time [**SW00**]. Therefore, the characteristic diffusion time to achieve equilibrium throughout the specimen volume by electrolytical method is so long that there always exists hydrogen concentration gradient in the material. To ensure the uniform distribution of hydrogen throughout the specimen, annealing treatment at 300-400 °C lasting 4-6 hours were performed under vacuum (i.e., samples placed in sealed quartz tubes).

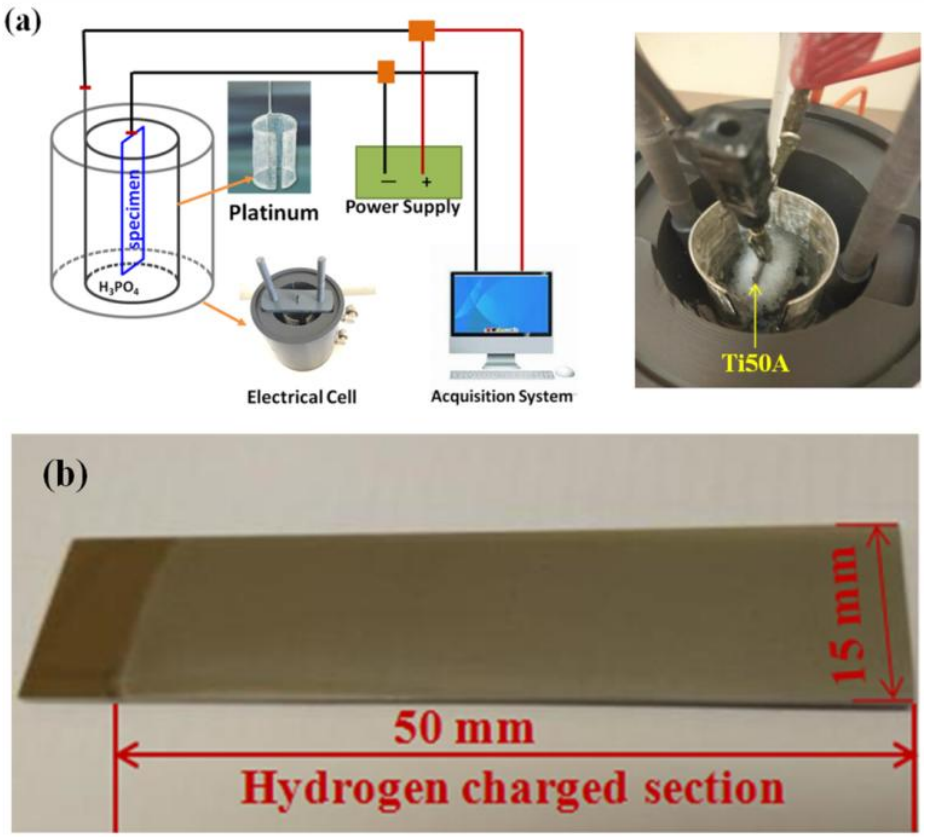

Figure 2. 4 A scheme of hydrogen charging system (a), hydrogenated Ti50A (b)

Table 2. 5 Hydrogen charging parameters by electrolytic method

Cathode	Anode	Electrolyte	Current density	Temperature	Duration	pH
Ti50A	Pt	$1/3H_3PO_4$ + 2/3glycerin	2.0 mA/cm^2	20-22°C	72, 108 and 168h	0.70

2.3.2 Hydrogen charging by molecular hydrogen gas

Compared to the electrolytical charging method, the characteristic diffusion time to achieve equilibrium throughout the specimen volume is of the order to seconds by gaseous hydrogen charging. Therefore, to maintain a single β phase and to have a uniform distribution of hydrogen throughout the sample volume, the hydrogen charging by molecular hydrogen gas was employed to the β-titanium alloy *β-21S*. The instrument of gaseous-hydrogen charging system of the Professor Ravi Chandran of the University of Utah in Salt Lake City, U.S.A has been used in this study.

The samples were loaded with hydrogen using the following procedures: firstly, the samples were placed in the charging furnace at 10^{-4} Pa; subsequently, the furnace temperature was increased to 1123 K for 10 min to dissolve any surface oxides; and then H_2 gas with Ar, was introduced at a predetermined pressure, which was maintained for a time sufficient to reach equilibrium throughout the specimen volume; finally, the specimens were furnace cooled at a constant flow of hydrogen and Ar gas. In this method, different hydrogen concentration can be obtained by controlling the partial pressure of hydrogen gas and the charging time. The final hydrogen concentrations and the corresponding hydrogen gas pressure will be given in **Table 4. 1**.

It should be mentioned that, at the temperature of 1123 K, the characteristic diffusion time to achieve equilibrium throughout the specimen volume is of the order of seconds; the diffusion coefficient at 1000 K is approximately 10^{-8} m^2/s, as shown in **Figure 1. 10.** Hydrogen absorption can therefore occur during cooling, with the final H/M value being achieved at some indeterminate temperature at which a surface oxide forms and prevents further entry of hydrogen. Consequently, the final dissolved hydrogen in β-21S alloy is not only dependent on the pressure during charging, but on the pressure in the furnace chamber during cooling and the cooling rate, as reported in the previous studies **[TR01]**. The amount of hydrogen dissolved in the sample was measured via the inert gas fusion instrument (LECO TCH-600) in the professor Ravi Chandran's lab at the University of Utah, USA.

2.4 Mechanical tests

As it has been demonstrated in previous studies, hydrogen has a significant impact on the mechanical properties of titanium and titanium alloys [**TR01, EG06 and YL10**]. In the current

work and before studying the cold rolled behavior, the microhardness, tension, compression and nanoindentation tests were employed to reveal hydrogen effects on the mechanical properties of Ti50A and β21S alloy.

2.4.1 Microhardness test

Vickers hardness was measured on the cross section of specimen using a Microhardness Tester (DIN50190/1) under a load of 50 g applied during 10 s. The microhardness under this load provides information of the individual grain. The microhardness profile from the up-surface to the bottom-surface was performed in a zigzag mode at intervals of 0.05 mm. **Figure 2. 5** shows a scheme of microhardness measurements performed on the surface and cross-section of Ti50A.

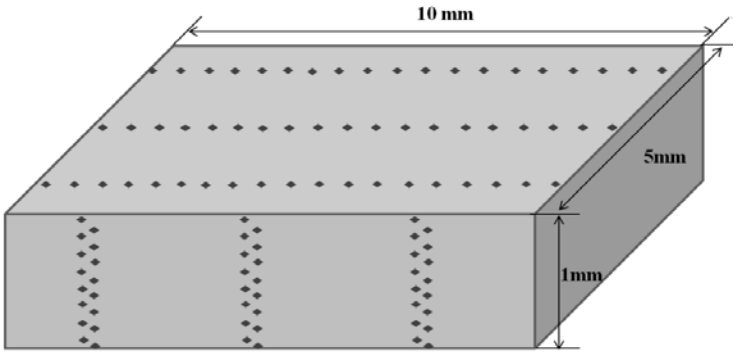

Figure 2. 5 A scheme of microhardness measurement performed on the surface and cross-section of Ti50A

2.4.2 Tension test

Tensile test specimens were extracted from the as-received sheet by means of water jet cutting to avoid the microstructure affected by temperature. The dimension of tensile specimen was presented in **Figure 2. 6**, strains were measured using extensometer. Room temperature tensile tests were performed using an Instron tensile test machine at a strain rate of 0.01 s^{-1}, to examine hydrogen effect on the tensile behavior of β-21S alloys. The displacement in the gage portion was recorded using an extensometer. At least two tests were performed for each hydrogen concentration.

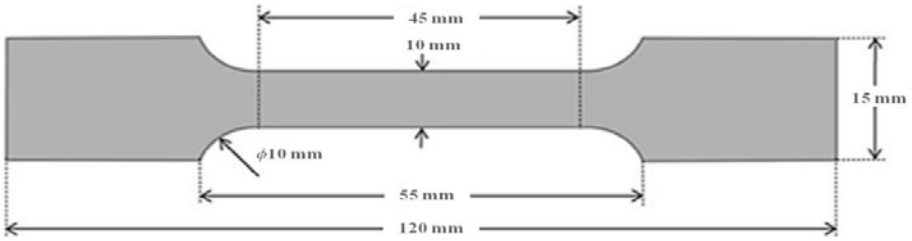

Figure 2. 6 Dimension of tension specimen

2.4.3 Compression test

Similar to tensile test, compressive test was employed to reveal the effect of hydrogen on the compressive behavior of the commercial pure titanium Ti50A and metastable beta-titanium β-21S alloy. Room temperature compression tests were conducted at a strain rate of $1 \times 10^{-3}s^{-1}$ using a Zwick 120T machine. Tests performed on the commercial pure titanium Ti50A are further described in Appendix B. The dimension of the sample for compression test on β-21S alloy is shown in **Figure 2. 7**. The strain was determined by the **formula 2.1**:

$$\varepsilon_c = \frac{H_c - H_0}{H_0} \times 100\% \qquad \textbf{(2.1)}$$

where H_0 is the initial height of specimen before compressive test, H_c is the height of the specimen during compressive test.

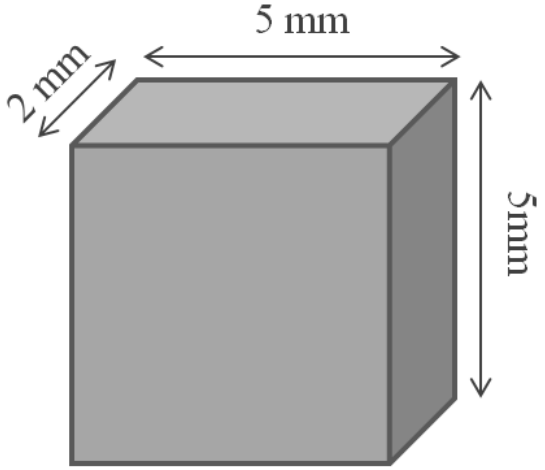

Figure 2. 7 Dimension of compression specimen

2.4.4 Nanoindentation test

In the current study, nanoindentation is employed to measure the mechanical property within a grain in the hydrogenated Ti50A. Nanoindentation is a variety of indentation hardness tests applied to small volumes. Compared to the traditional indentation test (macro or micro indentation), it provides high spatial resolutions to place the indents and a real-time load-displacement (into the surface) data while the indentation is in progress. Moreover, it is capable of measuring both the plastic and elastic deformation of the material under test.

Figure 2. 8 shows a typical indentation "load-displacement" indentation curve during indenting process, S is the tangent to the unloading curve (S=dp/dh). Applied force and depth are measured

dynamically during the load-unload cycle. In the process of indentation, a record of penetration depth h is made, and then the area of the indent is determined using the known geometry of the indentation tip. Hardness and elastic modulus can be calculated directly from the resultant load-displacement curve. Sample modulus can be determined from force-displacement curve equations **2.2, 2.3, 2.4**, indenter properties (modulus and Poisson's ratio) and sample Poisson's ratio. For example, for the isotropy materials, the sample modulus E_{IT} can be determined from the combination of **equations 2.2** and **2.3.** In **equation 2.2**, E_r stands for the reduced modulus, S is the tangent to the unloading curve as indicated **Figure 2. 8** in A_p is the projected contact area determined from the contact depth h_c and β is a geometric factor (dependent on the indenter shape) which corrects for the usage of pyramid indenter. In **equation 2.3,** E_i and ν_i are the modulus and Poisson's ration of the indenter, respectively, while ν_s is Poisson's ratio of the tested sample.

$$E_r = \frac{\sqrt{\pi}}{2\beta}\frac{S}{\sqrt{A_p}} \qquad \textbf{(2.2)}$$

$$\frac{1}{E_r} = \frac{(1-\nu_s^2)}{\mathrm{E_{IT}}} + \frac{(1-\nu_i^2)}{E_i} \qquad \textbf{(2.3)}$$

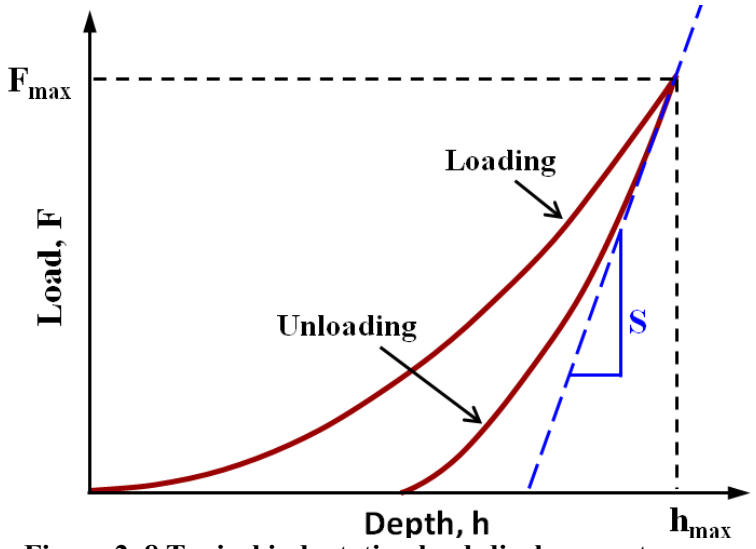

Figure 2. 8 Typical indentation load-displacement curve

In nanoindentation test, small loads and tip sizes are used, so the indentation area may only be a few square micrometers or even nanometers. This gives rise to problems in determining the hardness, as the contact area is easily not found. In the present work, the standard tip named

Berkovich tip (142.3°) is employed, which has a three-sided pyramid geometry providing high precision. The maximum load is 1.00 mN, and the loading/unloading rate is 2.00 mN/min.

2.5 Cold rolling process

Recent studies have reported that interstitially dissolved hydrogen can facilitate the formation of vacancies, dislocations and stacking faults under plastic deformation **[TG10, BV10, GK14, KS10 and DB15].** These effects can be explained by the **defactant** concept **[K07 and K09]**, the basis of which is that a decrease in the overall free energy is caused by the segregation of hydrogen atoms at the neighboring defects. Therefore, if hydrogen is first dissolved as a defactant into titanium alloys to facilitate the formation of dislocations upon cold rolling and then removed from the material by means of an the annealing process, the dislocation density and the concomitantly properties such as hardness/strength will be increased.

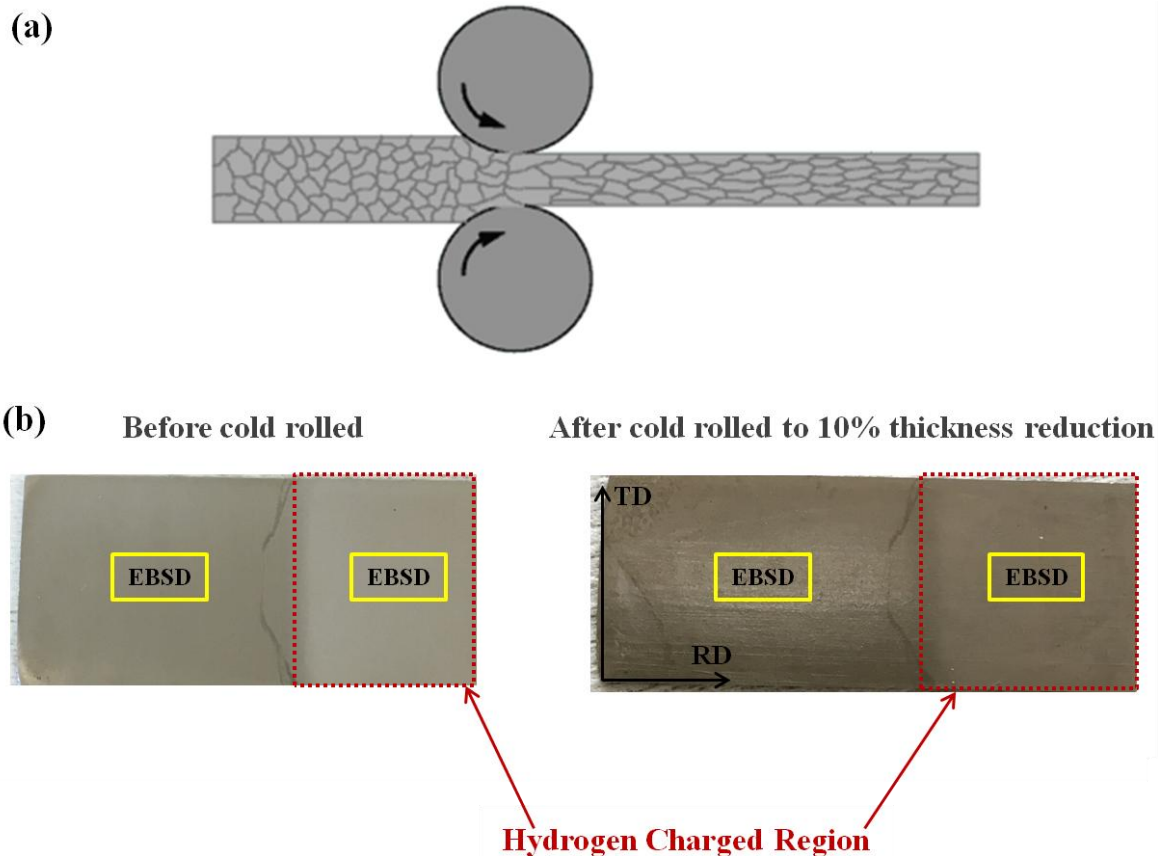

Figure 2. 9 A scheme of cold rolling process (a) and an example of cold rolled Ti50A (b)

Based on this motivation, following hydrogenation, cold rolling was undertaken to inspect how hydrogen acts on the cold rolling behavior. The hydrogenated samples were deformed at room temperature by normal symmetric rolling using a fixed rolling speed. The same velocity was

imparted to two rollers of the same size: the roller rotation speed was 63 rpm, giving a circumferential velocity of 0.73 m/s. Unidirectional multi-pass rolling was carried out using ~1 pct. reduction per pass. Samples were extracted from the rolled sheet after thickness reduction of 10% and 50% for microstructural analysis. A scheme of cold rolling process and an example of hydrogenated Ti50A before and after cold rolling are shown in **Figure 2. 9** (EBSD detected regions are indicated by yellow rectangles).

2.6 Annealing treatment

The first report on the dependency of the recrystallization and recovery behavior with hydrogen was provided by Golstov and coworkers on the deformed pure palladium **[GG06]**. More recently, Shan and co-workers **[SZ08]**, who studied the flow softening of the α phase in Ti-6Al-4V-xH alloy, have reported that the hydrogen improved the dynamic recrystallization (DRX) occurring during mechanical loading at high temperature.

According to these reports, the combined effect of hydrogen and plastic deformation on recrystallization in Ti50A and β-21S alloy was investigated in this study. Therefore, following cold rolling, the hydrogenated specimens were finally subjected to annealing treatment at pre-determined temperature for several minutes and air-cooled. **Table 2. 6** gives the parameters of annealing treatments performed on the cold rolled Ti50A and β-21S alloys.

Table 2. 6 Parameters of the annealing treatments performed on cold rolled Ti50A and β-21S alloys

	Sample thickness, mm	Temperature, °C	Time, min	Cooling condition
Ti50A	0.5	675	5	Furnace cooling
β-21S	0.9	800	5	Air cooling

2.7 Polishing preparation

In the present work, hydrogen was introduced into Ti50A by an electrolytic method. Prior to hydrogen charging, to emphasize the hydrogen-affected region, the thickness of the as-received Ti50A was reduced by mechanical polishing followed by an annealing treatment performed in the vacuum for 2 h at 350 °C in order to relieve the potential residual stresses generated during sample preparation. The sample surfaces were then polished using successively SiC papers of 300, 500, 1000, 2000 and 4000 grit to remove the oxidized and contaminated layers. Then, to

minimize the undesired factors affecting hydrogen evolution in the material microstructure, the samples were vibration polished for 2 h to remove residual stresses and deformed layers. The final thickness of the sample for hydrogenation was around 1.0 mm.

In addition, the standard metallurgical polishing process is applied to all samples for SEM-EBSD characterization: samples were grinded on 1000, 1200, 2400 and 4000 grit SiC paper manually on a struers LabPol-21S equipment, and then electrolytically polished at 5°C and 30 V for 10 seconds in a solution of 100 ml perchloric acid and 900 ml methanol using a Struers LectroPol-3 to remove the surface deformation layer caused by grinding. A binocular lens (Leica Stereomicroscope) is used to verify the quality of sample preparation for subsequent microstructure morphology and SEM-EBSD analysis.

2.8 Microstructural characterization

The microstructural evolution was studied by considering the aspects of morphology, structure, and crystallography. Depending on the size scale of the specific microstructure, analyses by means of X-ray diffraction, scanning electron microscope coupled with electron backscatter diffraction and transmission electron microscope were performed to thoroughly characterize the microstructural evolution in the materials under various conditions.

2.8.1 X-ray diffraction

To qualitative identify the phase structure and measure the texture of deformed specimen, the XRD measurements were undertaken using Cu-K_α radiation with a wavelength of 0.154 nm. For each measurement, the sample is tilted from 1.25 to 71.25° with a step size of 2.5°/s. At each of the tilting, the sample is rotated by 360° with a step size of 0.1°/s. The instrumental broadening profile was obtained by measuring a standard strain-free LaB6 powder.

2.8.2 Scanning electron microscopy

To investigate microstructure details, a JEOL-6500F field emission gun scanning electron microscope equipped with an EBSD detector and the AZtec acquisition software package (Oxford Instruments) was used. The morphology was characterized by secondary electron imaging(SEI) image. The SEM is equipped with a backscattered electron acquisition camera to perform Electron Back-Scattered Diffraction (EBSD) measurements which provides crystallographic orientation information of the observed surface. The acquisition and online indexation is realized by the Oxford Channel 5 software. The working voltage was set to be 15

KV. To ensure a reliable orientation determination, the minimum number of detected bands is set to 7. The maximum mean angular deviation (MAD) allowed between the theoretical EBSD pattern and the experimental EBSD pattern was set to 1. The orientation data were manually and automatically acquired respectively. For automatic orientation mapping, the beam control mode was applied. The step size of mapping depends on the grain size and will be detailed in the following chapters. For individual orientation of the locally deformed microstructure, the EBSD orientation data were analyzed using the Analysis Tools for Orientation Map (ATOM) software [**BF15**].

2.8.3 Transmission electron microscopy

For TEM observations, thin foils were extracted from the hydrogenated samples by ionic micromachining from selected areas previously localized by SEM-EBSD. Extraction was performed with a Focused Ion Beam (FIB) Zeiss Auriga 40 equipped with both electronic and ionic columns (Gemini and Orsay Physics Cobra, respectively). For most part of the machining process, an ionic Ga beam of 30 kV was used. Before extraction, thin foils were finished under a beam of 2 kV to eliminate amorphous layers due to the high energy abrasion. Then, microstructures were observed in a Philips TEM 200 CX for both imaging and phase determination upon a working voltage set at 200kV.

References

[BH93] T. Boellinghaus, H. Hoffmeister, L. Reuter, Proceedings of the International Conference on Supermartensitic Stainless Steels, Bruxelles, (**1993)** 264.

[BF15] B. Beausir, J.-J. Fundenberger, Université de Lorraine - Metz, ATOM - Analysis Tools for Orientation Maps, http://atom-software.eu/ **2015**.

[BV10] A. Barnoush, H. Vehoff, Recent developments in the study of hydrogen embrittlement: Hydrogen effect on dislocation nucleation, Acta Mater. 58 (**2010**) 5274-5285.

[BW02] C.L. Briant , Z.F. Wang, N. Chollocoop, Hydrogen embrittlement of commercial purity titanium, Corros. Sci.44 (2002) 1875-1888.

[CB13] Y.Z. Chen, H.P. Barth, M. Deutges, C. Borchers, F. Liu, R. Kirchheim, Increase in dislocation density in cold-deformed Pd using H as a temporary alloying addition, Scripta Mater. 68 (**2013**) 743-746.

[CD00] H.J. Christ, M. Decker, S. Zeitler, Metall. Mater. Trans. A 31 (**2000**) 1507-1517.

[DB15] M. Deutges, H.P. Barth, Y.Z. Chen, C. Borchers, R. Kirchheim, Hydrogen diffusivities as a measure of relative dislocation densities in palladium and increase of the density by plastic deformation in the presence of dissolved hydrogen, Acta Mater. 82 (**2015**) 266-274.

[DJ00] M.J. Donachie, Jr., Titanium: a Technical Guide, Second Edition, ASM, **2000**, ISBN 0-87170-686-5. SAN: 204-7586.

[EG06] D. Eliezer, E. Tal-Gutelmacher, C.E. Cross, Th. Boellinghaus, Hydrogen trapping in β-21S titanium alloy, Mater. Sci. Eng A 421 (**2006**) 200-207.

[GG06] V.A. Goltsov, D.A. Glyakov, G.I. Zhirov, Int. J. Hydrogen Energy 31 (**2006**) 211-216.

[GK14] V. Gaspard, G. Kermouche, D. Delafosse, A. Barnoush, Hydrogen effect on dislocation nucleation in a ferritic alloy Fe–15Cr as observed per nanoindentation, Mater. Sci. Eng. A 604 (**2014**) 86-91.

[HF98] J. Huez, X. Feaugas, A.L. Helbert, I. Guillot and M. Clavel, Damage process in commercially pure α-titanium alloy without (Ti40) and with (Ti40-H) hydrides, Metall. Mater. Trans. A 29 (**1998**) 1615-1628.

[HU96] D.A. Hardwick, D.G. Ulmer, in: A.W. Thompson, N.R. Moody (Eds.), Hydrogen Effects in Metals, TMS, Warrendale, PA, **1996**, p. 735.

[K07] R. Kirchheim, Reducing grain boundary, dislocation line and vacancy formation energies by solute segregation. I. Theoretical background, Acta Mater. 55 (**2007**) 5129-5138.

[K09] R. Kirchheim, Int. J. Mat. Res. 100 (**2009**) 483.

[KS10] M. Krystian, D. Setman, B. Mingler, G. Krexner, M.J. Zehetbauer, On the formation of super-abundant vacancies in Pd-H deformed by high pressure torsion, Scripta Mater. 62 (**2010**) 49.

[LP03] C. Leyens, M. Peters (Eds.), Titanium and Titanium Alloys: Fundamentals and Applications, Wiley-VCH Verlag GmbH, **2003,** Weinheim.

[LW07] G. Lütjering, and J.C. Williams, Titanium (Engineering Materials and Processes). **2007**, Berlin Heidelberg: Springer.

[N96] H.G. Nelson, in: A.W. Thompson, N.R. Moody (Eds.), Hydrogen Effects in Metals, TMS, Warrendale, PA, **1996**, p. 699.

[P97] B.G. Pound, Acta Mater. 45 (**1997**) 2059.

[S00] P.A. Sundaram et al., Determination of the diffusion coefficient of hydrogen in Gamma Titanium Aluminides during electrolytic charging, Acta mater. 48 (**2000**) 1005-1019.

[SR03] P. Sofronis, I.M. Robertson, Y. Liang, D.F. Teter, N. Aravas, in: N.R. Moody, A.W. Thompson, R.E. Ricker, G.S. Was, R.H. Jones (Eds.), Hydrogen Effects on Material Behavior and Corrosion Deformation Interactions, TMS-AIME, Warrendale, PA, **2003**, p. 537.

[SH94] S.N. Sankaran, R.K. Herrmann, K.E. Wiedemann and R.N. Shenoy, in Microstructure-Property Relationships in Titanium Alloys. TMS, Warrendale, PA, **1994**, P. 215.

[SW00] P.A. Sundaram, E. Wessel, H. Clemens, H. Kestler, P.J. Ennis, W.J. Quadakkers and L. Singheiser, Determination of the diffusion coefficient of hydrogen in gamma titanium aluminades during elctrolytic charging, Acta Mater. 48 (**2000**) 1005-1019.

[SZ08] D. Shan, Y.Y. Zong, et al., The effect of hydrogen on the strengthening and softening of Ti-6Al-4V alloy, Scripta Mater. 58 (**2008**) 449-452.

[TG10] E. Tal-Gutelmacher, R. Gemma, C.A. Volkert and R. Kirchheim, Hydrogen effect on dislocation nucleation in a vanadium (1 0 0) single crystal as observed during nanoindentation,

Scripta Mater. 63 (**2010**) 1032-1035.

[TR01] D.F. Teter, I.M. Robertson, H.K. Birnbaum, Acta Mater. 49 (**2001**) 4313.

[W97] H. Wipf, Hydrogen in Metals Ill, H. Wipf, ed., Springer-Verlag, New York, **1997**, PP. 51-91.

[WB98] Z.F. Wang, C.L. Briant, K.S. Kumar, Corros. Sci. 54 (**1998**) 553-560.

[YS93] G.A. Young, J.R. Scully, Scripta Mater. 28 (**1993**) 507.

[YL10] B.G. Yuan, C.F. Li, H.P. Yu and D.L. Sun, Influence of hydrogen content on tensile and compressive properties of Ti-6Al-4V alloy at room temperature, Mater. Sci. Eng. A 527 (**2010**) 4185-4190.

Chapter 3 Hydrogen evolution and its effects on mechanical properties in Ti50A

3.1 Introduction

The commercially pure titanium Ti50A has been widely used in key engineering applications covering a variety of areas, such as chemical industrial,marine, biomaterials, etc., due to its unique combination of mechanical and chemical properties [**LW03, DJ00**]. In most of these applications, the components operate in environment that can act as sources of hydrogen after dissociation of the H_2 molecules on Ti surfaces [**WF08**]. Consequently, understanding the interaction of hydrogen with this material is important so that its properties can be controlled and reliably predicted.

Since hydrogen has a low solubity in α-titanium at room temperature, hydride can be formed at the grain boundaries as a consequence of hydrogen supersaturation. The hydride precipitation is influenced by various factors such as material composition, oxygen content, texture, stress states et al. [**G03, CD07 and CCB17**]. Numerious studies have showed that the hydrogen-induced degradation of mechanical properties in titanium and zirconium alloys, is closely related to the hydrogen content and its interaction with the dislocations **[C81, BD15, RX12, CCB17 and CG17**]. Therefore, the present work is aiming at thoroughly inspecting the hydrogen evolution and its effects on the mechanical properties of Ti50A using combined XRD, SEM-EBSD and TEM analyses.

3.2 Results and discussion

3.2.1 Microstructure of as-received Ti50A

To emphasize the hydrogen-affected region, the thickness of the as-received (AR) samples mechanically cut from the sheet was reduced by mechanical polishing followed by an annealing treatment performed in the vacuum for 2 h at 350 °C in order to relieve the potential residual stresses generated during sample preparation. The XRD pattern of annealed Ti50A is shown in **Figure 3. 1**. We can see that the pattern consists only of the α phase; no indication of hydride precipitation is observed. Fitting the XRD pattern with MAUD program, the lattice parameters of α phase are calculated to be a=0.293 nm and c=0.465 nm, giving a c/a ratio of 1.587. Then the microstructure of the annealed Ti50A was investigated using SEM-EBSD microscopy. **Figure 3.2** gives the Inverse-Pole-Figure (IPF) map with grain boundaries and pole figures of the annealed Ti50A. We can see that the initial microstructure (**Figure 3.2**a) is composed of

equiaxed grains with a mean grain size of about 12 ± 0.8 μm (3500 grains). In addition, there exists a typical rolling texture of α-titanium characterized by two components at ±30° tilted from the normal direction (ND) to the transverse direction (TD) in the annealed Ti50A, as presented in (**Figure 3.2**b).

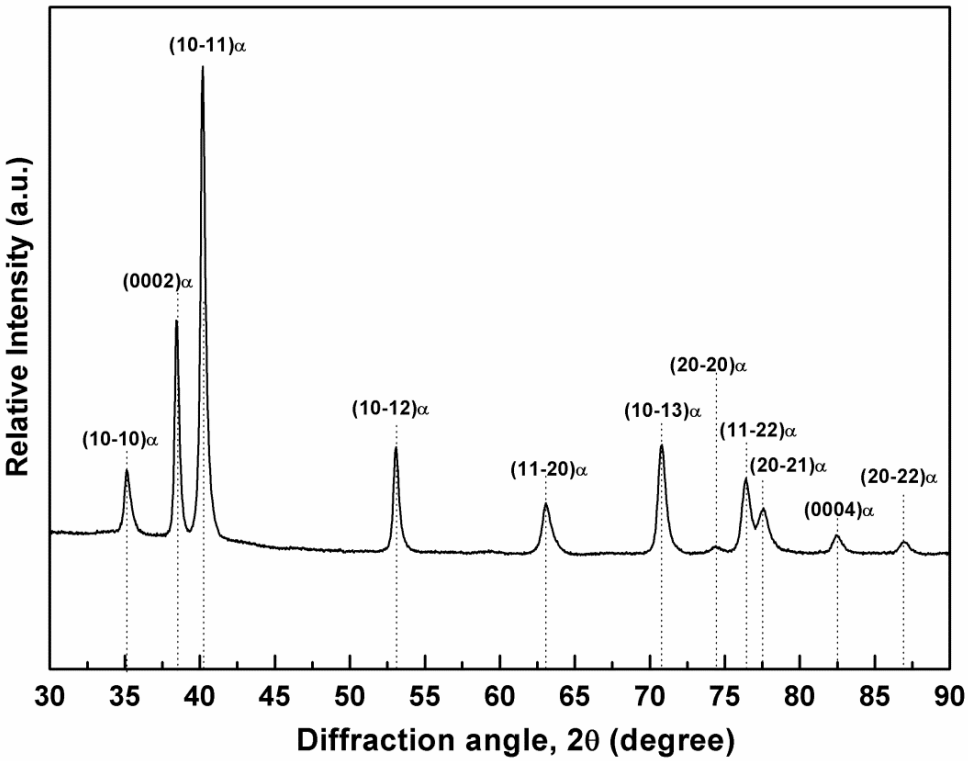

Figure 3. 1 XRD pattern of as-received Ti50A after annealing treatment

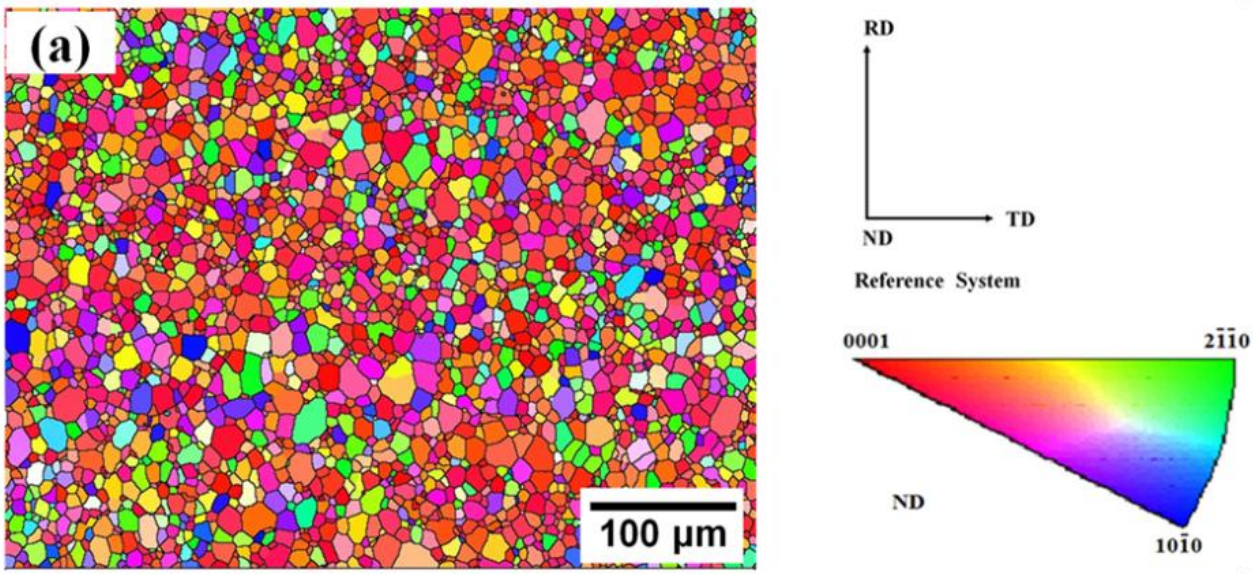

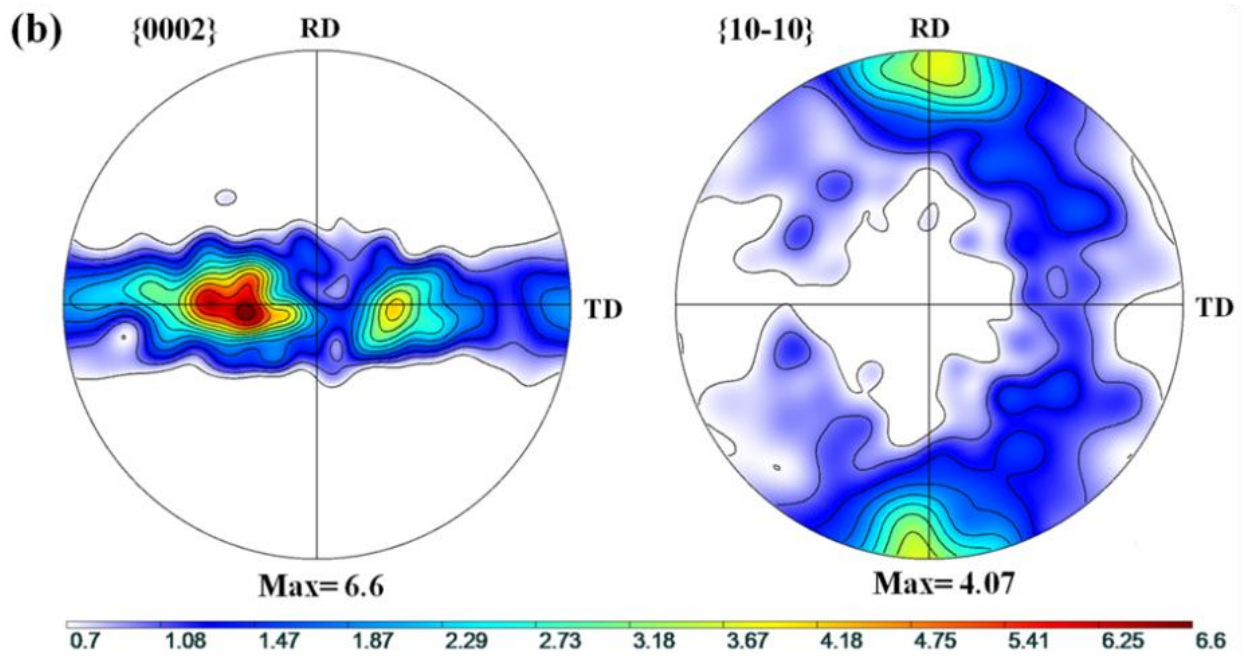

Figure 3. 2 IPF (Inverse-Pole-Figure) map with grain boundaries (a) and pole figures (b) of As-received Ti50A

3.2.2 Hydrogen induced phase transformation and microstructural evolution

3.2.2.1 XRD analyses

Before XRD measurements, the amounts of hydrogen absorbed in the samples were determined via the inert gas fusion instrument (LECO TCH-600) at the University of Utah in Salt Lake City, U.S.A. **Table 3. 1** gives the values of the hydrogen concentration determined by LECO and those calculated from Faraday's Law [**DB15**], respectively. It is worth noting that a small amount of hydrogen was already detected in the as-received state. This can be explained by the high affinity of Ti with H and the catalytic property of Ti that favors the dissociation of H_2 molecules at the surface, as mentioned by Darbha Srinivas and Paul Ratnasamy [**SR07**]. It can be seen that during electrolytic charging, the actual hydrogen concentration absorbed in the specimens were much lower than that determined by the Faraday' law. That is because the formation of H_2 bubbles at the surface consume a large number of hydrogen atoms. Moreover the dissolved hydrogen concentration increased linearly with the charging time, which indicates that lattice diffusion appears to be the rate controlling mechanism in the process of hydrogen charging in Ti50A.

Table 3. 1 Hydrogen contents for different charging times at current density of 2 mA/cm^2

Charging times	0 h	72 h	108 h	168 h
Hydrogen content measured by LECO, ppm	23.32 ± 2.30	65.17 ± 3.50	88.53 ± 4.00	138.05 ± 6.50
Hydrogen contents determined by Faraday's Law [DB15], ppm	/	761.76 ± 5.85	1142.64 ± 6.40	1777.44 ± 8.50

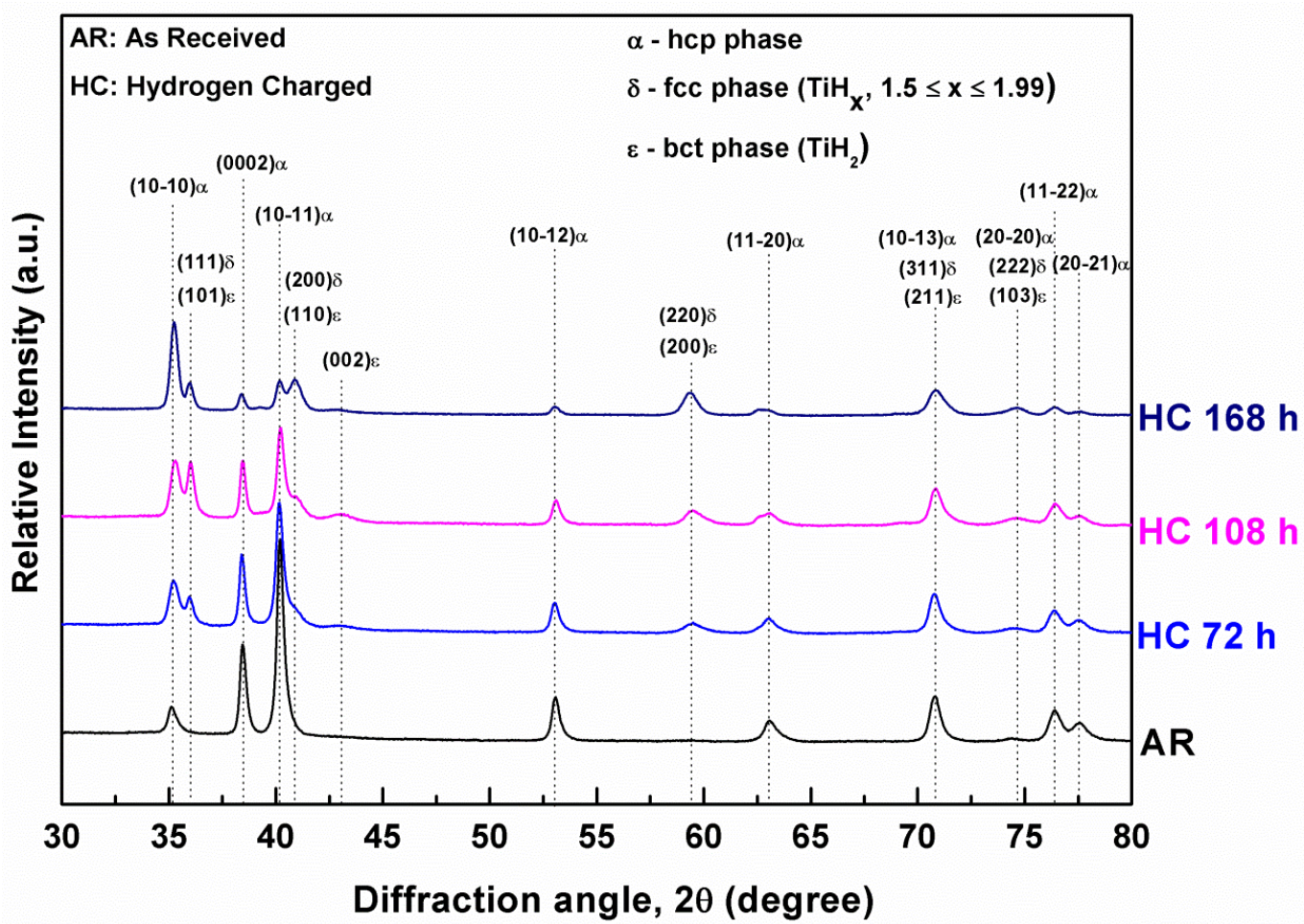

Figure 3. 3 XRD patterns of Ti50A (as received) and Ti50A (HC) subjected to different hydrogen charging times

The X-ray diffraction patterns after 72 h hydrogen charging time, as shown in **Figure 3. 3**, evidenced the precipitation of two types of hydrides, i.e., δ-TiH_x and ε-TiH_2, for a concentration of about 60 ppm. To estimate the thickness of the hydride layer, the hydrogenated sample was firstly mechanical polished layer by layer, and then the polished sample was installed at the XRD

instrument to detect the hydride phases. Those two procedures were repeated several times until no hydride could be detected. Therefore, by measuring the thickness of the polished sample, the removed hydride layer can be calculated. Under these H charging conditions, and reminding that XRD cannot detect phase of small size and present in low volume fraction, the thickness of the hydride layer was estimated to be about 20 ± 2 μm. The TiH_x ($1.5 \leq x \leq 1.99$) δ-hydride has a face centered cubic (fcc) lattice (a = 0.4445 nm) with the hydrogen atoms occupying the tetrahedral interstitial sites (CaF2 structure), while the TiH_2 ε-hydride has a body centered tetragonal (bct) lattice with a = 0.312 nm and c = 0.418 nm (JCPDS-PDF 9-371) **[WE02, LX13]**. As observed in the XRD patterns, the intensity of the diffraction peaks corresponding to the hydride phases increased with the charging time, suggesting an increase in the volume fraction of hydrides formed in the sample. According to the binary constitution phase diagram of Ti-H system, the terminal hydrogen solubility in the alpha phase is only approximately 1500 ppm and decreases rapidly with decreasing temperature. At room temperature, the terminal hydrogen solubility in α-titanium is quite negligible (~8.35 ppm) **[N96]**. It should be mentioned that, at low concentration, hydrogen atoms dissolved in the α-solid solution occupying interstitial sites of the hexagonal lattice and can be defined as quasi-mobile hydrogen atoms; at higher hydrogen concentration, above the expected terminal solubility limit, the formation of hydride takes place; these atoms bonded to Ti will be referred as bonded hydrogen. Furthermore, as suggested by Briant [**BW02**], the formation of hydrides beneath the surface layer required the existence of a supersaturated solution of hydrogen in the α-phase.

In addition, it can be noticed that the XRD peaks corresponding to the matrix α phase became broadened as the charging time increased. Williams et al. **[W76]** have pointed that the hcp α-phase to the δ-TiH_x phase transformation resulted in an approximately 20.8% volume expansion, and this volume effect associated with the hydride formation led to a local plastic deformation of the matrix accompanied by an increase in the dislocation density. Therefore, the broadening peaks of α-phase can be attributed to the occurrence of local deformation caused by the phase transformation within the sample.

3.2.2.2 SEM-EBSD characterizations

SEM microscopy was used to investigate the surface morphology of the hydrogenated Ti50A-H (hydrogen charged for 168 h). **Figure 3. 4** shows the SEM (SEI) images taken on the surface of

Ti50A without hydrogen (**Figure 3. 4**a) and after hydrogenation for 168 h (**Figure 3. 4**b). After hydrogen charging for 168 h, plate-like hydrides were found to precipitate from the matrix α phase. As observed, the hydrides are heterogeneously distributed on the matrix, which indicates that the formation of hydride is orientation dependent. The orientation relationship between hydride and α phase will be addressed by EBSD in the following context.

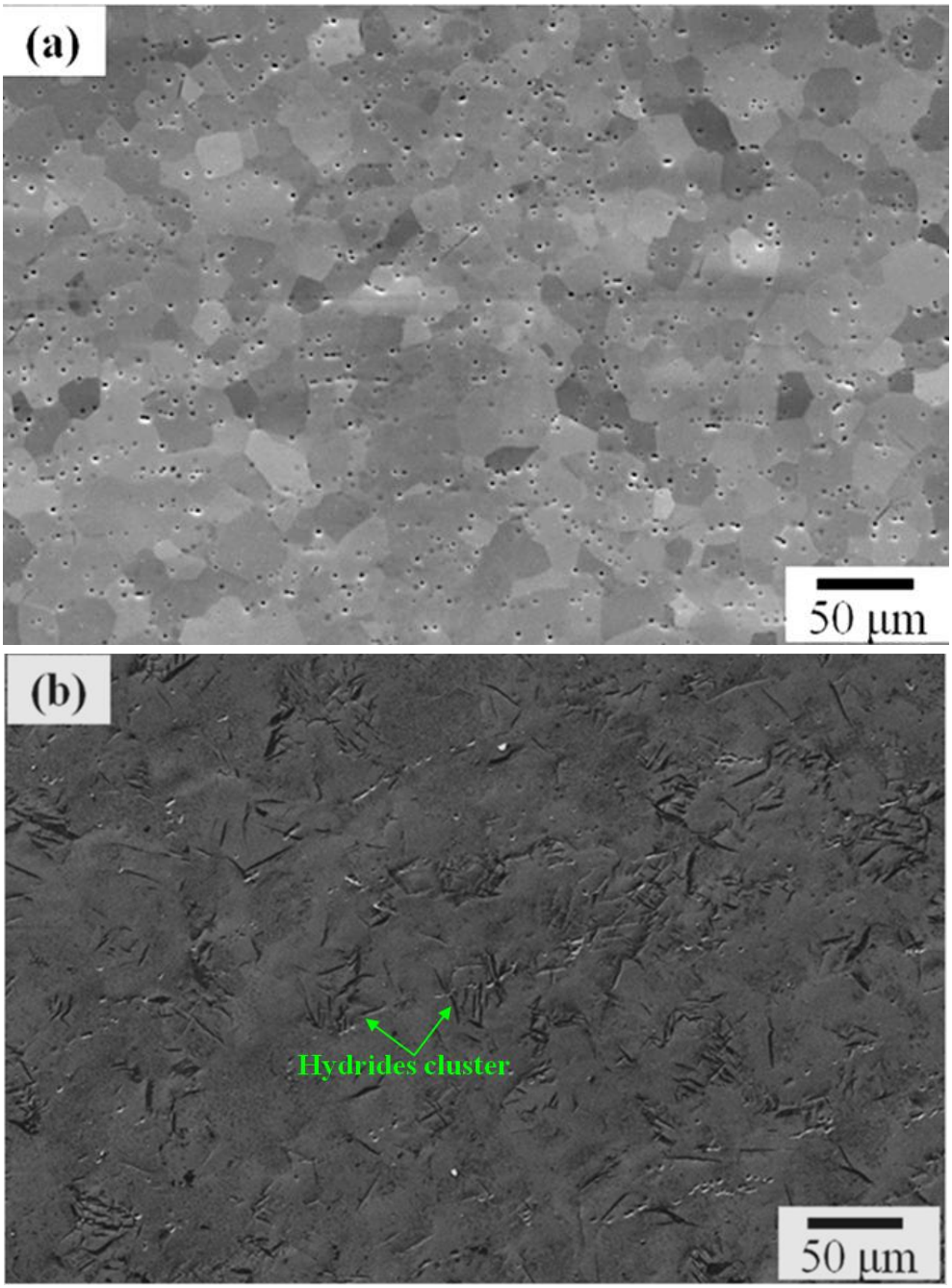

Figure 3. 4 SEM (SEI) images taken on the surface of as received Ti50A (a) and the specimen hydrogen charged for 168 h (b)

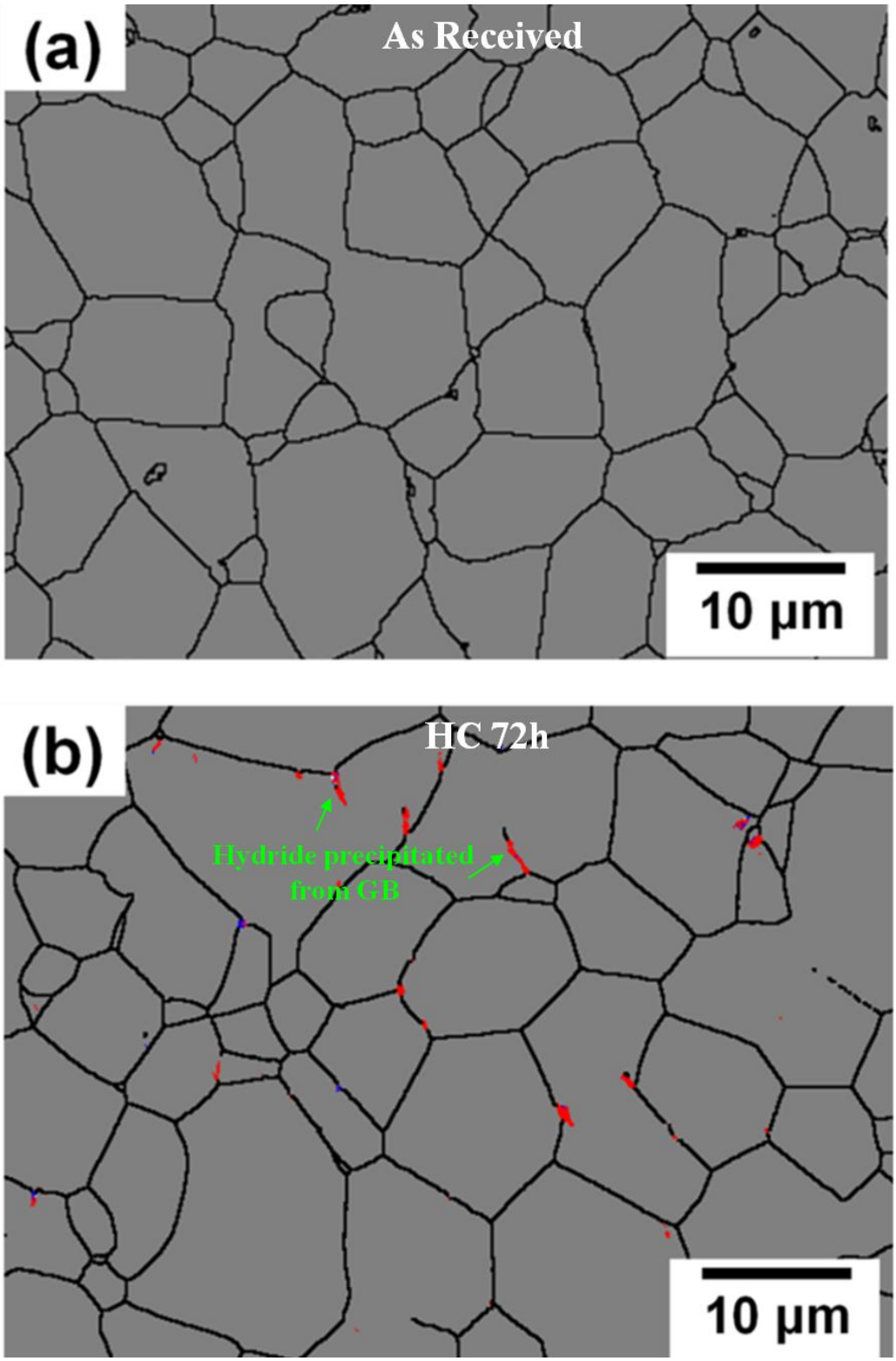
(a)
As Received
10 μm
(b)
HC 72h
Hydride precipitated from GB
10 μm

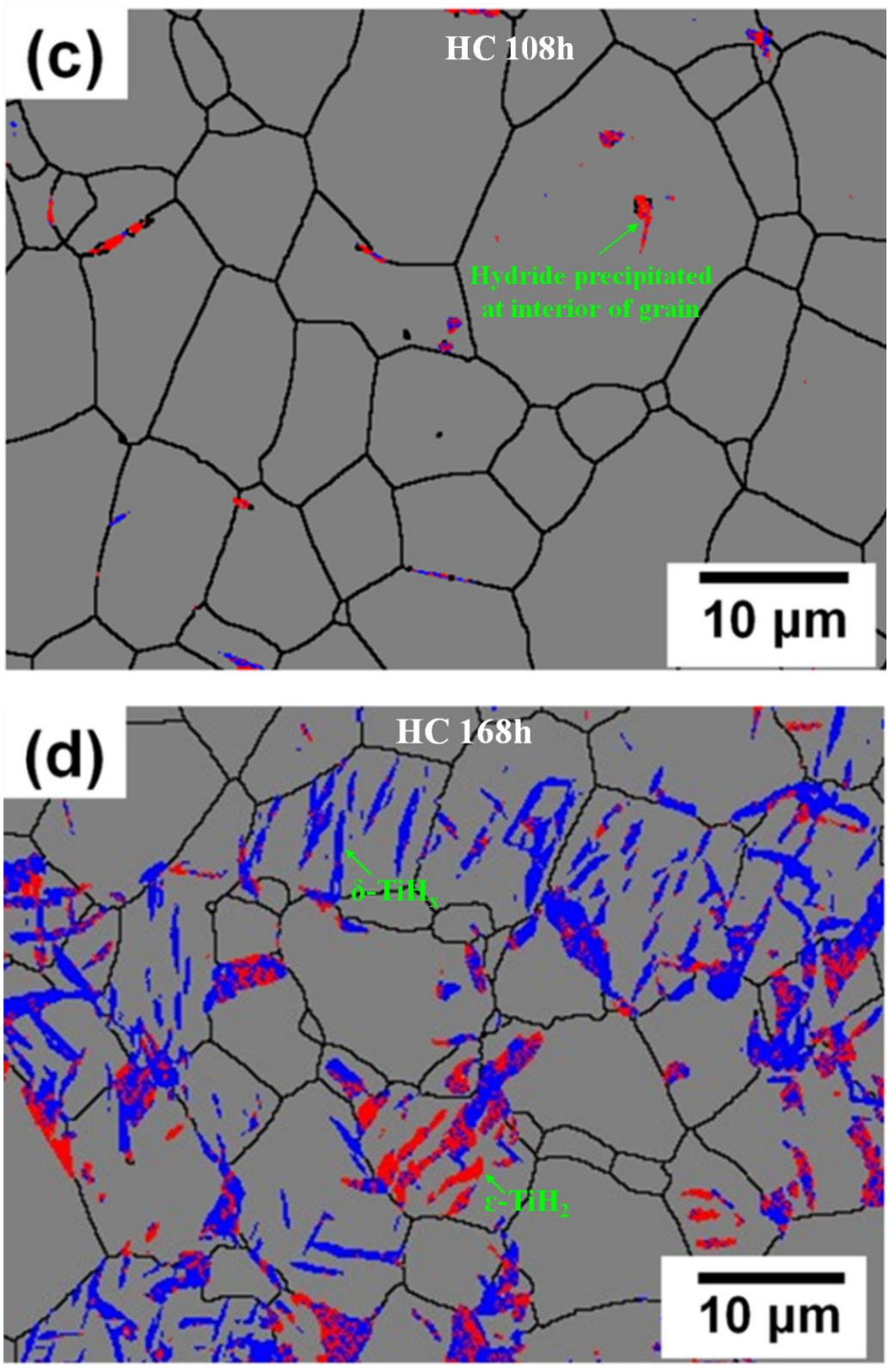

Figure 3. 5 EBSD phase maps of as-received Ti50A (a), hydrogen charged for 72 h (b), 108 h (c) and 168 h (d); (the red, blue and gray colors corresponding to ε-TiH_2, δ-TiH_x hydrides and the matrix α phase).

To quantitatively investigate the hydrogen evolution, the microstructures of Ti50A samples after 72, 108 and 168 h hydrogen charging were characterized by EBSD technique**.** Prior to EBSD measurements, the hydrogenated samples were electrolytically polished at 5 °C and 30 V for 10 seconds in a solution of 100 ml perchloric acid and 900 ml methanol to remove the etched surface by the acid solution H_3PO_4 during hydrogen charging**.**

Figure 3.5 gives the EBSD phase maps of the hydrogenated Ti50A. As observed in the phase maps of the sample after for 72 h hydrogen charging (**Figure 3.5b**), a small quantity of needle-like hydrides could be detected at the grain boundaries. This is due to the fact that grain boundaries acts as the preferential trapped regions for hydrogen atoms and sites for the nucleation of hydrides. The ε-TiH_2, α-TiH_x and α phases are displayed in, respectively, red, blue and gray colors in (**Figure** 3.5). As the charging time increased to 108 h (**Figure 3.5**c), hydrides grew into the interior of the α grains. After hydrogen charging for 168 h (7 days), in addition to hydrides formed at the grain boundaries, a considerable amount of δ-TiH_x hydrides with an average thickness of less than 1.0 μm and a length of about 7.0 μm was found inside the α-grains (**Figure 3.5**d).The area fractions of δ-TiH_x and ε-TiH_2 hydrides calculated by Channel 5 software were 12.5 ± 0.3% and 4.9 ± 0.5% (data from 5 maps), respectively. It should be mentioned that a layer of around 10 μm thickness was removed from the surface by electropolishing in order to perform the EBSD analyses. The hydride on the surface of the hydrogenated sample cannot be determined, but the amount of hydride reported in this work corresponds to that of the subsurface of the hydrogenated samples.

Table 3. 2 Area fractions of hydride phases as a function of the distance from the sample surface.

Depth from the surface, μm	Area fraction of the hydride phase δ-TiH_x , %	Area fraction of the hydride phase ε-TiH_2, %
10 ± 5	12.50 ± 0.05	4.95 ± 0.05
25 ± 5	0.30 ± 0.03	0.20 ± 0.03
50 ± 5	0.10 ± 0.01	0.10 ± 0.01
100 ± 5	0	0

Additionally, to determine the amount of each hydride phase found at each depth, the hydride area fractions were determined by EBSD measurements performed on the hydrogenated samples

after layer-by-layer removal by means of electropolishing. The variations of the hydride area fractions with the distance from the sample surface are given in **Table 3. 2**. This table shows that hydride could not be detected beyond 50 μm from the top surface in agreement with the XRD data.

To examine thoroughly the hydrogen evolution, EBSD measurements were also performed on the cross section of the 168 h hydrogenated sample. **Figure 3. 6**a shows the SEM image of the specimen taken on the cross section. Details of the phase maps corresponding to the A, B and C selected regions in **Figure 3. 6**a are shown in **Figure 3. 6**b, c and d, respectively. The distance form position A to the top surface is about 10 μm. In addition, **Figure 3. 6**e shows the phase map acquired with a small step size of 0.10 μm corresponding to the selected area outlined by discontinuous line in **Figure 3. 6**b. These observations indicated that the amount of hydrides is rapidly decreasing from the near surface (region A) though the formation of a low volume fraction of hydride can nevertheless be locally detected in the mid-thickness (region C) particularly along grain boundaries. Assuming a bulk diffusion and considering a value of the coefficient of diffusion equal to 1.3×10^{-14} m^2/s at T = 25°C [**PH68**], the 2nd Fick's law predicts that hydrogen atoms should diffuse till a distance of approximately 200 μm after hydrogen charging for 168 h. This result also observed by Takasaki et al. [**TF96**], suggests that the formation of hydride taking place near the surface and perhaps the compressive residual stresses in the α-phase, tend to make the diffusion of hydrogen toward the center of the sample rather difficult. Therefore, the actual depth of hydrogen diffusion into the sample is, in reality, very small compared to the sample half-thickness (500 μm) due to the formation of hydride layer.

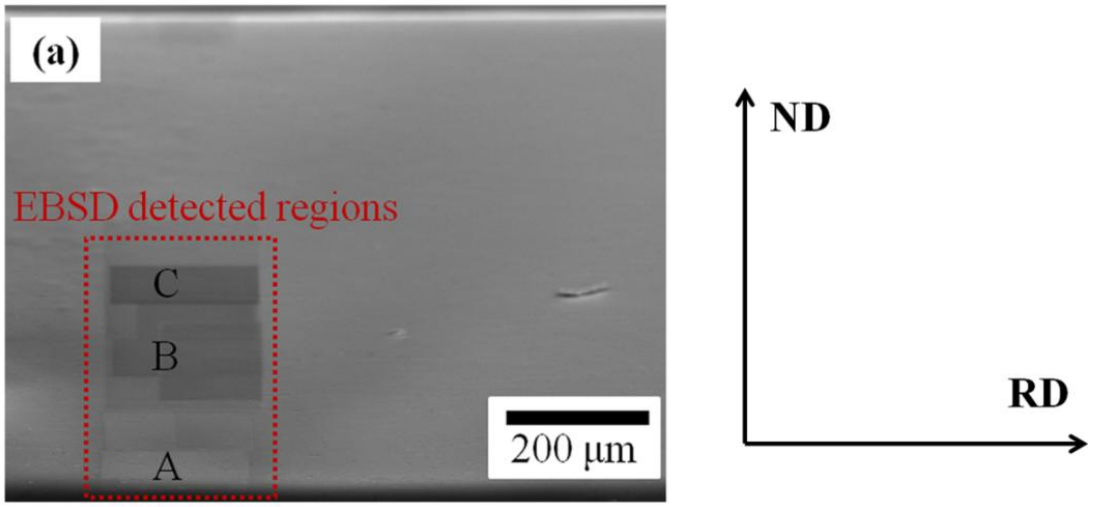

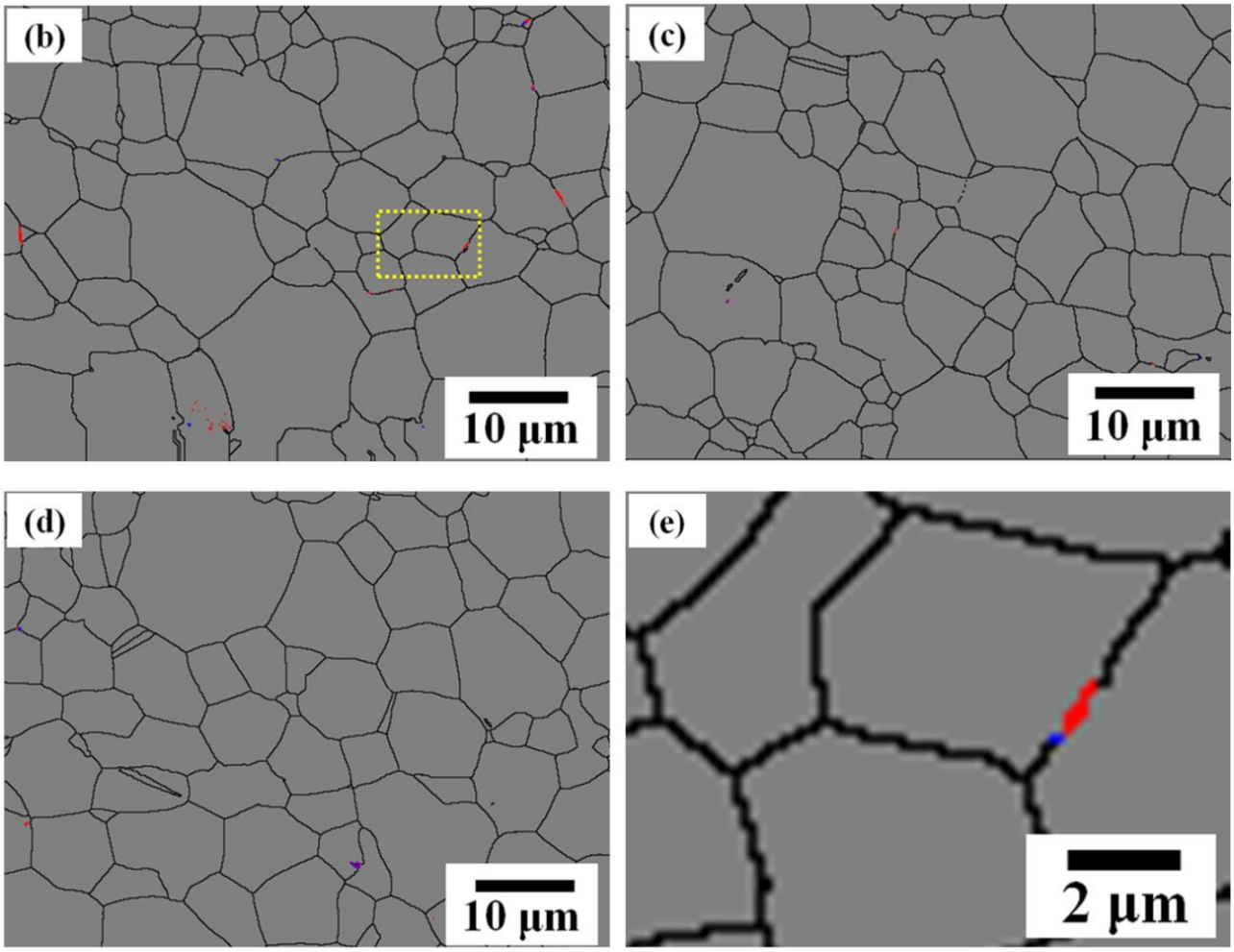

Figure 3. 6 SEM image of hydrogenated Ti50A-H taken on the cross-section (a); EBSD phase maps (b), (c) and (d) corresponding to the regions A, B and C; the magnification phase map (e) indicating the selected area in (b).

As mentioned above, the distribution of hydride is not uniform throughout the sample, indicating that the precipitation of hydride is related to the orientation of the α grains. Therefore, the crystallographic orientation relationships (OR) between the hydrides and the α-matrix (hcp) were analyzed using EBSD measurement. **Figure 3. 7** shows the band contrast (BC) and Euler angles (φ_1, Φ, φ_2,) maps taken on the sub-surface of hydrogenated Ti50A (hydrogen charged for 168 h). To clearly see the distribution of hydrides, the α grains containing hydrides and those without hydrides were noted by the Arabic numbers. As observed, most of the hydrides are distributed as clusters inside of the α grain and the two types of hydrides (δ-TiH_x and ε-TiH_2) always coexist within one α-grain. Meanwhile, there exist several hydrides with different orientations precipitated within one α-grain e.g. grains 7, 8, 29, 36, 38, 51, 52 and 56. Since the δ-hydride

(TiH_x, fcc) is the stable phase and that it can well identified by EBSD, the present work is focusing on the crystallographic orientation relationship between the δ-hydride and the α-phase.

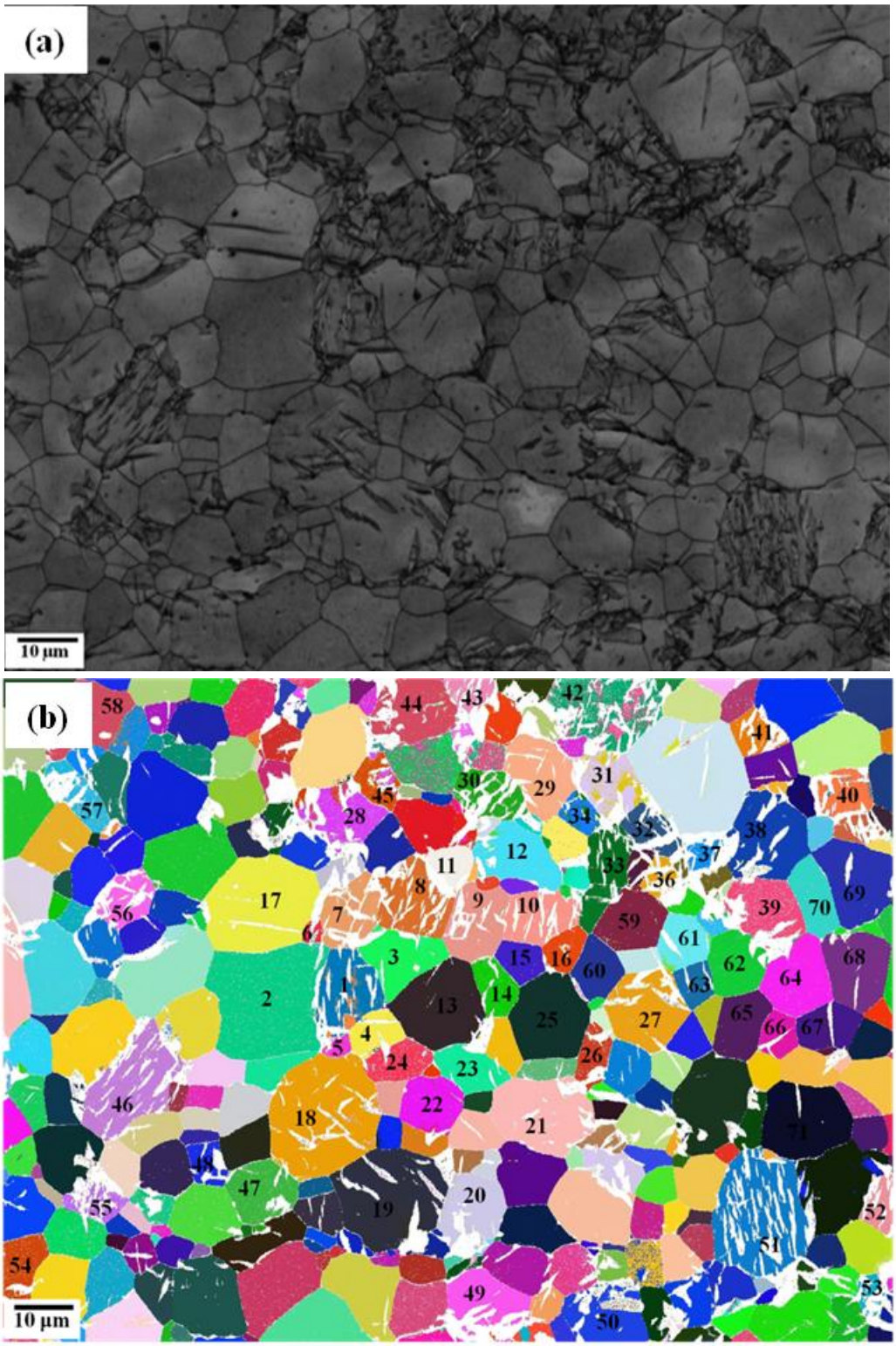

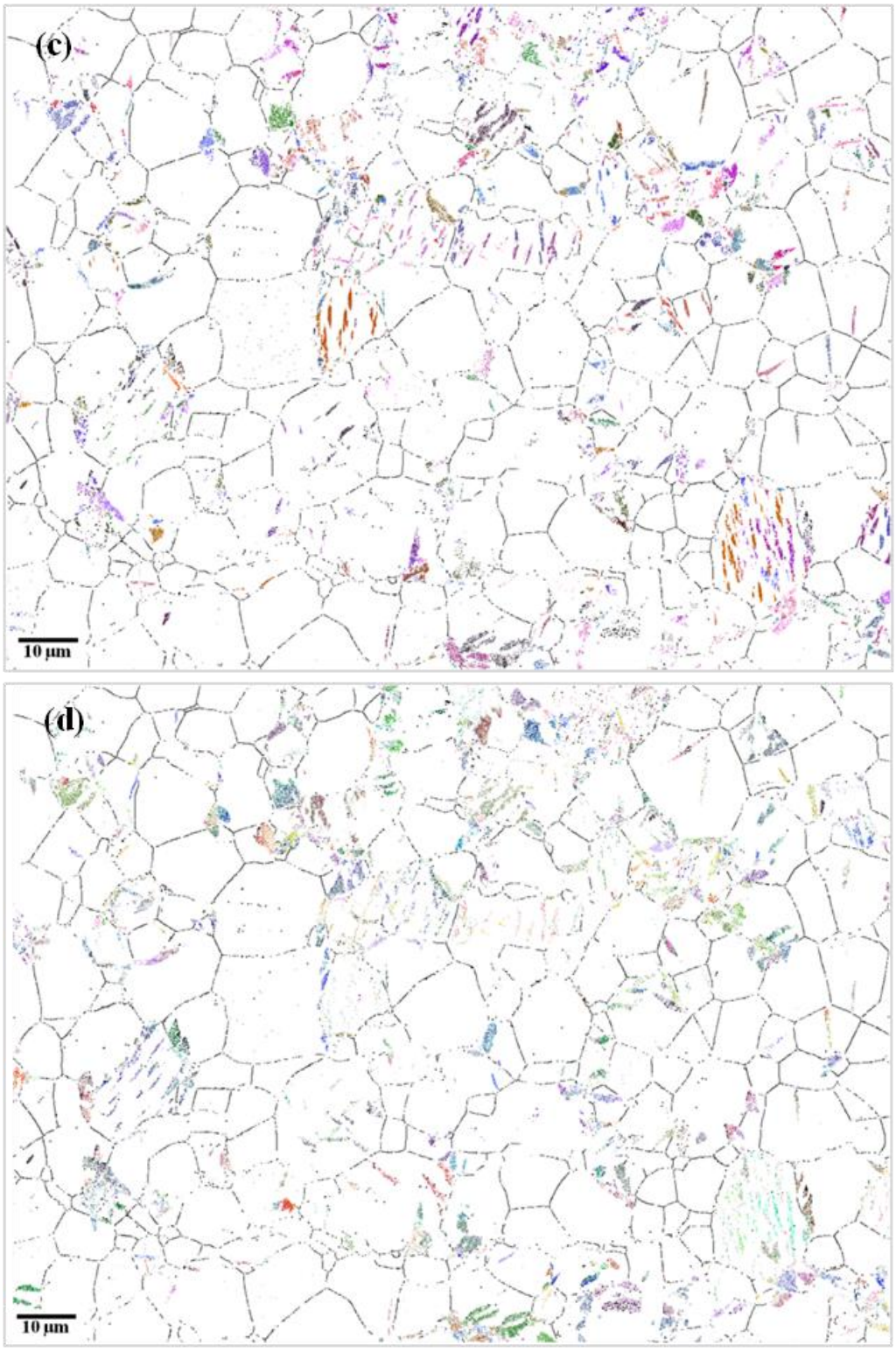

Figure 3. 7 Band Contrast (BC) and Euler angles maps (φ_1, Φ, φ_2,) of the specimen charged for 168 h. (a) BC map; (b), (c) and (d) Euler maps of α-matrix, δ-hydride (fcc) and ε-hydride (bct), respectively.

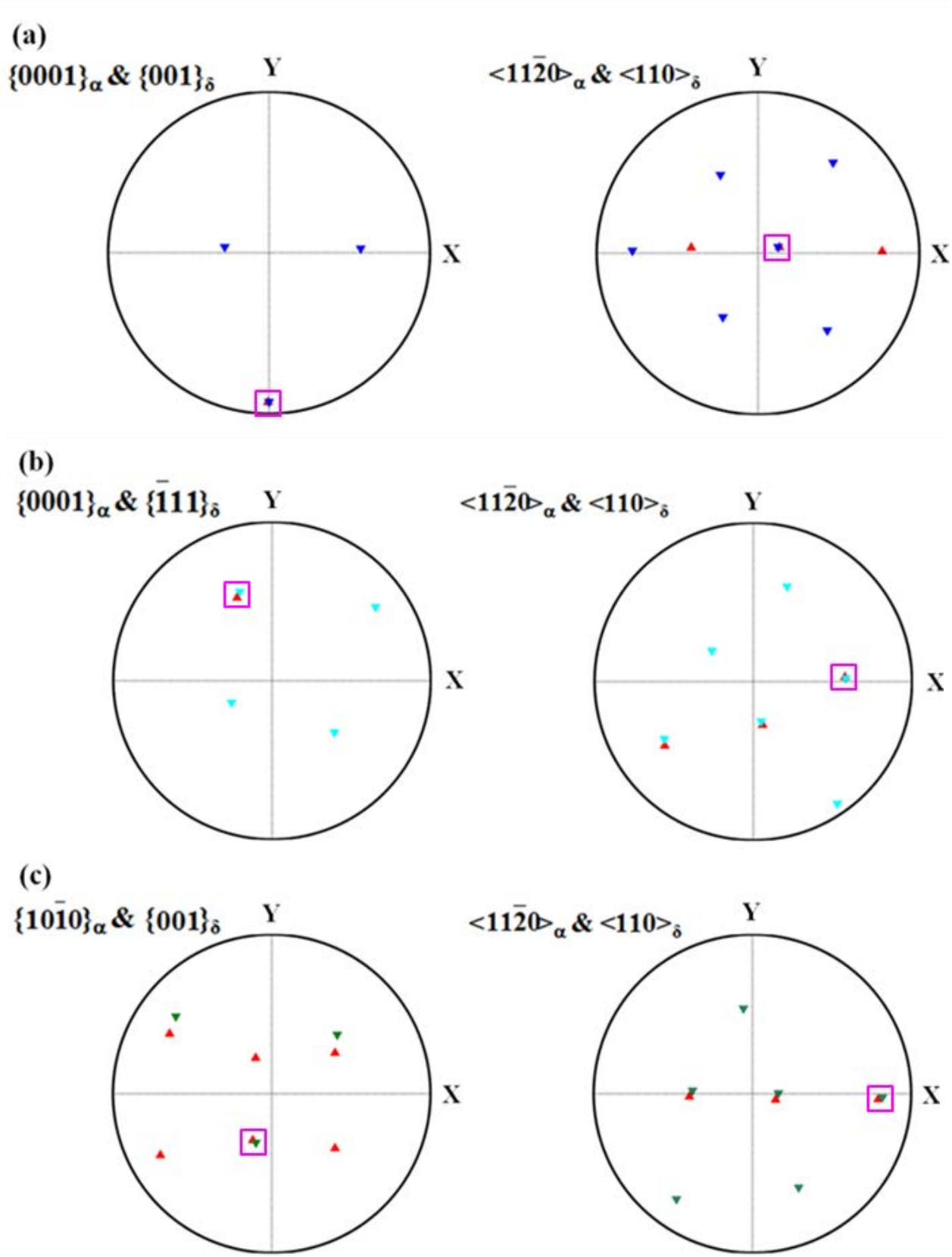
(a)
{0001}α & {001}δ
Y
X
<11$\bar{2}$0>α & <110>δ
Y
X
(b)
{0001}α & {$\bar{1}$11}δ
Y
X
<11$\bar{2}$0>α & <110>δ
Y
X
(c)
{10$\bar{1}$0}α & {001}δ
Y
X
<11$\bar{2}$0>α & <110>δ
Y
X

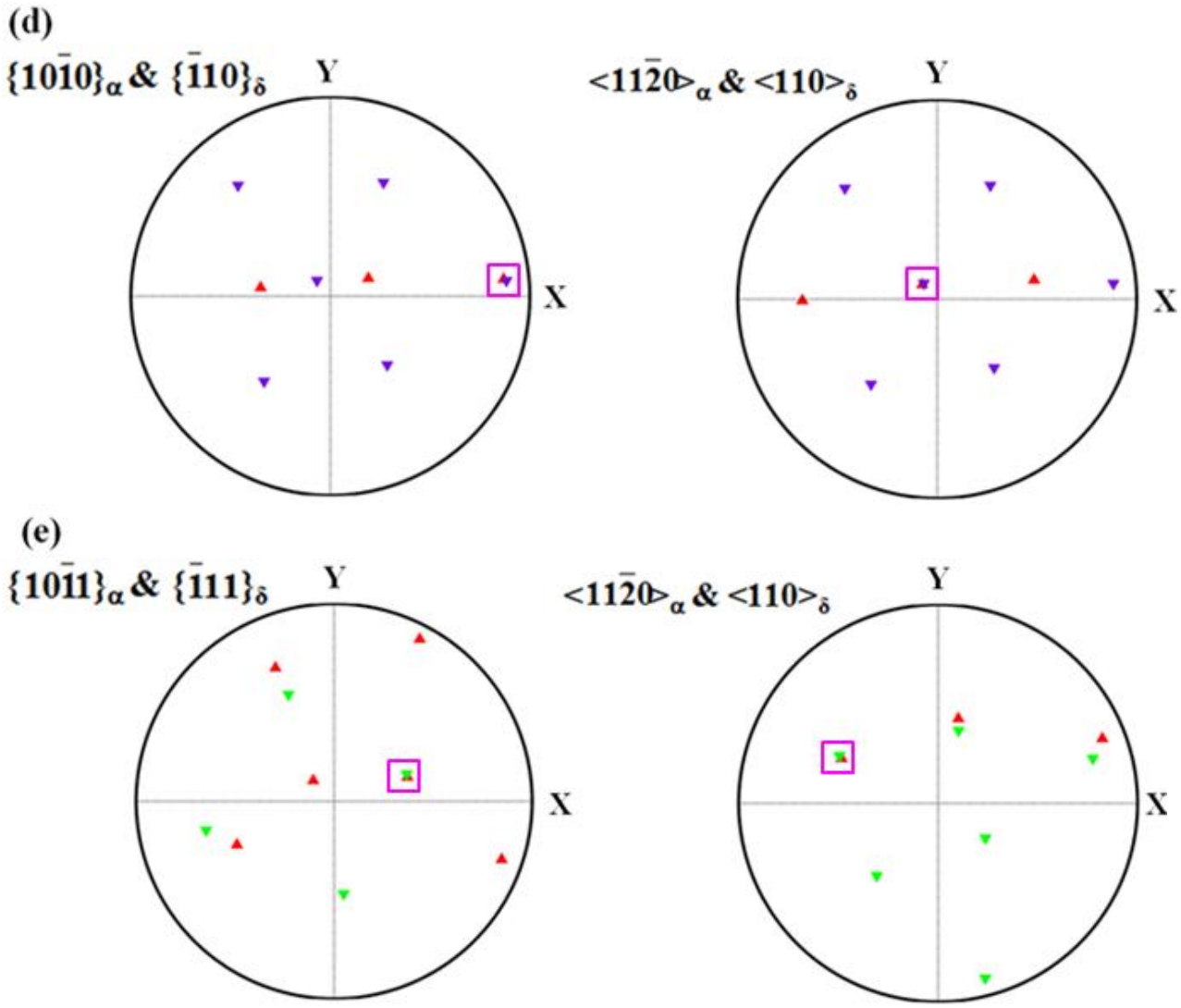

Figure 3. 8 Stereographic projections of the matrix α phase and the hydride δ-TiHx (fcc) of the corresponding orientation relationship (OR) plane and OR direction. (the overlapped projections of α and δ-hydride indicated by pink frame).

The orientation relationships (OR) between the δ-hydride and the α-matrix were resolved by the corresponding OR plane and OR direction stereographic projections of the two phases in **Figure 3. 8**. For example, one $\{001\}_\delta$ plane of the δ-hydride parallels to one $\{0001\}_\alpha$ plane of the α-matrix; and the projection of one $<110>_\delta$ direction for δ-hydride overlaps one $<11\bar{2}0>$ projection of the α-matrix, as indicated by the pink rectangle in **Figure 3. 8**a. Using the stereographic projections, five specific ORs between the δ-hydride and α-matrix were obtained as given in **Table 3. 3** (data obtained from 3 maps). Previous works enabled the determination of several orientation relationships (OR1, OR2, OR3 and OR4) between the δ-hydride and the α-phase in α-

Ti and Zr by TEM characterization as shown in **Table 1. 5** **[BS88, ZR90, ZK94, CC07, CC11, CCB17 and CG17]**. Both OR1 and OR2 have been frequently detected in this study. In addition, as it can be observed in **Figure 3. 8**c, d and e, and in **Table 3. 3**, three new orientation relationships (ORs) between the matrix and δ-hydride have been worked out, which have been designated OR3', OR4' and OR5', respectively.

Table 3. 3 Orientation relationship between martensite α and δ-hydride determined by electron backscatter diffraction (EBSD). The Euler angle is expressed in Bunge's notation **[BE80, BE81]**. (The Euler angles listed in the table below represent the mean orientation of the matrix and δ-hydride, respectively.)

Grain ID	Phase	Euler angles (φ_1, Φ, φ_2,)	**Orientation Relationships (OR)**	Frequency of grains with OR
1	Matrix-α	(179.63, 94.23, 15.11)	**OR1***	25%
	Hydride-δ	(262.23, 31.01, 8.58)	$\{0001\}_\alpha // \{001\}_\delta$ & $<11\bar{2}0>_\alpha // <110>_\delta$	
30	Matrix-α	(22.86, 120.92, 5.5)	**OR2***	38%
	Hydride-δ	(133.75, 22.98, 35)	$\{0001\}_\alpha // \{\bar{1}11\}_\delta$ & $<11\bar{2}0>_\alpha // <110>_\delta$	
40	Matrix-α	(178.94, 85.91, 16.78)	**OR3'**	7%
	Hydride-δ	(342.19, 35.81, 64.69)	$\{10\bar{1}0\}_\alpha // \{001\}_\delta$ & $<1\bar{2}10>_\alpha // <110>_\delta$	
33	Matrix-α	(4.32, 81.16, 7.85)	**OR4'**	14%
	Hydride-δ	(105.82, 39.04, 74.77)	$\{10\bar{1}0\}_\alpha // \{\bar{1}10\}_\delta$ & $<1\bar{2}10>_\alpha // <110>_\delta$	
38	Matrix-α	(14.85, 46.4, 39.66)	**OR5'**	16%
	Hydride-δ	(262.15, 13.27, 68.45)	$\{10\bar{1}1\}_\alpha // \{\bar{1}11\}_\delta$ & $<1\bar{2}10>_\alpha // <110>_\delta$	

*Previous results reported in **[CD07, CG17]**

Compared to TEM characterization, EBSD provides, on a larger scale, information on the crystallographic orientation relationships between the δ-hydride and the α-matrix. The quantitative analysis (presented in **Table 3. 3**) showed that the grains having the δ-hydrides satisfying the OR2 ($\{0001\}_\alpha // \{\bar{1}11\}_\delta$ & $<11\bar{2}0>_\alpha // <110>_\delta$) (**Figure 3. 8**b) are the most frequently observed in the hydrogenated samples, indicating that there exists a higher fraction of α grains having a particular orientation which facilitates the precipitation of δ-hydrides following the OR2. As mentioned above, there exists a typical rolling texture of α-titanium characterized by two components at ±30° tilted from the normal direction (ND) to the transverse direction (TD) **[CY05, ZD11]** in the annealed Ti50A. Therefore, it is reasonable to suppose that this type of

texture could have an effect on the precipitation of hydrides. Since the OR1 and OR2 are the most frequent ORs observed in the hydrogenated Ti50A, **Figure 3. 9b** gives the {0002} pole figure of α grains with the OR1 and OR2. We can see that the orientations of α grains satisfying OR1 and OR2 are clearly different, with OR2 observed for grains having the crystallographic orientation in the center of the stereographic projection, i.e., <0001> // ND, and OR1 for grains with <0001> // TD. The orientations of the α-parent grains following the OR2 are thus closely related to the texture component (shown in **Figure 3. 9a**).

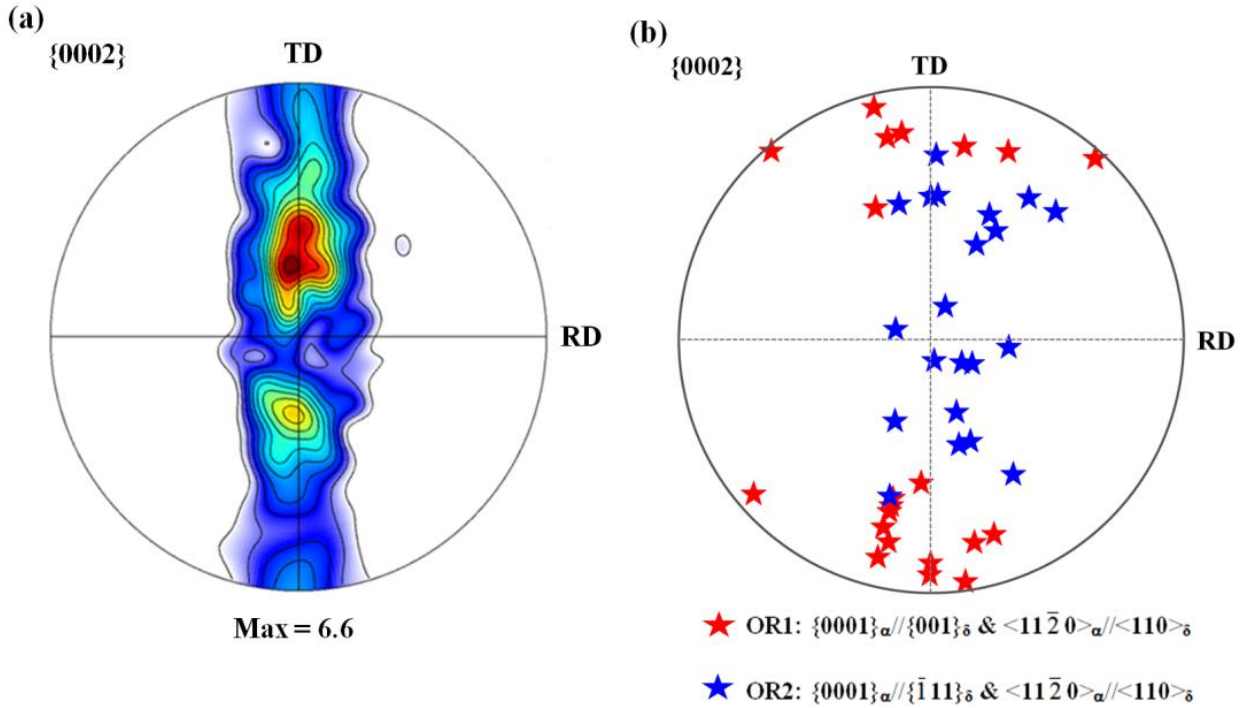

Figure 3. 9 Effect of texture on the orientation relationship between the α-matrix and the δ-hydride, (a) {0002} pole figure of as-annealed Ti50A; (b) {0002} pole figure of grains with OR1 and OR2.

Though an unique hydride is found in grains having OR2-type orientation relationship (example: grain number 61, 63, 66-69, 71, etc. in **Figure 3. 7**b), it should be mentioned that the clusters of hydrides observed nearly parallel in the α grains mainly satisfied the OR1 (shown in **Figure 3. 7**), which could be indicative of the smaller resistance of the phase transformation for this orientation relationship. As reported by Feaugas and co-workers using TEM observation in Ti40 [**CC07 and CC17**], the interface plans for OR1 are $(10\bar{1}0)_\alpha$ // $(2\bar{2}0)_\delta$. In the view of energy, the tetrahedral sites on the $\{10\bar{1}0\}$ planes are the preferential positions for the hydrogen atoms to occupy in the hcp cell [**BR82, DB02**]. The $(10\bar{1}0)_\alpha$ prismatic planes of the hexagonal phase having tetrahedral interstitial sites as well as the $(2\bar{2}0)_\delta$ plans of the fcc phase having octahedral interstitial sites, the

large number of hydrides with OR1 type orientation observed in the hydrogenated sample suggests that the interficial energy is lower for the precipitation of δ-hydride following this orientation relationship. Additionally, the prismatic slip a/2 $<11\bar{2}0>$ $\{10\bar{1}0\}$, being an easiest slip mode in the α phase, can be readily activated to relax the internal stress generated by the hydride precipitation.

3.2.2.3 TEM investigations

TEM analyses were performed to confirm the structure of the hydrides. Prior to TEM characterization, the hydrides were firstly localized by SEM, as shown in **Figure 3. 10**a, and a thin foil (**Figure 3. 10**b) was then extracted by FIB. **Figure 3. 10**c showing the TEM micrograph of the hydrogenated specimen taken from this thin foil confirms the presence of the two types of hydrides observed within one α grain.

TEM bright field images taken from the different areas of the matrix (corresponding to the selected region A and B in **Figure 3. 10**c) are shown in **Figure 3. 10**d and e. It can be noticed that the two hydrides have totally different morphologies, which is consistent with our SEM-EBSD observations. **Figure 3. 10**f displays the selected area electron diffraction (SAED) pattern obtained from the area circled in **Figure 3. 10**e. As shown in this pattern, the observed δ-TiH_x hydride having an fcc phase structure with $<\bar{1}12>$ zone axis was precipitated from the $<000\bar{1}>$ zone axis of the α (hexagonal) phase. The dark field TEM micrographs made by selecting two reflections corresponding to both the δ-TiH_x hydride and α phase (circled on the SAED pattern) are also included in **Figure 3. 10**f. In contrast, the ε-TiH_2 hydride with bct phase structure (corresponding to **Figure 3. 10**d) exhibits a weak electron diffraction pattern. It should be mentioned, the maximum temperature for having a stable ε-TiH_x phase is about 25°C. This is in accordance with the EBSD results presented above, and indicating that the structure of ε-TiH_x hydride is unstable under the irradiation of electron beams from FIB and TEM **[WE02, LX13]**.

3.2.3 Hydrogen/Hydride effects on mechanical properties in Ti50A

3.2.3.1 Hydrogen/ Hydride effects on microhardness property

Following hydrogen charging for different times in Ti50A, microhardness measurements were conducted on the surface of hydrogenated Ti50A alloys. **Figure 3. 11** shows the variation of hardness with hydrogen concentration, as observed, the value of hardness increases gradually

with the increase of the hydrogen concentration increasing. In hydrogenated Ti50A sample, hydrogen can be found in two states: the quasi-mobile hydrogen at solid solution and the bonded hydrogen in the forms of hydrides. Hence, the increase in hardness can be attributed to the increasing volume fraction of hydrides and the solid solution strengthening caused by the dissolved hydrogen.

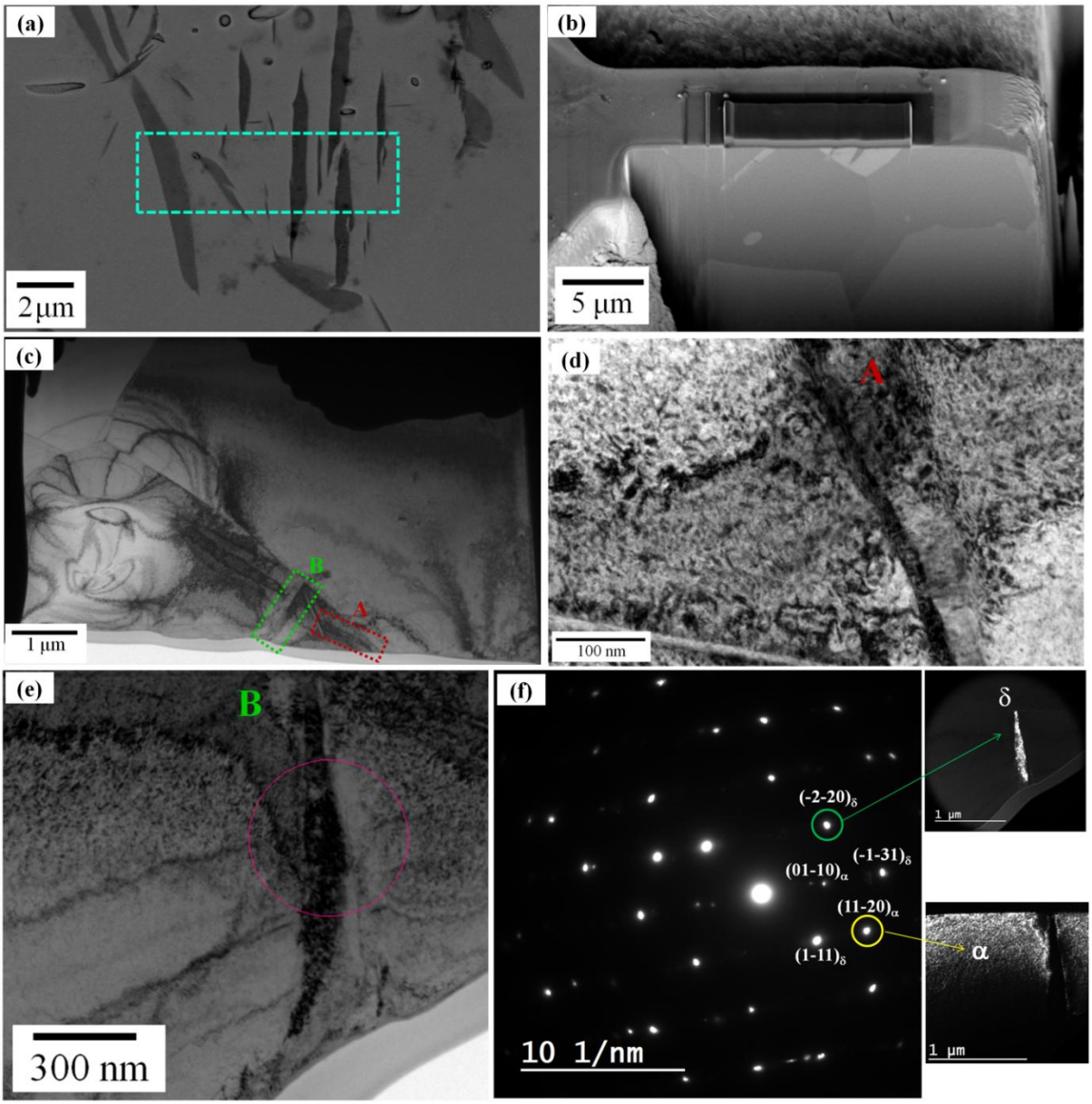

Figure 3. 10 SEM and TEM investigations of hydrogenated specimen. (a) SEM (SEI detector) image; (b) the selected area in (a) extracted by FIB); (c) TEM micrograph of the same area; (d) and (e) TEM bright field images of the matrix taken from the area A and B indicated in (c), respectively; (f) SAED pattern corresponding to the circled area in (e) and dark-field images obtained from the circled SAED pattern (pointed by the arrows).

On the other hand, microhardness measurements were performed on the cross-section of hydrogenated Ti50A samples. **Figure 3. 12** shows the microhardness profiles of hydrogenated Ti50A under different hydrogen charging times. We can see that, there exists an obvious hardness gradient in thickness of the hydrogenated Ti50A. For example, after hydrogen charging for 168 h, the value of hardness is rapidly decreasing from the surface to a distance of 75 μm beneath the surface. The decreasing hardness value is indicative of a decreasing volume fraction of hydrides throughout the sample cross-section. As described above in paragraph *3.2.2.2*, the diffusion of hydrogen into sample becomes rather difficult owing to the formation of hydride takes place in the subsurface region. Therefore, the actual depth of hydrogen diffusion into the sample is, in reality, very small compared to the sample half-thickness (500 μm). It should be mentioned that these hydrides formed not because the sample electrode is being saturated with hydrogen, as can be clearly deciphered from **Figure 3. 12**, but rather as a result of the rate of deposition of hydrogen on the electrode surface greater than the rate of diffusion of hydrogen into the electrode.

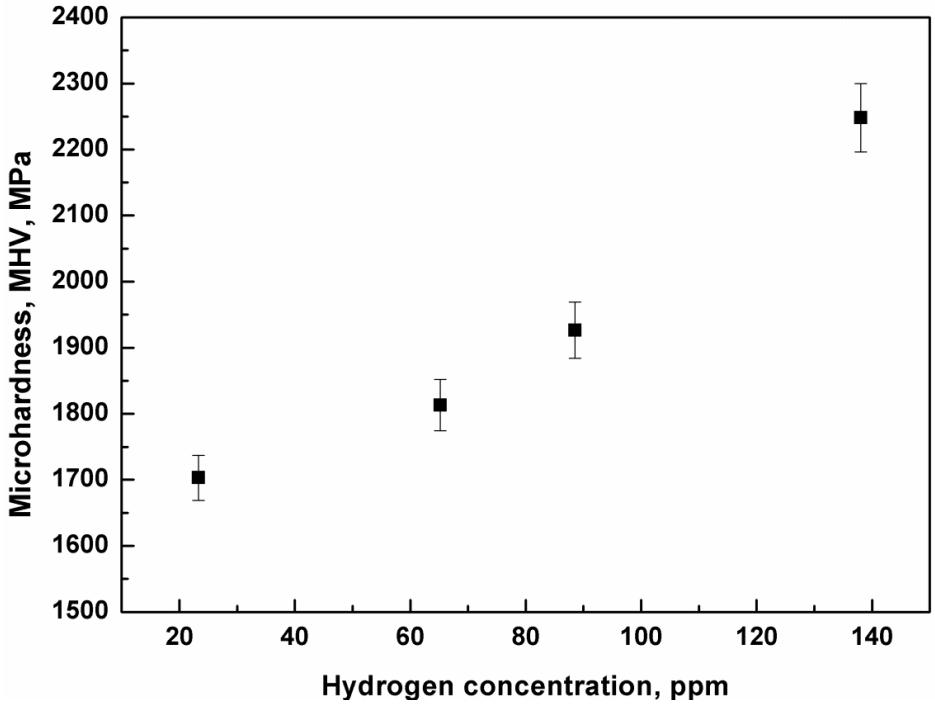

Figure 3. 11 Variation of the microhardness measured on the top surface as a function of hydrogen concentration for hydrogenated Ti50A

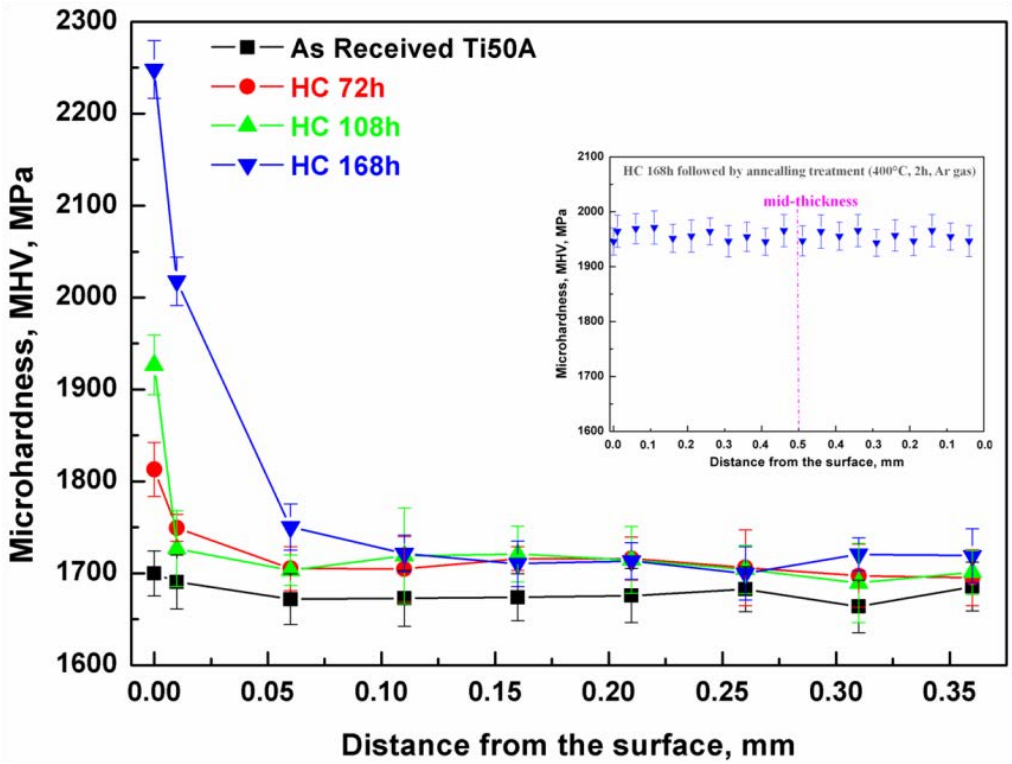

Figure 3. 12 Microhardness profile of the hydrogenated Ti50A; The microhardness profile for the as-received Ti50A is given for comparison. In inset, microhardness profile after annealing at 400C for 2 hours.

In order to facilitate further analyses, the hydrogenated Ti50A were annealed for 2 hours at 400 °C under Ar gas. The inserted chart in **Figure 3. 12** shows the microhardness profile of the hydrogenated Ti50A after the annealing treatment. Assuming a Fickian diffusion mechanism, such annealing should enable the diffusion of hydrogen toward the center of the sample, thus providing a uniform distribution of hydrogen without generating grain growth.

3.2.3.2 Hydrogen/ Hydride effects on nanoindentation property

Nanoindentation was performed to investigate hydrogen/hydride effects on the local scale in Ti50A, e.g. the interior of α grain and hydride, grain boudnary and interface between hydride and α phase. Before nanoindentation, EBSD analyses were conducted on the pre-hydrogenated Ti50A (hydrogen charging for 168 h) to determine the position of the hydride within the specimen, as shown in **Figure 3. 13**a. After nanoindentation tests, the positions of measured regions are identified with the Arabic numerals from 1 to 9, as shown in **Figure 3. 13**b and c. For example, numbers 2, 3 and 9 represent the tested positions which are inside of the hydrides, and numbers 1, 5, 6 and 7 represent the locations which are the interface between the α-phase and the

hydride. **Figure 3. 13**d shows the magnification of the selected area in **Figure 3. 13**c. The outline of the three hydrides is marked with white lines. During a load-unload cycle, the variations of the applied load versus the indentation depth were measured dynamically, as illustrated by the typical of "load-displacement" curves shown in **Figure 3. 14**. As observed, under the same load, the displacement recorded for hydride is the smallest, indicating that the hydrides have the highest hardness. Hardness and the reduced modulus were calculated directly from the resultant Load-Displacement curves, and have been presented in **Table 3. 4**.

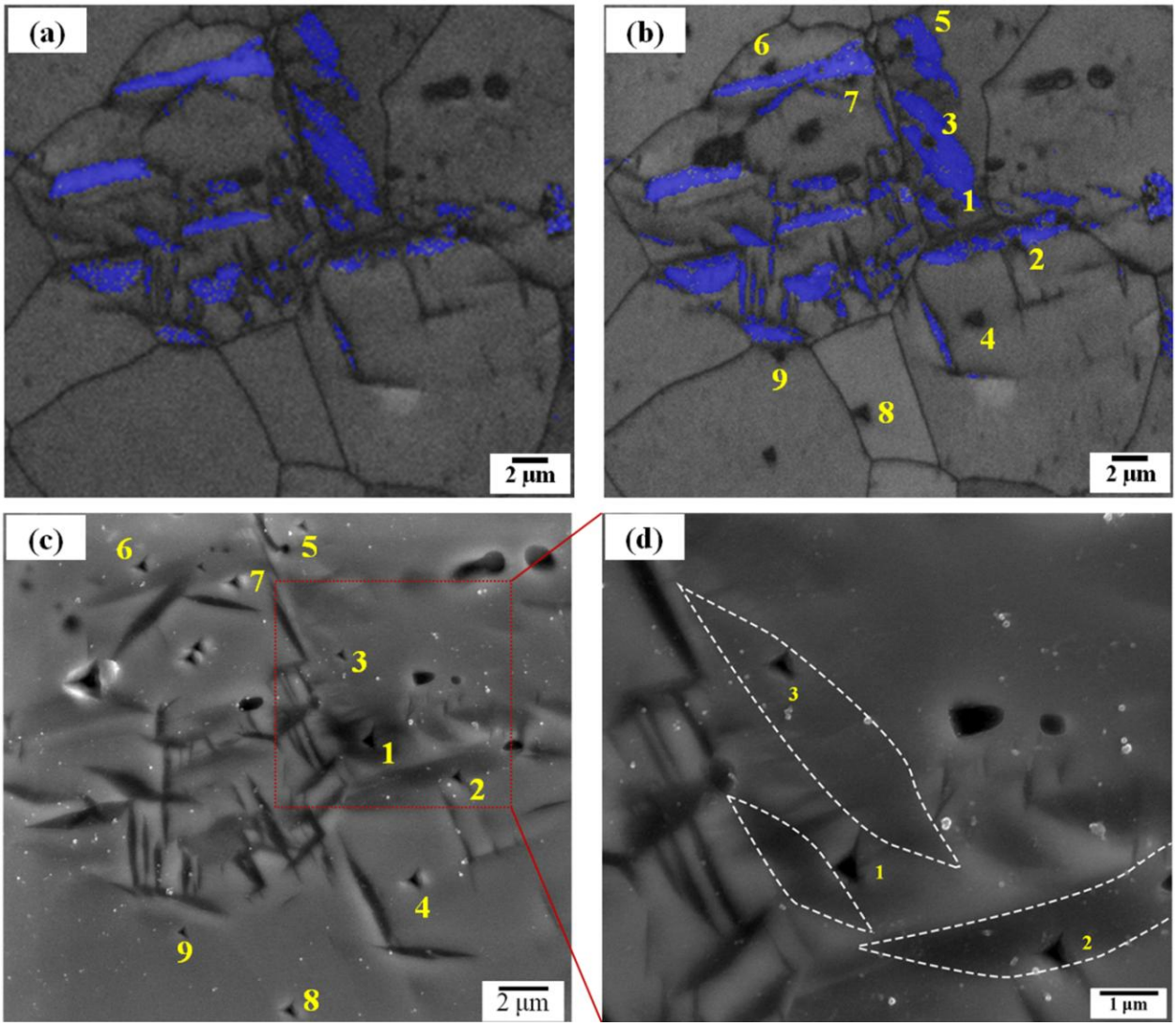

Figure 3. 13 SEM-EBSD micrograph of nanoindentation measured region. (a) EBSD map before nanoindentation, (b) EBSD map after nonaindentation, (c) SEM image after nanoindentation and (d) the magnification of selected region in (c).

Table 3. 4 Hardnesss and reduced elastic modulus calculated from the Load-Displacement curves

	1	2	3	4	5	6	7	8	9
Position	Interface	Hydride	Hydride	α	Interface	Interface	Interface	GB	Hydride
HVIT	207.8	245.5	246.7	175.0	218.1	202.6	207.4	187.4	257.0
Er	90.6	87.4	97.9	84.3	86.7	84.4	85.0	85.8	92.0

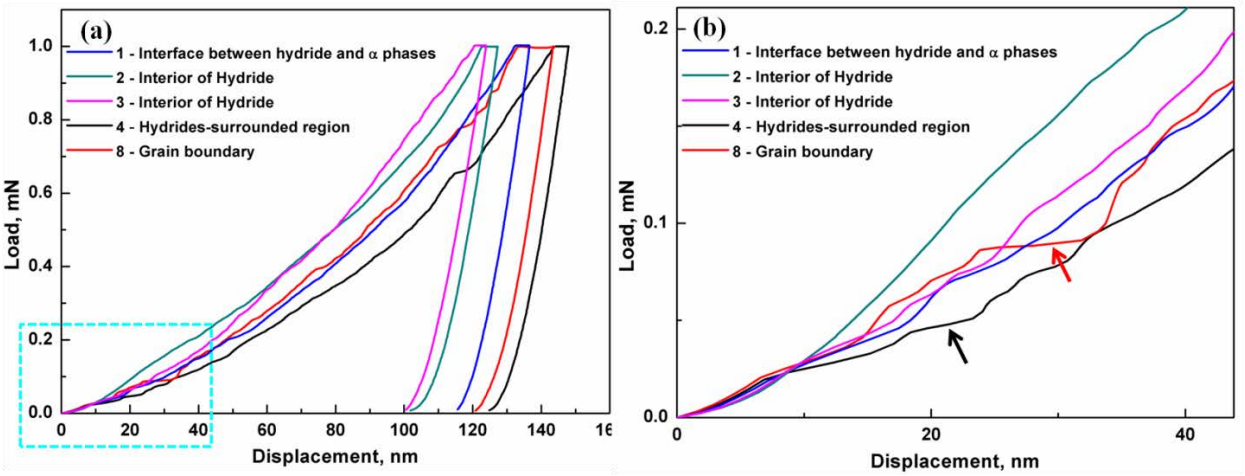

Figure 3. 14 Load-Displacement curves of hydrogenated Ti50A (a), (b) indicating the enlarged zone in (a)

Due to the anisotropy of the hcp crystal structure, the method for the calculation of the elastic modulus of the polycrystal α-titanium is not yet well established. Although, the elastic modulus of the sample Ti50A cannot be determined now, the effect of hydrogen on dislocation nucleation can be obtained by the analysis of the "pop-ins" on the load-displacement curves **[BV06, BV08, BV09]**. Since in nanoindentation experiments the lateral dimensions of the volume of the deformed material are significantly smaller than the mean dislocation spacing in annealed metals, plastic deformation in these ranges occurs via homogeneous nucleation of new dislocation loops, and is marked by this sudden jump in the indentation depth during a steady increase in the load [**BV06, BV08, BV09 and NB06**]. As shown in **Figure 3. 14**, the curves for the hydrides-surrounded region and the grain boundary exhibited obvious multiple pop-ins during loading. Since we have postulated above that the precipitation of hydrides is due to hydrogen supersaturation at defects, hydrides are surrounding by the hydrogen-riched regions. The observation of multiple pop-ins can thus provide information on the activation of different slip systems. However, there is no observation of pop-ins on the load-displacement curve for the hydrides, indicating that the absence of dislocations nucleation inside of the hydrides.

Additionally, for the hydrogen-riched region (position 4) both pop-in load and pop-in displacement depth were smaller in comparison to the grain boundary (position 8), as indicated by the arrows in **Figure 3. 14**b. This observation is consistent with the results of Barnoush and Vehoff **[BV06, BV08, BV09]** and Nibur et al. [NB06]. These results suggested that the presence of the dissolved hydrogen atoms lowered the activation energy required for dislocations nucleation.

3.2.3.3 Hydrogen/ Hydride effects on compressive property

In the current work, the effect of hydrides on the mechanical behavior of pure titanium Ti50A was also investigated by means of compression test. The samples containing different hydrogen contents were compressed to the engineering strain up to a maximum of 15% (shown in Appendix B). In order to follow the effect of hydrides on the deformation mechanisms under compression loading, the grains containing clusters of hydrides were carefully marked by nanoindentation prior to deformation. Microstructural examinations were thus performed by SEM-EBSD before and after deformation.

Among the grains revealed in the map of the hydrogenated Ti50A prior to deformation, shown in **Figure 3. 15**a, some contain hydrides while other do not. Since the activation of slip system is dependent on the grain orientation, grains with two different orientations referred as A and B were selected as the grains containing hydrides. The inserted SEM image corresponding to the marked grain B shows clearly the hydrides prior to deformation. **Figure 3. 15**b shows the SEM micrograph of the same pre-marked region after compression test. The magnified SEM micrographs of the compressed grains A and B are shown in **Figure 3. 15**c and d, respectively. No hydrides fragmentation but slip traces were observed in the deformed grains, as indicated by the arrows. Details of the slip traces are shown in micrographies taken at higher magnifications (**Figure 3. 15**e and f). The appearance of the slip traces across the hydrides indicated that the dislocations slip transferred from the matrix to the hydrides. This observation further confirmed that the hydrides had a certain ability to accommodate the strain imposed on the specimen, as reported by many authors **[BB69, IB72, BJ94, BP94, GF01, HF98, VS16, CL03, CLL04, CL04, CLZ04, VA03 and AB03].** For example, some of these studies [**BJ94, BP94 and VS16**] showed that hydrides were able to align themselves parallel to the applied stress before their fracture.

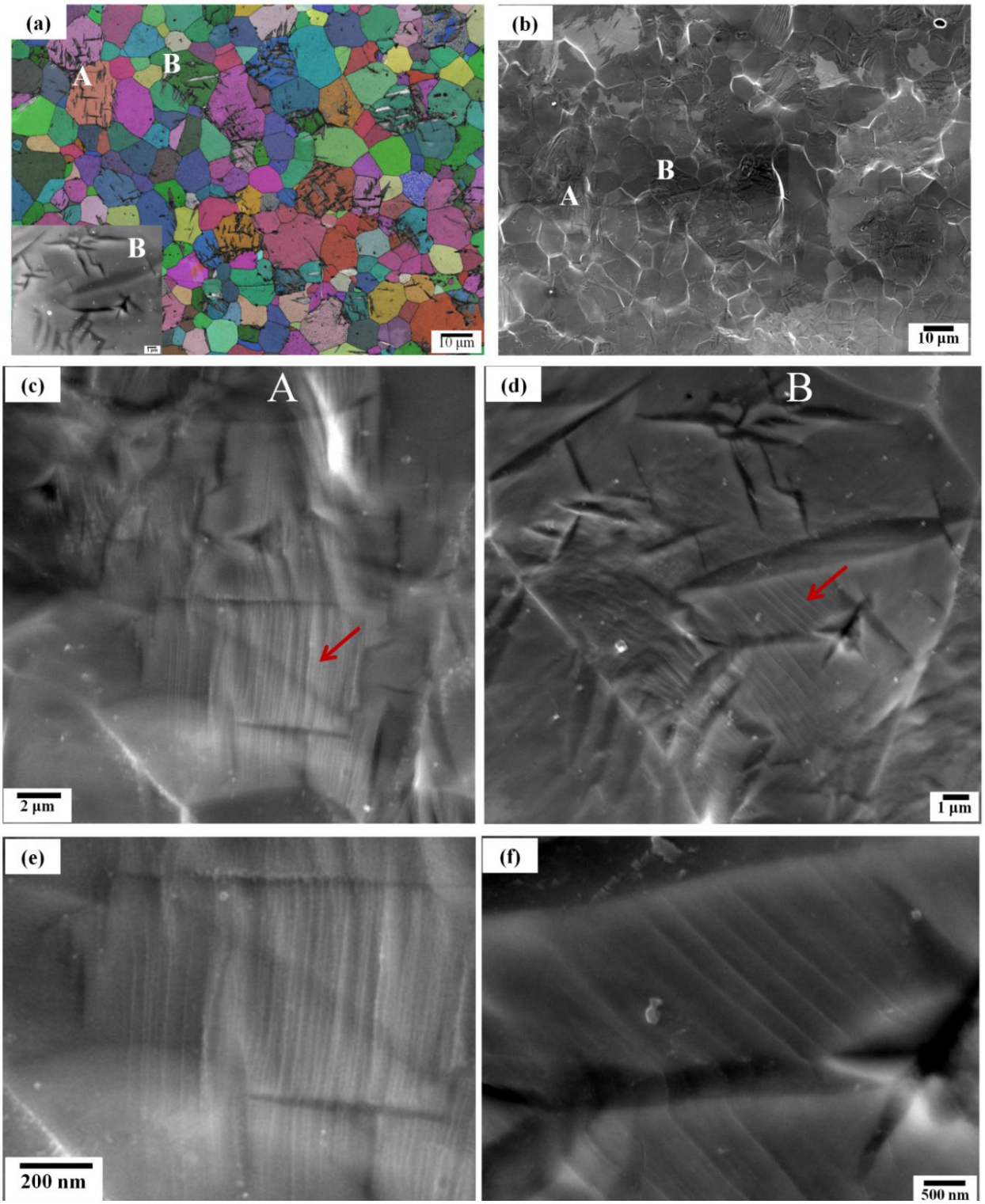

Figure 3. 15 (a) EBSD map of hydrogenated Ti50A (hydrogen charged for 168 h) prior to compression test; (b) SEM micrograph of the same region after compression test; (c) and (d) magnification of the compressed grains A and B, respectively (slip traces indicated by the arrows); (e) and (f) magnification of slip traces within grain A and B, respectively.

TEM observations revealed that there existed a large number of possibilities in the interactions between the dislocations and the hydrides [GF01, HF98, CL03, CLL04, CL04 and CLZ04]. These interactions depend on not only the nature of the hydride, but also on the orientation relationship between the α phase and the hydrides as well as the thickness of the hydrides. Therefore, the dependency of slip on the orientation relationship was investigated first and then the effect of hydride thickness on slip was stated.

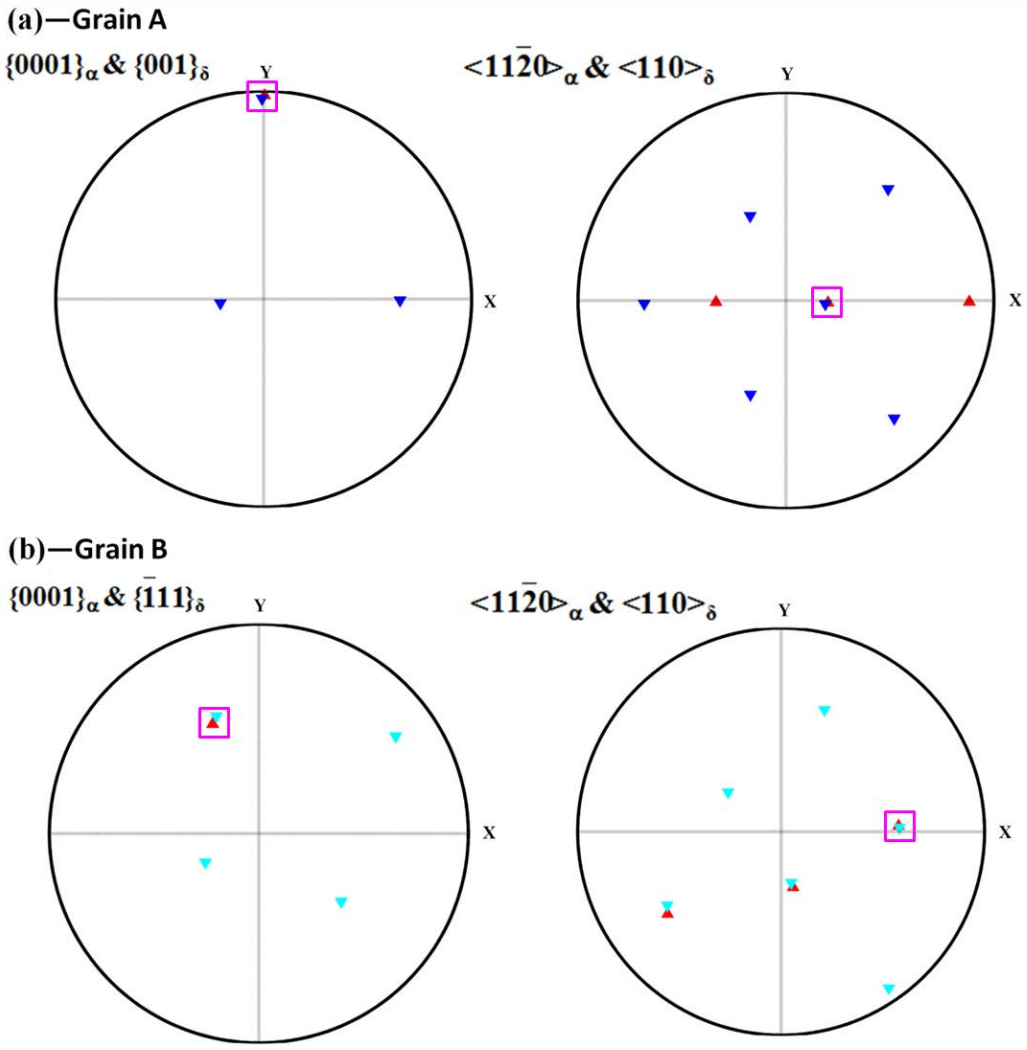

Figure 3. 16 Stereographic projections of the matrix α phase and the hydride δ-TiHx (fcc) of the corresponding orientation relationship (OR) plane and OR direction for grain A (a) and B (b), respectively.

The orientation relationships between the α grains and δ-hydrides are shown in **Figure 3. 16.** In grain A (**Figure 3. 16**a), the orientation relationship satisfied the OR1. While in grain B (**Figure 3. 16**b), the orientation relationship belonged to the OR2. For the OR1, the pile-ups of <11$\bar{2}$0>

dislocations at the interfaces plane $(10\bar{1}0)_\alpha$ between the δ-hydride and matrix leads to a local stress concentration, which may favor the dislocation transfer depending on the thickness of the hydride. We can see, in the same grain, slip traces can only be observed in the area containing very thin hydrides. As observed in **Figure 3. 15**e, the average thickness of the hydrides are less than 100 nm, which nearly has no negative effect on the dislocations transmission as evidence by the straight slip traces. As the thickness of the hydrides increased, the transfer of the dislocations slip became difficult leading to a weaker deformation.

In the case of OR2, the $<11\bar{2}0>$ dislocations at the δ-hydride/α-matrix interface $(10\bar{1}3)_\alpha$ can also transfer from the matrix to the hydride; however the angle between that interface plane $(10\bar{1}3)_\alpha$ and the $(10\bar{1}0)_\alpha$ plane is 30°, which makes the transfer of the deformation from the matrix to the hydride more difficult. On the other hand, the thickness of the hydride in grain B (**Figure 3. 15**f) increased to about 500 nm, which makes the dislocations transmission become difficult resulting the discontinuity of slip traces. Therefore, the results described above suggested that the influence of hydrides on dislocation slip depended not only on the nature of the hydride, but also on the orientation relationship between the matrix and the hydride as well as on the thickness of the hydride.

In hcp structure materials, twinning enables significant deformation of the lattice through crystal shear, often involving local atomic shuffling [**CM95**] with associated lattice reorientation. In the present study, the effect of hydride on twinning was completed by the quasi-in situ compression test conducted on the Ti50A hydrogenated for 168 h. **Figure 3. 17**a shows the BC map with the identified hydrides for the undeformed Ti50A, the δ-hydride (fcc) and ε-hydride (bct) are indicated by the yellow and green colors. The grains with/without hydrides were noted by the Arabic numerals (1, 2, 3... etc.). The corresponding IPF map of matrix is shown in **Figure 3. 17**b, the hydrides are marked by the white color. After compression test (15% thickness reduction), deformation twinning were activated in the sample, as shown in **Figure 3. 17**c and d (i.e., BC map showing the identified twin boundaries as well as the hydrides), the boundaries of compression twin CT1 $\{11\bar{2}2\}<11\bar{2}\bar{3}>$ and tension twin TT1 $\{10\bar{1}2\}<\bar{1}011>$ were indicated by the red and blue colors, respectively. Those two types of twins were found not only in the grain without hydrides but also in the grains containing cluster of hydrides (grain numbers: 3, 4, 9, 14, 15, 25, 28, 42, 49, 50, etc.).

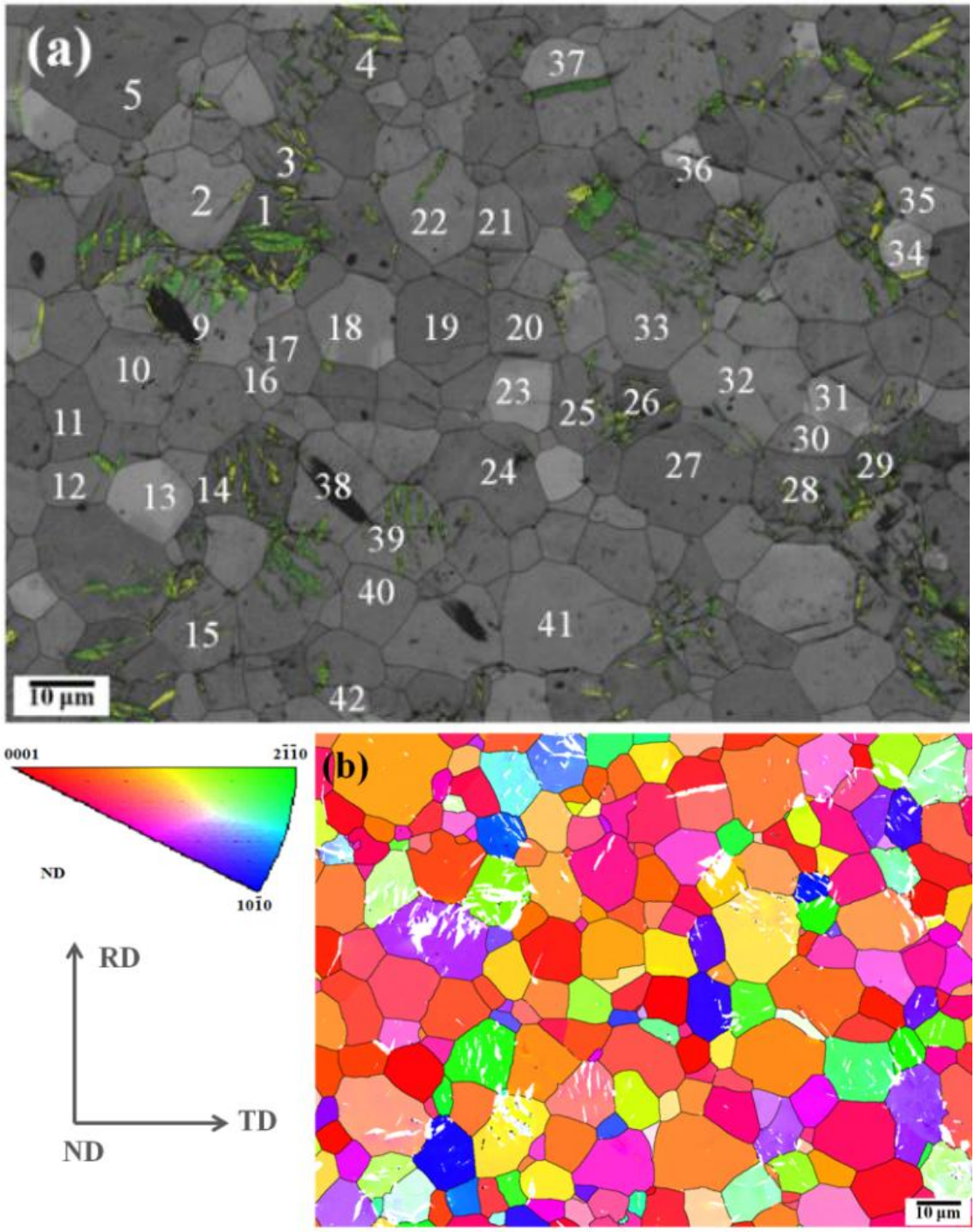

Figure 3. 17 Effect of hydrides on twinning in (168 h hydrogen charging) Ti50A under compression test. (a) BC map with the identified hydrides for the undeformed Ti50A (δ-hydride and ε-hydride indicated by green and yellow colors, respectively); (b) the corresponding IPF map of the matrix (the hydrides marked by the white color); (c) and (d) the BC maps with the hydrides as well as the identified twin boundaries for the compressed Ti50A (the red and blue colors indicating the boundaries of the compression twins CT1 and the tension twins TT1, respectively).

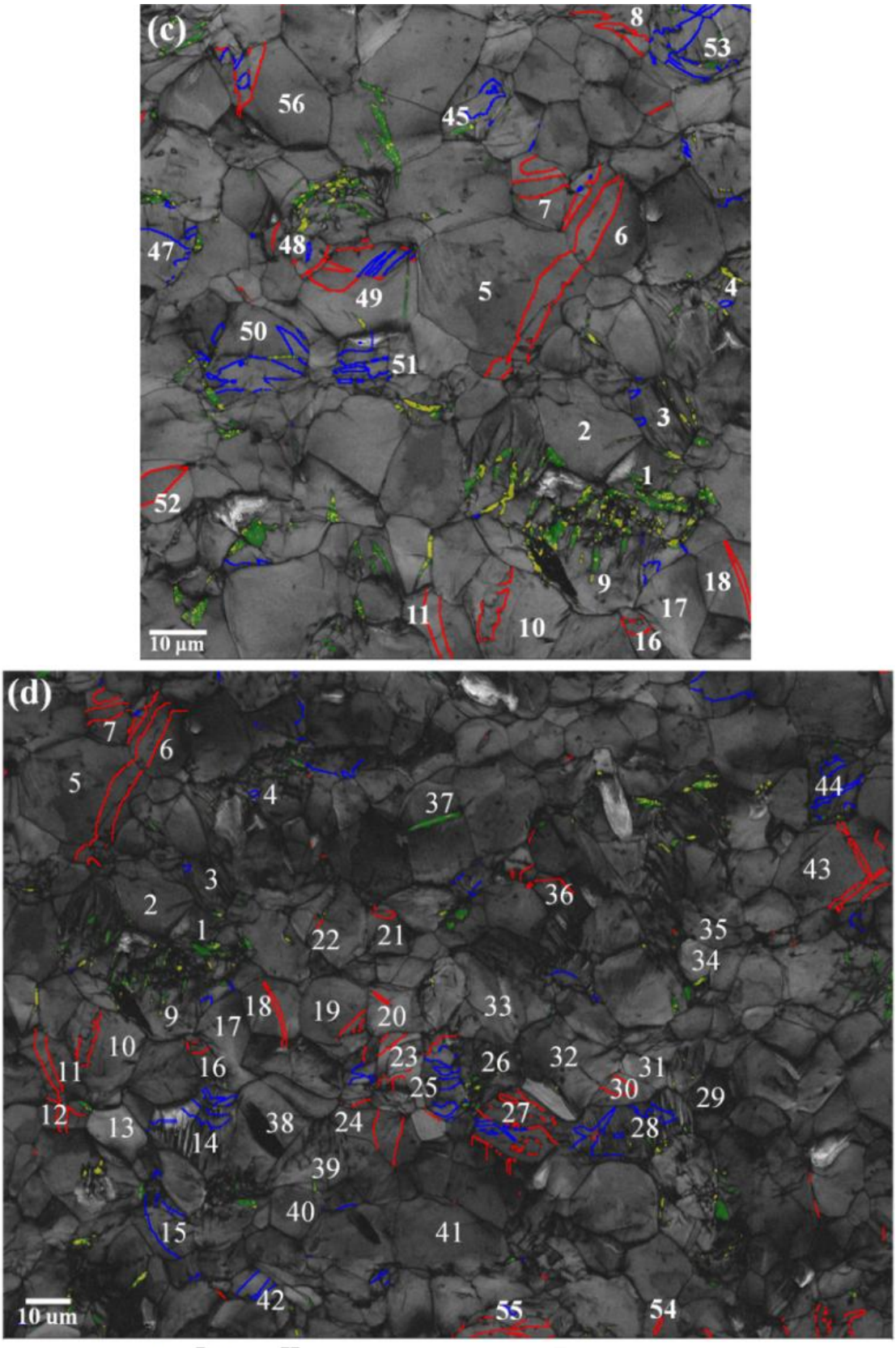

$\{10\bar{1}2\}\langle 10\bar{1}\bar{1}\rangle$ TT1 $\{11\bar{2}2\}\langle 11\bar{2}\bar{3}\rangle$ CT1

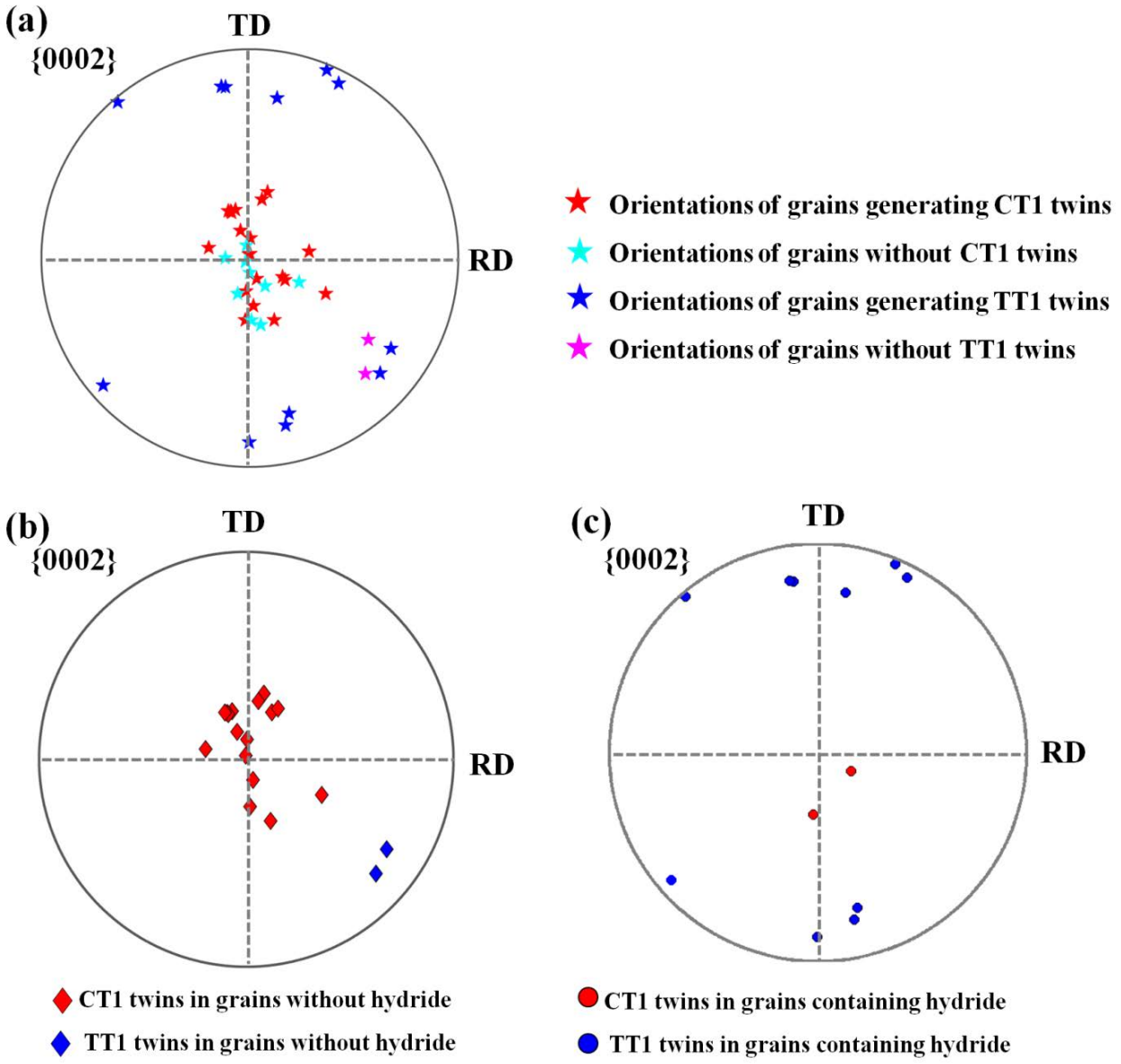

Figure 3. 18 {0002} pole figure of grains with/without CT1 and TT1 twins (168 h hydrogen charging).

The polarity of twinning enables tension twins to easily occur when tensile stresses are imposed on the c-axis and compressive stressed on the a-axis, while compression twins easily form when compressive stresses act on the c-axis [**BD14**]. Therefore, the dependency of twinning on grain orientation was stated first and then the effect of hydrides on twinning was investigated. **Figure 3. 18**a shows the orientations of the parent grains where the tension twin TT1 and the compression twin CT1 form, as indicated by the {0002} pole figure, in which the red and blue colors indicated the orientations of the parent grains generating the CT1 twins and the TT1 twins, respectively.

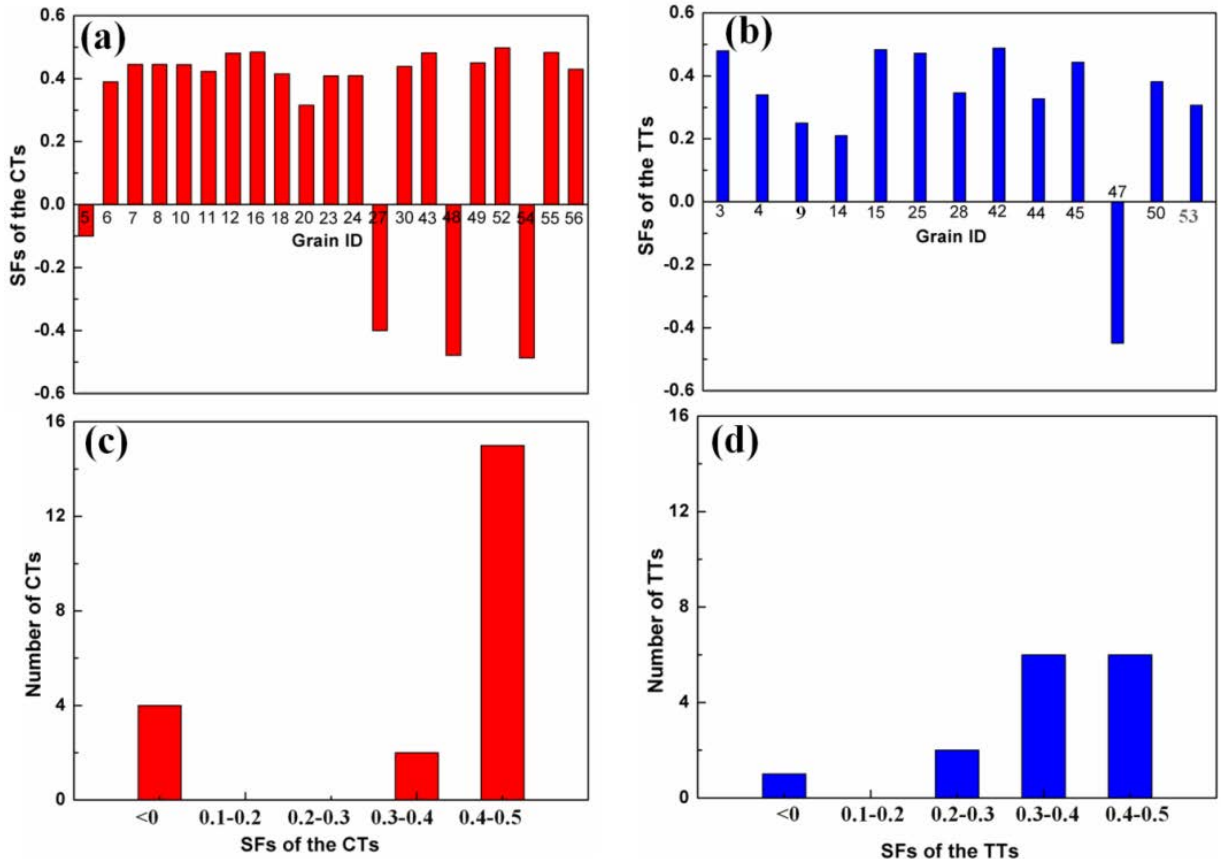

Figure 3. 19 Schimd Factors (SFs) of the compression twins CT1 (a) and of the tension twins TT1 (b), numbers of the compression twins CT1 (c) and the tension twins TT1 (d) at different SFs.

According to the Schmid law, the activation of slip or twinning system is dependent on the grain orientation [**SH05, GJ06**]. The Schmid's law states that the resolved shear stress (τ) is equal to the stress (σ) applied to the material multiplied by the cosine of the angle (Φ) between the normal of the slip plane and the direction of the applied stress and the cosine of the angle (λ) between the slip direction and the direction of the applied stress, as expressed by the following equation,

$$\tau = \sigma \cos(\emptyset) \cos(\lambda) = \sigma * m \qquad (3.1)$$

where m is known as the Schmid factor.

The Schmid factors (SFs) of those parent grains are given in **Figure 3. 19**a and b. The value of SFs varied between -0.5 and 0.5, the negative SF means the direction of twinning shear is opposite to the applied stress direction. The numbers of the CT1 twins and the TT1 twins at different SFs are presented in **Figure 3. 19**c and d. Compared to the TT1 twins, there exists a higher fraction of the CT1 twins with the SFs varying from 0.4 to 0.5. Generally, the slip or twinning system is easier to be activated with high SFs. The generation of the twins with low SFs

may thus result from the local stress. Indeed, the activation of twinning depends not only on the geometric shear and orientation relationships, but also on the nature of the hcp lattice often requiring additional shuffle steps to accommodate the twinning shear at the atomic scale **[CM95]**. For example in **Figure 3. 18**a, there are the well-orientated parent grains where the compression (tension) twins CT1 (TT1) do not form, as indicated by the green and pink colors, respectively. The absence of twinning in those well-orientated parent grains could be attributed to the deviation of local stress from the external one.

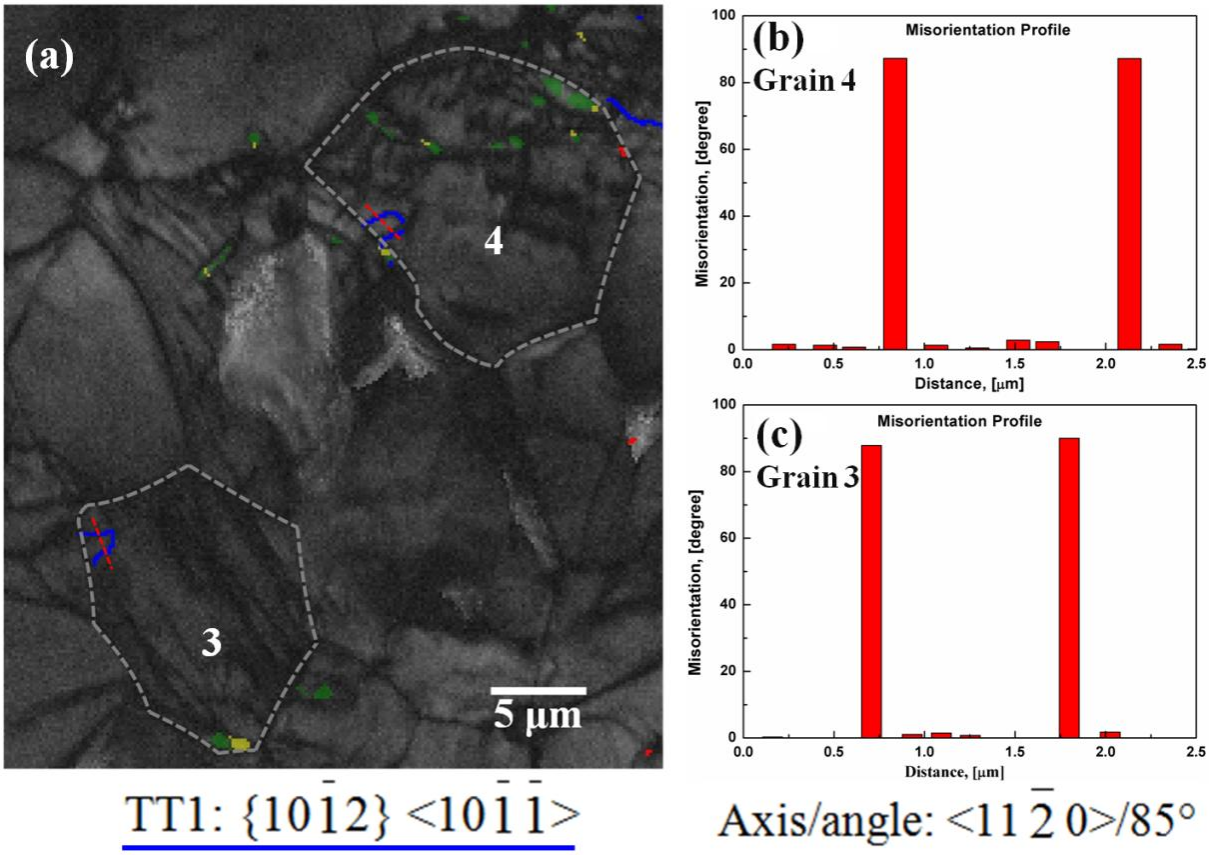

Figure 3. 20 Magnification of grains 3 and 4 shown in Figure 3.17d (a), and the misorientation profiles of the tension twin TT1 boundaries indicated by the red color in grains 4 (b) and 3 (c), respectively.

Hydrides are generally considered as a hard/brittle phase having no/less plasticity at room temperature. The load-unload tests showed that the presence of hydrides generated the long-distance internal stresses which harden the α-titanium **[GF01]** and zircaloy-4 **[R00]**. However, the observation of twins in the grains containing hydrides (grains number: 3, 4, 9, 14, 15, 25, 28, 42, 45, 49, 50, 51 and 53 in **Figure 3. 17**c and d) suggested that the hydrides had a certein ability to accommdate the shear strain imposed on the specimen. As shown in **Figure 3. 18**c, the c-axis

of the α grains containing the hydrides were nearly perpendicular to the ND (loading direction), which facilitated the formation of TT1 twins. In this figure, the red and blue circles correspond the orientations of parent grains in which the CT1 and the TT1 twins form, respectively. For the α grains without hydrides (**Figure 3. 18**b), the orientations of parent grains generating the CT1 and the TT1 twins are indicated by the red and blue rhombus, respectively. Compared to the CT1 twins, a higher fraction of the TT1 twins generated in the parent grains containing hydrides.

Table 3. 5 Information of the hydride-containing grains generating the TT1 twins (grain ID, the orientation between matrix and hydrides (OR), the average thickness of hydrides and the illustration of the arrangement of hydrides and TT1 twins).

Grain ID	OR	Thickness of hydrides, nm	Illustration of hydrides (yellow) and TT1 twins (blue) in α grain
3	OR1	450	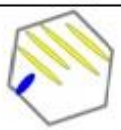
4	OR1	500	
9	OR1	500—1000	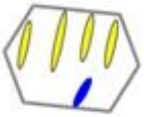
14	OR1	400	
15	OR1	180	
25	OR1	400	
28	OR1	450	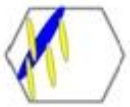
42	OR1	700	

To detail the effect of hydrides on twinning, an example of the TT1 twin formed in the grain containing hydrides is shown in **Figure 3. 20 (**grains 3 and 4 taken at higher magnification). The grain boundaries of grains 3 and 4 are outlined by the dashed lines. According to the appropriate axis/angle relationships for identification of the twin boundaries in EBSD map **[BC81],** the twins observed in grains 3 and 4 were the TT1 tension twins, as indicated by the blue color. The misorientation profile corresponding to those two twin boundaries are presented in **Figure 3. 20**b and c, respectively. As demonstrated above, the transfer of dislocation slip from the matrix to the hydrides was dependent on the orientation relationship (OR) between the matrix and the hydrides as well as the thickness of the hydrides. Based on the observations from **Figure 3. 17**, the OR, the thickness of the hydrides, and the illustration of the arrangment of the hydrides and the TT1 twins in the hydride-containing grains are presented in **Table 3. 5**.

In all of these hydride-containing grains, the OR between the matrix and the hydrides satisfied the OR1 $\{0001\}_\alpha//\{001\}_\delta$ & $<11\bar{2}0>_\alpha//<110>_\delta$. For this OR1, the presence of $<11\bar{2}0>$ dislocations at the interface $\{10\bar{1}0\}$ in the form of pile-up results in a high local stress, which may facilitate the TT1 twinning. Deformation twinning is generally explained with a step-wise nucleation, propagation and growth mechanism **[BD15].** Although no direct correlation between the nucleation of twinning and the hydride is established now, the effect of hydrides on twinning growth was obtained. For example in grains 3, 4 and 9, the TT1 twin nucleated at the grain boundary but stopped growing due to the existence of the cluster of hydrides with an average thickness more than 450 nm. While, the observations of the thicker twins in grains (14, 25, 28) showed that the cluster of hydrides with small size (thin and/or short) had negligible effect on the twin growth.

3.3 Conclusion

In this chapter, the microstructural evolution in commercial pure titanium Ti50A upon hydrogen charging by electrolytic method was thoroughly inspected by means of XRD, TEM and SEM-EBSD characterizations. The results showed that two types hydrides (δ-TiH_x, ε-TiH_2) were precipitated in the α phase matrix, and that the volume fraction of these hydrides increased as the charging time increased. The broadened diffraction peaks corresponding to the α-phase, revealed an increase in the density of dislocations necessary to accommodate the misfit between hydrides and the matrix. Five orientation relationships (OR), three of them being new orientation

relationships ever reported, between the α-phase and the hydride δ-TiH_x were determined by the analyses of the corresponding OR plane and OR direction stereographic projections of the two phases in the pole figures. Moreover, the correlation between the texture and the precipitation of hydrides was established. It was found that the existence of the rolling texture facilitated the precipitation of δ-hydride following the OR2-type orientation.

Microhardness tests showed an increase of the hardness value measured on the surface as the hydrogen charging time increased which could be explained by the increased volume fraction of hydrides in the subsurface region. Meanwhile the observation of the hardness gradient illustrated a marked gradient of the hydrogen concentration from the surface toward the center of the sample, which could be attributed to an obstruction of the hydrogen diffusion by the hydride layers. Nanoindentation measurements in the hydrogen-riched region showed that both pop-in load and pop-in displacement depth were smaller in comparison to those observed in the interior of α-grain, indicating that the presence of the dissolved hydrogen atoms lowered the activation energy required for dislocations nucleation in α-titanium.

The deformation mechanisms were investigated by microstructural analyses performed on specific region of the hydrogenated specimen before and after compression loading. The observation of slip traces and tension twins in the grains containing hydrides, suggested that the hydrides had a certain ability to accommodate the imposed shear strain, depending on the orientation relationships between the matrix and the hydrides and on their thickness. Although no direct correlation between the nucleation of twinning and the hydride was established now, the effect of hydrides on twinning growth was discussed.

Reference

[AB03] S. Arsen, J. Bai, P. Bompard. Hydride embrittlement and irradiation effects on the hoop mechanical properties of Pressurized Water Reactor (PWR) and Boiling-Water Reactor (BWR) ZIRCALOY cladding tubes: Part III. Mechanical behavior of hydride in stress-relived annealed and recrystallized ZIRCALOYs. Metall. Mater. Trans. A 34 (**2003**) 579-588.

[BB69] K.G. Barraclough, C.J. Beevers. Some observations on the deformation characteristics of bulk polycrystalline zirconium hydrides. Part. 1: The deformation and fracture of hydrides based on the δ-phase. J. Mater. Sci. 4 (**1969**) 518-525.

[BD15] B. Barkia, V. Doquet, J.P. Couzinié, I. Guillot, E. Héripré. In situ monitoring of the deformation mechanisms in titanium with different oxygen content. Mat. Sci. Eng. A 636 (**2015**) 91-102.

[BP94] J. Bai, C. Prioul, D. François. Hydride embrittlement in ZIRCALOY-4 plate: Part I. Influence of microstructure on the hydride embrittlement in ZIRCALOY-4 at 20°C and 350°C. Metall. Mater. Trans. A 25 (**1994**) 1185-1197.

[BR82] R. Khoda-Bakhsh, D.K. Ross, Determination of the hydrogen site occupation in the α phase of zirconium hydride and in the α and β phases of titanium hydride by inelastic neutron scattering, J. Phys. F: Met. Phys. 12 (**1982**) 15-24.

[BS88] D. Banerjee, C.G. Shelton, B. Ralph, J.C. Williams. Acta Mater. 36 **(1988)** 125.

[BV06] A. Barnoush, H. Vehoff, Int. J. Mater. Sci. 97 (**2006**) 1224.

[BV08] A. Barnoush, H. Vehoff, Corros. Sci. 50 (**2008**) 259.

[BV09] A. Barnoush, Ch. Biess, H. Vehoff, J. Mater. Res. 24 (**2009**) 1105.

[BJ94] J. Bai, N. Ji, D. Gilbon, C. Prioul, D. François. Hydride embrittlement in ZIRCALOY-4 plate: Part II. interaction between the tensile stress and the hydride morphology. Metall. Mater. Trans. A 25 (**1994**) 1199-1208.

[CCB17] E. Conforto, S. Cohendoz, C. Berziou, P. Girault, X. Feaugas, Formation and dissolution of hydride precipitates in Zirconium alloys: Crystallographic orientation relationships and stability after temperature cycling. *Mat. Sci. Forum* 879 (**2017**) 2330-2335.

[C81] H. Conrad. Effect of interstitial solutes on the strength and ductility of titanium. Prog. Mater. Sci 26, (**1981**) 123-403.

[CC11] E. Conforto, D. Caillard, Edge-to-Edge matching at Ti-TiH interfaces: kinetics of hydride growth and clustering of precipitates with different orientation relationships, Solid State Phen. 172-174 (**2011**) 242-247.

[CD07] E. Conforto, D. Caillard. A fast method for determining favourable orientation relationships and interface planes: Application to titanium-titanium hydrides transformations. Acta Mater. 55 (**2007**) 785-798.

[CM95] J.W. Christian, S. Mahajan, Deformation twinning. Prog. Mater. Sci. 39 (1995) 1-157.

[CG17] E. Conforto1, E. Guillot, X. Feaugas, Solute hydrogen and hydrides phases implications on the plasticity of zirconium and titanium alloys: a review and some recent advances, Phil. Trans. R. Soc. A. ***2017*** *(doi:10.1098/)*

[CL03] C.Q. Chen, S.X. Li, K. Lu. The deformation behaviors of gamma hydrides in titanium under cyclic straining. Acta Mater. 51 (**2003**) 931-942.

[CLL04] C.Q. Chen, S.X. Li, K. Lu. Dislocation interaction with hydrides in titanium containing a low hydrogen concentration. Philos. Mag. 84 (**2004**) 29-43.

[CL04] C.Q.Chen, S.X. Li, Tensile and low-fatigue behaviors of commercially pure titanium containing γ-hydrides. Mater. Sci. Eng. A 387-389 (**2004**)470-475.

[CLZ04] C.Q. Chen, S.X. Li, H. Zheng, L.B. Wang, K. Lu. An investigation on structure, deformation and fracture of hydrides in titanium with a large range of hydrogen contents. Acta Mater. 52 (**2004**) 3697-3706.

[CY05] Y.B. Chun, S.H. Yu, S.L. Semiatin, S.K. Hwang, Effect of deformation twinning on microstructure and texture evolution during cold rolling of CP-titanium, Mater. Sci. Eng. A 398 (**2005**) 209-219.

[DB02] C. Domain, R. Besson, A. Legris, Atomic-scale Ab-initio study of the Zr-H system: I. Bulk properties, Acta Mater. 50 (**2002**) 3513-3526.

[DB15] M. Deutges, H.P. Barth, Y.Z. Chen, C. Borchers and R. Kirchheim, Hydrogen diffusivities as a measure of relative dislocation densities in palladium and increase of the density by plastic deformation in the presence of dissolved hydrogen, Acta Mater. 82 (**2015**) 266-274.

[DJ00] M.J. Donachie Jr., Titanium: A Technical Guide, Second Edition ASM, 2000 204-7586 (ISBN 0-87170-686-5. SAN).

[G03] I. Guillot, UTC-ECP-EDF report **2003**.

[GF01] I. Guillot, X. Feaugas, M. Clavel. Dislocation-hydride interactions at low plastic strain in titanium, Scripta Mater. 44 (**2001**), 1011-1017.

[GJ06] S. Godet, L. Jiang, A.A. Luo, J.J. Jonas, Scripta Mater. 55 **(2006)** 1055.

[HF98] J. Huez, X. Feaugas, A.L. Helber, I. Guillot I, M. Clavel. Damage process in commercially pure α-titanium alloy without (Ti40) and with (Ti40-H) hydrides. Metall. Trans. A 29 (**1998**), 1615-1628.

[IB72] P.E. Irving, C.J. Beevers, Some observations on the deformation characteristics of titanium hydride, J. Mater. Sci. 7 (**1972**) 23-30.

[LW03] G. Lütjering, J.C. William, Titanium: Engineering Materials and Processes, Springer, **2003**.

[LX13] Y. Liu, W. Xiang, G.L. Zhang, B.Y. Wang, Surface and phase transformation characteristics of titanium hydride film under irradiation of pulsed ion beam, Appl. Surf. Sci. 285 (2013) 557-563.

[N96] H.G. Nelson, Hydrogen Effects in Metals, (Eds.: A. W. Thompson, N.R. Moody), (TMS, Warrendale, PA, **1996**) pp. 699-715.

[NB06] K.A. Nibur, D.F. Bahr, B.P. Somerday, Acta Mater. 54 (**2006**) 2677.

[PH68] T.P. Papazoglou, M.T. Hepworth, Diffusion of hydrogen in titanium, Trans. AIME 242 (**1968**) 682-685.

[R00] N. Rupa, Effect of hydrogen and hydrides on the viscoelastic behavior of recrystallized zircaloy-4, PhD thesis, Université de Technologie de Compiègne, France, **2000**.

[RX12] M. Rautenberg, X. Feaugas, D. Poquillon, J.M. Cloué. Microstructural characterization of creep anisotropy at 673 K in the M5 (R) alloy. Acta Mater. 60 (**2012**) 4319-4327.

[SH05] T. Sawai, A. Hishinuma, J. Phys. Chem. Solids 66 **(2005)** 335.

[SR07] D. Srinivas and P. Ratnasamy, Influence of Particle size and interaction with the support on redox and catalytic properties of metals, metal oxides and metal complexes, in

Nanotechnology in Catalysis Vol. 3, edited by Bing Zhou, Scott Han, Robert Raja, Gabor A. Somorjai, Springer Science, **2007**.

[TF96] A. Takasaki, Y. Furuya, K. Ojima and Y.Taneda, in Hydrogen Effects in Materials, ed. A. W.Thompson and N. R. Moody. TMS, Warrendale, PA, 1996, p. 799.

[VA03] M. Veleva, S. Arsen, M.C. Record, J.L. Bechade, J. Bai Hydride embrittlement and irradiation effects on the hoop mechanical properties of Pressurized Water Reactor (PWR) and Boiling-Water Reactor (BWR) ZIRCALOY cladding tubes: Part II. Morphology of hydrides investigated at different magnifications and their interaction with the processes of plastic deformation. Metall. Mater. Trans. A 34 (**2003**) 567-578.

[VS16] M.A. Vicente Alvarez, J.R Santisteban, P. Vizcaíno, G. Ribarik, T. Ungar. Quantification of dislocations densities in zirconium hydride by X-ray line profile analysis. Acta Mater. 117 (**2016**) 1-12.

[W76] J.C. Williams: Effect of hydrogen on behavior of materials, (Eds.: A. W. Thompson, I. M. Bernstein), (AIME, New York, NY, **1976**) pp. 367-380.

[WE02] T. Wang, F.Eichhorn, D. Grambole, A new Ti/H phase transformation in the $H2^{+}$ titanium alloy studied by x-ray diffraction, nuclear reaction analysis, elastic recoil detection analysis and scanning electron microscopy, Phys. Condens. Matter 14 (**2002**) 11605-11614.

[WF08] M. Wilde, K. Fukutani, Penetration mechanisms of surface-adsorbed hydrogen atoms into bulk metals: experiment and model, Phys. Rev. B 78 (2008) 115411.

[ZD11] S.V. Zherebtsova, G.S. Dyakonova, A.A. Salemb, S.P. Malysheva, G.A. Salishchev, S.L. Semiatin, Evolution of grain and subgrain structure during cold rolling of commercial-purity titanium, Mater. Sci. Eng. A 528 (**2011**) 3474-3479.

[ZR90] P. Zheng, M.O. Ruault, D. Fournier, R.G. Saint-Jacques. J. Mater. Sci. Lett. 9 (**1990**) 75.

[ZK94] C. Zhang, Q. Kang, Z. Lai. Acta Mater. 42 (**1994**) 2555.

Chapter 4 Hydrogen-induced microstructural evolution and its effects on mechanical properties in β-21S alloy

4.1 Introduction

A previous study undertaken by Teter and co-workers to better understand the effects of hydrogen on the bulk mechanical properties of β-21S alloy found that an abrupt ductile-to-brittle transition occurred above a critical hydrogen concentration (H/M = 0.215) **[TR01]**. The operative mechanism behind this phenomenon was considered to be related to hydrogen-induced decohesion. However, this conclusion was based on the assumption that the β-21S alloy had a constant microstructure during hydrogen charging. Indeed, hydrogen as a β phase stabilizer decreasing the β-transus temperature, can alter the microstructure of this alloy upon cooling. It is therefore important to investigate the change of the microstructure induced by hydrogen and its effect on the mechanical properties of β-21S alloy.

Following this proposition, we aimed to thoroughly describe the hydrogen-induced microstructural evolution and its effects on the mechanical properties in β-21S alloy using XRD, SEM-EBSD and TEM analyses. To compare with the data from the reference **[TR01]**, the same hydrogen charging procedure and parameters were used in the current work.

4.2 Results and discussion

4.2.1 Microstructure of as-received β-21S alloy

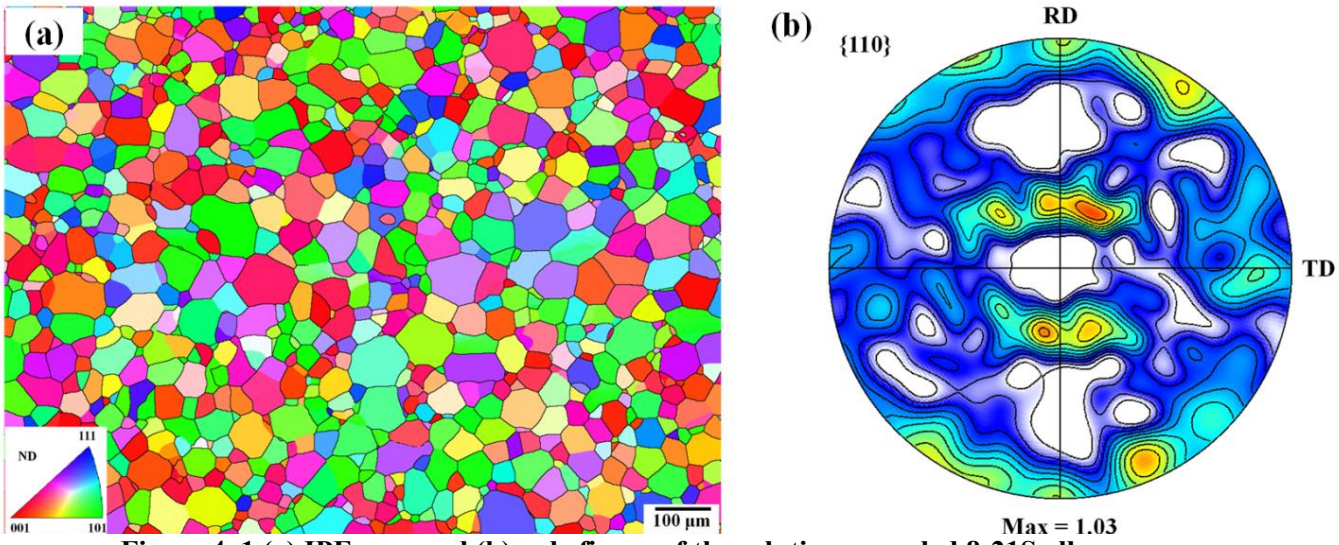

Figure 4. 1 (a) IPF map and (b) pole figure of the solution annealed β-21S alloy.

The material used was the TIMETAL®21S titanium alloy received in the solution annealed state in the form of 1.8 mm thick sheet. The β-21S alloy contained only the BCC β-phase with an average grain size of 35.0 ± 2.0 μm, as shown in **Figure 4. 1**. No internal substructure is observed. The pole figure revealed a very weak bcc-rolled residual texture in the solution-annealed sample.

4.2.2 Hydrogen-induced microstructural evolution in β-21S alloy

4.2.2.1 XRD analysis

In the present study, the hydrogen effect on the microstructure of β-21S alloy was first investigated by means of XRD analyses. The XRD patterns corresponding to different hydrogen concentrations (H/M indicating the ratio of hydrogen to metal, H/M ≤ 0.460) are shown in **Figure 4. 2**. The patterns consist only of the β-phase; no indication of α-phase and hydride precipitation are observed. However the β-phase peaks were found to shift to lower 2θ values with the increase of hydrogen concentration indicating the lattice expansion of β-phase induced by the dissolved hydrogen. Indeed, the interstitially dissolved hydrogen atoms are trapped preferably in areas of local stress concentrations, such as vacancies, dislocations, phase and grain boundaries, which cause crystal lattice expansion as well as lattice distortion **[K01, SC01]**.

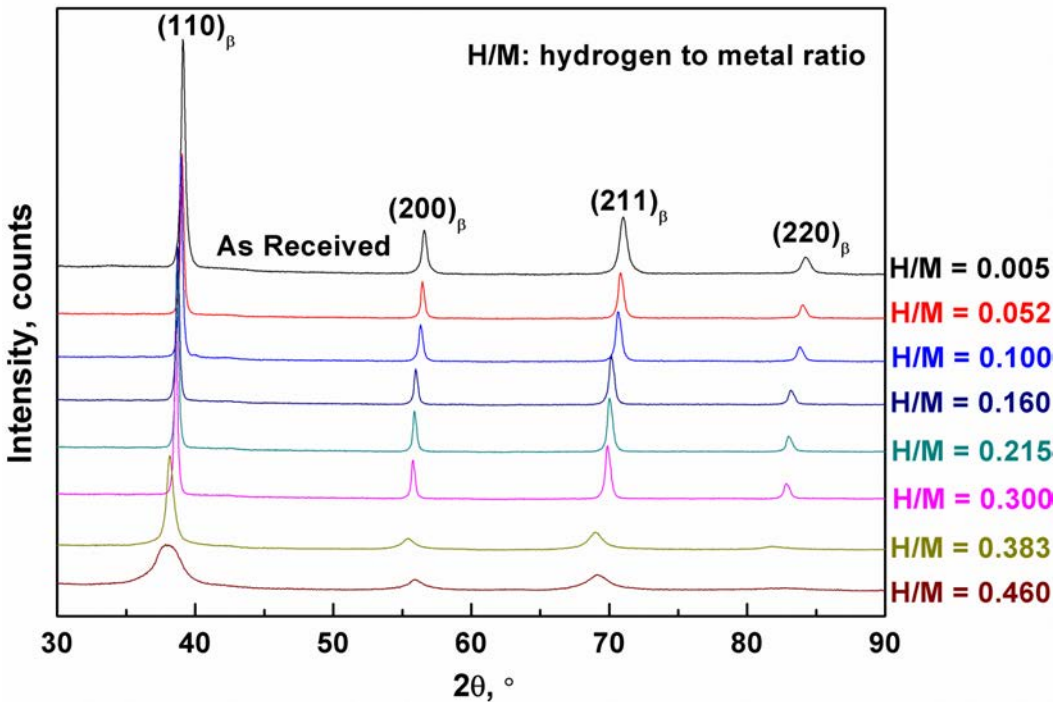

Figure 4. 2 Measured XRD profiles of Beta-21S with different H/M ratios

By fitting the obtained XRD patterns with the MAUD software, the values of the lattice parameter can be determined, as shown in **Table 4. 1.** The data in red color is consistent with that reported by Teter and coworkers **[TR01]**, at which the abrupt ductile-brittle transition occurs. **Figure 4. 3** presents the relative change in the lattice parameter (i.e., $[(a_H - a_O)/a_O]$) as a function of hydrogen concentration; the reference data is given for comparison. In the hydrogen concentration range 0.052 < H/M < 0.460, the relative change in lattice parameter is linearly related to the hydrogen concentration, indicating that no hydrides are precipitated in this concentration range (a plateau would exist in **Figure 4. 3** if a second phase formed) and that hydrogen atoms are in β-solid solution. Using a least squares fit to the data in the solid solution range, the relative change in lattice parameter as a function of hydrogen contents was expressed as

$$[(a_H - a_o)/ a_o] = 3.06 \times 10^{-4} + 0.0508(H/M) \qquad \textbf{(4.1)}$$

with a coefficient of correlation, R = 0.996. Compared to the equation $[(a_H - a_o)/ a_o] = 5.08 \times 10^{-4} + 0.0436(H/M)$ obtained in the reference for the same alloy [**TR01**], the equation **(4.1)** in the current experiment showed a slightly larger value of the slope. This minor difference resulted from the accuracy of the measurement for hydrogen contents. Using these data, the partial molar volume of hydrogen in the β-phase can be calculated to be 1.36 cm^3mol^{-1}, which is in good agreement with the values obtained by others **[L81, GM81, TR01].**

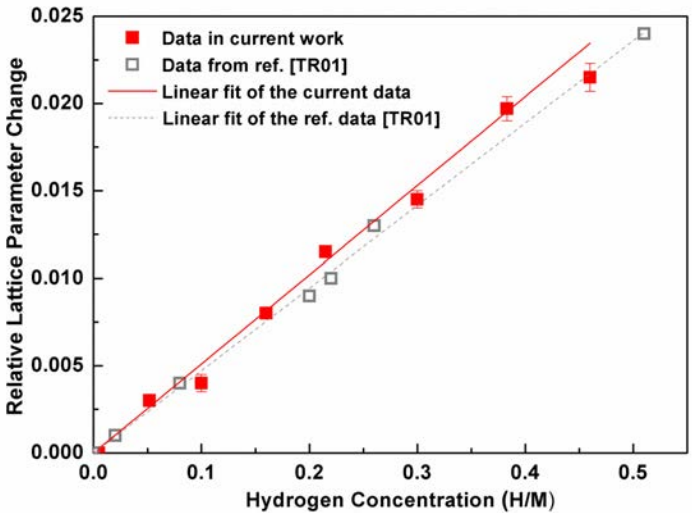

Figure 4. 3 Relative change in the lattice parameter $[(a_H - a_o)/ a_o]$ of the β-phase as a function of hydrogen concentration. A least squares regression analysis yields the fit to the data given by y = $[(a_H - a_o)/ a_o] = 3.06 \times 10^{-4} + 0.0508(H/M)$ with a coefficient of correlation R = 0.996.

In addition, it can be noticed that the XRD peaks became broadening for hydrogen concentration exceeding 0.3 (H/M > 0.3). The possible explanations of this observed trend could be the presence of lattice strain and/or composition gradients caused by hydrogen. It should be pointed out that, at the temperature of 1123 K, the hydrogen diffusion rate is so fast that the equilibrium throughout the specimen volume can be obtained in few minutes. Therefore, hydrogen is almost uniform distributed throughout the sample volume, and this can be evidenced from the microhardness profile shown in **Figure 4. 8**b. On the other hand, the peak broadening resulting from the lattice strain can be calculated from the full width at half maximum (FWHM) **[TE07]**. **Figure 4. 2** gives the value of FWHM for $(110)_\beta$ diffraction peak at different hydrogen concentrations. It can be seen that, the amount of broadening was very small in the hydrogen concentration range 0.052 < H/M < 0.300. While as the hydrogen concentration increased to H/M = 0.460, the peak broadening was obviously increased. Thus, the observation of peak broadening was attributed to the lattice strain generated by the addition of hydrogen. Moreover, fitting the XRD pattern using the MAUD program, it was estimated that the addition of hydrogen led to a volume expansion of the β phase of about 6.607% at the hydrogen concentration H/M = 0.460.

Table 4. 1 Hydrogen charging conditions of β-21S, lattice parameter, relative volume change of the BCC lattice and hydrogen concentrations of studied samples

Sample series	H_2 charging pressure (kPa)	Lattice parameter (Å)	Relative volume change of BCC lattice, %	Hydrogen concentration	
				(at. %)	(H/M)
As received	N/A	3.247	/	0.500	0.005
1123-1	1	3.256	0.834	4.940	0.052
1123-2	5	3.259	1.113	9.091	0.100
1123-3	10	3.273	2.421	13.793	0.160
1123-4	**25**	**3.285**	**3.552**	**17.695**	**0.215**
1123-5	35	3.294	4.405	23.077	0.300
1123-6	50	3.311	6.030	27.660	0.383
1123-7	100	3.317	6.607	31.530	0.460

Table 4. 2 The full width at half maximum (FWHM) for (110) peak at different hydrogen concentrations (H/M)

H/M	0.052	0.100	0.160	0.215	0.300	0.383	0.460
$(FWHM)_{110}$	0.275±0.003	0.276±0.003	0.275±0.003	0.276±0.003	0.278±0.003	0.346±.005	0.665±0.008

4.2.2.2 SEM-EBSD characterizations

Since hydrogen decreases the temperature of the allotropic transformation (β-transus temperature) **[SC01]**, it improves the stability of the β-phase upon cooling. It is therefore important to state the microstructural evolution induced by hydrogen and to understand the potential reason for the observation of peak broadening in **Figure 4. 2**.

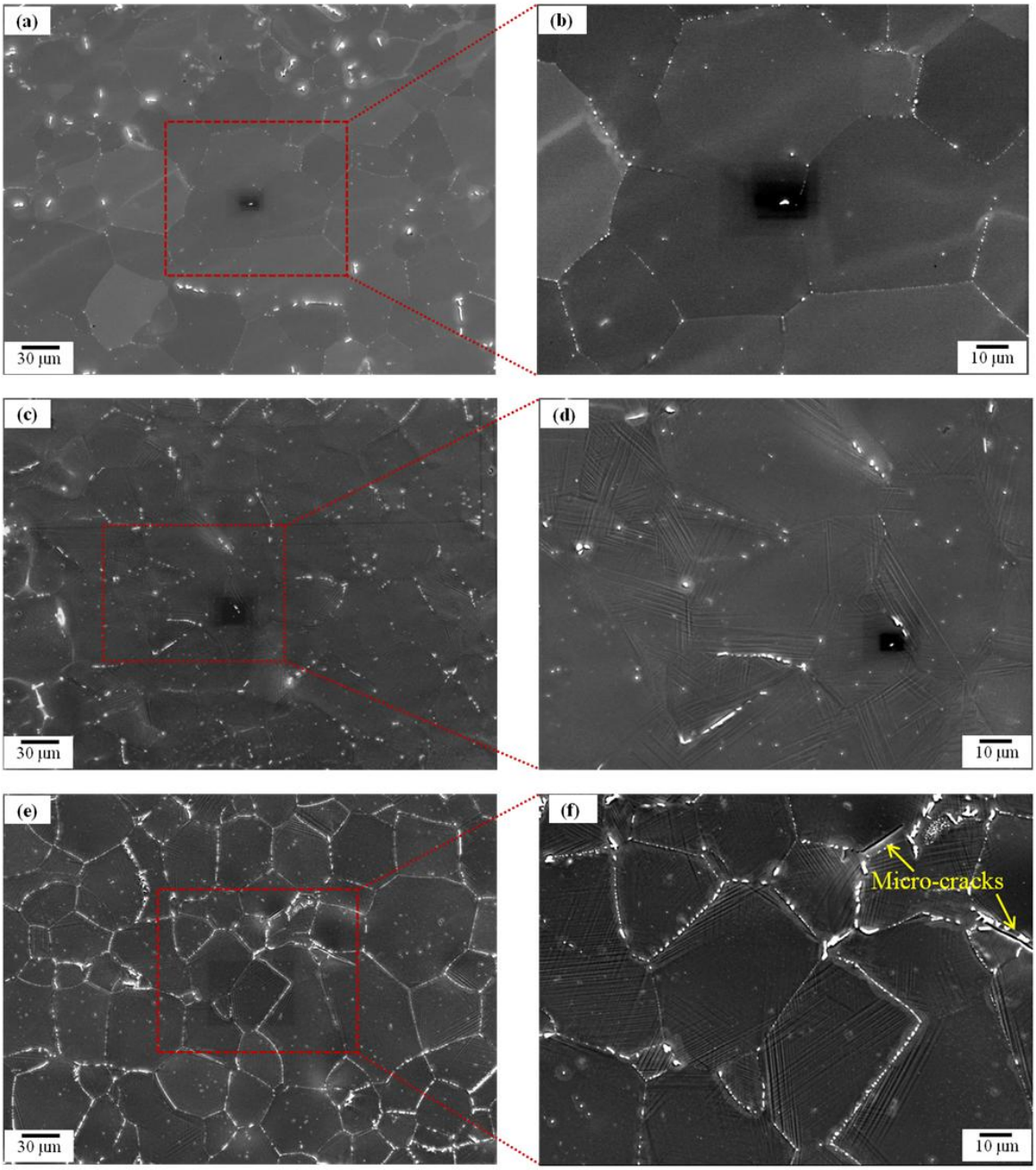

Figure 4. 4 SEM images taken on the cross-section of hydrogenated β-21S alloys. (a) and (b) H/M = 0.215; (c) and (d) H/M = 0.383; (e) and (f) H/M = 0.460.

Figure 4. 4 shows the SEM micrographs taken on the cross-section of hydrogenated β-21S alloys containing different hydrogen concentrations. For example, **Figure 4. 4**a and b give the SEM image of hydrogenated β-21S alloy with hydrogen concentration H/M = 0.215, at which the abrupt ductile-brittle transition occurred as reported by Teter et al. **[TR01]**. Confirming the XRD analyses, it can be seen that the microstructure consisted of only equiaxed β grains; no α-phase or hydride was noticed. However, as hydrogen concentration increased to H/M = 0.380, the plate-like structures precipitated from the matrix β phase, as shown in **Figure 4. 4**c and d. When the hydrogen concentration was further increased to H/M = 0.460, an increasing number of plate-like structures could be detected throughout the sample, as shown in **Figure 4. 4**e and f. This plate-like morphology appeared like the martensite structure commonly observed in the deformed or quenched metastable β-titanium alloys **[CW87, MT04 and CZ16]**. The appearance of the micro-cracks as indicated by the arrows suggested that there existed large local stress concentration at grain boundaries in the hydrogenated β-21S alloy.

Table 4. 3 Orientation information of the martensite variants and the matrix determined by electron backscatter diffraction (EBSD). The Euler angles are expressed in Bunge's notation [**BE80, BE81**]. (The Euler angles listed in the table below represents the mean orientation of the martensite variants and the matrix, respectively.)

Phase	Notation	Euler angles (φ_1, Φ, φ_2), (°)
Martensite	α_1	(30.76, 99.70, 173.74)
	α_2	(85.01, 70.50, 59.11)
	α_3	(149.92, 59.80, 139.65)
	α_4	(163.25, 117.76, 66.32)
Matrix	β	(203.58, 35.81, 10.65)

To further examine this martensite structure, EBSD analyses were conducted on the cross-section of hydrogenated sample containing hydrogen concentration H/M = 0.460. **Figure 4. 5a** shows the SEI micrograph of the measured region. The observed β grains are labeled with A, B, C, D, E, F and G. **Figure 4. 5b** gives the BSE micrograph of the grain A with higher magnification. As observed, four different orientated martensite α" plates as indicated by Arabic numerals coexist within one β grain. The martensite plates having the common stretch direction (1 and 2) are distributed alternatively in β grain. To have a precise value of Euler angle for the individual

martensite plates, we manually measured the orientations of the martensite α'' plates and the matrix (β phase). For example, in grain A, four different oriented martensite variants, α_1'', α_2'', α_3'' and α_4'', were detected. This martensite α" phase has an orthorhombic structure with the same structure of stress-induced martensite α" **[CW87, LX98 and MT04]**. The details of the orientation information of the four martensite variants and the matrix are listed in **Table 4. 3**.

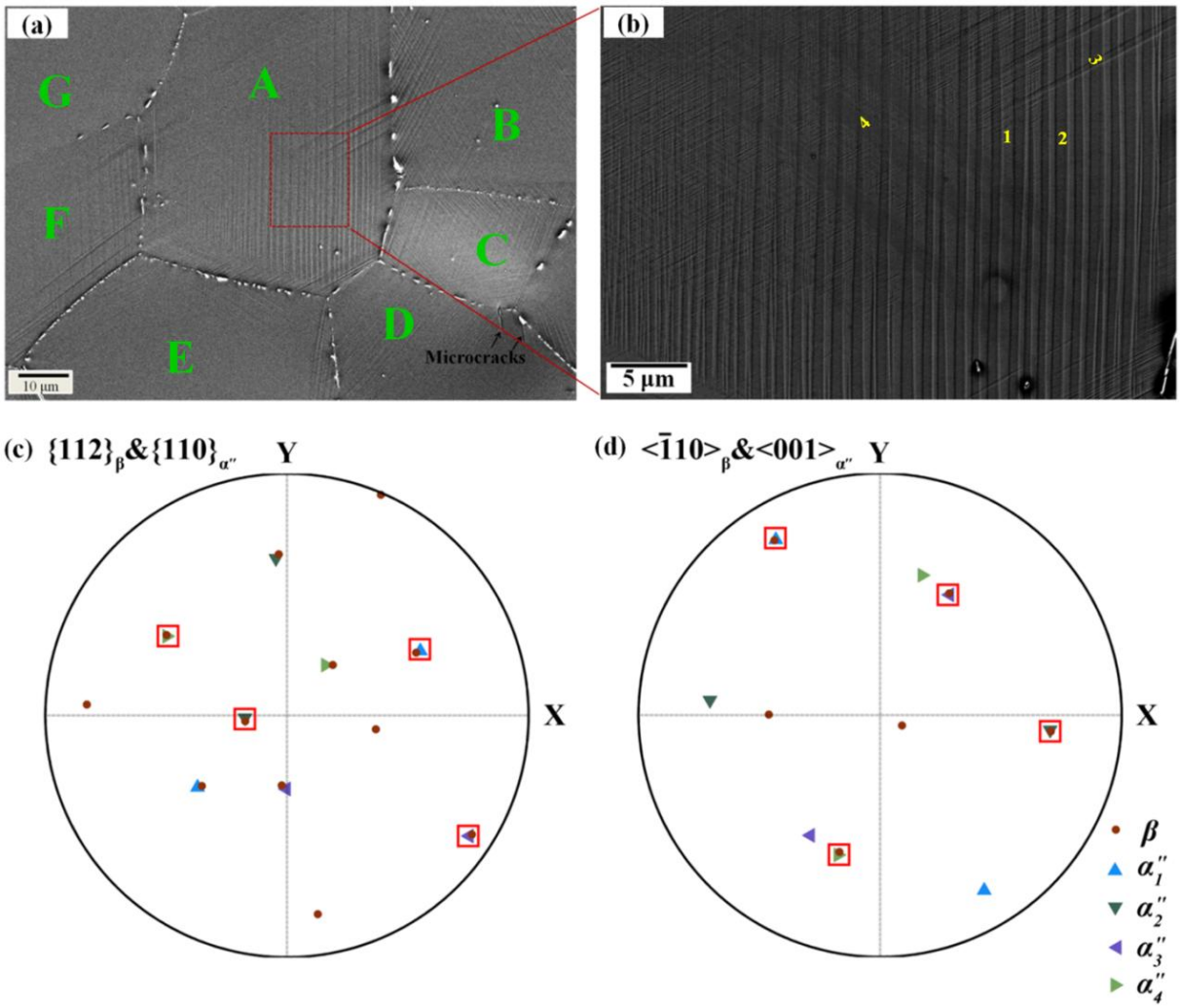

Figure 4. 5 Martensite characterization by EBSD measurements. (a) SEI micrograph of martensite α"; (b) BSE micrograph of the EBSD detected area; (c) the stereographic projections of the planes $\{112\}_\beta$ and $\{110\}_{\alpha''}$ and (d) the stereographic projections of the directions $<\bar{1}10>_\beta$ and $<001>_{\alpha''}$. (the overlapped projections of β and α" indicated by red frame)

The orientation relationships (ORs) that specific as $\{112\}_\beta//(110)_{\alpha''}$ & $<\bar{1}10>_\beta//[001]_{\alpha''}$ were recognized in previous studies in the metastable β-Ti alloys **[CW87, MT04 and CZ16]**. In the present alloy, these ORs were further confirmed by the corresponding OR plane and OR direction stereographic projections of the two phases in **Figure 4. 5c and d**. From the stereographic

projections, we can find that each martensite variant possesses one $\{110\}_{\alpha''}$ plane parallels to one $\{112\}_{\beta}$ plane of the matrix phase. The projection of the $<001>_{\alpha''}$ direction for each martensite variant overlaps one $<\bar{1}10>_{\beta}$ projection of the matrix phase. Hence, this conventional OR is also the effective one between the two phases in the present alloy. The results described above showed that, the formation of a four-variants network of martensite α'' plates deeper beneath the sample surface with conventional α''/β orientation relationships, i.e. $(110)_{\alpha''}//\{112\}_{\beta}$ and $[001]_{\alpha''}//<\bar{1}10>_{\beta}$, with a thickness ranging from 250 to 400 nm.

As well known, martensite transformation is diffusionless, displacive solid state structure transformation. It usually occurs by quenching or deformation in metastable β-titanium alloys, such as Ti-10V-2Fe-3Al et al. **[CW87, LX98, MT04, PK07, PK08 and CZ16]**. In the present work, the martensite transformation occurred unexpectedly in the process of hydrogen charging. Neither quenching nor mechanical deformation could be the reason for this observed phase transformation. Regarding the influence of alloying elements on the martensite start temperature (Ms), some controversies still remain in the scientific comminity. It has been recognized that the Ms temperature decreases monotonically with the increasing content of the β-stabilizing elements in the metastable β-Titanium alloys. Following this principle, the addition of hydrogen as β-stabilizing element should stabilize the β-phase and suppress the martensite α'' phase during the cooling process. However, the appearance of martensite plates for high hydrogen concentration ($H/M \geq 0.380$) disagreed with this principle. This means that the stability of β-phase cannot be increased monotonically with increasing the hydrogen concentration upon cooling. In the hydrogen concentration range $0.052 \leq H/M \leq 0.300$, the addition of hydrogen suppressed the decomposition of the β-phase on cooling. However, as the hydrogen concentration was further increased to $H/M = 0.380$, a large distortion of the bcc lattice occurred due to the hydrogen concentration stress. Using ab initio calculations, people have demonstrated that the cohesive energy was changed at a grain boundary in Ni due to hydrogen segregation [**ZW00**]. This is consistent with the observation of the micro-cracks at grain boundaries (**Figure 4. 4**f) in the specimen having the largest hydrogen concentration. Though the mechanism responsible for this martensite transformation is unclear, it is reasonable to assume that a large internal stress generated by the filling of the hydrogen atoms at the interstitial sites and the segregation of hydrogen atoms at grain boundaries, gives rise to the additional shuffling of titanium atoms in

alternate $\{110\}_\beta$ planes, which result in the transformation into a C-centered orthorhombic crystal structure.

4.2.2.3 TEM investigations

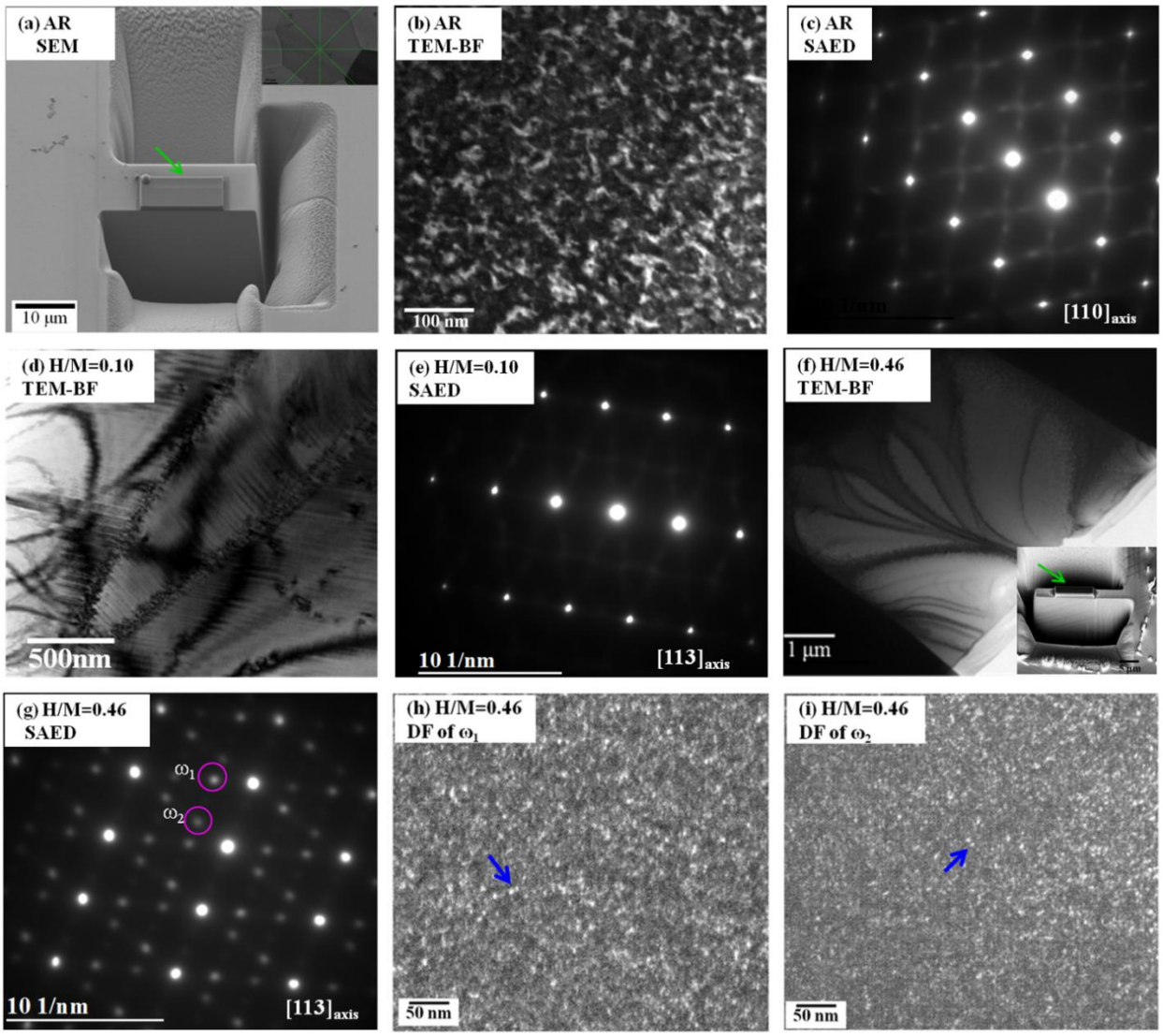

Figure 4. 6 TEM characterization of the as-received and hydrogen charged β-21S alloys. (a) SEM image of as-received β-21S alloy being prepared by ionic micromachining; (b) TEM-BF micrograph of as-received β-21S alloy; (c) SAED pattern of as-received β-21S alloy; (d) TEM-BF micrograph of the hydrogen charged β-21S alloy with hydrogen concentration H/M = 0.10, and the insert image indicating the sample being prepared by ionic micromachining; (e) the corresponding SAED pattern of the hydrogenated β-21S alloy; (f) TEM-BF micrograph of the hydrogen charged β-21S alloy containing hydrogen concentration H/M = 0.46; (g) The corresponding SAED pattern of the hydrogenated β-21S alloy and (h), (i) the DF images of the athermal ω phasevariants, ω_1 and ω_2, respectively.

Characterizations by means of TEM were performed to investigate the local-scale microstructure of the hydrogenated β-21S alloy containing high content of hydrogen. **Figure 4. 6**a shows the

SEM image of the as-received β-21S alloy being prepared by ionic micromachining (as indicated by the arrow). The inserted micrograph is a magnification of the selected grain, no internal structure can be observed. **Figure 4. 6**b shows bright-field (BF) image of thin foil extracted from the as-received β-21S alloy. The corresponding selected area electron diffraction (SAED) pattern is shown in **Figure 4. 6**c. Diffused streaks in the electron diffraction pattern are typical of athermal ω phase as it has been reported in the as-received (air-quenched) β-21S alloy by Teter et al. **[TR01]**. This is because the formation of athermal ω phase cannot be avoided in β-titanium alloys no matter how fast the cooling rate is performed. Therefore, in the as-received specimen there exists a very low volume fraction of athermal ω particles. Attempts to resolve image the ω precipitates using the streaks were not successful.

Figure 4. 6d shows the BF image of hydrogenated β-21S alloy containing hydrogen concentration H/M = 0.10. The low-angle boundary arrays and stacking faults were observed inside the β grain. **Figure 4. 6**e shows the corresponding SAED pattern. Compared to the as-received β-21S alloy, the intensity of the diffuse streaks associated with the athermal ω phase was found to be decreased, indicating that the volume fraction of the athermal ω phase was reduced further because it became less stable upon hydrogen addition. This observation was consistent with earlier reports **[I87, CW87, I94 and TR01]** and confirms that hydrogen stabilizes the β phase and suppresses the formation of athermal ω phase in metastable β-titanium alloys upon cooling.

The specimen containing the largest high hydrogen concentration of H/M = 0.46 was too brittle so that the thin foil for TEM observation could not be prepared by the traditional method. Therefore, the thin foil was extracted from the hydrogenated specimen (previously localized by SEM-EBSD shown in **Figure 4. 6**b) using the ionic micromachining. The TEM-BF image of the thin foil is shown in **Figure 4. 6**f, the insert micrograph showed that the thin foil (as indicated by the arrow) was being prepared by the ionic micromachining. The corresponding SAED pattern is presented in **Figure 4. 6**g. No martensite α" (orthorhombic) could be detected but a new phase having a hexagonal structure referred to ω-phase was observed. Moreover, the observed ω phase has two variants, ω_1 and ω_2, as indicated by the pink circles. The dark-field (DF) images corresponding to the selected two variants ω_1 and ω_2 are shown in **Figure 4. 6**h and i, respectively. It can be seen that, those two ω variants have the same morphology and are found in the form of nano-sized particles as indicated by the arrows randomly distributed in the matrix β phase. This

morphology is typical structure of athermal ω-phase, which is usually formed by quenching in metastable β-titanium alloys **[CW87, MT04, ME14, LN16 and CZ16].**

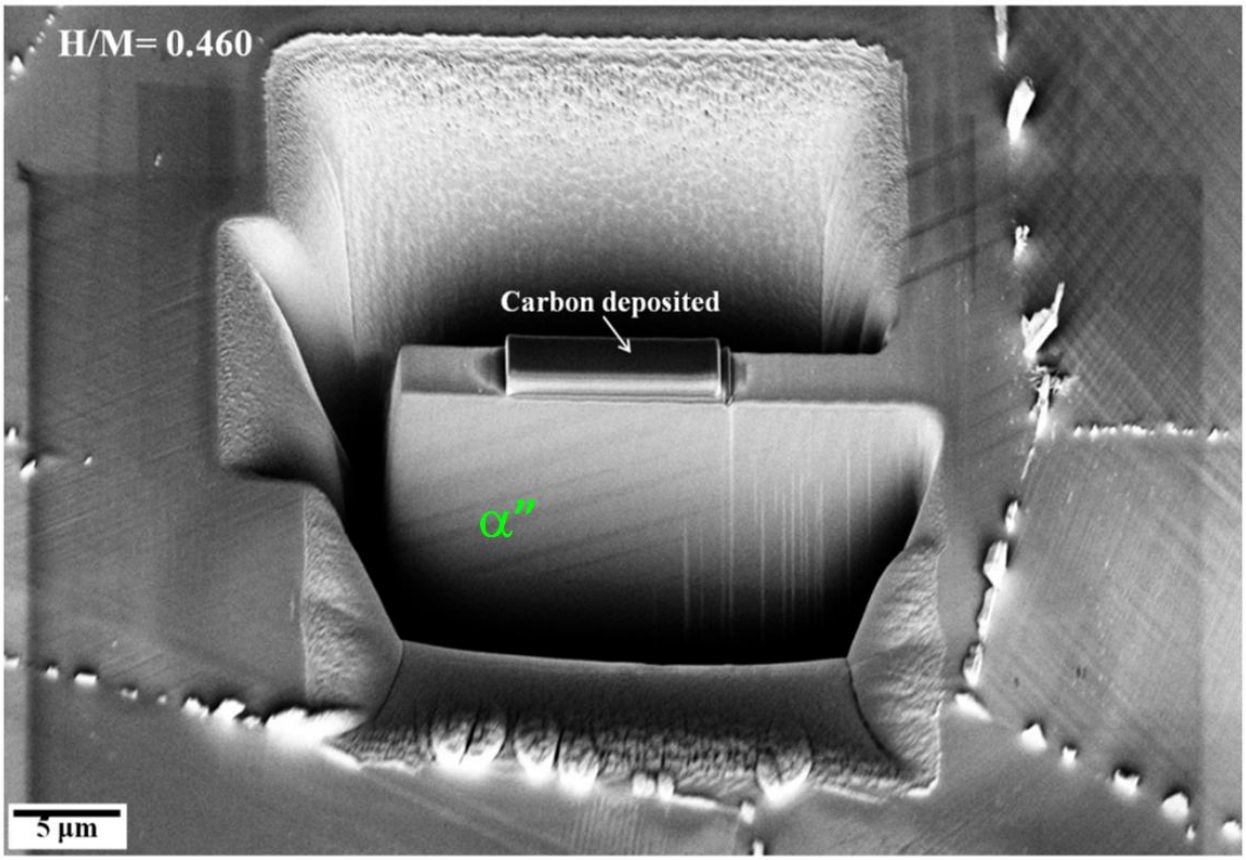

Figure 4. 7 SEM micrograph of hydrogenated β-21S alloy (H/M = 0.460) being prepared by the ionic micromachining.

Two questions naturally arises: why the martensite phase α" disappeared after ionic micromachining, and how does this athermal ω phase form? The probable reason for the disappearance of martensite α" is that the relief of internal stresses due to the escape of pre-dissolved hydrogen atoms during ionic micromachining. It should be mentioned that the martensite plates were still observed in the middle progress of the preparation of the thin foil by ionic micromachining, as shown in **Figure 4. 7**. To protect the surface from contamination, a layer of carbon was deposited on the selected area (corresponding to **Figure 4. 5**b) prior to ionic micromachining. The martensite dissolution therefore occurred in the last stage of ionic micromachining due to the spontaneous dehydrogenation. As the thickness of the thin foil is reduced down to 100 nm, hydrogen atoms are easier to egress due to the high vacuum and the less tight bonding.

Consequently, the formation of athermal ω-phase enabled a relaxation of the elastic stresses caused by the volume expansion from the β phase to the α" martensite. Indeed, Mantani and co-workers have proposed that the formation of the ω-phase resulted from the relaxation of the strain induced by the volume expansion from the β phase to the α" martensite **[MT04]**. Moreover, recent study **[LN17]** has demonstrated that this deformation-induced ω phase transformation can be triggered by elastic strain or stress without plastic deformation.

4.2.3 Hydrogen effects on mechanical properties in β-21S alloy

4.2.3.1 Hydrogen effects on microhardness property

Following hydrogenation by gaseous method, microhardness measurements were perfomed to reveal the hydrogen-induced hardening in β-21S alloys. The change of hardness as a function of hydrogen concentration is shown in **Figure 4. 8**a. The microhardness increases with increasing hydrogen concentration but in a non-linear manner. As observed, there exist two stages of hardening during hydrogen charging. In the hydrogen concentration range $0.052 \leq H/M \leq 0.300$, the first stage of hardening occurred by a solid solution strengthening owing to the dissolved hydrogen atoms at interstitial sites. When hydrogen concentration exceeds 0.300 (as evidenced by the ratio $H/M \geq 0.383$), and as mentioned above, the hydrogen-induced martensite transformation occurred, therefore brought to the hardening in the second stage characterized by a larger slope in the hardness versus H/M ratio.

It should be mentioned that, according to the literature **[TR01]**, the hydrogen concentration for hydride formation in β-21S alloy is H/M = 0.67. In the present work, the maximum hydrogen concentration in β-21S alloy is about H/M = 0.460, i.e., well below the reported hydrogen concentration at which hydride formation takes place. **Figure 4. 8**b shows the microhardness profiles on the cross-section of hydrogenated β-21S alloys. The constant value of microhardness with the sample thickness indicates that, hydrogen is uniformly distributed throughout the sample. Nevertheless a minor increase in hardness at the surface is probably due to the presence of the oxidized layer formed during cooling process.

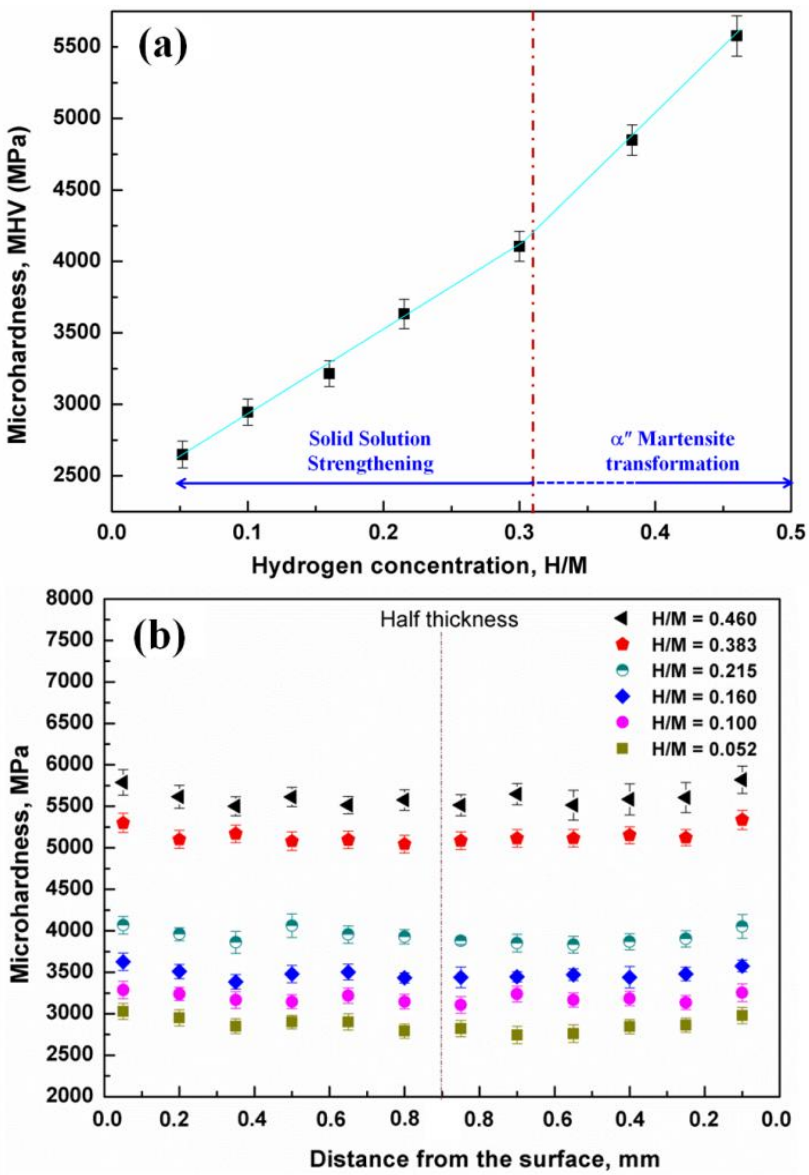

Figure 4. 8 Change of microhardness as hydrogen concentration in β-21S alloy

4.2.3.2 Hydrogen effects on tensile property

Tensile tests were performed to examine hydrogen effect on the tensile behavior of β-21S alloy. As shown in **Figure 4. 9**, the tensile properties (tensile strength and ultimate elongation) of specimen decreased with increasing hydrogen concentration. Compared to the as-received sample (H/M = 0.005), the tensile strength decreased by about 12% for the samples containing a hydrogen concentration H/M = 0.215, while the ultimate elongation decreased from 35% of the specimen with H/M = 0.005 to 4.8%. For each hydrogen concentration, the tensile tests were repeated twice. The reproductivity of the tensile properties is illustrated by the small dispersion of

the stress-strain curves obtained for the samples charged with H/M = 0.215 and given in the inserted chart in **Figure 4. 9**. It should be mentioned that, no stress-plateau in the tensile stress-strain curves was observed, indicating that there is no occurrence of stress-induced martensite transformation **[LX98, ME14, PK07 and PK08]** in β-21S alloy. These results further confirmed that, the observation of martensite α" phase in the hydrogenated β-21S alloy was induced by hydrogen addition, althrough the mechanism is still unclear.

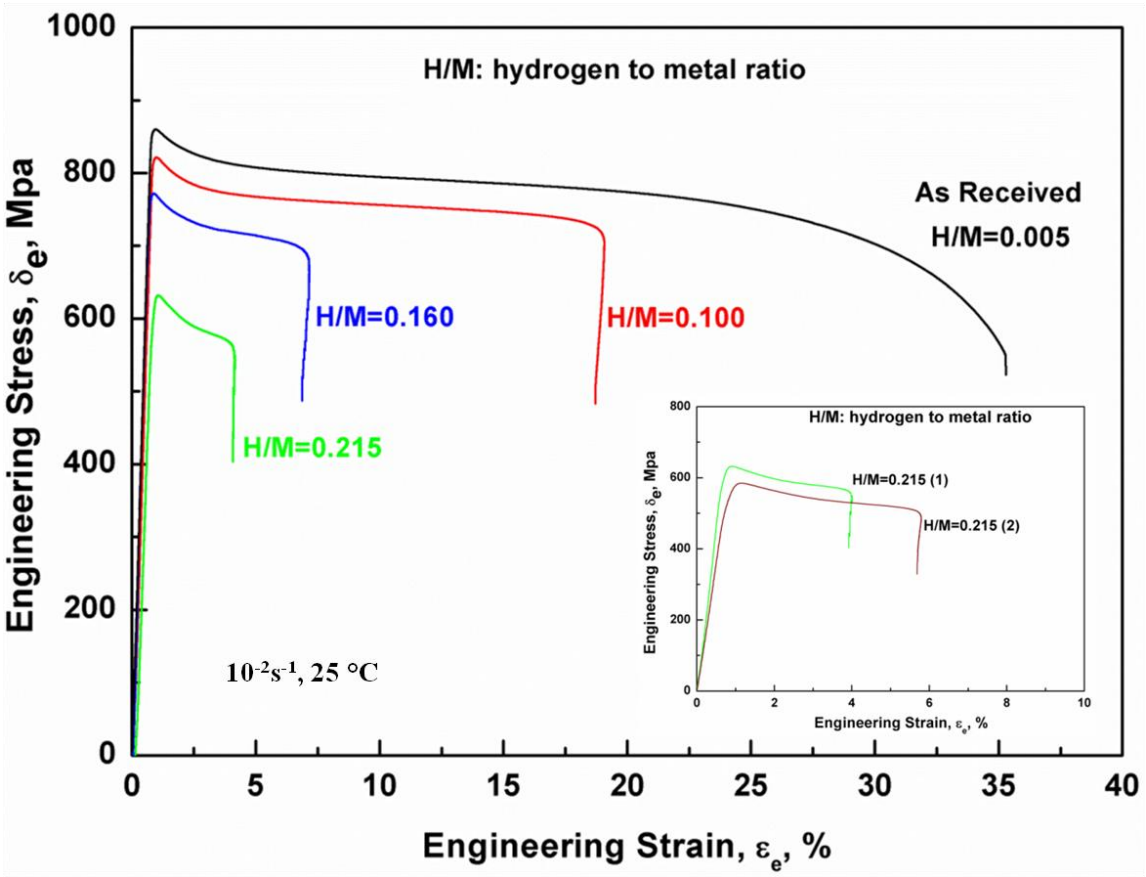

Figure 4. 9 Tensile curves of the hydrogenated β-21S alloys

Figure 4. 10 gives the variation of the tensile yield strength and ultimate elongation with the hydrogen concentration in β-21S alloys. The data from reference **[TR01]** is superimposed for comparison. As shown in **Figure 4. 10**a, the yield strength decreased with increasing hydrogen concentration. Compared to the data from the reference **[TR01]**, the yield strength in the current experiment showed an obviously decreasing trend with the increase of the hydrogen concentration. The decrease of yield strength in tensile test seems to be in contradiction with the increase of the microhardness shown in **Figure 4. 8**. However the microhardness test induced non-uniform deformation in the small volume of materials. The smaller volume of plastic

deformation might activate the different deformation mechanism than uniaxial tensile test. For example, no twinning could be detected in an investigation of nanoindentation in α-titanium **[ZY12]**. Though this study provides information at the grain level, complementary analyses would be required on the grain boundaries which are known to control the global mechanical properties.

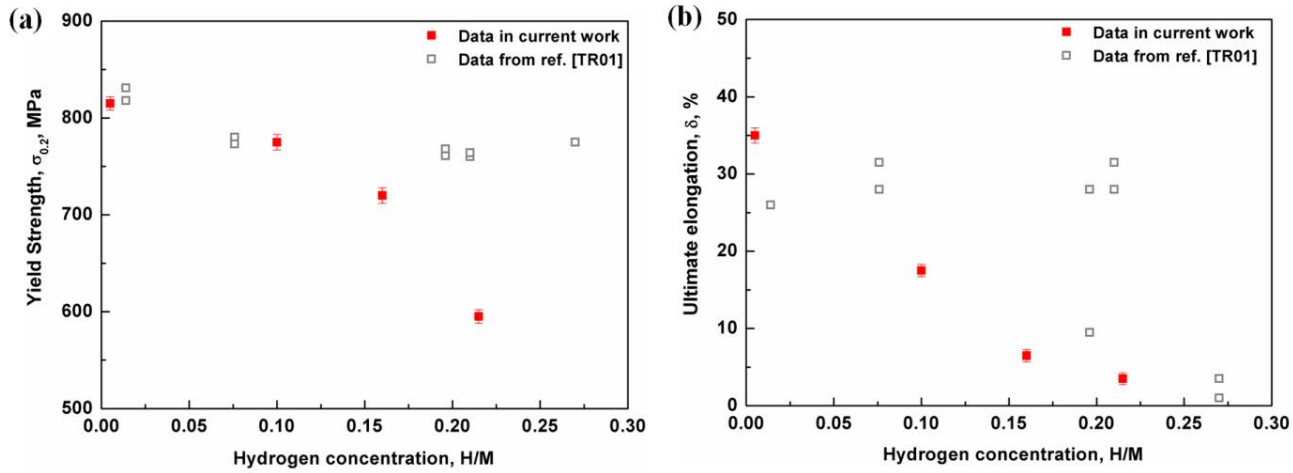

Figure 4. 10 The variation of tensile yield strength and ultimate elongation with hydrogen concentration in β-21S alloys (tha data in the current work is the mean value from the repeat experiments, the data from the reference is the individual value from the repeat experiments)

Figure 4. 10b shows the gradual decrease of the ultimate elongation with the increasing hydrogen concentration. In the case of data reported by Teter and coworkers **[TR01]**, the strain-to-failure was initially fairly constant as the hydrogen concentration increased but, from a critical hydrogen concentration, the strain-to-failure was reported to decrease abruptly to zero. Teter and coworkers attributed this behavior was attributed to the hydrogen-induced decohesion at the grain boundaries. The difference in the yield strength and the elongation between the current work and Teter and coworkers'work could be attributed to several factors such as the grain sizes, the sample sizes, and the strain rates. For example, the grain size of the β-21S alloy in the reference was about 25 μm smaller than that of the specimens used in the current work (with an average of 35 μm). Additionally, the strain rate for the current experiment was $10^{-2}\ s^{-1}$, i.e., much more larger than that in Teter and coworkers' work ($10^{-5}\ s^{-1}$). All these factors resulted in the different tensile behavior between the current experiments and the reference **[TR01].**

In the view of the microstructure, the specimens containing lower hydrogen concentration (H/M < 0.160) exhibit a ductile behavior characterized by coalescence of microvoids on the fracture

surface, as shown in **Figure 4. 11**a-c. In contrast, as the hydrogen concentration increased to H/M = 0.215, both the number and size of microvoid coalescences on the fracture suface decreased rapidly as shown in **Figure 4. 11**d, which is indicative of the marked reduction of the ductility. The obvious loss of ductility suggests that, for high hydrogen concentration, the solute hydrogen decreases the cohesive energy and, hence, the fracture stress of the lattice. There have been many variations on this suggestion, though no direct measurement of the change in cohesive energy due to hydrogen has been reported. Recently, ab initio calculations of the change in cohesive energy at a grain boundary in Ni due to hydrogen segregation have been made **[ZW00]**, suggesting that for high hydrogen concentration, hydrogen decreases significantly the metal-metal bonding. The observed results in the current work indicated that hydrogen had devastating effect on the tensile property of β-21S alloy.

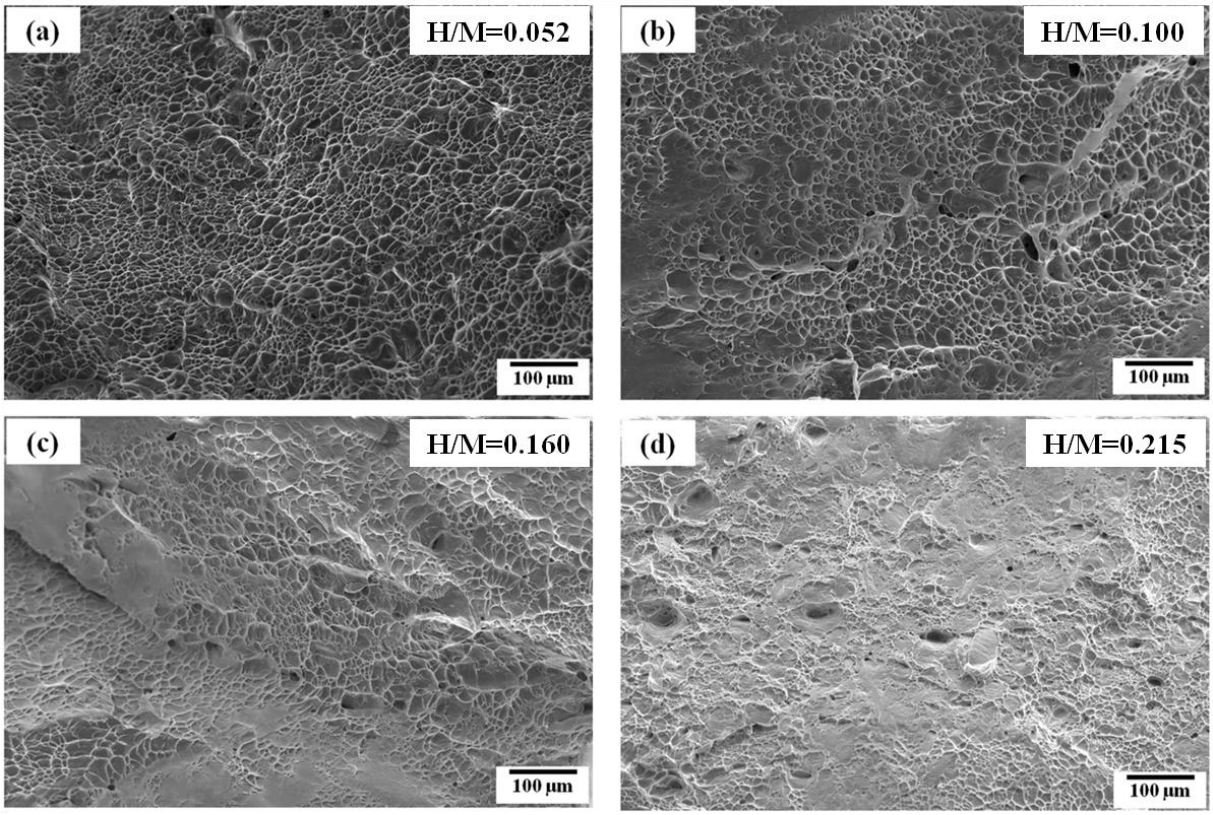

Figure 4. 11 SEM fractographs of the fracture surface of tensile specimens tested at 298 K. (a) H/M = 0.052, (b) H/M = 0.100, (c) H/M = 0.160 and (d) H/M = 0.215.

4.2.3.3 Hydrogen effects on compressive property

To complement the investigation by uniaxial tensile mode, compressive tests were carried out to inspect hydrogen effect on the mechanical behavior of β-21S alloy. In order to have a plane strain

condition, three plates were glued to each other layer by layer. The thickness of the glue was estimated to be less than 1 μm. Therefore, its effect on the compressive behavior of Ti50A can be neglected.The pre-hydrogenated samples were compressed to the strain up to a maximum of 27.5%. **Figure 4. 12** shows the compression curves of the hydrogenated β-21S alloys. The insert chart shows an example of the compression test performed twice for a hydrogen concentration of H/M = 0.100. The compression strength was found to fisrt decreased progressively as the H/M increased to pass through a maximum value for H/M = 0.160, before increasing and reaching a strength for H/M = 0.300 larger than the initial value, and eventually decreasing abruptly to almost zero at H/M = 0.383. **Figure 4. 12** also indicates that the Young's modulus tend to decrease drastically for H/M > 0.383.

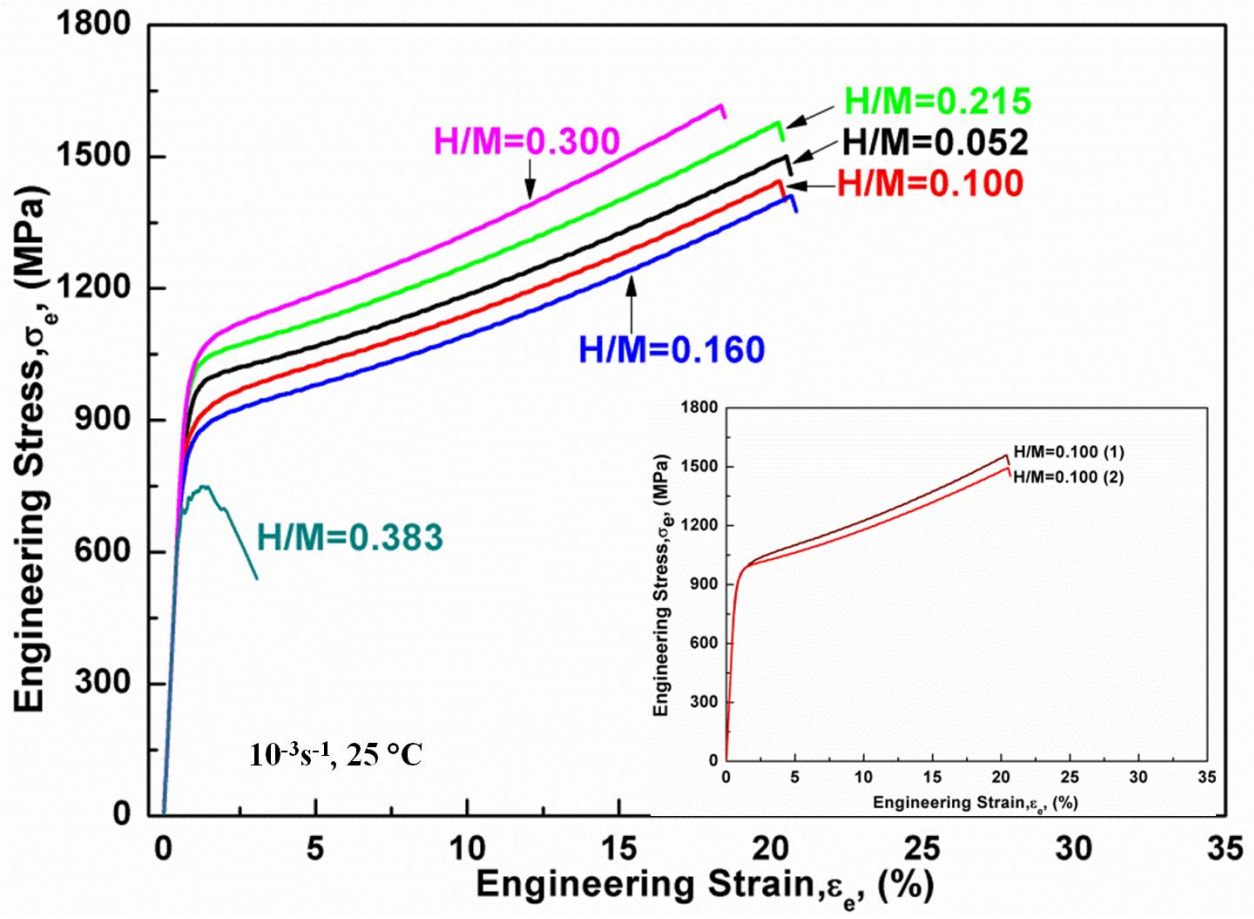

Figure 4. 12 Compressive curves of the hydrogenated β-21S alloys

The variations of the compressive and tensile yield strength as a function of hydrogen concentration in β-21S alloy are shown in **Figure 4. 13**. It can be seen that, hydrogen has distinct effect on the tensile and compressive properties of β-21S alloy. In the case of tensile test, the

gradual decrease in yield strength can be attributed to the combination of hydrogen-induced softening and hydrogen-induced decohesion. On the one hand, the required shear stress for dislocation slip can be reduced due to the hydrogen-enhanced dislocations mobility [**SR88, FR98**]. On the other hand, the lattice bonding can be weakened/reduced with the increase of hydrogen concentration, as previously mentioned **[ZW00, TR01]**. Additionally, tensile stress can accelerate the microcracks nucleation and propagation at grain boundaries and promote the intergranular fracture. Therefore, the hydrogen-induced fracture occurred easiler under the tensile stress.

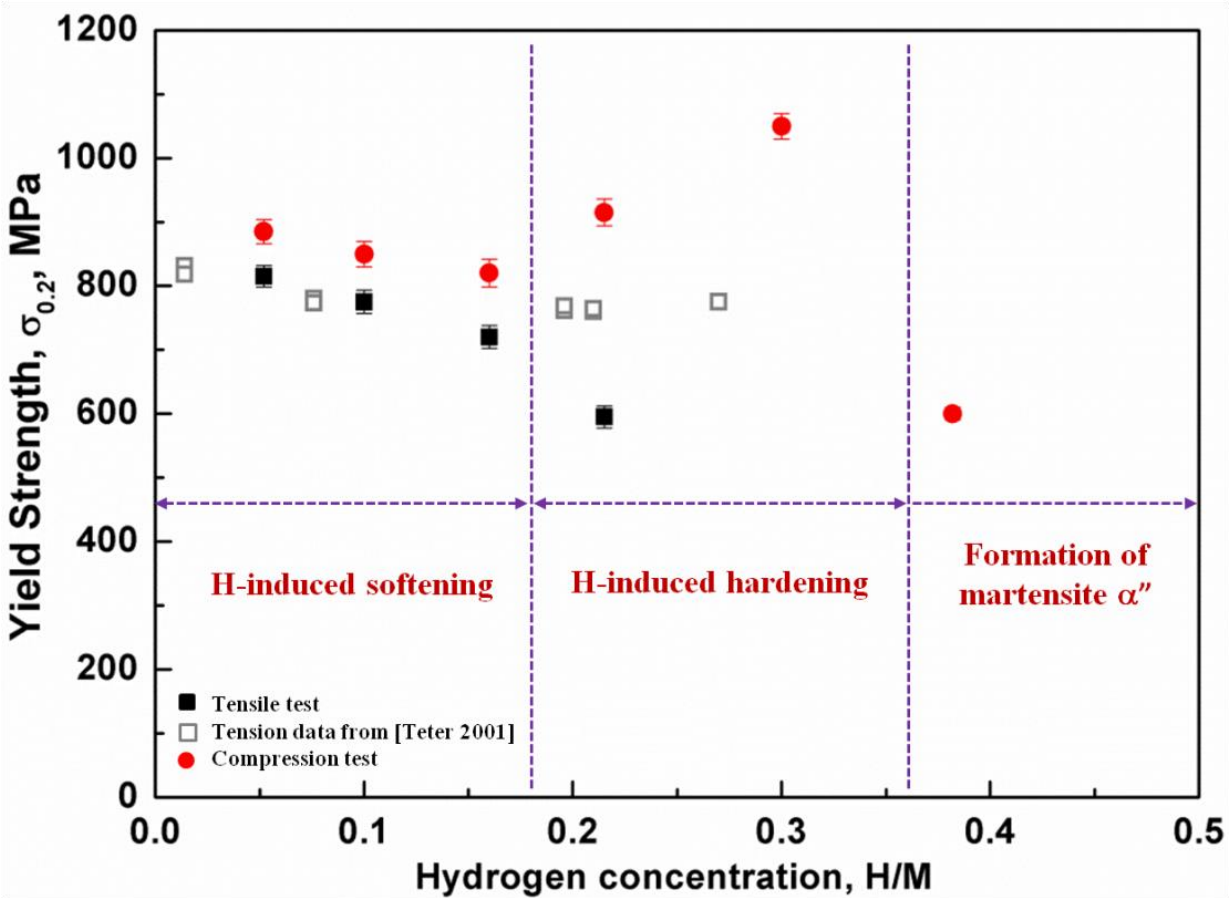

Figure 4. 13 Tensile and compressive yield strength as a function of hydrogen concentration

In contrast, the effect of hydrogen on the compressive behavior can be divided into three distinct stages depending on the hydrogen concentration, as indicated in **Figure 4. 13**. The first stage (H/M < 0.160) corresponds to a hydrogen induced-softening. The second stage (0.160 < H/M < 0.300) indicated the occurrence of hydrogen-induced hardening, in which the hydrogen-induced solid solution strengthening overwhelmed the hydrogen-induced softening. Microstructural

observations indicate that the grains were therefore less deformed as evidenced in **Figure 4. 14**d and e.

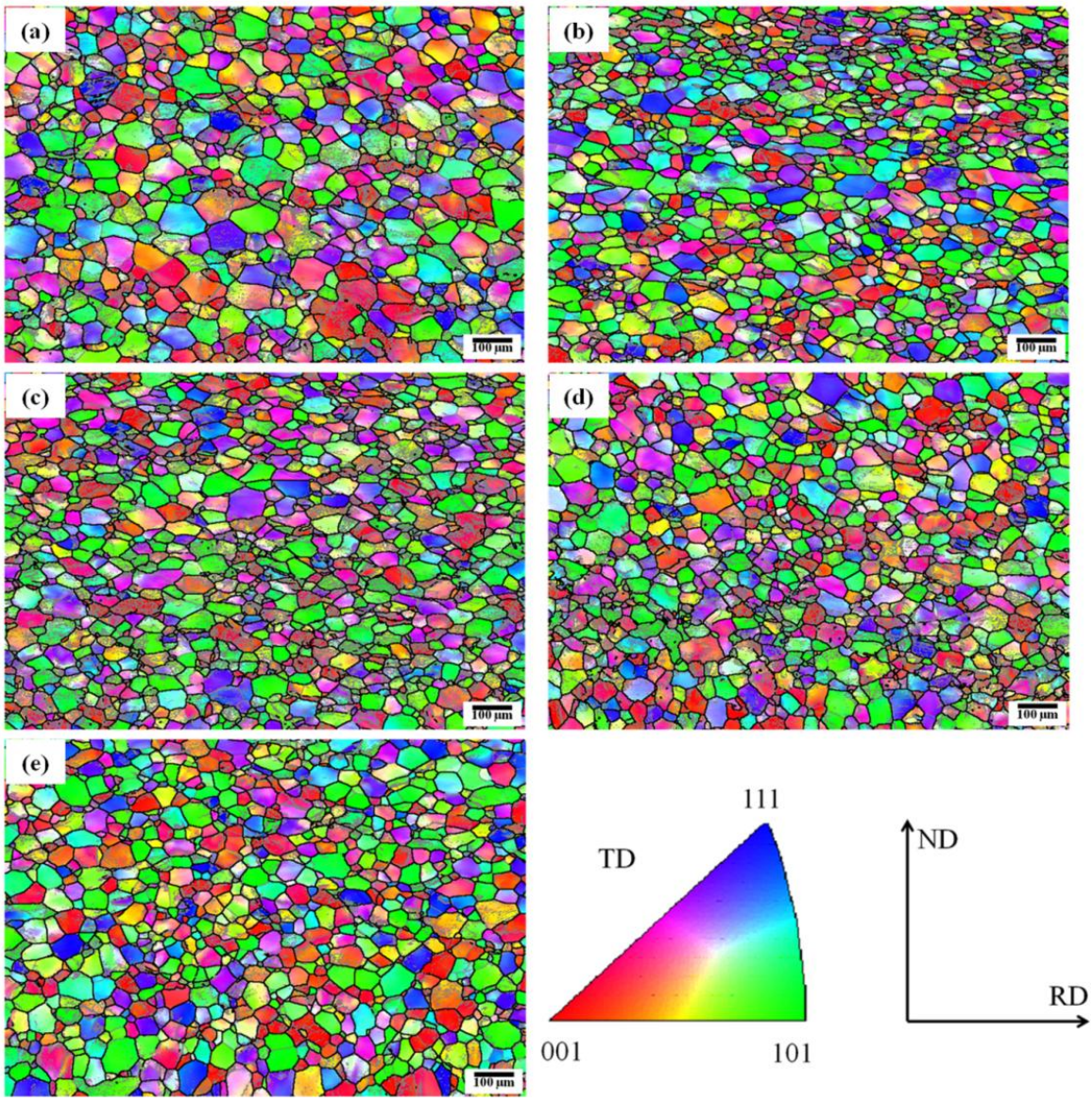

Figure 4. 14 IPF maps taken on the cross-section of the hydrogenated β-21S alloys under compression test: (a) H/M=0.052, (b) H/M=0.100, (c) H/M=0.160, (d) H/M=0.215 and (e) H/M=0.300.

This transition from softening to hardening with increasing hydrogen concentration can be explained by a change of the rate determining step as proposed by Kirchheim **[K12]**, in which the mobile hydrogen atoms will affect both kink formation and kink motion at screw dislocations. At a low hydrogen concentration (H/M < 0.160), the rate determining step is the formation of the kink pairs, in which the kink formation energy is reduced by hydrogen addition based on the defactant concept, therefore leading to a softening. While at a high hydrogen concentration

(0.160 < H/M < 0.300), the segregating of large amounts of hydrogen atoms to the kink pairs exerted an increasing solute drag on the moving kinks, therefore resulting in a hardening. The last stage (H/M > 0.300) exhibited an abrupt loss of yield strength due to the formation of martensite α"; the fracture surface of this sample exhibited a total brittle morphology as shown in **Figure 4. 15** (i.e., no observation of local plasticity) though reported beyond H/M = 0.27 by Teter and coworkers **[TR01]**. It should be noted that, this type of martensite α" is fairly hard (HV = 5177 MPa) but quite brittle as indicated by the compressive curve (no ductility).

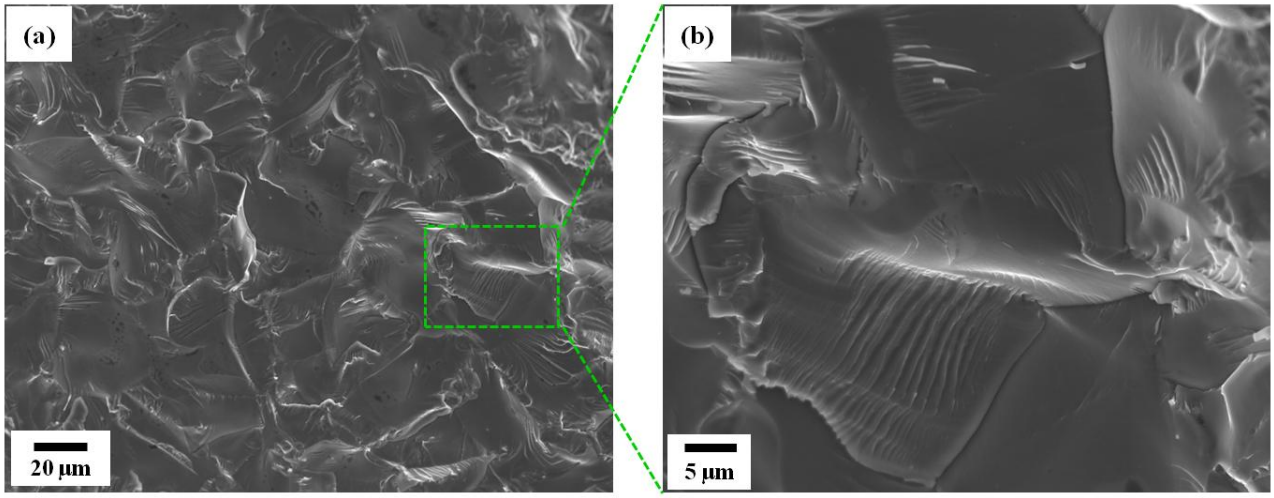

Figure 4. 15 SEM micrograph of the fracture surface of the compressed specimen having hydrogen concentration H/M = 0.383.

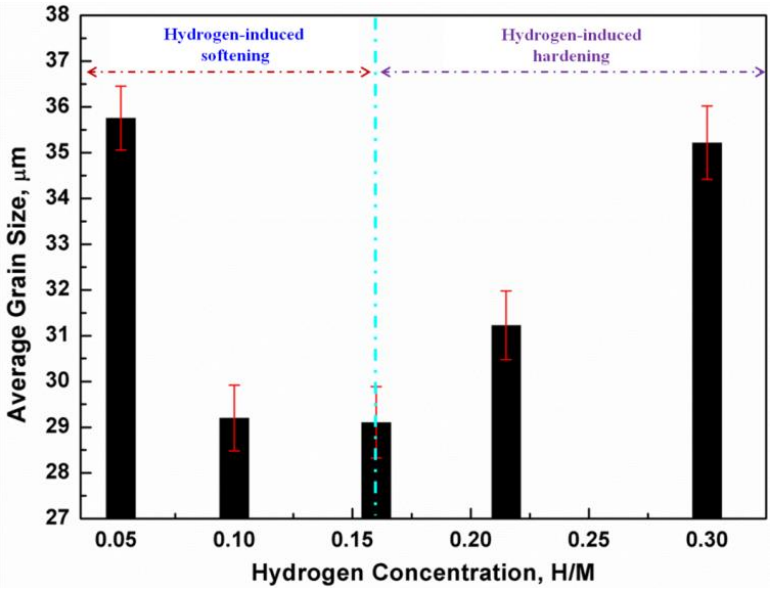

Figure 4. 16 Variation of grain size as hydrogen concentration in compressed β-21S alloys

The variation of the grain size with hydrogen concentration measured after compression tests is shown in **Figure 4. 16**. As observed, the grain size decreased as hydrogen concentration increased to H/M = 0.160, and then increased gradually. A thorough observation in the change of the microstructure in this hydrogen concentration range indicated a moderate decrease in the grain size as shown in the IPF maps in **Figure 4. 14**. However this moderate reduction in the grain size is not significant to result in strength hardening as usually explained by the Hall-Petch effect.

4.3 Conclusions

In this chapter, the hydrogen-induced microstructural evolution and its effects on the mechanical properties (hardness, tension and compression) of the β-21S alloy charged by gaseous method were thoroughly inspected using the measurements of XRD, SEM-EBSD and TEM. The main conclusions are summarized in the followings:

1. In the hydrogen concentration range 0.052 < H/M < 0.300, the microstructure consisting of the single β-phase showed that the dissolved hydrogen atoms expanded the BCC β-lattice and suppressed the decomposition of the β phase upon cooling. The relative change in the lattice parameter followed a linear relationship with the hydrogen concentration $[(a_H - a_o)/ a_o] = 3.06 \times 10^{-4} + 0.0508(H/M)$, showing that no hydrides were formed in this concentration range.

2. As the hydrogen concentration increased beyond H/M = 0.300, a martensite phase with plate-shape morphology was formed at the grain boundary and grew into the interior of the grains in β-21S alloy charged with H/M = 0.380. For further increase in the hydrogen concentration, i.e., H/M = 0.460, considerable amounts of plate-shape martensites were produced in the sample. These results suggested that a large concentration of hydrogen atoms weakened the interatomic bonds between the metallic atoms of the matrix, therefore brought to a large lattice shear causing the martensite transformation. Though the mechanism responsible for this martensite transformation is unclear, it is reasonable to assume that a large internal stress generated by the filling of the hydrogen atoms at the interstitial sites and the segregation of hydrogen atoms at grain boundaries, gives rise to the additional shuffling of titanium atoms in alternate $\{110\}_\beta$ planes, which result in the transformation into a C-centered orthorhombic crystal structure.

3. The effect of hydrogen on the microhardness revealed two stages of hardening mechanism in the β-21S alloy. In the hydrogen concentration range 0.052 < H/M < 0.300, the hydrogen-

induced solid solution hardening occurred. As the hydrogen concentration increased to H/M = 0.380, the hydrogen-induced martensite transformation occurred, therefore brought to the precipitation hardening in the second stage.

4. Tensile and compressive tests showed that hydrogen had dissimilar effect on the tensile and compressive properties of β-21S alloy. Under tension loading, the decrease of the yield strength with the increase of hydrogen concentration suggested that the addition of hydrogen atoms decreased the required stress for dislocations slip and the cohesion energy. In the case of compression test, the change of yield strength with hydrogen concentrations was divided into three distinct stages. In the first stage ($0.052 < H/M < 0.160$), the rate determining step is the formation of the kink pairs, in which the kink formation energy is reduced by hydrogen addition based on the defactant concept, therefore leading to a softening. In the second stage ($0.160 < H/M < 0.300$), the segregation of large amounts of hydrogen atoms to the kink pairs exerted an increasing solute drag on the moving kinks, therefore resulting in a hardening. In the last stage ($H/M > 0.380$), the abrupt loss of yield strength was associated with the formation of brittle martensite phase α".

Reference

[BE80] H.J. Bunge, C. Esling, J. Muller. The role of the inversion centre in texture analysis, J. Appl. Cryst. 13 (**1980)** 544-554.

[BE81] H.J. Bunge, C. Esling, J. Muller. The influence of crystal and sample symmetries on the orientation distribution function of the crystallites in polycrystalline materials, Acta Cryst. A 37 (**1981**) 889-899.

[CW87] J.E. Costa, J.C. Williams and A.W. Thompson, The effect of hydrogen on mechanical properties in Ti-10V-2Fe-3Al, Metall. Trans. A 18 (**1987**) 1421-1430.

[CZ16] W. Chen, J.Y. Zhang, S. Cao et al., Strong deformation anisotropies of ω-precipitates and strengthening mechanisms in Ti-10V-2Fe-3Al alloy micropillars: Precipitates shearing vs precipitates disordering, Acta Mater. 117 (**2016**) 68-80.

[FR98] P.J. Ferreira, I. M. Robertson and H.K. Birnbaum, Acta mater. 46 (**1998)** 1749.

[GM81] W.W. Gerberich, N.R Moody, C.L. Jensen and C. Heyman, in Hydrogen Effects in Metals. AIME, Warrendale, PA, **1981**, p. 731.

[I87] A.A. Ilyin, Phase and Structure Transformations in Titanium Alloys Alloyed with Hydrogen Ivestiya VUZ, Tsvetnaya Metallurgiya, 1(**1987**) 96-101.

[K01] E. Kunze, Korrosion und korrosionsschutz. 3th ed. Weinheim: Wiley-VCH Verlag; **2001.**

[K12] R. Kirchheim, Solid solution softening and hardening by mobile solute atoms with special focus on hydrogen, Scripta Mater. 67 (**2012**) 767-770.

[L81] J.F. Lynch, Acta metall. 29 (**1981**) 537.

[I94] A.A. Ilyin, Some Aspects of Interaction of Hydrogen with Metallic Materials, Izvestiya ANSSSR: Metally 5 (**1994**) 65-70.

[LN16] H.H. Liu, M. Niinomi, M. Nakai, K. Cho, Athermal and deformation-induced ω-phase transformation in biomedical beta-type alloy Ti-9Cr-0.2O, Acta Mater. 106 (**2016**) 162-170.

[LN17] H.H. Liu, M. Niinomi, M. Nakai, K. Cho, H. Fujii, Deformation-induced ω-phase transformation in a β-type titanium alloy during tensile deformation, Scripta Mater. 130 (**2017**) 27-31.

[LX98] Y. Liu, H. Xiang, J. Alloys. Compd. 270 (**1998**) 154-159

[MT04] Y. Mantani, Y. Takemoto, M. Hida, A. Sakakibara, M. Tajima, Phase transformation of α" martensite structure by aging in Ti-8 mass%Mo alloy, Mater. Trans. 45 (2004) 1629-1634.

[ME14] X. Min, S. Emura, K. Tsuchiya, T. Nishimura, K. Tsuzaki, Mater. Sci. Eng. A 590 (2014) 88-96.

[PK07] A. Paradkar, S. Kamat, A. Gogia, B. Kashyap, Mater. Sci. Eng. A 456 (**2007**) 292-299.

[PK08] A. Paradkar, S. Kamat, A. Gogia, B. Kashyap, Mater. Sci. Eng. A 487 (**2008**) 14-19.

[SC01] O.N. Senkov, B.C. Chakoumakos, J.J. Jonas, F.H. Froes. Effect of temperature and hydrogen concentration on the lattice parameter of beta titanium. Mater. Res. Bull. 36 (**2001**) 1431-40.

[SR88] D. S. Shih, I. M. Robertson and H.K. Birnbaum, Acta metall. 36 (**1988**) 111.

[TE07] E. Tal-Gutelmacher, D. Eliezer, Th. Boellinghaus, Investigation of hydrogen-deformation interactions in β-21S titanium alloy using thermal desorption spectroscopy, J. Alloys Compd. 440 (**2007**) 204-209.

[TR01] D.F. Teter, I.M. Robertson, H.K. Birnbaum, Acta Mater. 49 (**2001**) 4313.

[ZW00] L. Zhong, R. Wu, A.J. Freeman and G.B. Olson, Phys. Rev. B: Condens. Matter 62 (**2000**) 13938.

Chapter 5 Hydrogen effects on the behavior of cold rolling and recrystallization in Ti50A and β-21S alloy

5.1 Introduction

Since titanium has a high affinity for hydrogen, many works have been focused on the hydrogen-related degradation of mechanical properties. One interest aspect of using hydrogen as constituent element is that it could be removed from titanium and its alloys owing to the positive enthalpy of solution of Ti-H system at high temperature [W97, M51]. Recently, a new term "defactant" (defects acting agents) has been introduced [K09] to explain the mechanisms behind hydrogen embrittlement in Cu, Al, Ni et al., in which the defect formation energy was reduced by hydrogen addition [BV10].

On the other hand, experiments performed by Krystian et al. [KS10] have demonstrated that the formation of superabundant vacancies can be produced under high-pressure torsion in the presence of hydrogen. Also, Deutges and coworkers [DB15], who studied the effect of hydrogen on the density and arrangement of dislocations in cold-rolled palladium-hydrogen alloys, have reported that hydrogen can increase the dislocation density and lead to homogeneously distributed dislocations throughout the whole material.

Therefore, if hydrogen, initially dissolved as defactant into metals to facilitate the formation of vacancies, dislocations and stacking faults under cold deformation, is then subsequently removed by vacuum annealing, this will consequently enhanced the concomitantly properties such as hardness and strength. However, few studies have been focused on the effect of hydrogen on cold rolling and recrystallization behavior of titanium-based materials. Hence, this chapter aimed at providing a thorough description of the effect of hydrogen on the microstructural evolution during cold rolling and the subsequent annealing in α-titanium Ti50A and β-titanium β-21S alloy.

5.2 Results and discussion

5.2.1 Hydrogen effects on cold rolling behavior in Ti50A

In the following paragraph the variation of the microstructure during either 10% or 50% thickness reduction by symmetrical cold rolling will be firstly described for un-charged and hydrogen charged Ti50A. The attention has been particularly focused on the hydride-twinning interaction on function of the hydrogen concentration.

5.2.1.1 At low strain (ε_{eq} = 0.12)

Knowing that the electrolytic method resulted in an inhomogeneity of the hydrogen distribution in Ti50A sample, annealing treatment at 400 °C for 2 h was performed under inert atmosphere on the pre-hydrogenated Ti50A samples prior to cold rolling (see **Figure 3. 12**). Subsequently, normal symmetric rolling was employed to impose a small strain on the pre-hydrogenated Ti50A. Unidirectional multi-pass rolling was carried out using ~1% reduction of the thickness per pass. The total thickness reduction was about 10%, which corresponds to the equivalent von Mises strain ε_{eq} = 0.12. Then EBSD measurements were used to reveal the effect of hydrogen on twinning deformation in commercially pure titanium deformed by cold rolling.

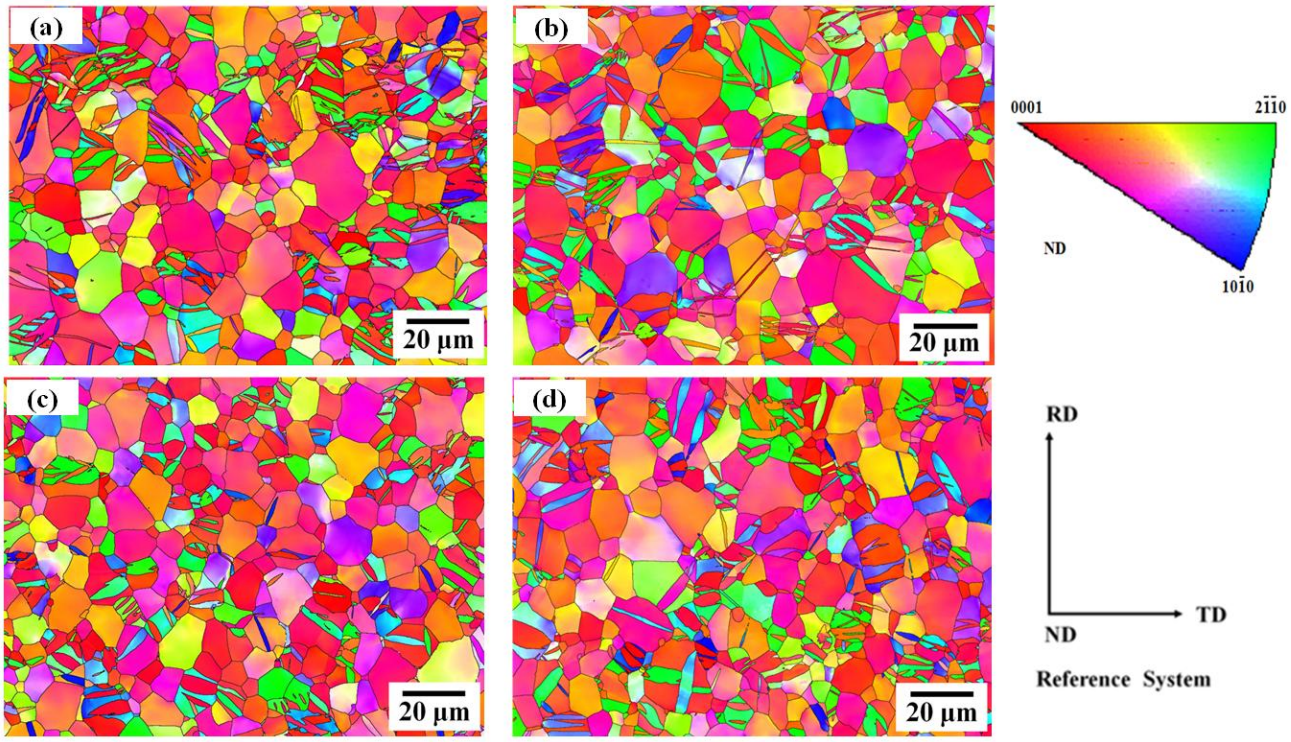

Figure 5. 1 IPF maps with the grain boundary for cold rolled Ti50A after 10% thickness reduction. (a) un-charged Ti50A; (b), (c) and (d) hydrogen charged for 72 h, 108 h and 168 h, respectively.

Considering the shear strain on the ND surface generated as a consequence of the friction between the rollers and the sample, mechanical and vibratory polishing were applied in order to eliminate the highly deformed and polluted surface. For that purpose, a layer of around 10 µm in thickness was removed before microstructural observations. The IPF maps taken on the rolling plane of cold rolled samples are shown in **Figure 5. 1**. The same color code to represent the orientation of the ND axis with respect to the crystal reference system was used as that in Chapter

3. A boundary misorientation of 15° was used to define the grain boundaries **[ZD11]**. Due to the experimental error in evaluating orientations by EBSD **[H99]**, grain-boundary misorientations below 2° were excluded from the data analysis.

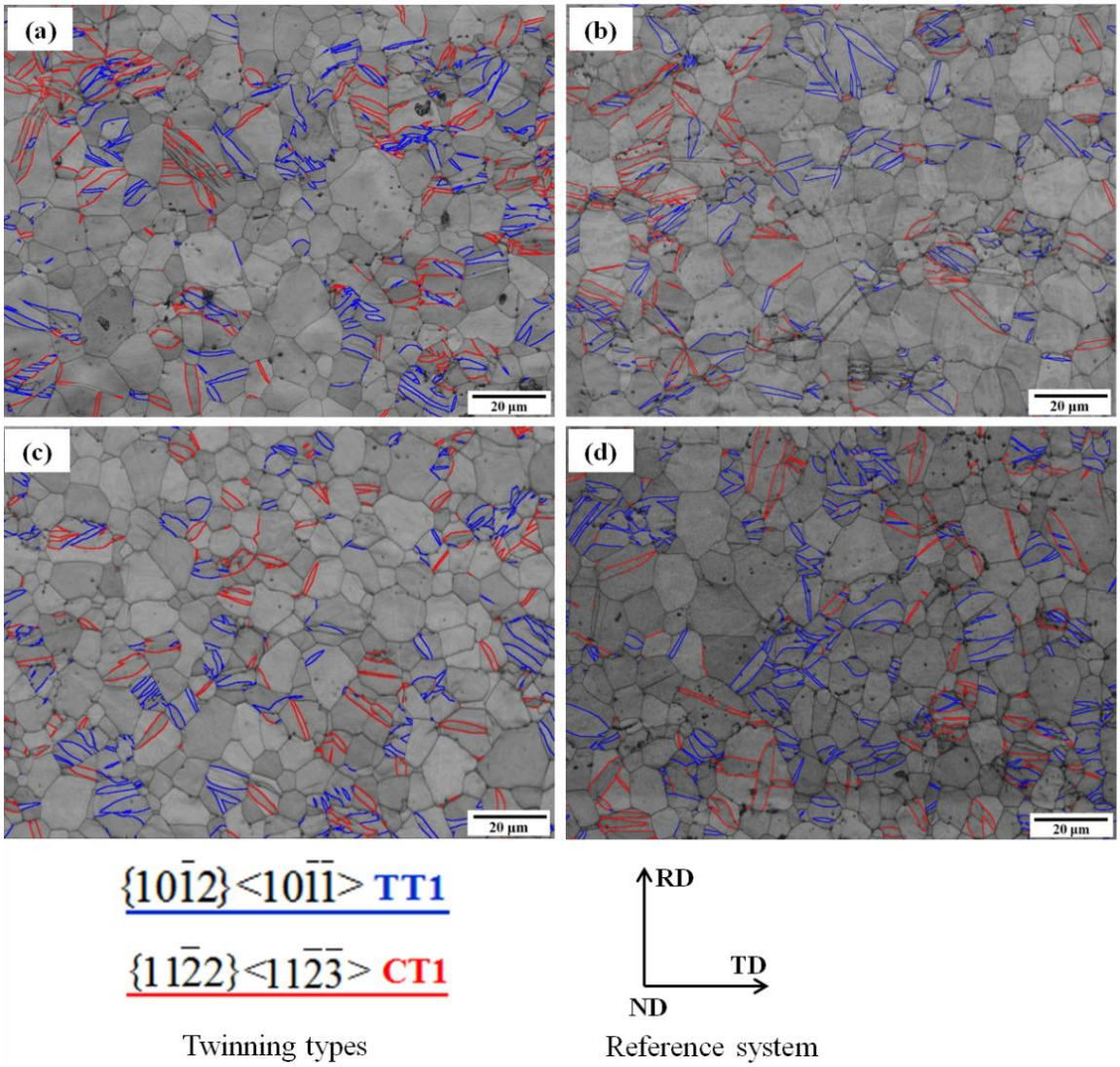

Figure 5. 2 BC maps of cold rolled Ti50A after 10% thickness reduction. (a) un-charged Ti50A; (b), (c) and (d) hydrogen charged for 72 h, 108 h and 168 h, respectively. (The red and blue color corresponding to the compressive twins CT1 and the tension twins TT1, respectively.)

As shown in **Figure 5. 1**, for a strain ε_{eq} = 0.12 applied to charged and un-charged Ti50A samples by cold rolling, a large number of twins were produced within the majority of α grains. According to an axis-angle relationship **[BC81]** for identifying twin boundaries in the EBSD map, the observed twinning systems in the present work are summarized in **Table 5. 1**.These twins are the most commonly observed twins in deformed α-titanium. As explained in Chapter 3, tension

twin relates to the aspect of introducing a positive strain along the c-axis of the parent grain and compression refers to a negative component along the c-axis [**Y81**]. **Figure 5. 2** shows the band contrast (BC) maps corresponding to IPF maps (**Figure 5. 1**) with the identified twin boundaries. The red color indicates the compression twin $\{11\bar{2}2\}<11\bar{2}\bar{3}>$ CT1, whereas the blue color corresponds to the $\{10\bar{1}2\}<\bar{1}011>$ TT1 tension twin, respectively. This analysis revealed an increasing number of TT1 tension twins in the microstructure of cold rolled Ti50A samples as the hydrogen charging time increased. It should be outlined that, when hydride plates are found parallel with the rolling direction (RD), the applied stress resulted in hydride fragmentation, causing weaker Kikuchi patterns of the hydride phase after cold rolling.

Table 5. 1 The frequently observed twinning systems in the present work

Twinning system	$\{10\bar{1}2\}<\bar{1}011>$	$\{11\bar{2}2\}<11\bar{2}\bar{3}>$
Name	Tension twin TT1	Compression twin CT1
Angle (°)	84.78	64.62
Axis	$<11\bar{2}0>$	$<10\bar{1}0>$

Table 5. 2 Number of twins detected by EBSD (from 4 maps) in the cold rolled samples

	Number of TT1	Number of CT1	Number of Detected Grains
AR - CR 10	495	520	2105
HC72 -CR 10	580	518	2068
HC108 - CR10	620	522	2056
HC168 - CR10	763	520	2062

The grain-to-grain misorientation distributions of the cold rolled samples at strain ε_{eq} = 0.12 are shown in **Figure 5. 3**. The green line in **Figure 5. 3**a is the random distribution (grain-to-grain) of misorientation angle expected for hexagonal structure without any texture **[M04]**. For a value of the equivalent applied strain ε_{eq} = 0.12, two obvious high-angle-boundary peaks corresponding to 65° and 85° were observed. Mirroring the twins observed in the BC maps (**Figure 5. 2**), these peaks can be associated with the CT1 compression twin $\{11\bar{2}2\}<11\bar{2}\bar{3}>$ and TT1 tension twin $\{10\bar{1}2\}<\bar{1}011>$ described in detail in Chapter 3**[BC81]**. Compared to CT1, an increasing number of TT1 twin boundaries is produced as the hydrogen charging time increased.

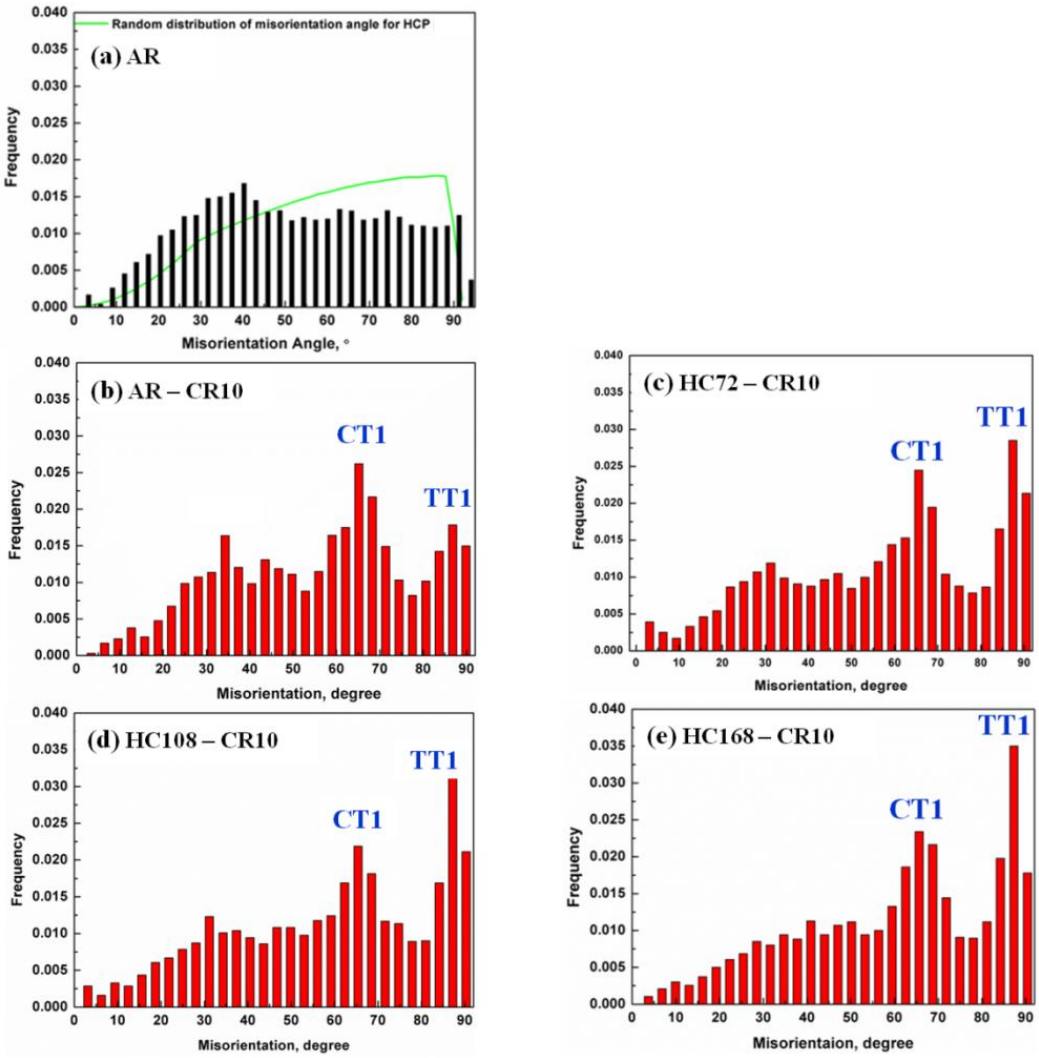

Figure 5. 3 The misorientation distributions (grain-to-grain) of samples (AR: as received, CR: cold rolling of 10% thickness reduction, HC + CR: cold rolled following hydrogenation for different times; TT1{$10\bar{1}2$}<$\bar{1}011$> and CT1{{$11\bar{2}2$}<$11\bar{2}\bar{3}$>.

Additionally, the number of twins detected by EBSD in the cold rolled samples is shown in **Table 5. 2.** Around 2000 grains measured from 4 maps were detected for each sample. From the data given in this table, the number of TT1 and CT1 twins per area as a function of the hydrogen concentration is shown in **Figure 5. 4**. As the hydrogen concentration increased, the TT1 twin shows an increasing frequency while that of the CT1 twin was kept almost constant. As it is well known, the interstitially dissolved hydrogen atoms are preferably trapped in areas of local stress concentrations, such as vacancies, dislocations, precipitations, phase and grain boundaries, which cause crystal lattice expansion as well as lattice distortion **[KK01, SC01].** For example, when hydrogen is present in pure α-titanium, it tends to increase the c/a ratio of the hcp lattice, leading

to the reduction of lattice shearing resistance **[SD96, CY05]**. Yoo **[Y81]** has demonstrated, in a study on the variation of the twinning shear with the axial ratio (c/a), that the increase in c/a ratio can reduce the twinning shear of tension twin TT1. With the increase of the c/a ratio, twinning becomes the main deformation mechanism in metals with hexagonal structure. Additionally, hydrogen atoms attracted by the stress field along dislocations can pin and hinter their sliding displacement. To accommodate tensile or compression strains along the c-axis of the hexagonal lattice, a larger number of deformation twinning must then be activated.

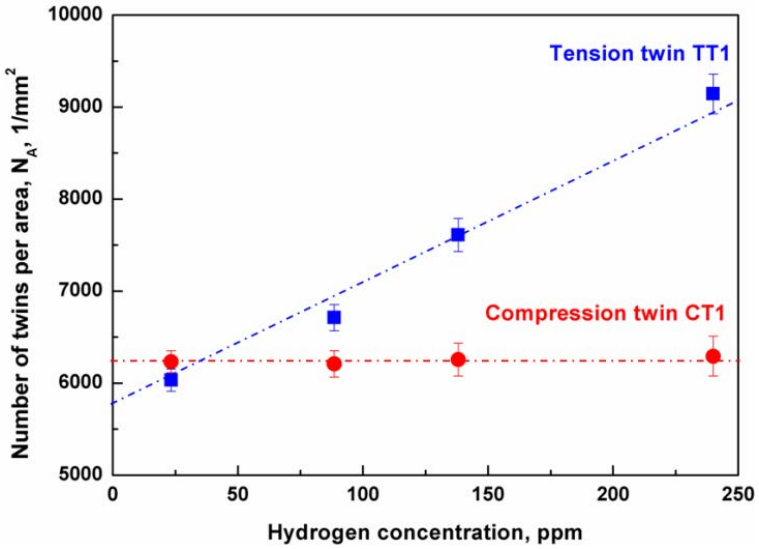

Figure 5. 4 Number fraction of twins as a function of hydrogen concentration.

It is well known that deformation twinning is characterized by significant rotations of the crystal lattice, corresponding to a cooperative movement of atoms by a fraction of the atomic spacing in an array **[CM95]**. To reveal the effect of grain orientations on twinning under cold rolling, the orientations of the parent grains in which the tension twin TT1 and the compression twin CT1 form are shown by the {0002} pole figure in **Figure 5. 5**. In those {0002} pole figures, the red and blue colors indicated the orientations of the parent grains where the CT1 twins and the TT1 twins form, respectively. As observed, the orientations of the parent grains generating the CT1 twins are characterized by the c-axis of the grains nearly parallel to the ND, while the orientations of the parent grains producing the TT1 twins tend to perpendicular to the ND. In the conventional rolling process, the state of the sample is considered to be nearly plane strain. Thus, the generation of these twins is facalitated by the external stress according to the orientations of the grains and the polar nature of twinning **[Y81, CM95, BD15]**. This implies that tension (compression) twinning is easily activated under compression (tension) perpendicular to the c-

axis of the crystal or tension (compression) along the c-axis. Though the location of the blue colored stars and red colored stars satisfied the grain orientation dependence, the green color in these figures outlines abnormal orientations of the parent grains in which tension twin unexpectedly formed. Though the exact mechanism need to be elucidated, recent works by Wang and Beyerlein and those by Britton and coworkers suggested that the activation of those tansile twins might be induced by the local stress **[WB12, BD15]**. For example, the molecular dynamics (MD) simulations of the dislocation reactions at tilt boundaries in Mg **[WB12]** successfully modeled the twin nucleation driven by local stress and dislocation reactions at grain boundaries.

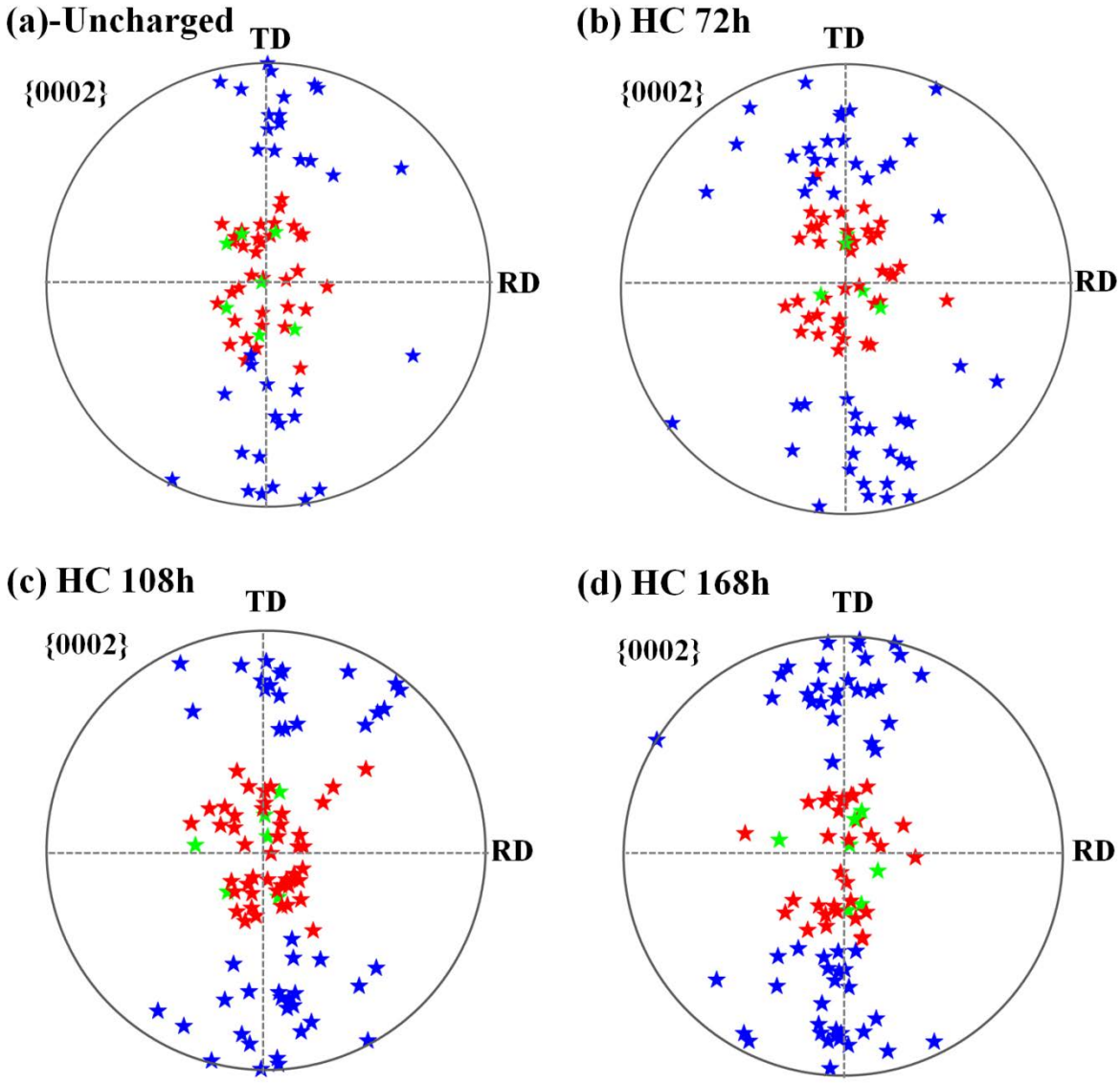

Figure 5. 5 {0002} pole figure of the parent grains forming the compression twin CT1 and tension twin TT1 after cold rolled to 10% thickness reduction. (a) un-charged Ti50A; (b), (c) and (d) hydrogen charged for 72 h, 108 h and 168 h, respectively. (The red and blue colors indicating the normal orientation of the parent grains generating the CT1 twins and the TT1 twins, respectively.

The green color corresponding to the abnormal orientation of the parent grains producing the TT1 twins.)

The influence of hydrogen on twinning was further investigated by EBSD analyses performed on the cross-section of the cold rolled Ti50A after 168 h hydrogen charging by electrolytic method. For that particular purpose, the EBSD analysis was realized on the un-charged and hydrogenated regions of the same sample after 10% thickness reduction (ε_{eq}= 0.12) by cold rolling.

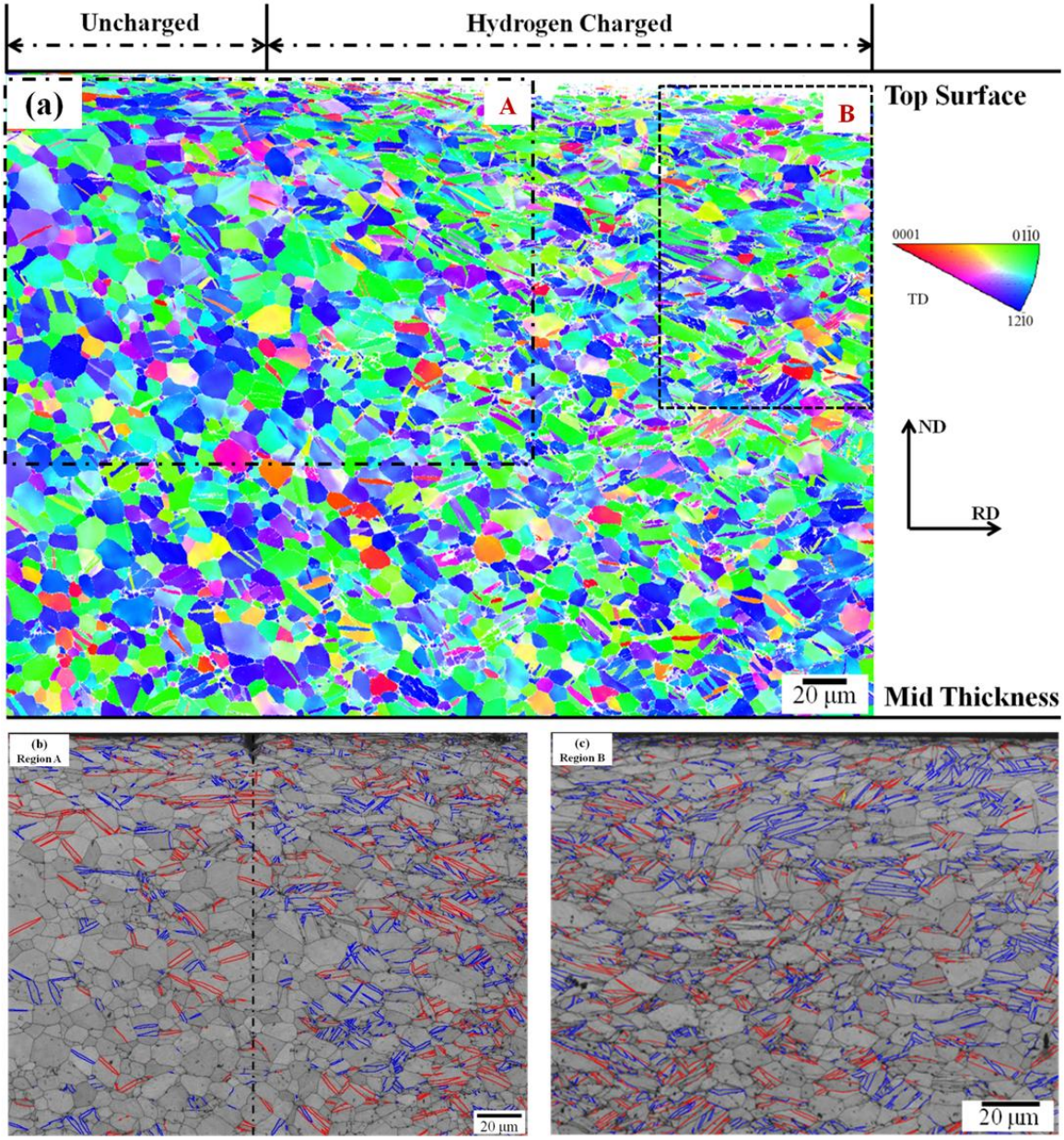

Figure 5. 6 IPF maps taken on the cross-section of cold rolled (ε_{eq} = 0.12) Ti50A consisted of the non-hydrogenated and hydrogenated regions (a) and BC maps with twin boundaries (b) and (c) corresponding to the selected region A and B, respectively. (the red and blue green

colors indicating the compression twin CT1 $\{11\bar{2}2\}<11\bar{2}\bar{3}>$ and tension twins TT1$\{10\bar{1}2\}<\bar{1}011>$ respectively.)

As shown in **Figure 5. 6**a, the IPF map was taken from the TD plane containing the RD and the ND. The EBSD detected region is from the top surface to the mid-thickness of the cold rolled sample. After 10% thickness reduction by cold rolling, the pre-charged region exhibits much more twins than that of the uncharged. Meanwhile, an obvious refinement of the microstructure was observed in the hydrogen charged region. This is because, when a twin forms within a grain, it divides the initial grain into three domains, and thus inevitably changes the dimension of the grain. The twin can be regarded as a new grain with its own dimension and crystallographic orientation. Therefore, microstructure refinement occurs through deformation twinning. **Figure 5. 6b** and **c** (BC maps with the twin boundaries) corresponds to the selected regions A and B in **Figure 5. 6**a. Region A is the transition zone between the un-charged and the charged regions. Compared to the transition region, an increasing number of the TT1 twins formed in the full-charged region. The probable reason for this phenomenon can be credited to the existence of the residual stresses generated by the hydride formation in the subsurface layer. As reported by Feaugas et al. [**FC09, GF01**], the phase transformation from α-titanium to the hydrides resulted in an approximately 15% volume expansion, inducing thus a high level of local stresses.

Although the precise mechanisms of twinning are less well understood than for slip-based deformation mechanism, the formation of twinning can be divided into the following steps: incubation, nucleation, propagation and growth. The incubation is the process of accumulation of enough stress within the material large enough to generate a twin nucleus, often through stresses of piled-up dislocations resulting in slip-stimulated mechanisms **[YM11, BC09, BE09, WY11]**. Such process provides a heterogeneous twin nucleation mechanism that requires a significantly lower of stress in comparison to the homogeneous route found in nearly perfect single crystals **[CM95]**. Once a sufficient level of stress is present on the active twinning system, the twin may nucleate through the generation of one, or several, so-called 'twinning dislocations' that contain not only the traditional slip-like Burgers vector but also a twinning step, as it was proposed by Wang and coworkers **[WH09].** Therefore, the results described above suggested that the formation of tension twin $\{10\bar{1}2\}<\bar{1}011>$ can be facilitated due to the increase of c/a ratio owing to the hydrogen addition and the existence of local stress generated by the hydrides precipitation.

5.2.1.2 At medium strain (ε_{eq}=0.80)

Cold rolling process was also performed on the pre-hydrogenated Ti50A-H as well as the as-received Ti50A for a larger level of equivalent strain (ε_{eq}=0.80), corresponding to 50% thickness reduction. The XRD patterns of cold rolled samples are shown in **Figure 5. 7**, and those of the un-deformed samples have been plotted for comparison. A broadening of the diffraction peaks appeared for both the α and hydride phases after cold rolled to 50% thickness reduction by cold rolling, indicating that an heterogeneous internal strain was produced within the specimens.

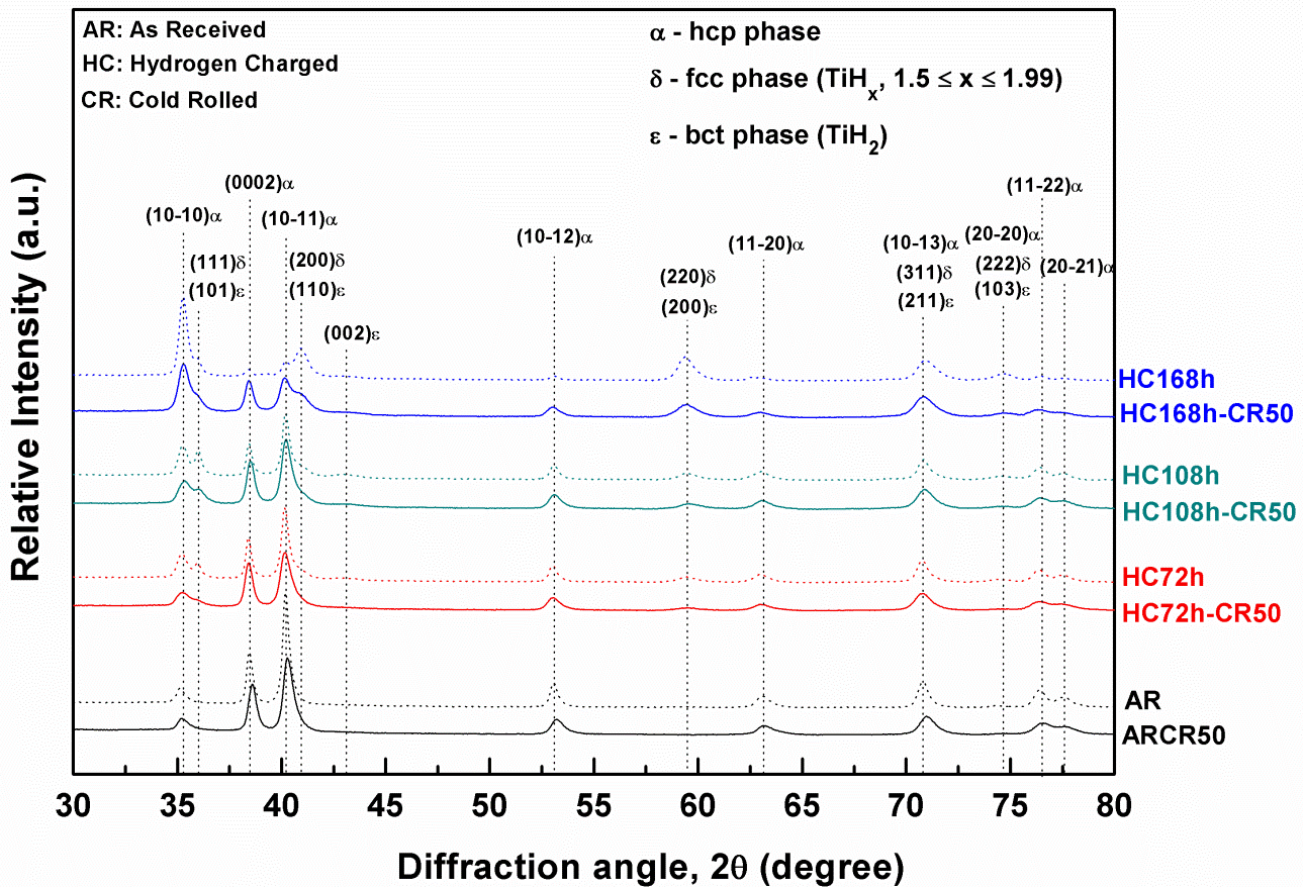

Figure 5. 7 XRD patterns of the as-received Ti50A and hydrogenated Ti50A-H before and after cold rolling of 50% thickness reduction.

To follow the evolution of microstructure under cold rolling, EBSD analyses were conducted on the as-rolled sample containing the un-charged and the charged (hydrogen charged for 168 h) regions, respectively. **Figure 5. 8** shows the IPF and BC maps obtained by EBSD in the rolling plane on the near surface region of sheets. After 50% thickness reduction, the microstructure consisted of a mixture of elongated grains, twins and low angle boundaries (blue lines). The presence of hydrogen/hydride leads to the c-axis <0001> become parallel to the ND, as compared

with the un-charged Ti50A (**Figure 5. 8a and c)**. Moreover, the hydrogenated Ti50A-H (**Figure 5. 8d**) exhibited a marked refinement of the microstructure with the average grain size of 1.1 ± 0.1 μm. It should be mentioned that, after cold rolling to 50% thickness reduction, the applied stresses resulted in a total hydride fragmentation, causing very weak Kikuchi patterns for identification of the hydride phase by EBSD.

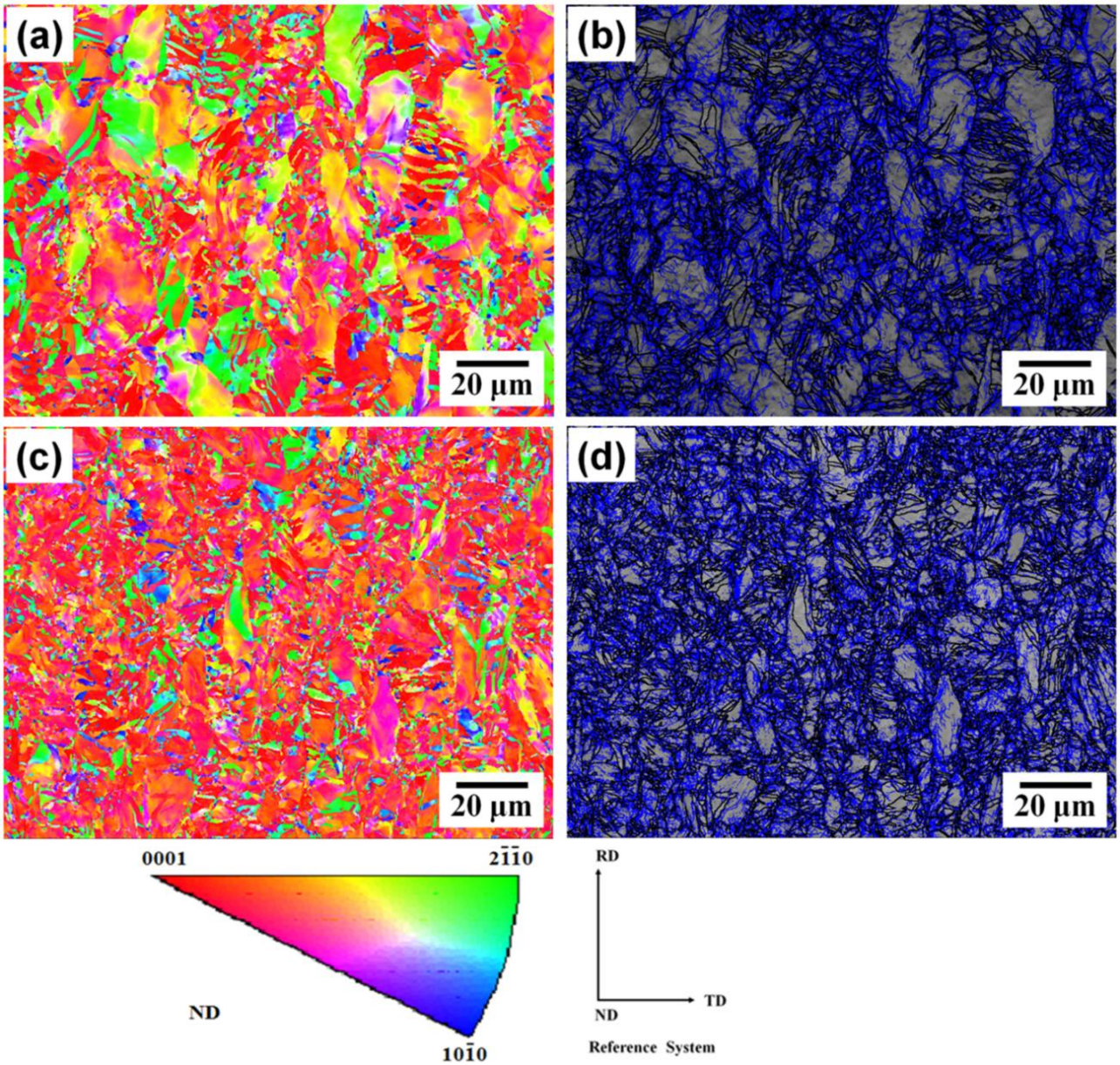

Figure 5. 8 IPF and BC maps taken on the rolling plane of cold rolled Ti50A after 50% thickness reduction. (a), (b) un-charged Ti50A and (c), (d) hydrogen charged for 168 h; (The HABs and LABs indicated by the black and blue lines, respectively).

In order to examine the occurrence of any restoration process, the misorientation between each pair of neighboring grains was calculated. **Figure 5. 9** presents the misorientation distribution of the first neighbors for un-charged Ti50A as well as that for the 168 h hydrogenated sample after 50% thickness reduction. Thorough observations of **Figure 5. 8b and d** revealed a considerable amount of LABs produced during 50% thickness reduction by cold rolling in both hydride-free and hydrogenated samples. These features associated to dislocation substructures are characterized by values of the misorientation angles lower than 15° **[ZD11]** in **Figure 5. 9**b and c.

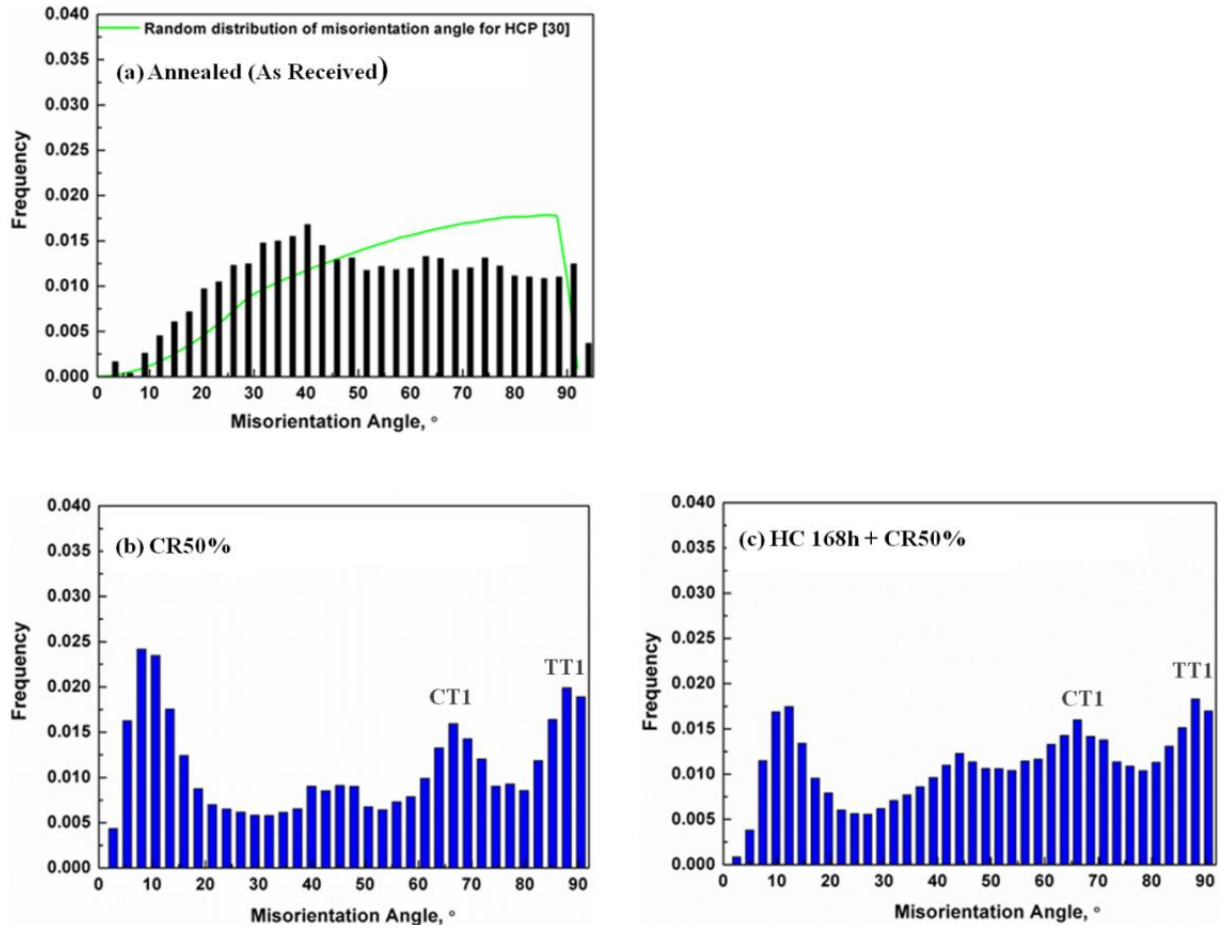

Figure 5. 9 The misorientation distributions (grain-to-grain) of samples (AR: as received, CR 50: cold rolled to 50% thickness reduction, HC 168 h: hydrogen charged for 168 h; (tension twin TT1$\{10\bar{1}2\}\langle\bar{1}011\rangle$ and compression twin CT1 $\{11\bar{2}2\}\langle11\bar{2}\bar{3}\rangle$)

If the boundaries associated with the twin-matrix interfaces evolved with continued straining into arbitrary HABs as a result of twin/dislocation interactions **[SM10, SK03]**, the dislocation substructure evolved as a result of the classical dynamical recovery during which dislocation multiplication should be mitigated by the dislocation annihilation and the formation of sub-boundaries. Consequently, after the exhaustion of twinning, the rate of increase of the dislocation

density with the applied mechanical straining might be expected to be close to that in the material deforming solely by dislocation slip mechanism but with a higher initial dislocation density. Compared to the uncharged Ti50A, an increase in the number of HABs was observed in hydrogenated samples as shown in **Figure 5. 9c**. As it is well documented, see for example Apps et al. work **[AB03]**, new HABs can be rapidly generated around the fine second-phase at relatively low strains. In as-rolled sample, the new HABs could be generated due to the strain incompatibility between the α-titanium matrix and the hydride phases. Therefore, the initial scale of the grain subdivision process could be refined resulting from the original and new high angle boundaries rotating. **Table 5. 3** gives the average grain size for each of the samples as calculated from these images by the ATOM software. The results indicated that the decrease in the grain size of the hydrogenated samples can be attributed to the deformation heterogeneity induced by the presence of hydrides in the hexagonal grains.

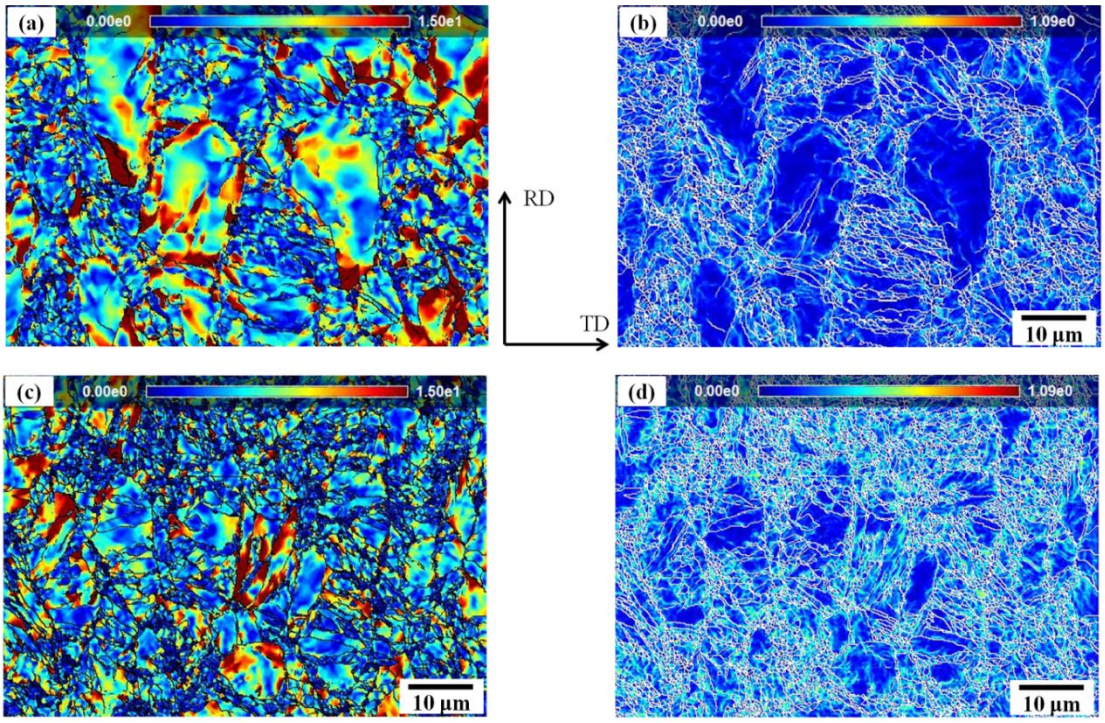

Figure 5. 10 Internal misorientation and GNDs maps taken from the samples after cold rolled to 50% thickness reduction. (a), (c) un-charged Ti50A and (b), (d) hydrogen charged for 168 h.

Hexagonal structures are well known for their anisotropic properties **[GW10, N53]** with easy <a> prismatic and basal slip systems but harder <c+a> pyramidal slip systems. The existence of grains with hard and soft orientations in Ti and other hexagonal metals leads to heterogeneity in the stress and strain distributions at the microstructural length scale. This results in relative large

strain gradients, which require the accumulation of high density of geometrically necessary dislocations (GNDs) during deformation **[YC10]**. On the other hand, in the presence of non-deformable hydrides (when the thickness of hydrides is larger than 500 nm according to Chaper 3), a strain incompatibility can be expected between both the hydride and α phase. This can be accommodated, as first proposed by Ashby **[A70]**, by the generation of GND at the interface of hydride/matrix. Hence, the evolution of internal strain is intimately related to the formation of specific arrays of GNDs. In the present work, the local strain gradient is represented by the internal misorientation due to the lattice curvature within the grain. **Figure 5. 10**a and c show the internal misorientation maps measured in 50 % cold rolled sample, which are corresponding to the IPF maps in **Figure 5. 8**a and c. The color scheme indicates the range of misorientation angle from 0 to 15°. As observed in the maps, there exists a large strain gradient from the centre of grain-to-grain boundary. The average values of internal misorientation reported in **Table 5. 3** revealed higher values for the hydrogenated samples, which can be interpreted from the larger strain gradient induced by hydrogen/hydride.

Table 5. 3 Average values of the grain size, the internal misorientation angle and the norm of geometrically necessary dislocations (GND).

	AR	CR50	HC168 + CR50
Average Grain Size, [μm]	12.0 ± 0.8	2.0 ± 0.2	1.1 ± 0.1
Norm of GND, [μm-1]	0.007 ± 0.002	0.175 ± 0.003	0.224 ± 0.003
Average Internal Misorientation angle, [°]	0.34 ± 0.19	1.50 ± 0.23	2.64 ± 0.20

***AR: As-received Ti50A; CR 50: cold rolled to 50% thickness reduction;**

***HC: hydrogen charged for 168 h.**

On the basis of Nye's theory describing the lattice curvatures induced by dislocations **[N53]**, Pantleon **[P08]** developed a method to obtain five components of the Nye's tensor, α**,** from 2D-orientation maps. From those five components, the norm of GND, a reasonable estimate of dislocation density, can be calculated and the results obtained with ATOM software are presented in **Figure 5. 10**b and d. The color scheme indicates the norm of GND ($\rho_{GND} = \sqrt{\alpha_{ij}\alpha_{ij}}$) in the range of 0 to 1.09. We can see that GNDs are not homogeneous distributed throughout the sample and that most of the GND are particularly piled up at the boundaries. Compared to the un-charged Ti50A (**Figure 5. 10b**), the pre-charged Ti50A (**Figure 5. 10d**) shows an increase in the

GND content after 50% thickness reduction ratio by cold rolling processing. It should be mentioned that the maps show only a subset of the total available data; in total, between 80 and 150 grains were mapped for each sample. The statistical data on the average norm of GND is given in **Table 5. 3**

Hydrogen-enhanced dislocation mobility was reported by Robertson and co-workers in a series of transmission electron microscope (TEM) studies performed on several metals, including α titanium **[RB86, RR90 and SR88]**. As pointed out above, there exist two states of hydrogen in the hydrogenated sample: the quasi-mobile hydrogen at solid solution and the bonded hydrogen in the forms of hydrides. Therefore, the density and distribution of dislocations generated during plastic deformation can be changed in the presence of hydrogen. On the other hand, hydrogen transported by dislocations has been confirmed by numerous experimental and simulation studies **[TT76, FL86, IJ97, MR11, NS12 and DM15]**. The dislocation transport models yield much faster diffusion rates than lattice diffusion, and they support the idea that dislocations can carry hydrogen deep into the specimen bulk or ahead of the plastic zone even at ambient temperature. Associated with these models **[TT76, MR11, DM15]** is the proposition that a local hydrogen supersaturation develop through stripping of the solutes off the moving dislocations by traps. Moreover, it has been demonstrated that hydrogen can reduce the required stress for the onset of plasticity, i.e., homogeneous dislocation nucleation owing to a reduction in the shear modulus, dislocation line energy and stacking fault energy **[BV10]**. Therefore, the results described in this study suggest that hydrogen/hydride can promote the formation of the geometrically necessary dislocations upon cold rolling in commercial pure titanium. From the data giving in **Table 5. 3**, the norm of GNDs (ρ_{GND}) seems to be correlated with the grain size **[KZ15]**. The norm of GNDs increased with the decrease of the grain size, which is in agreement with Littlewood and coworkers' suggestion that the increased amount of GNDs in smaller grains is possibly due to their pile-up near grain boundaries **[LW12]**.

It is well known that, during deformation the orientation of the individual grains of a polycrystalline metal change relative to the directions of the applied stress. These changes are not random and involve rotations, which are directly related to the crystallography of the deformation. As a consequence the grains acquire a preferred orientation referred as texture, which becomes stronger as deformation proceeds. In this chapter, the influence of hydrogen/hydride on the texture evolution upon cold rolling in α-titanium Ti50A was described based on an EBSD

investigation. **Figure 5. 11** shows the {0002} and {10-10} pole figures of the cold rolled Ti50A, the evolution of the overall texture was typical of the cold rolled CP-Ti sheet **[CY05]**. In the case of the specimen without hydrogenation (**Figure 5. 11a**), the {0002} pole figure consisted primarily of a split-TD basal texture component with a maximum intensity occurring at ± 30° from the ND toward the TD; weak components were located approximately 80-90° from the ND to the TD. In the {10-10} pole figure, the maximum intensity was located at the RD. Such pole figures are typical for the hot rolled titanium sheet products **[Z74]**.

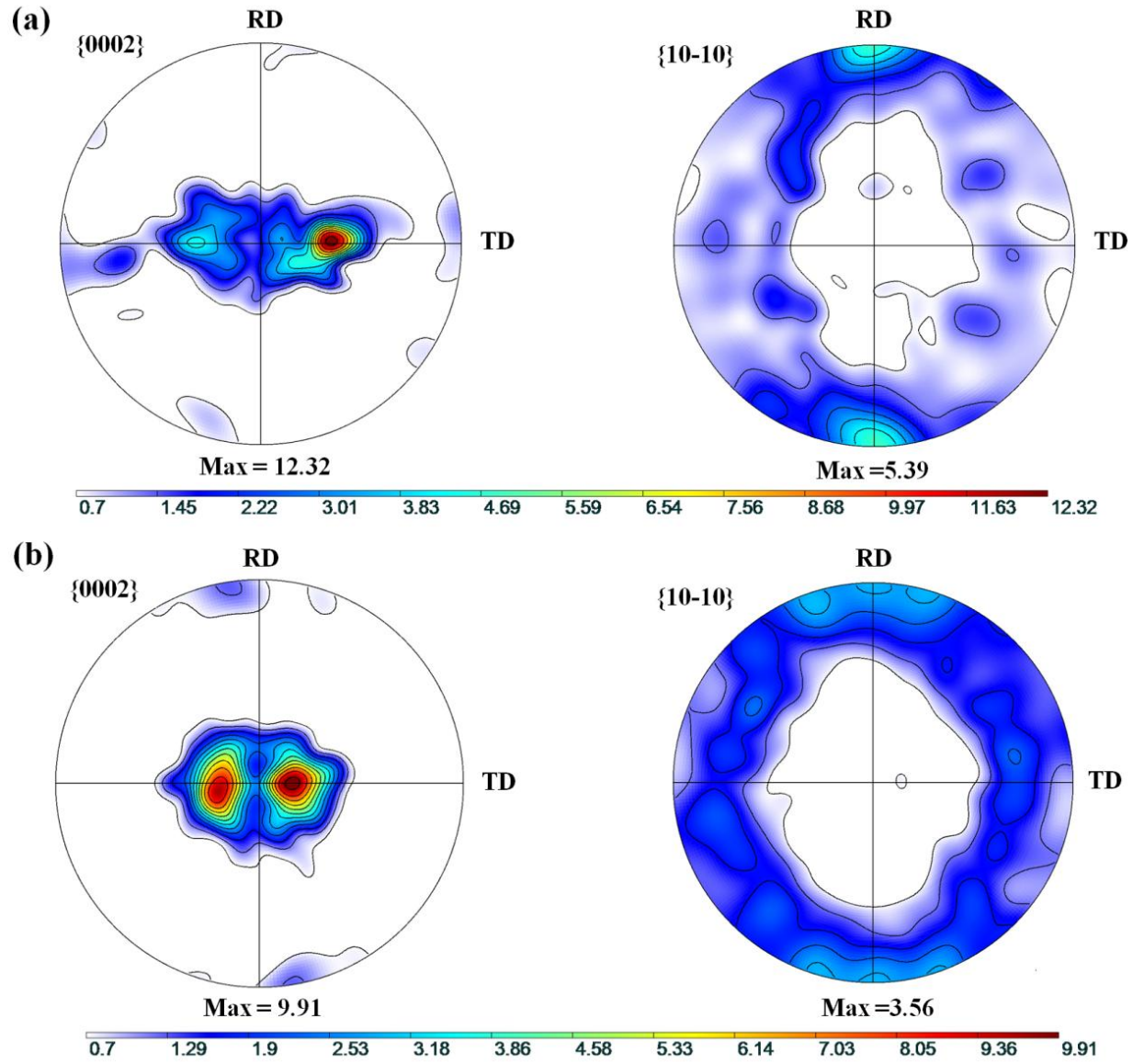

Figure 5. 11 Pole figures of cold rolled samples after 50% thickness reduction, (a) un-charged Ti50A and (b) hydrogen charged for 168 h.

As for the pre-charged Ti50A, a similar texture component was developed during cold rolling, as shown in **Figure 5. 11b**. The {0002} pole figure was characterized by a TD-split basal texture; however, the basal pole was tilted at a lower inclination angle of ± 20° from the ND toward the TD. Moreover, the texture components for the hydrogen charged Ti50A were sharper as compared to the un-charged sample. While, the maximum intensity was seen to weaken in the presence of hydrogen/hydride, from 12.32 (relative unit) of the un-charged sample to 9.91 (relative unit) of that with hydrogenation. Therefore, the results described above indicates that, the presence of hydrogen/hydride has a relative impact on grain/subgrain rotation during cold rolling, resulting in the c-axis becoming parallel to the ND.

5.2.2 Hydrogen effects on cold rolling behavior in β-21S alloy

As mentioned above, if hydrogen atoms are dissolved as a defactant into β-21S alloy to facilitate the multiplication of dislocations upon cold rolling, and then removed from the specimen by the vacuum annealing treatment, the dislocations density, and the concomitantly properties such as hardness/strength would be increased. Following this assumption, the β-21S alloy containing different hydrogen concentration was rolled to 50% thickness reduction ratio at room temperature, as described in Chapter 2.

5.2.2.1 Hydrogen effects on microstructural evolution under cold rolling ($\varepsilon_{eq} = 0.80$)

It was found that, in the hydrogen concentration range 0.052 ≤ H/M ≤ 0.160, the pre-hydrogenated β-21S alloys can be extensively rolled to 50% thickness reduction without any noticeable structural damage on the sample surface.

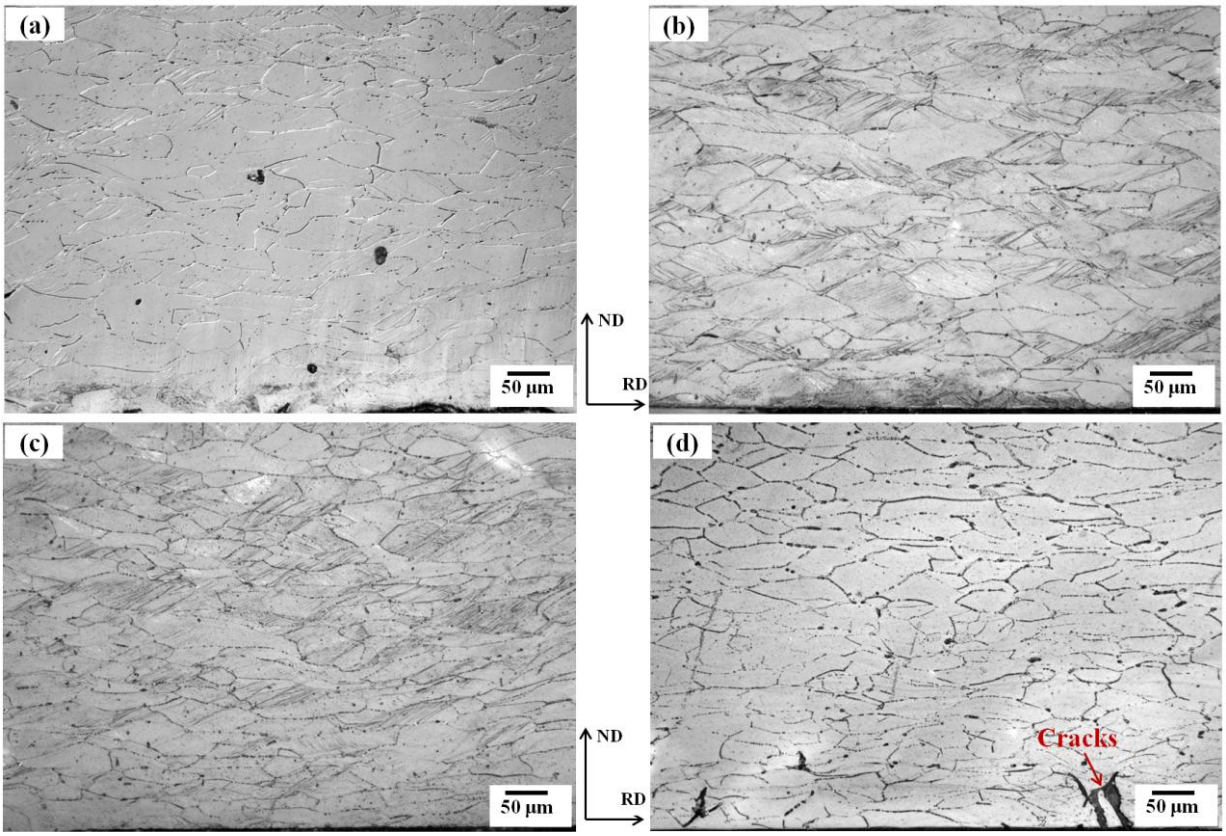

Figure 5. 12 Optical micrographs taken on the cross section of β-21S alloys after cold rolled to 50% thickness reduction, (a) H/M = 0.052, (b) H/M = 0.100, (c) H/M = 0.160 and (d) H/M = 0.215.

A typical example demonstrating the good cold-workability of hydrogenated β-21S alloy is shown in **Figure 5. 12**. Optical micrographs were taken on the cross section of cold rolled β-21S

alloys with hydrogen concentration H/M = 0.052 (**Figure 5. 12**a), H/M = 0.100 (**Figure 5. 12**b), H/M = 0.160 (**Figure 5. 12**c) and H/M = 0.215 (**Figure 5. 12**d), respectively. Under the symmetric-rolling condition, the samples are compressed in the ND and stretched in the RD. Therefore, the original equiaxed β grains became elongated along the RD after cold rolled to 50% thickness reduction. Additionally, deformation bands can be clearly observed in the samples with hydrogen concentrations H/M = 0.100 and H/M = 0.160. No shear band can be noticed, indicating that there is no severe shear deformation occurred. Nevertheless, several cracks were observed in the sample with the hydrogen concentration H/M = 0.215, as shown in **Figure 5. 12**d. This may be related to the hydrogen-induced decohesion as reported by Robertson **[TR01].**

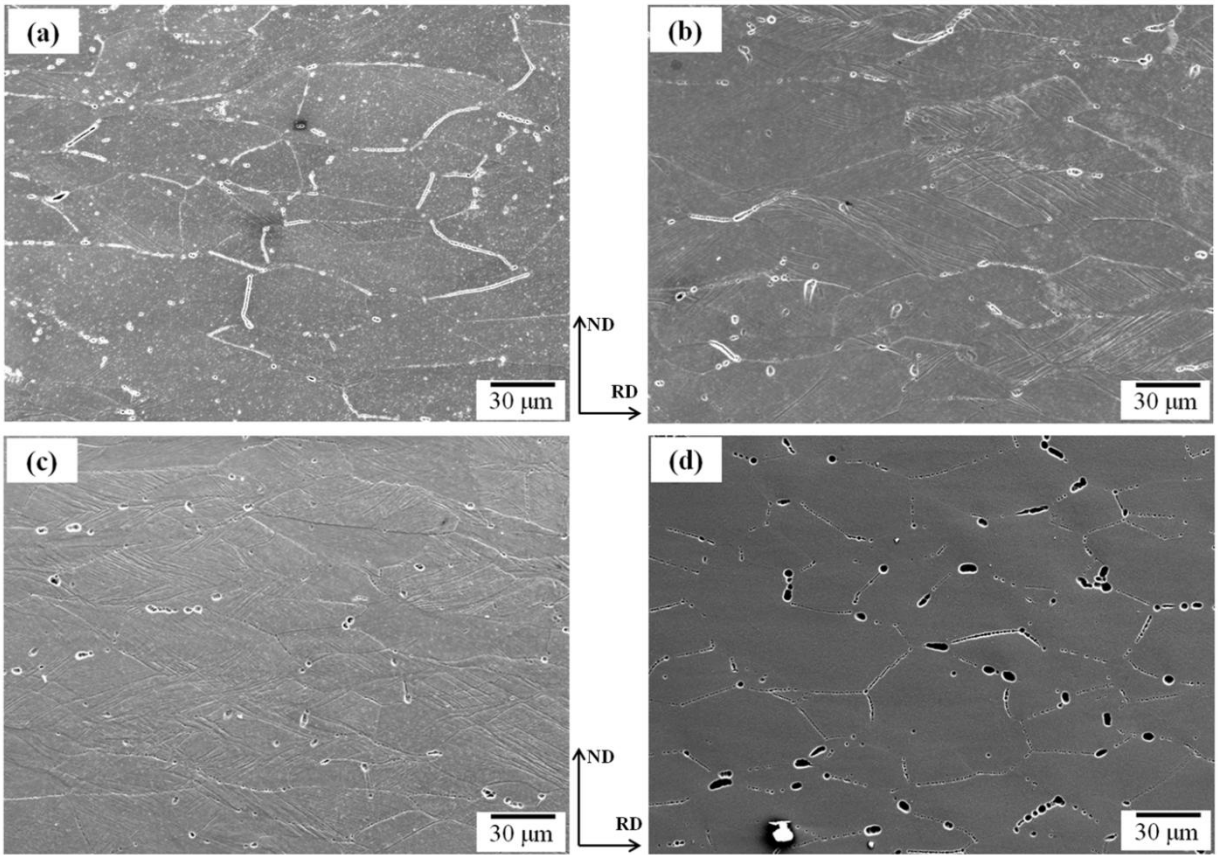

Figure 5. 13 SEM micrographs taken on the cross section (RD-ND) of β-21S alloys after cold rolled to 50% thickness reduction, (a) H/M = 0052, (b) H/M = 0.100, (c) H/M = 0.160 and (d) H/M = 0.215.

To further inspect the combined effects of hydrogen and cold rolling on the microstructural evolution in β-21S alloys, SEM analysis was conducted on the cross-section (RD-ND) of cold-rolled samples. As well known, though slip in bcc structure deformed at room temperature may occur on any of the {110}, {112} or {123} planes, it only takes place along the <111> close packed directions. A consequence of the slip occurring on these three possible different planes

along a common <111> direction is the wavy nature of the slip process called pencil glide which has been observed on the pre-polished surfaces of deformed specimens, as shown in **Figure 5. 13**. As the hydrogen concentration increased till H/M = 0.160 (**Figure 5. 13**a-c), a surprising observation was the increasing number slip bands/lines emergence on the surface of deformed samples. This is consistent with the fact that hydrogen in solid solution promotes planar glide and localization of plasticity in slip bands **[RM12, AO10, YS10 and AS12]**. However such lines were not clearly visible at the surface of samples with hydrogen concentration H/M = 0.215 as shown in **Figure 5. 13**d, suggesting a different mode of deformation. Though less slip bands/lines could be detected in the grains, a large number of etching-induced holes appeared at the surface of the rolled sample. To elucidate such surprising observation, EBSD was employed to better understand the dependence of cold rolling bahavior of β-21S alloy with the variation of hydrogen concentration.

Considering the shear strain on the surface generated by the friction between the rollers and the sample, the EBSD detected areas were selected on the middle region of the TD plane containing the RD and the ND. **Figure 5. 14** shows the IPF maps with HABs and LABs for the cold rolled β-21S alloys. In comparison to the un-deformed sample (**Figure 5. 14**a), the grains, after cold rolling to 50% thickness reduction, became elongated along the rolling direction, and low angle boundaries appeared in the interior of the deformed grains. In the hydrogen concentration range 0.052 < H/M < 0.160, an increasing number of low angle boundaries accompanying the grain subdivision were produced as the hydrogen concentration increased, as shown in **Figure 5. 14**b-d. Indeed, a series of in-situ TEM observations have demonstrated that hydrogen can enhance the dislocation mobility, and a theory referred as hydrogen-enhanced localized plasticity (HELP) has been proposed **[FR98, BA12, KD12, DK13 and CD02]**. However, as the hydrogen concentration increased till H/M = 0.215, the number of low angle boundaries decreased and the grains became less elongated (**Figure 5. 14**e). This observation is in contradiction with the theory of hydrogen-enhanced localized plasticity. Therefore, these observations combined with the compression data presented in Chapter 4 suggest that hydrogen has contradictory effects on the cold rolling behavior of β-21S alloy depending on the hydrogen concentration. As proposed by Kirchheim **[K12]**, the mobile hydrogen atoms have an impact on both kink formation and kink motion. For a low hydrogen concentration (H/M < 0.160), the rate determining step is the formation of the kink pairs at screw dislocations, in which the kink formation energy is reduced by hydrogen addition

based on the defactant concept, therefore leading to a softening. While at a high hydrogen concentration (0.160 < H/M < 0.300), the segregating of large amounts of hydrogen atoms to the kink pairs exerted an increasing solute drag on the moving kinks, therefore resulting in a hardening.

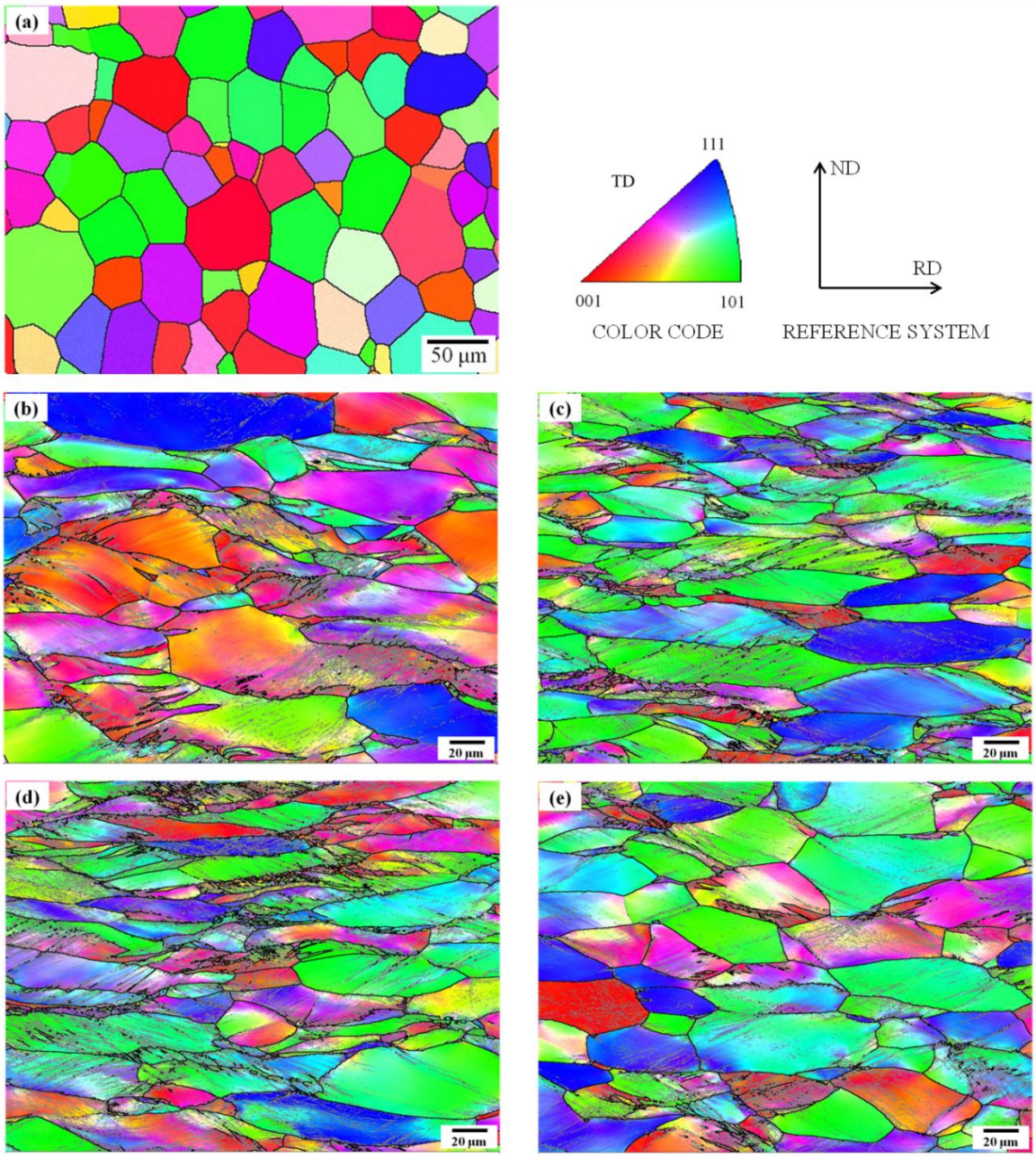

Figure 5. 14 IPF maps with the high angle boundaries (HABs) and the low angle boundaries (LABs) taken on the TD plane of cold rolled samples. (a) the un-deformed β-21S, (b) H/M = 0.052, (c) H/M = 0.100, (d) H/M = 0.160 and (e) H/M = 0.215. (HABs and LABs indicated by the black and grey colors, respectively).

5.2.2.2 Effect of hydrogen on dislocations density and arrangement upon cold rolling

In the current work, XRD measurement was employed to inspect the effect of hydrogen on dislocation density in the cold rolled β-21S alloys. The XRD spectra shown in **Figure 5. 15** consist of only the bcc β-phase suggesting that no transformation take place during cold rolling, even stress-induced phase transformation. Only a slight shift of the diffraction peaks towards higher angles indicates that the crystal lattice was under an internal compressive state of strain. In addition, an obvious peak broadening appeared after cold rolling to 50% thickness reduction. Generally, the peak broadening arises from two sources: instrument contribution and sample contribution. The normal way to measure the sample broadening contribution is to first determine the broadening of the instrument (β_{inst}) using a near-perfect sample whose broadening contribution is negligible, and then repeat the measurement with the desired sample to determine the total broadening, β_{total}.

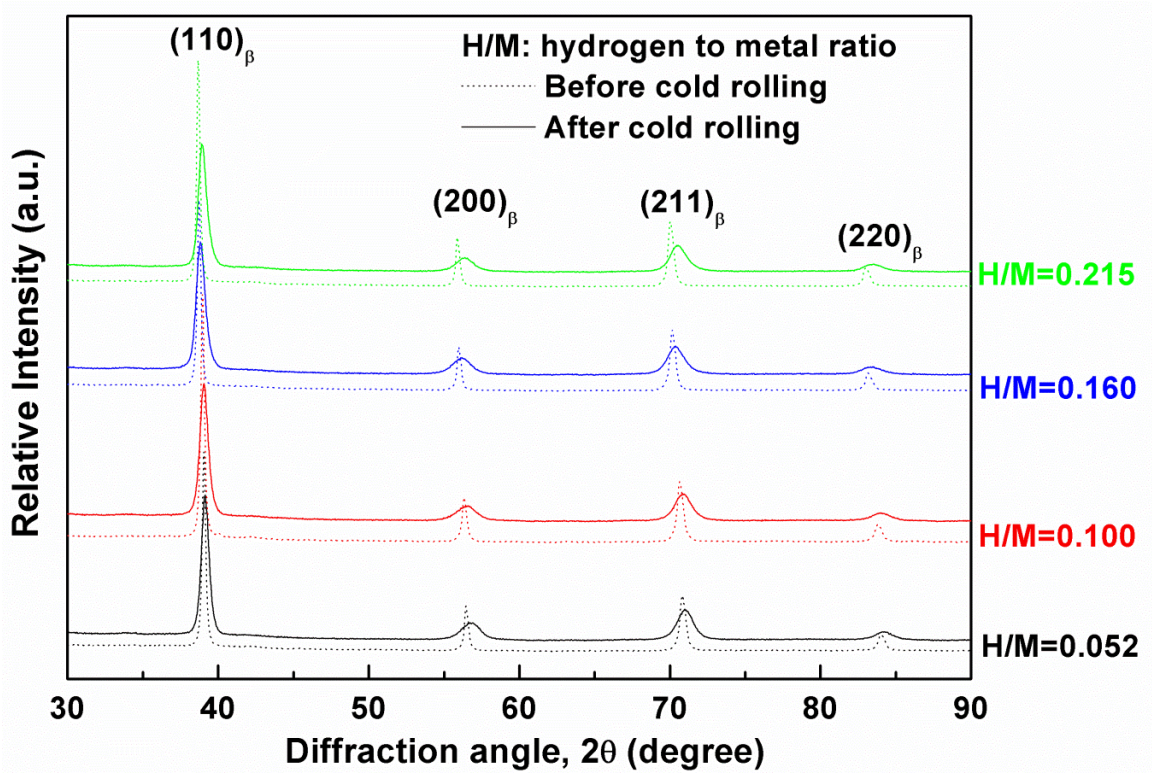

Figure 5. 15 XRD profiles of β-21S alloys before and after cold rolling, with different hydrogen concentrations.

In the present work, the instrument broadening contribution β_{inst} was measured separately using unstrained LaB_6 powder. To account for the peak broadening resulting from sample, the instrument contribution needs to be subtracted from β_{total}, as expressed in equation **5.1**:

$$\beta_{sample} = \beta_{total} - \beta_{inst} \quad (5.1)$$

Under cold deformation, both the grain size and internal strain can contribute to the observed peak broadening **[DB15]**. According to the method developed by Willamson and Hall **[WH53],** the internal strain ε and the grain size D of uniformly deformed *β-21S* alloys can be calculated from the XRD patterns. The relation of peak broadening to the grain size and the internal strain is**:**

$$\beta_{sample} = \beta_D + \beta_\varepsilon = \frac{\lambda}{D\cos\theta} + 2\varepsilon\tan\theta \quad (5.2)$$

Combined with the equation **5.1**, the equation **5.2** can be written as:

$$\cos\theta\ (\beta_{total} - \beta_{inst}) = \frac{\lambda}{D} + 2\varepsilon\sin\theta \quad (5.3)$$

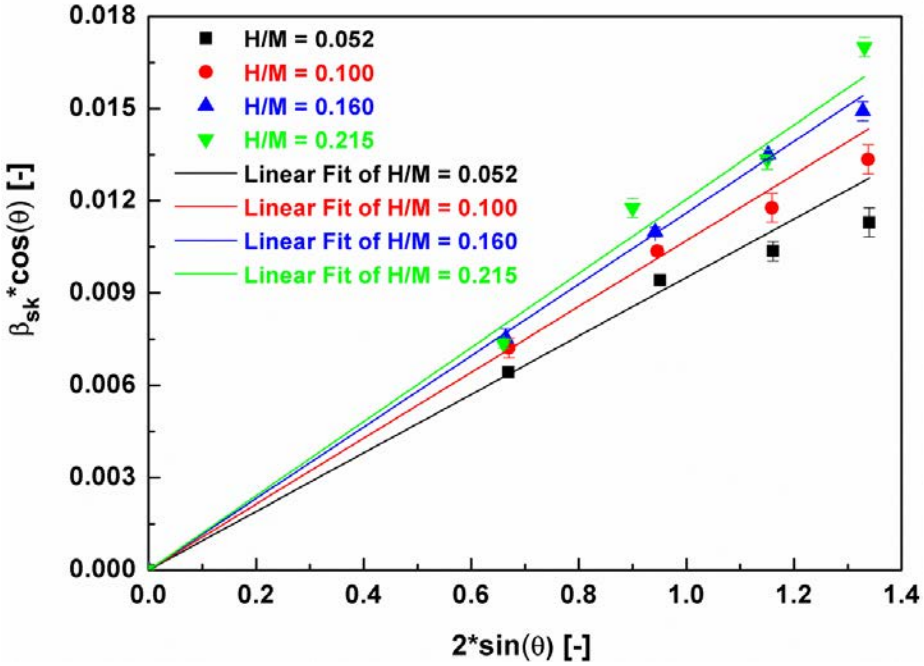

Figure 5. 16 Williamson-Hall plots for cold rolled samples with different hydrogen concentration

Fitting the measured peak with Lorentzian function, the integral breadth β related to the full width at half maximum of Lorentzian-shaped peaks can be determined **[WH53]**. Then, using a linear fit, ε and D can be acquired from the slope and the *y*-intercept using the X-ray wavelength λ. Since the average grain size of cold rolled β-21S alloys is not smaller than 30 μm according to optical micrographs, the contribution of the grain size to the Bragg peak broadening is considered to be negligible and the term $\frac{\lambda}{D}$ in equation **5.3** is set to zero. Performing a linear-least-squares fit on the measured data in **Figure 5. 15** and setting the intercept of the ordinate to zero, the lattice

strain ε of the sample can be derived by taking the slope of the fitted line, as shown in **Figure 5. 16**. Assuming that the internal strain was generated only by the dislocations, the dislocation density ρ can be calculated from ε **[WS56]:**

$$\rho = k\,\frac{\varepsilon^2}{b^2} \qquad (5.4)$$

where b is the Burgers vector and k is a geometrical constant, with k = 14.4 for body-centered cubic materials **[WS56]**. The values of dislocation densities corresponding to the different hydrogen concentrations can be estimated using the equation **5.4**, as shown in **Table 5. 4**. It can be seen that, the presence of an increasing concentration of hydrogen in β-21S alloys leads to increasing dislocations densities.

Indeed, the stored dislocations are generally divided into statistically stored dislocations (SSDs) that accumulate due to statistical entanglements, and geometrically necessary dislocations (GNDs) accommodating a lattice curvature from a strain gradient **[N53, BB55 and KZ15].** The stastically-stored dislocations (SSD) are considered by Arsenlis and Parks as evolving from random trapping processes during uniform plastic deformation **[AS99]**. Because GNDs are the consequence of a non-uniform deformation process, they have geometric consequences on the crystal lattice and, according to Nye **[N53]**, contribute to the stored energy and strain hardening during cold deformation, irrespective of the fact that the GND density represents only a few percent of the total dislocation density. Using ATOM software, the local strain gradient was represented by the internal misorientation within a grain. **Figure 5. 17a-d** shows the internal misorientation maps measured in 50% cold rolled samples, which are corresponding to the IPF maps present in **Figure 5. 14**b-e. Meanwhile **Figure 5. 17**e-h gives the GNDs maps corresponding to the IPF maps shown in **Figure 5. 14**b-e. The color scheme corresponds to the GNDs norm in the range of 0 to $6.5 \times 10^{-1} \mu m^{-1}$. For each GNDs map there were still some points without good indexed because either the point was too near a grain boundary, or the material was too highly deformed. We can see, the distribution of GNDs is not homogeneous throughout the sample and that most of the GNDs are piled up at the boundaries. In the hydrogen concentration range 0.052 < H/M < 0.160, an increasing amount of hydrogen leads to an increasing number of GNDs. While at hydrogen concentration H/M = 0.215, the GNDs exhibits a slight decreasing trend.

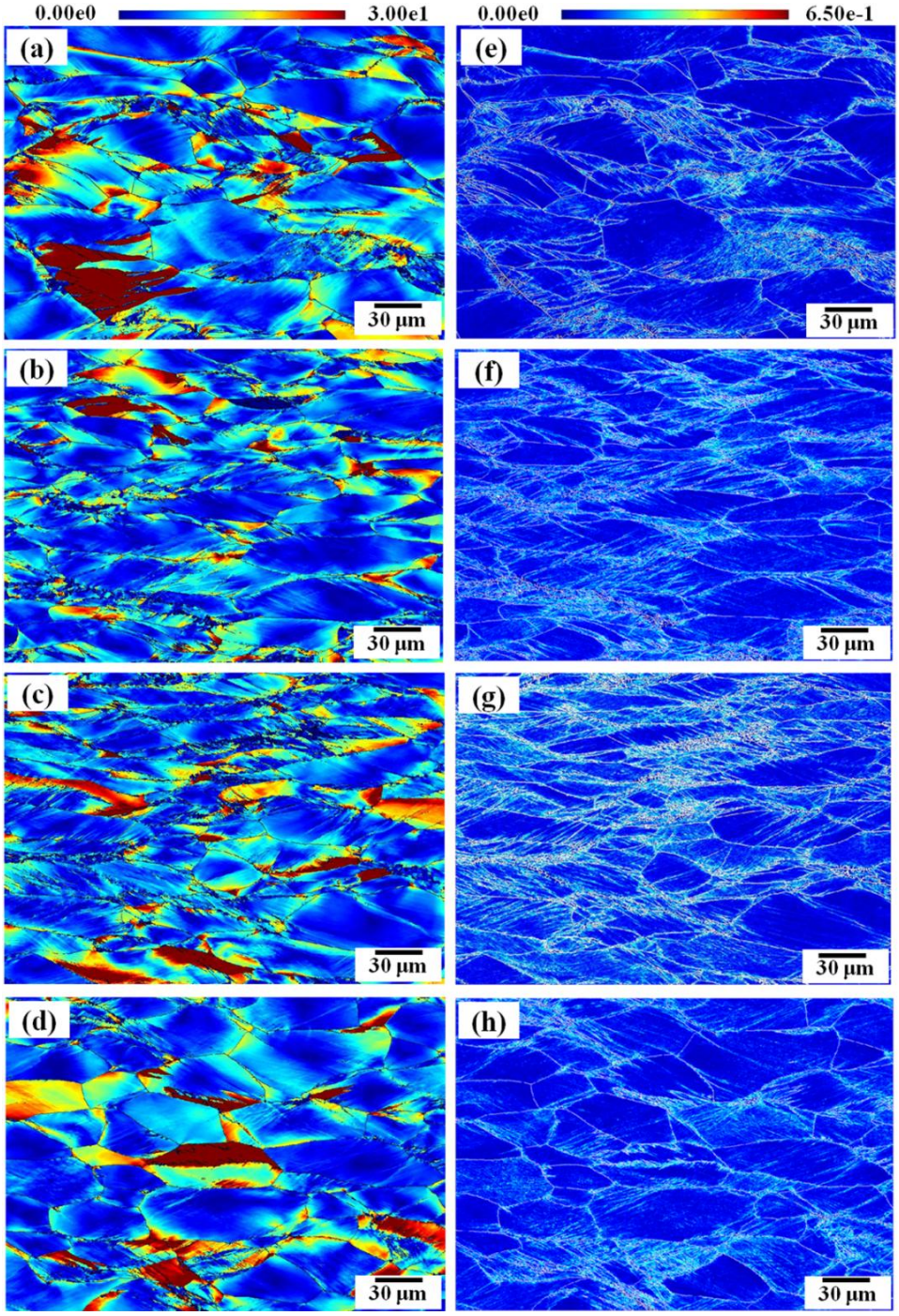

Figure 5. 17 Internal misorientation (a-d) and GNDs (e-h) maps of cold rolled β-21S alloys: (a, e) H/M = 0.052; (b, f) H/M = 0.100; (c, g) H/M = 0.160 and (d, h) H/M = 0.215.

By means of mapping the EBSD detected regions (maps not shown here), the average grain size and GNDs density can be obtained using ATOM software, as given in **Table 5. 4**. It should be mentioned that the maps (**Figure 5. 17**e-h) shows only a subset of the total available data; in total, between 80 and 150 grains were mapped for each sample. We can see that the presence of the

increasing amount of hydrogen leads to increasing GNDs densities and decreasing grain size till H/M = 0.160. As well known, the increase in dislocation density during deformation results from both the trapping of existing mobile dislocations and the generation of new dislocations. As for bcc metals, the dislocation mobility is reduced by a strong lattice friction due to the non-planar configuration of the screw dislocation cores **[WB13]**. In such a case, when hydrogen is present in β-21S alloy, a stronger lattice friction stems from the superposition between hydrogen-induced lattice distortion and screw dislocations. On the other hand, the segregation of hydrogen atoms to the dislocations can pin and immobilize the dislocations, which makes the movement of dislocation more difficult **[093, SZ08]**. Additionally, when hydrogen atoms are trapped at dislocation and/or grain boundaries, the new dislocations can be generated by the internal stresses arising from the hydrogen concentration gradient within a grain. For example, Oriani **[AO87]** using TEM has observed a large density of dislocations generated in the hydrogen charged Ti-30Mo alloy. Moreover, according to the concept "defactant" already mentioned in the previous chapters, the pre-dissolved hydrogen atoms expected to reduce the defect formation energy can result in an increase of dislocations density under cold rolling. Consequently, the results described above suggest that the generation of GNDs can be accelerated in the presence of hydrogen during cold deformation till H/M = 0.160.

Table 5. 4 Average grain sizes, GNDs density determined by EBSD and the total dislocation density determined by the method of Williamson and Hall using XRD patterns

Hydrogen concentration, (H/M)	Average grain sizes, [um]	GNDs density 10^{14}, $[m^{-2}]$	Total dislocation density 10^{15} , $[m^{-2}]$
0.052	12.87 ± 0.20	3.02 ± 0.06	4.50 ± 0.12
0.100	11.09 ± 0.20	3.76 ± 0.08	5.77 ± 0.13
0.160	9.32 ± 0.15	4.05 ± 0.05	6.78 ± 0.13
0.215	10.60 ± 0.10	3.92 ± 0.06	6.49 ± 0.12

As noted above, a slight decrease in the grain size can be observed as the hydrogen concentration increased till H/M = 0.160. This implies that the deformation-induced grain subdivision is facilitated in the presence of hydrogen. The exact mechanism responsible for this hydrogen caused grain refinement needs to be further investigated. **Figure 5. 18** shows the variation of

hardness as a function of hydrogen concentration in β-21S alloy before and after cold rolling. Prior to cold rolling, the increase of hardness with increasing hydrogen concentration in the hydrogen concentration range 0.052 < H/M < 0.215, was attributed to that the hydrogen-induced solid solution strengthening overwhelmed the hydrogen-induced softening, as discussed in Chapter 5. After cold rolling, the increase of hardness was attributed to the combined effects of the increasing dislocations density and the decreasing grain size.

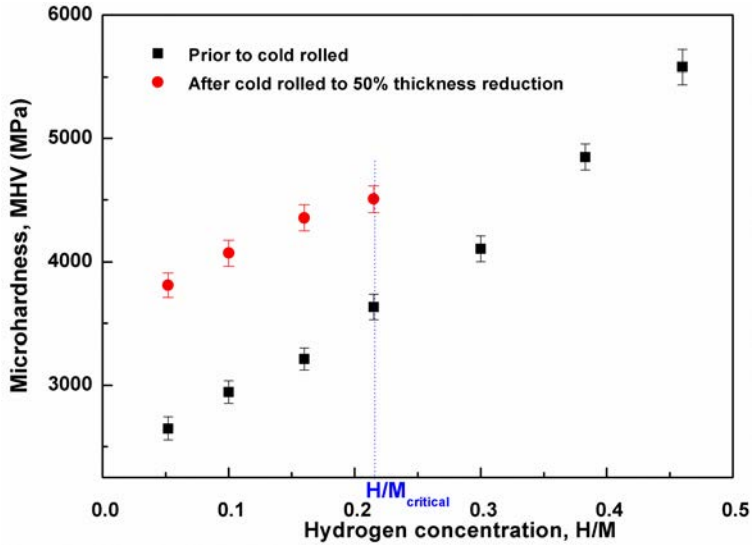

Figure 5. 18 Microhardness as a function of hydrogen concentration before and after cold rolling

5.2.2.3 Influence of hydrogen on texture evolution in β-21S alloy under cold rolling

To investigate the influence of hydrogen on the texture evolution in β-21S alloy under cold rolling, texture analysis was conducted by both XRD and EBSD analyses. **Figure 5. 19** shows the microtexture (IPF) maps of the cold rolled samples. As observed, there exist two typical rolling textures for bcc metals: α_{bcc}-fiber (<110> parallel to RD) and γ-fiber (<111> parallel to ND) **[SR08]**. Due to the fact that the most intense peak in the X-ray diffraction pattern of bcc metals is (110) as it is shown in **Figure 5. 20**, it is quite common to use (110) pole figures for the depiction of bcc texture**.** It can be seen that the cold rolled samples exhibit the typical rolling texture of bcc metals, which is (110) parallel to RD. Additionally, in the hydrogen concentration range 0.052 < H/M < 0.160, the texture intensity was slightly increased with the increase of hydrogen concentration, indicating that hydrogen can improve the development of rolling texture at room temperature. This is due to the fact that hydrogen promotes the dislocation mobility. However, at the higher hydrogen concentration H/M = 0.215, the hydrogen-induced solid solution strengthening occurred, therefore resulted in a weaker rolling texture component. Therefore, the

results obtained in the present work suggested that, there existed two competitive mechanisms associated with the dissolved hydrogen: the hydrogen-induced softening [**K12**] and the hydrogen-induced hardening.

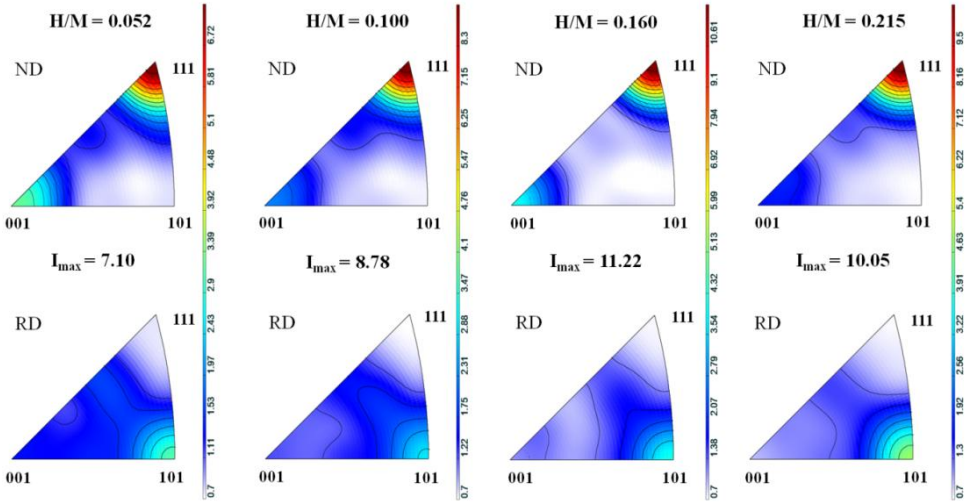

Figure 5. 19 Inverse-pole-figures of cold rolled β-21S alloys with different hydrogen concentrations.

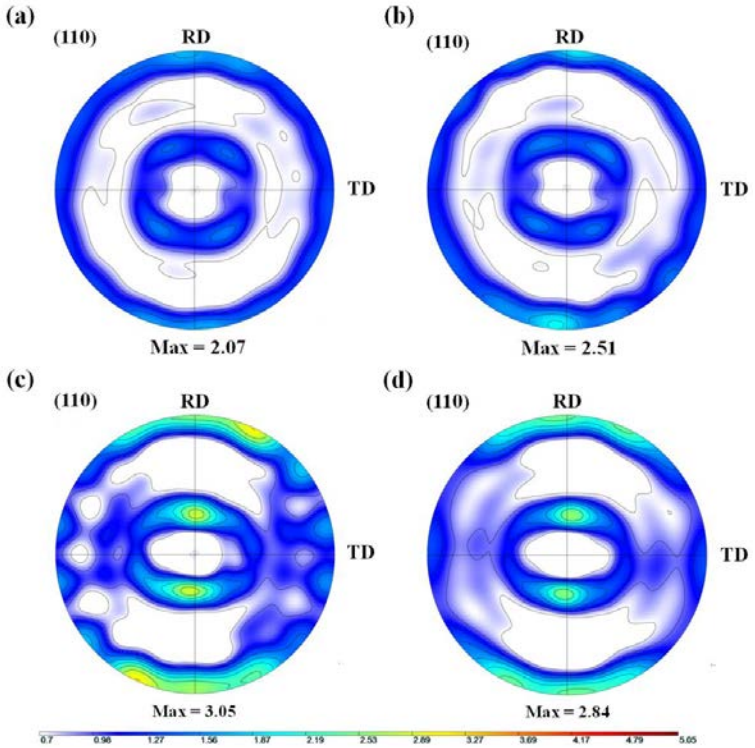

Figure 5. 20 Pole figures of cold rolled samples with different hydrogen concentrations measured by XRD. (a) H/M=0.052. (b) H/M=0.100. (c) H/M=0.160 and (d) H/M=0.215.

5.2.3 Combined influence of hydrogen and cold rolling on the recrystallization behavior in Ti50A and β-21S alloy

As mentioned before, titanium and titanium alloys are produced initially as billets, bloom or semi-finished cast products, which are then further processed in the solid state by forging, rolling, extrusion, etc., to an intermediate or final products. Among these procedures, intermediate annealing treatments are often performed to release the internal stress generated during cold or hot deformations. Recovery, recrystallization and grain growth are core elements of annealing treatments.

In the present work as previously demonstrated, the non-hydrogenated and hydrogenated specimens exhibited different microstructures upon cold rolled to 50% thickness reduction. It is therefore important to follow the evolution of microstructure in the subsequent annealing treatment. This is based on the fact that, the release of stored energy provides the driving force for dislocation recovery and grain recrystallization, but it is upon the nature of the microstructure that controls the development and growth of the nuclei that will depend the recrytallized grains and also their orientation.

5.2.3.1 Recrystallization behavior of hydrogenated Ti50A

To evaluate the combined influence of hydrogen/hydride and cold rolling on the recrystallization behavior of α-titanium Ti50A, the specimens without hydrogenation and with hydrogenation were annealed in sealed quartz tube at 675 °C during a short duration of 5 min. EBSD measurements were then employed to investigate the evolution of the microstructure under this annealing treatment.

Figure 5. 21 shows the IPF and GBs maps of the annealed Ti50A without hydrogenation (**Figure 5. 21**a and c) and hydrogenated for 168 h (**Figure 5. 21b** and **d**). In the GBs maps, black and white lines correspond to the HABs and LABs, respectively, as explicited in Chapter 2; blue, yellow and red colors indicate the fully recrystallized grains, grains having sub-structures and the deformed grains, respectively. It should be mentioned that the minimum misorientation angle to separate subgrains and grains are 1° and 15°, respectively. As observed in **Figure 5. 21**a and c, considerable new sets of equiaxied grains with less preferential orientations appeared in annealed Ti50A. The existence of the sub-structures indicated that recrystallization did not fully occur under this annealing treatment condition (5 min at 675°C). Compared to Ti50A without

hydrogenation, the hydrogenated specimen exhibited almost fully recrystallized grains **(Figure 5. 21**b and d), indicative of the presence of hydrogen/hydride facilitated the occurrence of recrystallization.

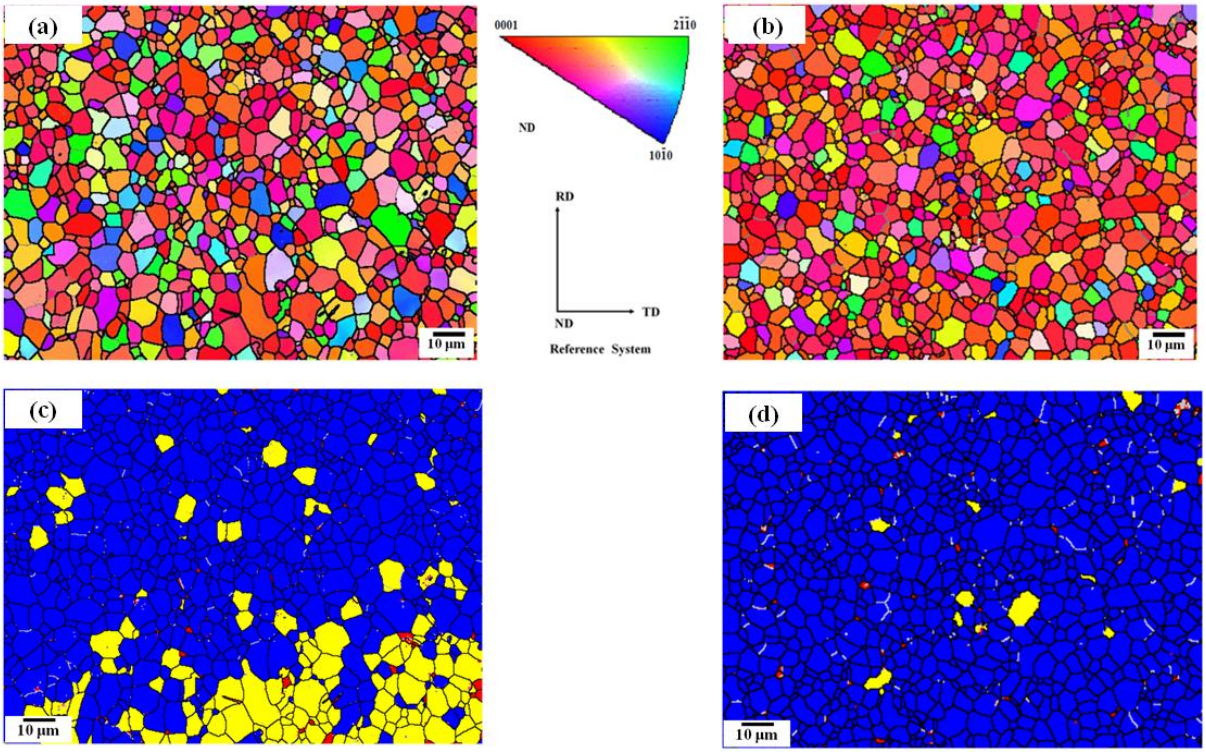

Figure 5. 21 IPF and GBs of the annealed Ti50A. (a), (c) without hydrogenation and (b), (d) hydrogenated for 168 h. (black and white lines corresponding to HABs and LABs, respectively; blue, yellow and red color indicating the fully recrystallized grain, grain having substructure and deformed grain, respectively. The minimum misorientation angle to separate subgrains and grains are 1° and 15°, respectively.)

The misorientation angle distributions of the cold rolled Ti50A specimens after annealing treatment are shown in **Figure 5. 22**a and b. In addition to the HABs, a very small fraction of LABs (misorientation angles lower than 15°) was observed in the specimen without hydrogenation (**Figure 5. 22a).** In comparison, the hydrogenated specimen **(Figure 5. 22**b) displayed negligible LABs, which suggests that the original structure was fully recrystallized owing to this annealing treatment. Moreover, no significant difference was observed in the grain size distribution for these two specimens, as shown in **Figure 5. 22**c and d, the distribution being derived using the area fraction method **[U70],** which was used in order to explore the nature of the distribution (for example, unimodal or bimodal). Compared to that of the hydrogen-free Ti50A, the distribution of grain size for the hydrogenated Ti50A was more narrow, indicating that the recrystallization and growth of new strain-free grains took place without abnormal grain

growth. The average grain sizes (taken as the equivalent circle diameter), calculated by the ATOM software **[BF15]** with a grain is defined as an area enclosed by a continous HABs, was found to decrease from 12.0 ± 0.8 μm for the as-received Ti50A down to 4.5 ± 0.4 μm and 4.3 ± 0.2 μm for, respectively, the cold-rolled + annealed hydrogen-free and hydrogenated Ti50A-H specimens.

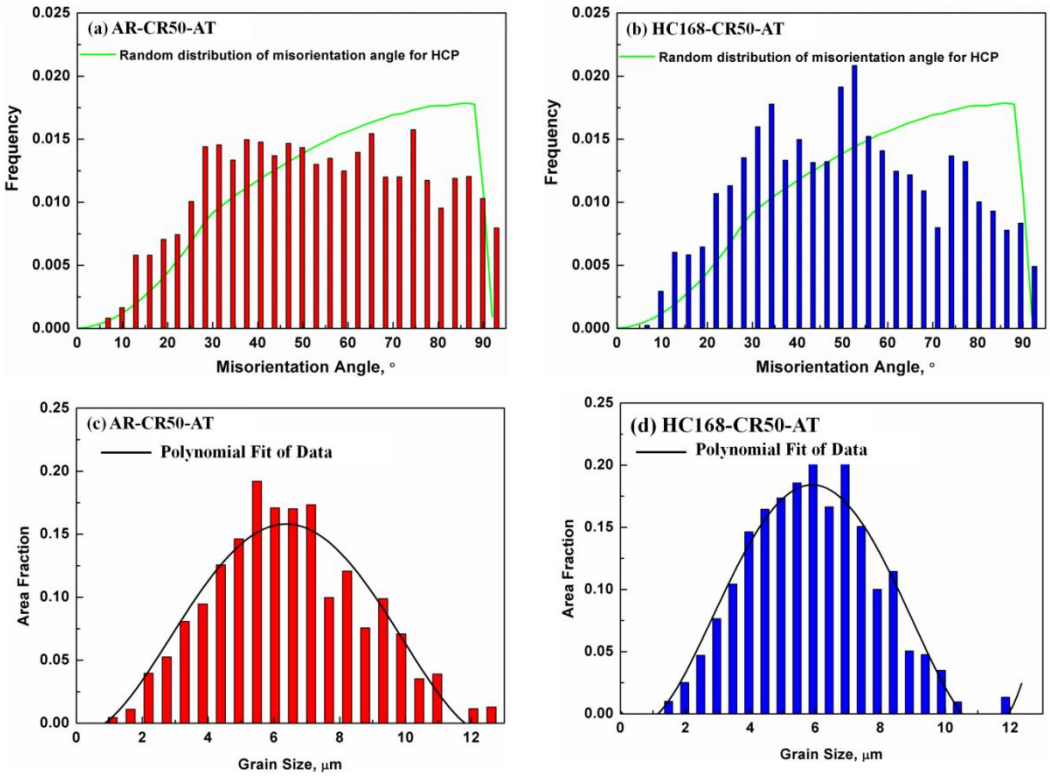

Figure 5. 22 Distributions of misorientation angles and grain sizes for Ti50A annealed 5 min at 675°C: (a), (c) hydrogen-free and (b), (d) hydrogenated for 168 h.

To further reveal the change of the texture resulting from this short-term annealing at 675 °C, the corresponding {0002} pole figures for the annealed specimens are shown in **Figure 5. 23**. The annealed texture of non-hydrogenated Ti50A (**Figure 5. 23**a) is characterized by TD-split basal texture with a maximum intensity occurring at ±30° tilted from the ND to the TD. This texture is typical of hot rolled CP-Ti sheets, as mentioned in Chapter 3. Meanwhile, the hydrogenated Ti50A was also characterized by a similar TD-split basal texture (**Figure 5. 23b**); however, the basal pole was more concentrated, characteristic of a well-developed texture. The maximum intensity for the non-hydrogenated and hydrogenated specimens remained similar at 7.96 and 7.58, respectively. Apart from the decrease in intensity, the textures after annealing at 675°C for

5 minutes for both hydrogen-free and hydrogenated Ti50A remained similar to those measured in the as-rolled state (

Figure 3. 2b). The maximum intensity of the hydrogenated specimen still occurs at ±20° from the ND to the TD while the basal pole of non-hydrogenated specimen is still ±30° from ND to TD with a larger spread for this orientation. This suggests that grain rotation occurred during the recrystallization process. The above results demonstrated that the presence of hydrogen/hydride has a significant impact on the recrystallization behavior of Ti50A. Considering the presence of hydride as the second phase, the intrinsic effect of hydrogen on the grain nucleation and growth during this short-term annealing treatment cannot be established yet.

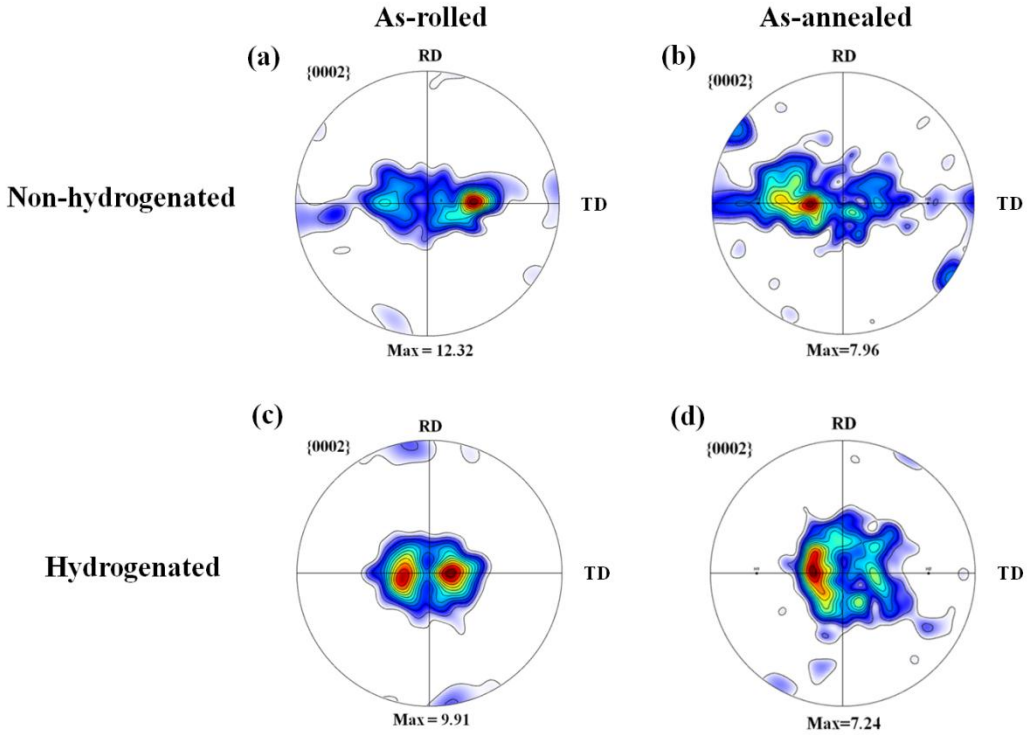

Figure 5. 23 Pole figures of the rolled and annealed Ti50A: (a), (b) hydrogen-free and (c), (d) hydrogenated for 168 h

5.2.3.2 Recrystallization behavior of hydrogenated β-21 alloys

To study the effect of hydrogen on the recrystallization behavior of cold rolled β-21S alloys, annealing treatments were performed at 800 °C for 5 min on specimens containing different hydrogen concentrations. The microstructural evolution during annealing process was characterized by the EBSD measurements. **Figure 5. 24** shows the IPF and GBs maps of the specimens after annealing treatment. In the GBs maps, black and gray lines correspond to the

HABs and LABs, respectively; the blue, yellow and red colors indicate the fully recrystallized grain, grain having sub-structures and the deformed grain, respectively. It should be mentioned, the minimum misorientation angle to separate subgrains and grains are 1° and 15°, respectively.

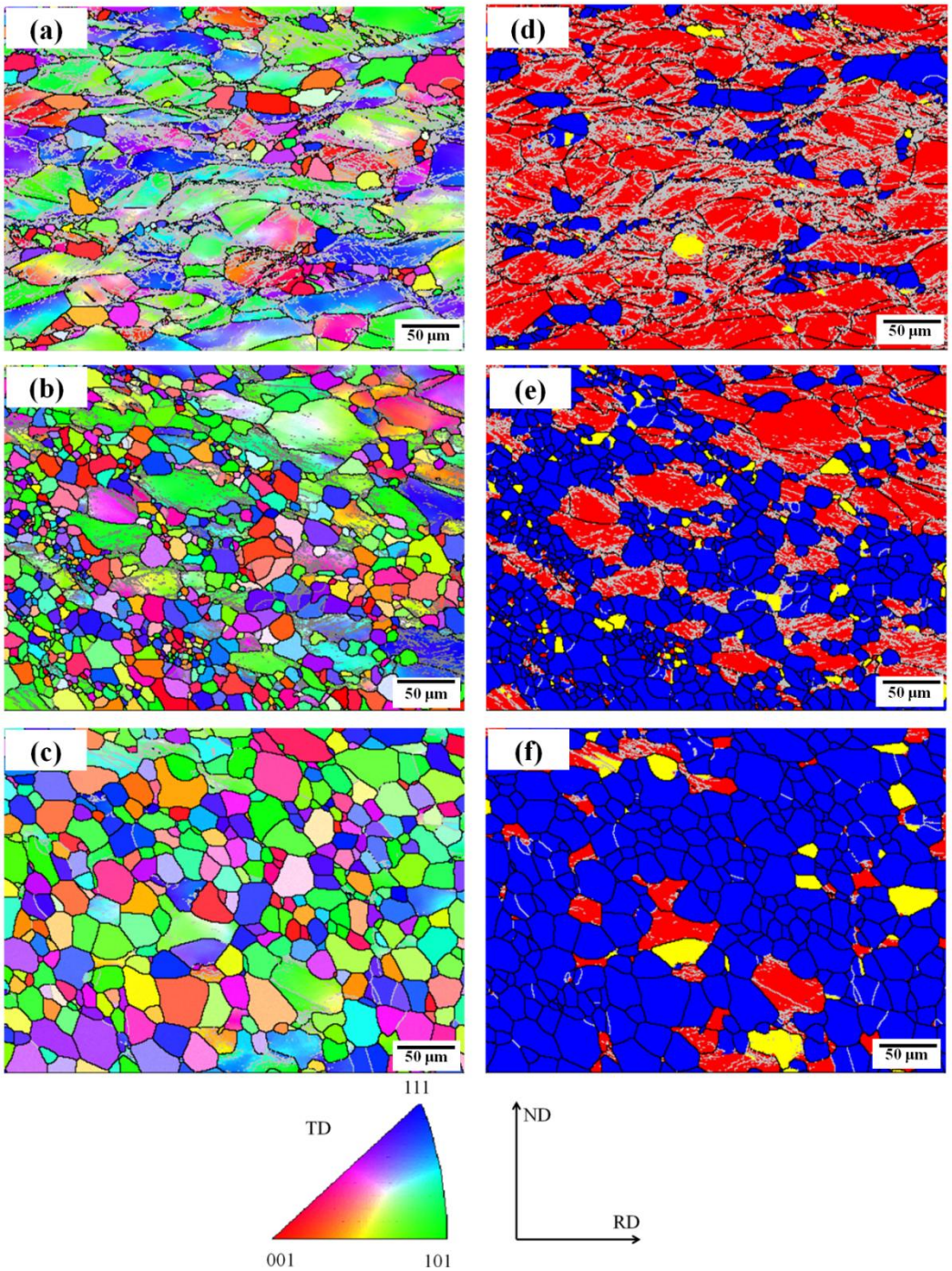

Figure 5. 24 IPF and GB maps of the annealed β-21S alloy, (a),(d) H/M = 0.052; (b), (e) H/M = 0.100 and (c); (f) H/M = 0.160. (black and white lines corresponding to the HABs and LABs, respectively; the blue, yellow and red colors indicating the fully recrystallized grain, grain having substructure

and deformed grain, respectively. The minimum misorientation angle to separate subgrains and grains are 1° and 15°, respectively.)

For hydrogen concentration H/M = 0.052 (**Figure 5. 24**a and d), a large number of deformed grains with low angle boundaries as well as dislocation-free grains were observed. The emergence of new recrystallized grains revealed that the onset of recrystallization under this annealing treatment. As hydrogen concentration increased to H/M = 0.100 (**Figure 5. 24**b and e), an increasing number of recrystallized grains (around 60% area fraction) was detected in the annealed specimen. A further increase in hydrogen concentration to H/M = 0.160 (**Figure 5. 24**c and f), the recrystallized microstructure consisting of equiaxed grains with minimal grain growth was found to represent approximately 88% of the whole area fraction of the annealed specimen.

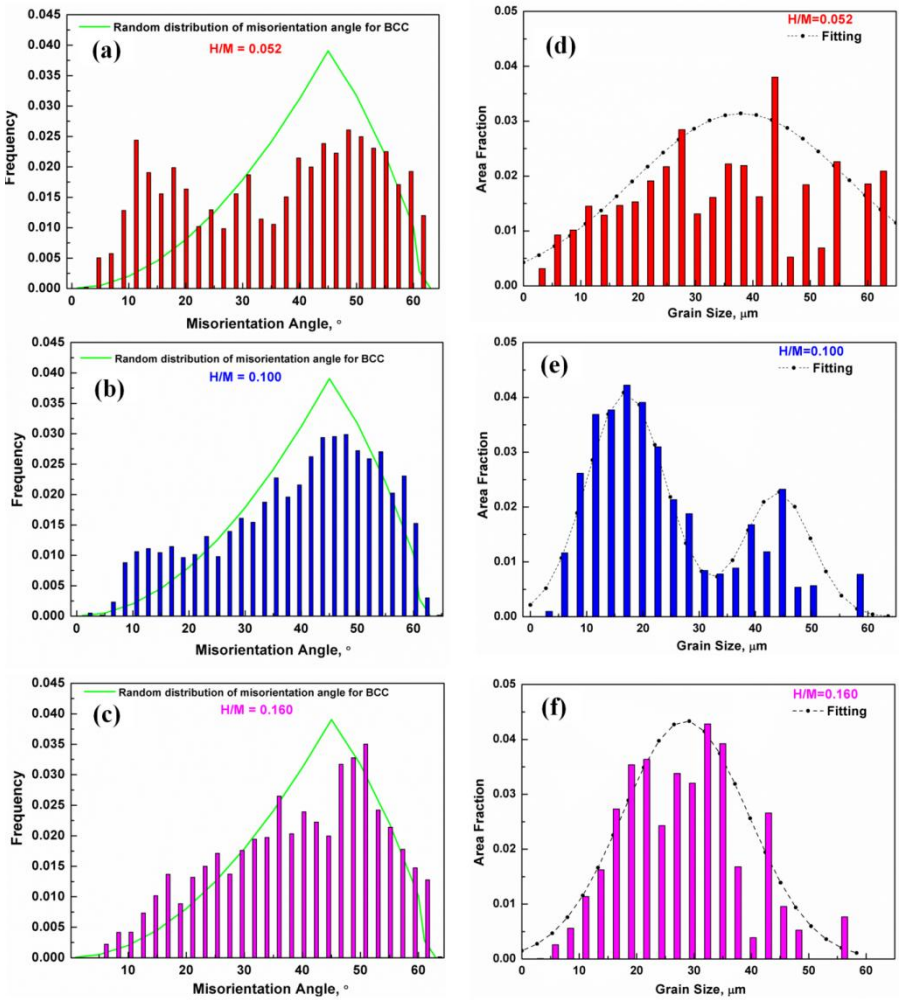

Figure 5. 25 The distributions of misorientation angle and grain size for the annealed β-21S alloys containing different hydrogen concentrations, (a), (d) H/M = 0.052; (b), (e) H/M = 0.100 and (c), (f) H/M = 0.160.

The microstructure changes due to short annealing were also investigated by the misorientation angle distributions of the first neighbors as shown in **Figure 5. 25**a, b and c, in which the green line is the random distribution (grain-to-grain) of misorientation angle expected for cubic structure without any texture **[M64]**. For the hydrogen concentration H/M = 0.052 (**Figure 5. 25a**), a high number fractions of LABs was observed mirroring the non-recrystallized microstructure shown in the IPF and GB maps (**Figure 5. 24**a and d). As the hydrogen concentration increased to H/M = 0.100 (**Figure 5. 25**b), an obvious decrease in the number fraction of LABs was seen due to the restoration of the microstructure. As the hydrogen concentration further increased to H/M = 0.160 (**Figure 5. 25**c), the misorientation angle distribution of the annealed specimen tends to be randomly distributed, indicating that the deformed microstructures were almost fully replaced by new dislocation-free grains.

Similar to Ti50A, the distributions of grain sizes for the annealed β-21S alloys using the area fraction method **[U70]** are presented in **Figure 5. 25**d, e and f**.** The distributions of grain size are described by Gaussian function, as indicated by the black curves. For the hydrogen concentration H/M = 0.052, the range of grain size was somewhat wide with variation from 2 μm to 62 μm due to the coexistence of small recrystallized and large deformed grains. For the hydrogen concentration H/M = 0.100, the distribution of grain size became more narrow with an average grain size of 12.1 ± 0.2 μm. With further increase in the hydrogen concentration to H/M = 0.160, a typical of normal distribution of grain size was observed, and the average grain size was found to be14.3 ± 0.3 μm.

Using the Channel 5 software, the area fraction of the recrystallized new strain-free grains was determined. **Figure 5. 26** shows the change of the recrystallization fraction with the hydrogen concentrations. An increasing area fraction of new recrystallized grains as the hydrogen concentration increased is clearly demonstrated in this figure. It should be noted that the density of dislocations played a significant role in the primary recrystallization process. It is well known that the driving force for primary recrystallization is the energy stored in dislocations. The energy per length unit for a dislocation [**G05**] is given by the **equation 5.5**

$$E_d = \frac{1}{2} G b^2 \qquad \textbf{(5.5)}$$

in which G is the shear modulus and b is the modulus of the Burgers vector. For a dislocation density ρ, the driving force for primary recrystallization **[G05]** is written as

$$P = \rho E_d = \frac{1}{2}\rho G b^2 \qquad \textbf{(5.6)}$$

Hence, an increasing dislocations density leads to an increasing driving force for the recrystallization. The calculated driving forces for the as-rolled specimens have been reported in **Table 5. 5**. This result shows that the as-rolled β-21S alloy has the largest driving force for primary recrystallization at the hydrogen concentration H/M = 0.160. As demonstrated above, the introduction of hydrogen into β-21S alloy prior to cold rolling had a large effect on the dislocation density and arrangement. The increased dislocation density can be interpreted as a reduction in the line energy due to hydrogen-dislocation interactions **[DB15]**. Therefore, the hydrogen-enhanced dislocations density is an indirect effect of hydrogen on the recrystallization.

Table 5. 5 The value of the driving force for recrystallization at different hydrogen concentrations

Hydrogen concentration, H/M	Stored dislocations density, $\boldsymbol{\rho}\times\mathbf{10^{15}}$, $[\boldsymbol{m^{-2}}]$	Driving force for recrystallization, P$\times\mathbf{10^{7}}$, $\boldsymbol{Jm^{-3}}$
0.052	4.50 ± 0.12	0.71 ± 0.03
0.100	5.77 ± 0.13	0.92 ± 0.04
0.160	6.78 ± 0.13	1.08 ± 0.02

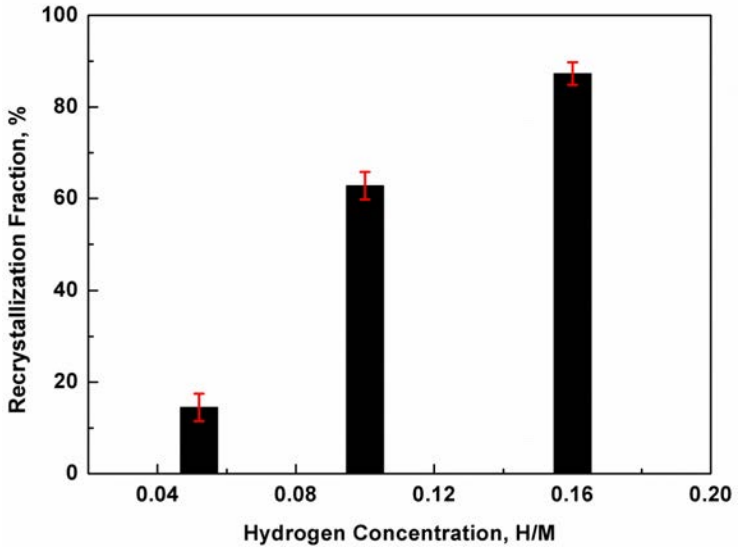

Figure 5. 26 Recrystallization fraction of the annealed β-21S alloys containing different hydrogen concentrations.

To further explore the combined effects of hydrogen and cold rolling on the grain nucleation and growth during the annealing process (at 800°C for 5 min), the evolution of texture was

investigated using the JTEX software. As shown in **Figure 5. 27**, the annealed samples also exhibited the typical of rolling texture of bcc metals, which is {110} parallel to RD, however the maximum intensity was found to decrease in comparison to the as-rolled specimens in **Figure 5. 20**. This results indicated that, the as-rolled texture component cannot be totally removed by this short-time annealing treatment.

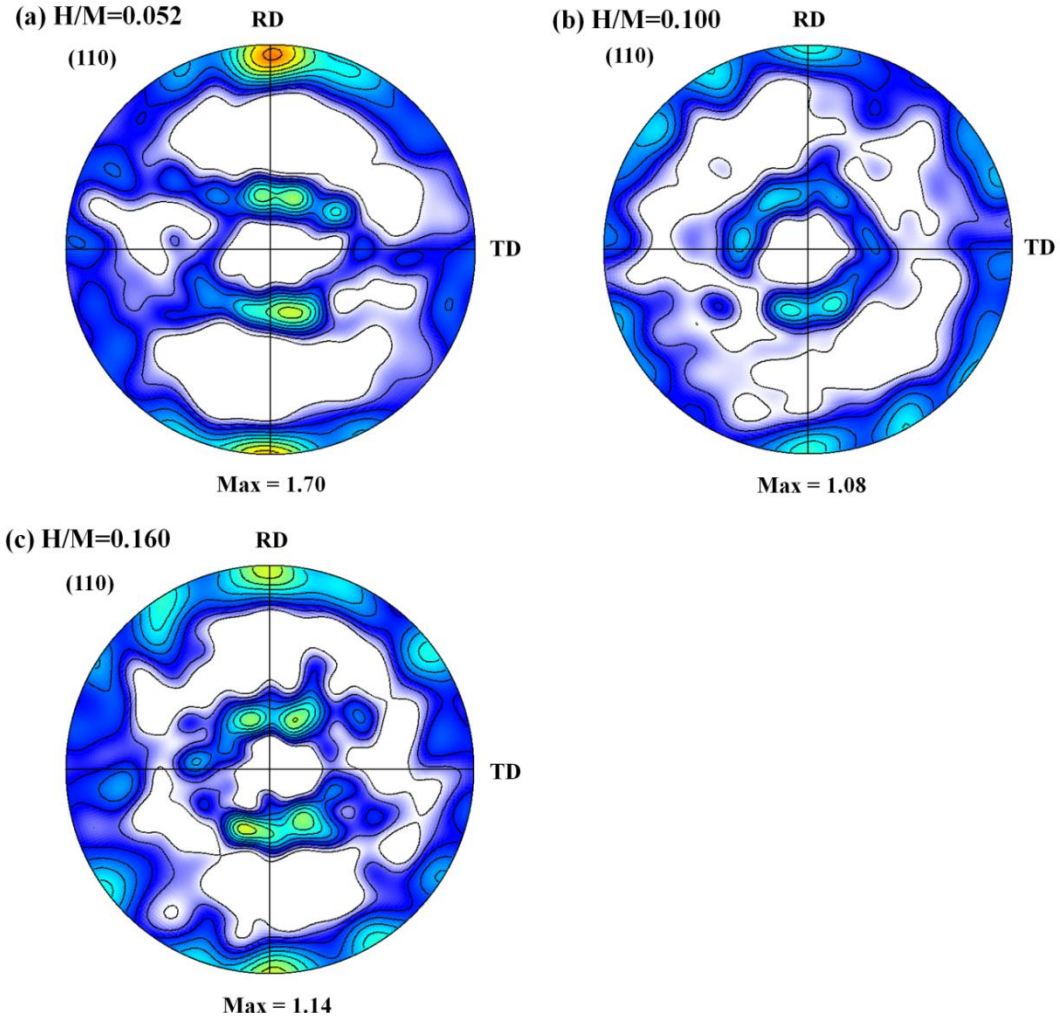

Figure 5. 27 Pole figures of the annealed β-21S alloys containing different hydrogen concentrations, (a) H/M = 0.052, (b) H/M = 0.100 and (c) H/M = 0.160.

5.3 Conclusion

The effects of hydrogen on the behaviors of cold rolling and on the recrystallization in α-titanium Ti50A and β-titanium β-21S alloys were investigated using combined XRD and SEM-EBSD analyses. The main conclusions are summarized as follows:

1. Upon application of low strain (εeq = 0.12) by the cold rolling, microstructural analyses showed that the formation of tension twin TT1 $\{10\bar{1}2\}<\bar{1}011>$ in Ti50A can be facilitated due to the increase of the c/a ratio by the hydrogen addition as well as the existence of the local stress generated by the hydride precipitation. For larger value of the applied strain by cold rolling, i.e., ε_{eq}= 0.80 (50% thickness reduction), twinning became almost saturated whereas an obvious microstructure refinement was observed in the pre-hydrogenated Ti50A-H as compared to that of hydrogen-free Ti50A deformed under the same conditions. This grain refinement was explained by an increase in the generation of high angle boundaries (HABs) around the hydride phase. In addition, considerable numbers of geometrically necessary dislocations (GND) were produced to accommodate the strain incompatibility between the hydride and matrix. On the other hand, the texture evolution showed that the presence of hydrogen/hydride rotated the c-axis became parallel to the ND.

2. The study of the cold rolling behavior of hydrogenated β-21S alloys showed that hydrogen had contradictory effects on the behavior of cold rolling, depending on the hydrogen concentration . In the hydrogen concentration range 0.052 < H/M < 0.160, the hydrogen atoms dissolved in the lattice enhanced the dislocations mobility and increased the dislocations density leading to a microstructure refinement as the hydrogen concentrations increased. In contrast, as the hydrogen concentration was increased to H/M = 0.215, the observation of less deformed β grains and the presence of micro-cracks suggested a strengthening of the grains by hydrogen-induced solid solution, which hindered the dislocations mobility.

3. The recrystallization investigated after a short-term annealing treatment was found to be accelerated in hydrogenated Ti50A-H in comparison to the sample treatment applied to hydrogen-free sample. In the case of β-21S alloy, the area fraction of the recrystallized grains was found to be strongly dependent on the hydrogen concentration. Although the direct/intrinsic effect of hydrogen on recrystallization cannot be established now, the results observed above suggested that the presence of hydrogen is an attractive element to accelerate the formation of new strain-free grains.

Reference

[A70] M.F. Ashby, The deformation of plastically non-homogeneous materials, Philos. Mag. 21 (1970) 399-424.

[AB03] P.J. Apps, J.R. Bowen, P.B. Prangnell, The effect of coarse second-phase particles on the rate of grain refinement during severe deformation processing, Acta Mater. 51 (**2003**) 2811-2822.

[AO87] M.E. Armacanqui and R.A. Oriani, Mater. Sci. Eng. A 91 (**1987**) 143-152.

[AO10] I. Aubert, J.M. Olive, N. Saintier, Mater. Sci. Eng. A 527 (**2010**) 5858.

[AS99] A. Arsenlis and D. M. Parks, Crystallographic Aspects of Geometrically- Necessary and Statistically-Stored Dislocation Density, Acta Mater. 47 (**1999**) 1597-1611.

[AS12] I. Aubert, N. Saintier, J.M. Olive, Scripta Mater. 66 (**2012**) 698.

[BA12] A. Barnoush, M. Asgari, R. Johnsen, Scripta Mater. 66 (**2012**) 414.

[BB55] B.A. Bilby, R. Bullough, E. Smith, Continuous distributions of dislocations: a new application of the methods of non-Riemannian geometry, Proc. R. Soc. A 231 (**1955**) 263-273.

[BC81] R. Bonnet, E. Cousineau, D.H. Warrington, Determination of near-coincident cells for hexagonal crystals, Related DSC Lattices, Acta Cryst. A 37 (**1981**) 184-189.

[BC09]T.R. Bieler, M.A. Crimp, Y. Yang, L. Wang, P. Eisenlohr, D.E. Mason, W. Liu, G.E. Ice, Strain heterogeneity and damage nucleation at grain boundaries during monotonic deformation in commercial purity titanium, JOM 61 (**2009**) 45-52.

[BD15] T.B. Britton, F.P. Dunne and A.J. Wilkinson, On the mechanistic basis of deformation at the microscale in hexagonal close-packed metals. Proc. R. Soc. A 471 (**2015**) 0881.

[BE09] T.R. Bieler, P. Eisenlohr, F. Roters, D. Kumar, D.E. Mason, M.A. Crimp, D. Raabe, The role of heterogeneous deformation on damage nucleation at grain boundaries in single phase metals, Int. J. Plast. 25 (**2009**) 1655-1683.

[BV10] A. Barnoush, H. Vehoff, Recent developments in the study of hydrogen embrittlement: Hydrogen effect on dislocation nucleation, Acta Mater. 58 (**2010)** 5274-5285.

[CD02] J.P. Chateau, D. Delafosse, T. Magnin, Acta Mater. 50 (**2002**) 1507-1522.

[CM95] J.W. Christian, S. Mahajan, Deformation twinning, Prog. Mater Sci. 39 **(1995)** 1-157.

[CY05] Y.B. Chun, S.H. Yu, S.L. Semiatin, S.K. Hwang, Effect of deformation twinning on microstructure and texture evolution during cold rolling of CP-titanium, Mater. Sci. Eng. A 398 (**2005**) 209-219.

[DB15] M. Deutges, H.P. Barth, Y.Z. Chen, C. Borchers, R. Kirchheim, Hydrogen diffusivities as a measure of relative dislocation densities in palladium and increase of the density by plastic deformation in the presence of dissolved hydrogen, Acta Mater. 82 (**2015**) 266-274.

[DK13] M. Deutges, I. Knorr, C. Borchers, C.A. Volkert, R. Kirchheim, Scripta Mater. 68 (2013) 71-74.

[DM15] M. Dadfarnia, M.L. Martin, A. Nagao, P. Sofronis, I.M. Robertson, Modeling hydrogen transport by dislocations, J. Mech. Phys. Solids 78 (**2015**) 511-525.

[FC09] X. Feaugas and E. Conforto, PlastOx 2007, Argeles sur Mer, France, EDP Sciences, (2009) 161-178.

[FR98] P.J. Ferreira, I.M. Robertson, H.K. Birnbaum, Acta Metall. 46 (1998) 1749.

[G05] G. Gottstein, Physical Foundations of Materials Science, Springer, 2005.

[GF01]I. Guillot, X. Feaugas, M. Clavel, Dislocation-hydride interactions at low plastic strain in titanium, Scripta Mater. 44 (2001) 1011-1017.

[GW10] J.C. Gong, A. Wilkinson, Investigation of elastic properties of single-crystal α-Ti using microcantilever beams, Philos. Mag. Lett. 90 (**2010**) 503-512.

[FL86] G.S. Frankel, R.M. Latanision, Hydrogen transport during deformation in nickel: Part II single crystal nickel, Metall. Trans. A 17 (**1986**) 869-875.

[H99] F.J. Humphreys, Quantitative metallography by electron backscattered diffraction, J. Microsc. 195 (**1999**) 170-185.

[IJ97] G. Itoh, T. Jinkoji, M. Kanno, K. Koyama, Effect of impurity hydrogen on the deformation and fracture in an Al-5 mass Pct mg alloy, Metall. Mater. Trans. A 28 (**1997**) 2291-2295.

[K01] Kunze E. Korrosion und korrosionsschutz. 3th ed. Weinheim: Wiley-VCH Verlag; **2001**.

[K09] R. Kirchheim, Int. J. Mater. Res. 100 (2**009**) 483.

[KD12] N. Kheradmand, J. Dake, A. Barnoush, H. Vehoff, Philos. Mag. 92 (**2012**) 3216.

[KZ15] P.J. Konijnenberg, S. Zaefferer, D. Raabe, Assessment of geometrically necessary dislocation levels derived by 3D EBSD, Acta Mater. 99 (**2015**) 402-414.

[KS10] M. Krystian, D. Setman, B. Mingler, G. Krexner, M.J. Zehetbauer, On the formation of Super-Abundant Vacancies in Pd–H deformed by High Pressure Torsion, Scripta Mater. 62 (**2010**) 49.

[LW12] P.D. Littlewood, A.J. Wilkinson, Geometrically necessary dislocation density distributions in cyclically deformed Ti–6Al–4V, Acta Mater. 60 (**2012**) 5516-5525.

[M51] A.D. McQuillan, An Experimental and Thermodynamic Investigation of the Hydrogen-Titanium System, Proc. R. Soc. A 204 (**1951**) 309-22.

[M64] J.K. Mackenzie, The distribution of rotation axes in a random aggregate of cubic crystals,

Acta metall., 12 **(1964)** 223.

[M04] A. Morawiec, Orientations and Rotations: Computations in Crystallographic Textures, Springer, **2004**.

[MR11] M.L. Martin, I.M. Robertson, P. Sofronis, Interpreting hydrogen-induced fracture surfaces in terms of deformation processes: A new approach, Acta Mater. 59 (**2011**) 3680-3687.

[N53] J.F. Nye, Some geometrical relations in dislocated crystals, Acta Metall. 1 (**1953**) 153.

[NS12] A. Nagao, C.D. Smith, M. Dadfarnia, P. Sofronis, I. M. Robertson, The role of hydrogen in hydrogen embrittlement fracture of lath martensitic steel, Acta Mater. 60 (**2012**) 5182-5189.

[O93] R.A. Orian, The physical and metallurgical aspects of hydrogen in metals, in ICCF4, Fourth International Conference on Cold Fusion.. Lahaina, Maui: Electric Power Research Institute 3412 Hillview Ave., Palo Alto, CA, **1993**.

[P08] W. Pantleon, Resolving the geometrically necessary dislocation content by conventional electron backscattering diffraction, Scripta Mater. 58 (**2008**) 994-997.

[RB86] I.M. Robertson, H.K. Birnbaum, An HVEM study of hydrogen effects on the deformation and fracture of nickel, Acta Metall. 34 (**1986**) 353-366.

[RM12] I.M. Robertson, M.L. Martin, J.A. Fenske, Influence of hydrogen on the behavior of dislocations in "Gaseous hydrogen embrittlement of materials in energy technologies", in: RP. Gangloff and B. Somerday (Eds.), Woodhead publishing, 2 (**2012**) 166.

[RR90] P. Rozenak, I.M. Robertson, H.K. Bimbaum, HVEM studies of the effects of hydrogen on the deformation and fracture of AISI type 316 austenitic stainless steel, Acta Metall. 38 (**1990**) 2031-2040.

[SC01] O.N. Senkov, B.C. Chakoumakos, J.J. Jonas, F.H. Froes. Effect of temperature and hydrogen concentration on the lattice parameter of beta titanium. Mater. Res. Bull. 36 (**2001**) 1431-1440.

[SD96] O.N. Senkov, M. Dubois, J.J. Jonas, Elastic moduli of titanium-hydrogen alloys in the temperature range 20°C to 1100°C, Metall. Mater. Trans. A 27 (**1996**) 3963-3970.

[SK03] A.A. Salem, S.R. Kalidindi, R.D. Doherty, Strain hardening of titanium: role of deformation twinning, Acta Mater. 51 (**2003**) 4225-4237.

[SM10] G. Salishchev, S. Mironov, S. Zherebtsov, A. Belyakov, Changes in misorientations of grain boundaries in titanium during deformation, Mater. Charact. 61 (**2010**) 732-739.

[SR88] D.S. Shih, I.M. Robertson, H.K. Bimbaum, Hydrogen embrittlement of α titanium: *In situ* tem studies, Acta Metall. 36 (**1988**) 111-124.

[SR08] B. Sander, D. Raabe, Texture inhomogeneity in a Ti-Nb-based β-titanium alloy after warm rolling and recrystallization, Mater. Sci. Eng. A 479 (**2008)** 236-247.

[SZ08] D.B. Shan, Y.Y. Zong, Y. Lv and B. Guo, The effect of hydrogen on the strengthening and softening of Ti-6Al-4V alloy. Scripta Mater. 58 (**2008**) 449-452.

[TR01] D.F. Teter, I.M. Robertson, H.K. Birnbaum, Acta Mater. 49 (**2001**) 4313.

[TT76] J.K. Tien, A.W. Thompson, I.M. Bernstein, R.J. Richards, Hydrogen transport by dislocations, Metall. Trans. A 7 (**1976**) 821-829.

[U70] E.E. Underwood. Quantitative stereology. Reading, (MA): Addison-Wesley; **1970**.

[W97] H. Wipf, Hydrogen in Metals Ill, H. Wipf, ed., Springer-Verlag, New York, 1**997**, PP. 51-91.

[WB12] J. Wang, I.J. Beyerlein, Atomic structures of symmetric tilt grain boundaries in hexagonal close packed (hcp) crystals, Model. Simul. Mater. Sci. Eng. 20 **(2012)** 024001.

[WH53] G.K. Williamson, W.H. Hall, Acta Metall. 1 (**1953**) 22.

[WH09] J. Wang, J.P. Hirth, C.N. Tome, $(\bar{1}012)$ Twinning nucleation mechanisms in hexagonal-close-packed crystals, Acta Mater. 57 **(2009)** 5521-5530.

[WS56] G.K. Williamson, R.E. Smallman, Philos. Mag. 1 (**1956**) 34.

[WY11] L. Wang, Y. Yang, P. Eisenlohr, T.R. Bieler, M.A. Crimp, D.E. Mason, Twin nucleation by slip transfer across grain boundaries in commercial purity titanium. Metall. Mater. Trans. A 41 **(2011)** 421-430.

[Y81] M.H. Yoo, Slip, twinning, and fracture in hexagonal close-packed metals, Metall. Trans. A 12 (**1981**) 409-418.

[YC10] D.K. Yang, P. Cizek, P.D. Hodgson, C.E. Wen, Microstructure evolution and nanograin formation during shear localization in cold-rolled titanium, Acta Mater. 58 (**2010**) 4536-4548.

[YS10] Y. Yagodzinskyy, T. Saukkonen, S. Kilpelainen, F. Tuomisto, H. H Anninena, Scripta Mater. 62 (**2010**) 155.

[YW11] Y. Yang, L. Wang, C. Zambaldi, P. Eisenlohr, R. Barabash, W. Liu, M.R. Stoudt, M.A. Crimp, T.R. Bieler, Characterization and modeling of heterogeneous deformation in commercial purity titanium, JOM 63 (**2011**) 66-73.

[Z74] U. Zwicker, Titanium and Titanium Alloys, Springer-Verlag, Berlin, **1974**.

[ZD11] S.V. Zherebtsova, G.S. Dyakonova, A.A. Salemb, S.P. Malysheva, G.A. Salishchev, S.L. Semiatin, Evolution of grain and subgrain structure during cold rolling of commercial-purity titanium, Mater. Sci. Eng. A 528 (**2011**) 3474-3479.

Conclusions and Perspectives

Conclusions

Based on the investigation of the hydrogen-induced microstructural evolutions and their effects on the mechanical properties, cold rolling behavior and recrystallization of α-titanium Ti50A and β-21S β-metastable titanium alloy, the main conclusions are summarized below:

(1) Combining the experimental characterization techniques of XRD, SEM-EBSD and TEM, the microstructural analyses of α-titanium Ti50A electrolytically charged with hydrogen revealed the precipitation of two types hydrides (δ-TiH_x, ε-TiH_2) in the α-phase matrix, with a volume fraction of these hydrides increasing with the charging time. The broadening of the diffraction peaks corresponding to α-phase indicated an increase in the density of dislocations necessary to accommodate the misfit between hydrides and the matrix. These hydrides precipitate from the grain boundaries having new orientation relationships (ORs) with the α-phase, and the study of the corresponding OR plane and OR direction stereographic projections of the two phases in the pole figures study enable the determination of three new orientation relationships between the hydride δ-TiH_x and the hexagonal matrix. Moreover, the correlation between the rolling texture and the hydride precipitation was also established. It was found that the existence of the rolling texture facilitated the precipitation of δ-hydride following the OR2-type orientation relationship. Microhardness tests showed that the hardness value increased as the hydrogen charging time increased due to the increased hydride volume fraction. A marked variation in the microhardness from the surface to the mid-section of the samples suggested the existence of a hydrogen concentration gradient attributed to the prevention of hydrogen diffusion by the hydride layers. Despite the increase in the microhardness, the occurrence of pop-ins in the load-penetration depth curves obtained by nanoindentation was proposed as the evidence of a lowering of the activation energy required for dislocations nucleation in the α-phase owing to the presence of the hydrogen atoms dissolved in the solid solution. Under the compression loading, the observation of slip traces and tension twins in the grains containing hydrides, suggested that the hydrides had a certain ability to accommodate the imposed shear strain, depending on the orientation relationships between the matrix and the hydrides as well as on the hydride thickness. Despite evidence of the direct correlation between the nucleation of twinning and the hydride, the growth of deformation twins appeared to be dependent upon the presence of hydrides in the α-grains.

(2) In β-titanium β-21S alloy, the combined analyses by means of XRD, SEM-EBSD and TEM showed that, the stability of the β-phase cannot be increased monotonically with increasing hydrogen content upon cooling. In the hydrogen concentration range 0.052 < H/M < 0.300, the observation of a single β-phase indicated that the addition of hydrogen suppressed the decomposition of the β-phase during cooling, while as the hydrogen concentration increased to ratio H/M = 0.460, the observation of a considerable number of plate-shape martensites α" suggested that a high content of hydrogen atoms can weaken the interatomic bonds between the matrix atoms, therefore brought to a large lattice shear causing the martensite transformation. Despite the mechanism responsible for this martensite transformation is still unclear, it was proposed that a large internal stress generated by the filling of the hydrogen atoms at the interstitial sites and the segregation of hydrogen atoms at grain boundaries, gave rise to the additional shuffling of titanium atoms in alternate $\{110\}_\beta$ planes, resulting in a C-centred orthorhombic crystal structure. Tensile and compressive tests showed that, hydrogen had distinct effect on the tensile and compressive properties of β-21S alloy. Under tension loading, a monotonous decrease of the yield strength with the increasing hydrogen concentration indicated that the addition of hydrogen decreased the required stress for dislocations slip and the cohesive energy of grain boundaries. In the case of compression test, the change of yield strength with increasing of hydrogen concentration was characterized by three distinct stages. The first two stages could be explained based on the defactant concept. In the first stage (0.052 < H/M < 0.160), the rate determining step could be attributed to the formation of dislocation kink pairs, in which the kink formation energy was reduced by hydrogen addition, therefore leading to a softening. In the second stage (0.160 < H/M < 0.300), the segregation of a large amount of hydrogen atoms to the kink pairs was supposed to exert an increasing solute drag on the moving kinks, therefore resulting in a hardening. In the last stage (H/M > 0.380), the abrupt loss of yield strength was associated with the formation of brittle martensite phase α".

(3) The effect of hydrogen on the cold rolling behavior of hydrogenated Ti50A under a low applied strain (ε_{eq} = 0.12) showed that, the formation of tension twin $\{10\bar{1}2\}\langle\bar{1}011\rangle$ can be facilitated due to the increase of the c/a ratio of the hexagonal lattice owing to the hydrogen addition as well as the existence of local stress generated by the hydride precipitation. Upon further increase of the rolling strain to ε_{eq} = 0.80 (50% thickness reduction), twinning became almost saturated whereas an obvious microstructure refinement was observed in the pre-

hydrogenated Ti50A-H as compared to that of hydrogen-free Ti50A samples. The observation of microstructural refinement was explained by an increase in the generation of high angle boundaries (HABs) around the hydride phases. In addition, our observation revealed a large number of geometrically necessary dislocations (GND), which were produced to accommodate the strain incompatibility between the hydride and matrix. The texture evolution showed that the presence of hydrogen/hydride rotated the c-axis became parallel to the ND, indicating that the basal slip became dominant in the presence of hydrogen/hydrides in the α-grains.

The influence of hydrogen upon cold rolling of the β-21S alloy revealed contradictory effects on the cold rolling behavior depending on the hydrogen concentrations. In the hydrogen concentration range $0.052 < H/M < 0.160$, the lattice dissolved hydrogen atoms enhanced the dislocations mobility and density leading to an pronounced microstructure refinement as the hydrogen concentration increased. While as the hydrogen concentration increased to $H/M = 0.215$, the observation of less deformed β grains as well as the presence of the micro-cracks indicated that the hydrogen-induced solid solution strengthening mechanism became dominant. On the other hand, the well-developed bcc rolling texture suggested that, the addition of hydrogen promote the development of the texture.

The combined effect of hydrogen and cold rolling deformation on the recrystallization behavior of the annealed Ti50A showed that, the pre-hydrogenated Ti50A contained a larger fraction of new recrystallized strain-free grains in comparison to that of uncharged samples. In the case of β-21S alloy, an increasing fraction of recrystallized grains in the annealed samples was found to be produced as the hydrogen concentration increased. Although the direct/intrinsic effect of hydrogen on recrystallization cannot be established yet, the results of this study suggested that the presence of hydrogen is favorable for the formation of new strain-free grains.

Perspectives

Though this study has been able to point out certain effects oh hydrogen on commercially pure Ti and metastable β-Ti alloy, it is far from being complete and arose a few questions that would need to be answered in future work.

1. The role of the hydride precipitation could be further elucidated by complementary microstructural observations. For example, mechanical tests should be performed at intermediate level of deformation in order to clearly investigate the relationship between hydride kinetics,

dislocation gliding and twin nucleation. The role of the crystallographic texture on the hydride precipitation could be clarified by performing such investigation on highly textured samples.

2. The role of the internal stress generated in the α-grains owing to the hydride precipitation on the twinning nucleation could be investigated by in-situ observation combining fine grid-marking on sample prior to electrolytically hydrogen-charging. This experimental investigation could be completed by modeling using, for example, the self-consistent model.

3. The observation of martensite α" in the bcc structure has been hindered by the lack of thermodynamic stability. Does it result from the stress-relaxation or the energy from the Ga ions during sample preparation? Also, the intrinsic factor for the transformation from martensite α" to athermal omega ω phase taking place during ionic micromachining needs to be further explored in the view of the interfacial and elastic strain energy. Thus the mechanism behind the hydrogen-induced martensite transformation in β-21S alloy requires still experimental investigation as well as simulation such as ab-initio calculations.

4. The determination of the recrystallization temperature and time has not been possible by the thermal analyses e.g. DSC, which has made the investigation difficult and time consuming. The temperatures applied during this study were determined by combining results published in scientific articles and a trial-and-error procedure. Complementary investigation in a wider range of temperature and time should be performed. In addition, the variation and particularly the recovery of the mechanical properties upon recrystallization treatment need to be studied thoroughly.

Appendix

Appendix A: Hydrogen diffusion coefficient determination by electrochemical method

To reveal the diffusion behavior of hydrogen in β-21S alloy at room temperature, the hydrogen was introduced into the sample by means of electrolytic method, as used for the pure titanium Ti50A. Electrochemical techniques enable the determination of the diffusion coefficient, details of the methods can be found in ref. **[WH81]**. In this case, the potential difference between the sample electrode and the platinum anode was monitored as a function of time while a constant current density was applied. The measured potential difference at the electrolytic cell provides a measure of the activity of the diffusing species, in this case hydrogen in the sample electrode, here the β-21S specimen.

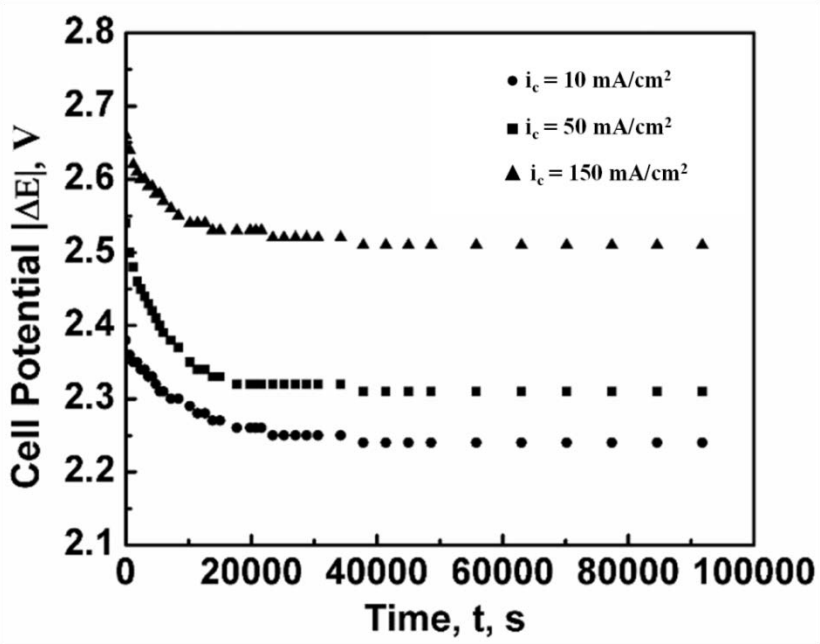

Figure A. 1 Variation of the cell potential difference with time for 24h hydrogen charging under different current densities.

The cell potential difference decreases with increasing dissolution of hydrogen on the electrode surface. The determination of the diffusion coefficient of hydrogen in β-21S titanium alloys then, is obtained by solving the Fick's second law as expressed in equation **(A-1)**. **Figure A. 1** shows the plots of absolute value of the cell potential difference $|\Delta E|$, between the sample electrode and the inert platinum anode as a function of time, i.e., for 24h hydrogen charging at room temperature under different current densities. It can be observed that the absolute potential difference $|\Delta E|$ clearly decreases with time for short times and became nearly linear for long

time durations. Since no hydrogen evolution or other corrosion processes were observed, the electrode potential and thereby, the cell potential, before the formation of hydride during electrolytic charging process, is attributed purely to diffusion **[SW00]**. In this case, then, the plots of the absolute value of the cell potential $|\Delta E|$ as a function of time is valid option for calculating the values of the diffusion coefficient of hydrogen in the β-21S titanium alloy samples using the shape of those plots before hydride formation takes place.

With the assumption of a constant value of D for small changes in composition, the Fick's second law (**A-1**) is solved for the initial (**A-2**) and boundary conditions (**A-3**) (**A-4**). Linear fits based on equation (**A-5**) for E *vs.* $t^{1/2}$ and equation (**A-6**) **[SW00]** for E *vs.* t were made from our data shown in **Figure A. 1**. The values of the regression coefficients for these fits were of the value of $R^2 > 0.9$. The E *vs.* $t^{1/2}$ curves are plotted in **Figure A. 2**. The values of hydrogen diffusion coefficients, D, can then be calculated using equations **(A-5)** and **(A-6)** **[SW00]** and those values are given in **Table A. 1**.

$$\frac{\partial C}{\partial t} = \frac{\partial}{\partial x}\left(D\frac{\partial C}{\partial x}\right) \qquad (1)$$

$$C = C_0 \quad 0 \ll x \ll L, \quad t = 0 \qquad (2)$$

$$-D\frac{\partial C}{\partial x} = \frac{I}{zFS} \quad x = 0, \quad t > 0 \qquad (3)$$

$$\frac{\partial C}{\partial x} = 0 \quad x = L, \qquad t \gg 0 \qquad (4)$$

$$\frac{dE}{dt^{1/2}} = \frac{2IV_m}{zFS(\pi D)^{1/2}}\left(\frac{dE}{d\delta}\right) \qquad (5)$$

$$\frac{dE}{dt} = \frac{IV_m}{zFSL}\left(\frac{dE}{d\delta}\right) \quad t > \frac{L^2}{D} \qquad (6)$$

Here, $(dE/d\delta)$ is the variation in potential of sample electrode with change in the hydrogen concentration, I is the current density, z is the change number of the electro-active diffusing species, F is the Faraday constant, S is the sectional area common to both the electrode and electrolyte, L is the sample half-thickness and V_m is the molar volume of the sample. Since the values of D are very similar for all three current densities, charging current density seems to have a negligible effect on D and hence lattice diffusion is believed to be rate controlling in the diffusion process. In comparison with the reported values of the diffusion coefficient calculated

for β-21S at 200 °C ($D = 0.75 \times 10^{-9}$ cm^2/s) **[CD00]** by gas hydrogen charging, the value obtained in this work by means of electrolytic charging are found to be slightly larger.

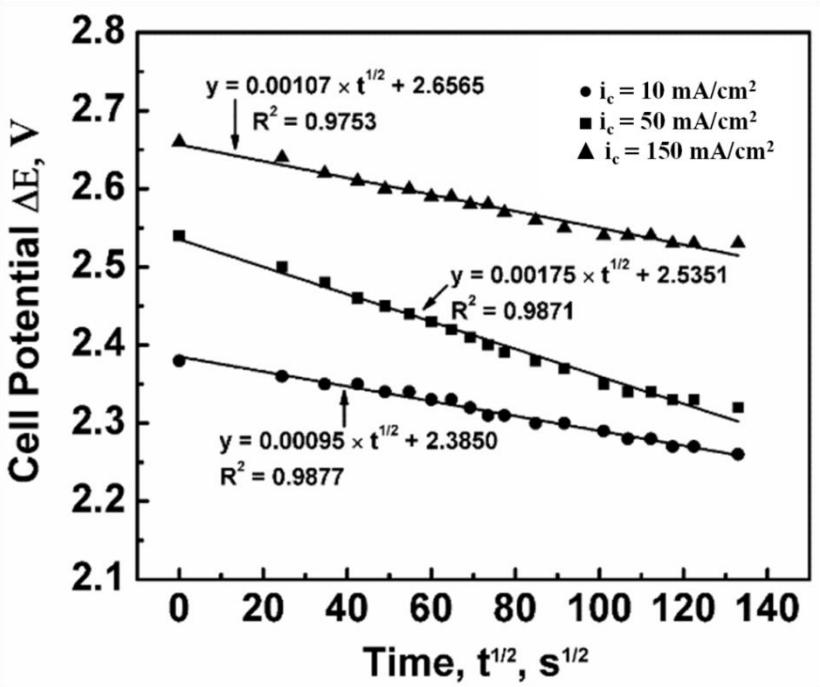

Figure A. 2 Potential vs. time curves at short times.

Table A. 1 Values of the hydrogen diffusion coefficient D for 24 h hydrogen charging under different charging current densities

Current densities mA/cm^2	10	50	150
D, cm^2/s	7.25×10^{-9}	6.81×10^{-9}	4.35×10^{-9}

Appendix B : Effect of hydrogen on compression behavior of Ti50A

In the current work, the effect of hydride on the mechanical behavior of pure titanium Ti50A was also investigated by means of compression test. The samples containing different hydrogen contents were compressed to the engineering strain up to a maximum of 15% (shown in **Figure B. 1**). In order to have a plane strain condition, four plates were glued to each other layer by layer. The thickness of the glue was estimated to be less than 1 μm. Therefore, its effect on the compressive behavior of Ti50A can be neglected.

The engineering strain-stress and true strain-stress curves of as-received (C_H=26ppm) and hydrogenated specimens are shown in **Figure B. 1**. The insert chart gave an example of the compression tests repeared for two times at each hydrogen concentration. The compressive strength and strain hardening increased with increasing hydrogen concentrations. This trend is consistent with the results reported by Briant **[BW02]** in Ti40. The increase of compression strength is due to the superimposed strenghtheing caused by hydride and hydrogen in the solid solution. Since the precipitation of hydrides is due to hydrogen supersaturation at defects, there exists a hydrogen-riched region surrounding the hydrides. The interstitially dissolved hydrogen causes the lattice distortion and then makes it difficult for the dislocations to pass through, therefore brings a solution strengthening to Ti50A. On the other hand, hydrides acting as obstacles for the dislocations slip resulted in the dislocations piles-up at the interface between hydride and α phase.

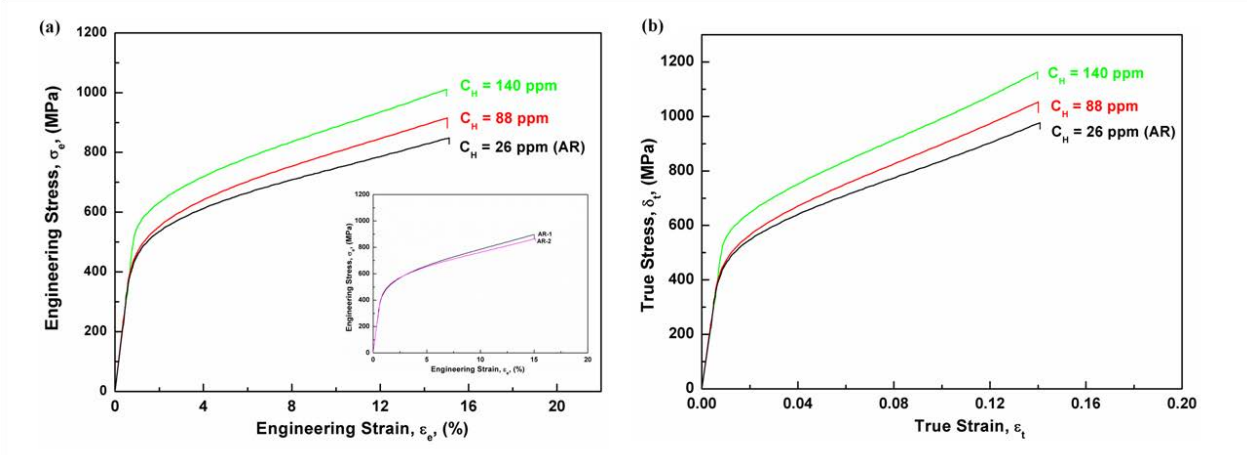

Figure B. 1 Engineering Stress-Strain curves (a) and true strain-stress curves of Ti50A with different hydrogen concentration

Appendix C : Effect of hydrogen on the friction and wear behavior of Ti50A and β-21A

C1 Introduction

The above data have demonstrated that the presence of hydrogen could affect the mechanical properties such as the hardness, yield stress and ductility of both Ti50A and β-21S, as well as the microstructural evolutions during cold rolling. Friction between the rolls and the metal strip being deformed is an important parameter since it influences the rolling force and other rolling process parameters and the final thickness and planarity, too. However the exact mechanism of friction is not fully understood. Different methods have been proposed to measure the friction coefficient along the roll bite in both cold and hot rolling **[L02]**. To complement the investigation on the effect of hydrogen on the rolling behavior, it as important to evaluate by a conventional tribological test the dependency of sliding friction with the hydrogen concentration.

A few tribological studies have already pointed out the decrease of the coefficient of friction in hydrogen environment. In an investigation on the sliding friction of Armco Fe against Armco Fe, Grzeskiewicz **[G88]** obtained a value of the coefficient of friction measured under hydrogen atmosphere of about 0.20, which corresponded to a value about 26% lower than the value measured under nitrogen environment and about 16% lower than that of the friction performed in laboratory air. This reduction of the coefficient of friction accompanied by a reduced 'stick-slip' behavior as well as a reduced metal transfer was interpreted by a lower value of surface energy for tests performed under hydrogen atmosphere.

More recently, Oshima et al. **[OT12]** compared the friction and wear of DLC coating against ∅4 mm ball 100Cr6 in hydrogen atmosphere with that of friction under vacuum and in air. They observed that the coefficient of friction under vacuum atmosphere was extremely high with a value reaching 2 and accompanied by a severe wear. In contrary, the coefficient of friction in hydrogen atmosphere was found to be even lower than that of the friction in air with a value less than 0.01 when the hydrogen pressure reached 5000Pa. The wear in hydrogen atmosphere was attributed to the embrittlement effect induced by hydrogen.

Though the experiments described above were performed in hydrogen atmosphere, Zhou et al. **[ZL10]** compared the tribological properties of samples charged by electrolytic method with those of uncharged samples. They investigated the friction behavior of 30 μm thick Ni-P coatings produced in both crystalline and amorphous states against Si_3N_4 ball of 4.75 mm, under a sliding

velocity of 0.02 m/s, and a load 3 N. For both crystalline and amorphous coatings charged with approximately 520 ppm, in the early sliding distance the coefficient of friction was found to be significantly lower than the coefficient of friction of un-charged samples. However the coefficient of friction started to increase progressively to reach value of un-charged samples. These coatings being intrinsically brittles, authors assumed that the absorbed surface layer lubricates the surfaces.

Sliding friction tests were thus performed using a pin-on-disk type facility on Ti50A and β21S charged with different hydrogen concentration and the tribological behavior is compared with those of un-charged samples.

C2 Experimental procedure

Figure C. 1 Tribological test facility

The equipment used for this investigation was the Pin-on-disc TRN SN1000014721 of the TriTex company. Tests were performed in air with the following tribology testing conditions :

- reciprocal motion
- 100Cr6 steel balls
- P = 2 N
- sliding distance = 10 mm
- frequency = 0,5 Hz (v_{max} = 15,7 mm/s)
- number of cycle = up to 1000 cycles

(≈ 20 meters)

The samples were charged with hydrogen based on the same methods as those described in Chapter 2, i.e., electrolytic method for Ti50A and gas method for β-21S. Before tests, the surfaces of the samples were polished up to 4000 SiC emery paper. After tests, the wear tracks were observed by optical microscopy and secondary electron microscopy. Values of friction and wear were averaged on a minimum of two tests.

C3 Results

C3-1 Effect of hydrogen on the friction behavior of Ti50A

Figure C. 2 presents the variation of the coefficient of friction of un-charged and charged Ti50A for tests performed on a sliding distance up to 0,6 m.

For the un-hydrogenated Ti50A, the friction was found to have a relatively constant behavior with value between 0.10 and 0.15. For Ti50A samples charged with 80 ppm H, from the initial

sliding distance, the value increased slightly to reach a constant value of about 0.22. In the sample with higher H concentration, the value of the coefficient of friction was found to be larger with stabilized value of about 0.32, suggesting the coefficient of friction recorded during short sliding distance increased proportionally to the H concentration.

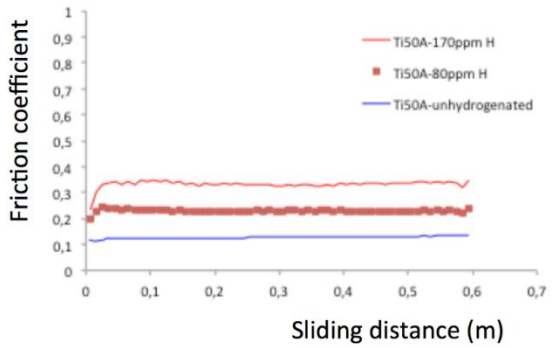

Figure C. 2 : Variation of the coefficient of friction for un-hydrogenated and hydrogenated Ti50A with 80 and 170 ppm on a short sliding distance (up to 0,6 m).

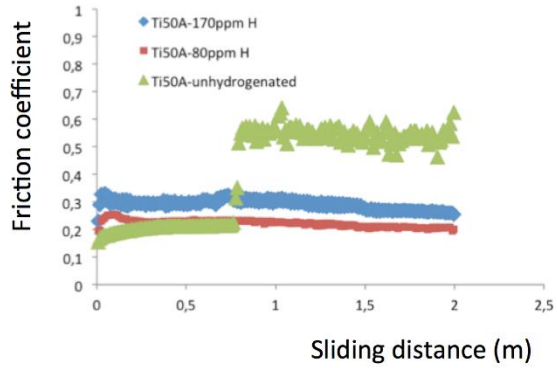

Figure C. 3 Variation of the coefficient of friction for un-hydrogenated and hydrogenated Ti50A with 80 and 170 ppm on a short sliding distance (up to 2 m).

The results of friction tests performed on a distance up to 2 m are presented in **Figure C. 3**. In the early stage of the friction, i.e., sliding distance inferior to 0.6 m, the value of the coefficient of friction are in agreement with those presented in **Figure C. 2**: the coefficient of friction increased as the H concentration increased. However it can be observed that the coefficient of friction of the un-hydrogenated Ti50A increased abruptly for a sliding distance of about 0.75-0.8 meters. In comparison, the coefficient of friction remained approximately constant for both hydrogenated Ti50A samples.

In the **Figure C.** 4, the friction behavior of the un-hydrogenated Ti50A followed the exact pattern as described above characterized by a initially low coefficient of friction followed by a sharp increase to about 0.5-0.6 after a sliding distance inferior to 1 m. For the Ti50A charged with 80 ppm H, the friction behavior is found to be similar to that reported in **Figures C.** 2 and 3, e.g., a friction coefficient of about 0.2 as long as the sliding distance is inferior to 7 m. Then beyond this sliding distance of 7 m, the coefficient of friction suddenly increased to reach a value similar to that of the un-hydrogenated sample, i.e., between 0.5 and 0.6. In contrast, the friction behavior for the Ti50A charged with 170 ppm H, remained constant up to 2 m sliding distance.

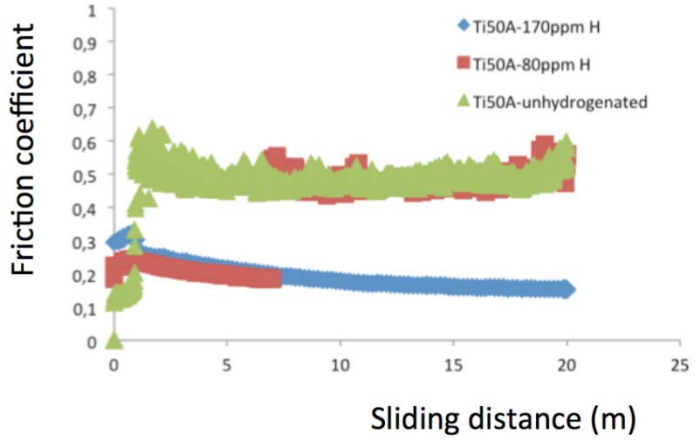

Figure C. 4 Variation of the coefficient of friction for un-hydrogenated and hydrogenated Ti50A with 80 and 170 ppm on a short sliding distance (up to 20 m).

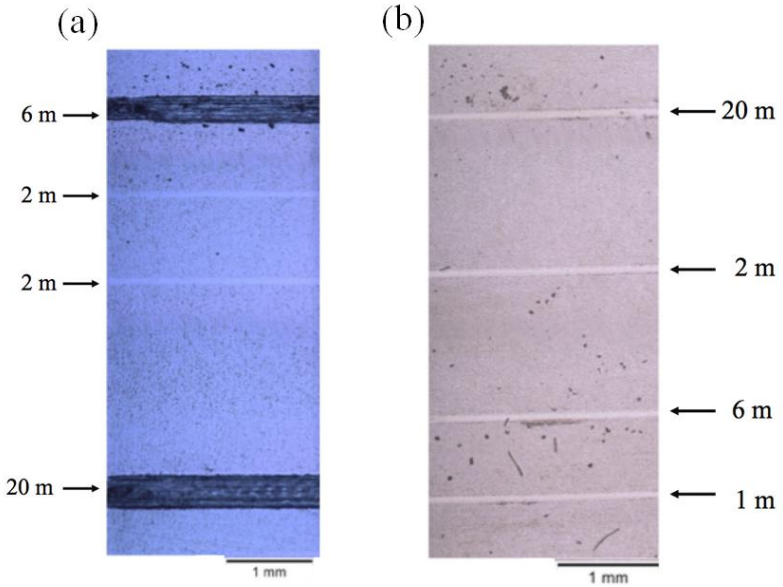

Figure C. 5 Wear track on : a) Ti50A + 80 ppm H sample, b) Ti50A + 170 ppm H sample.

Some of the wear tracks corresponding to different friction test conditions are shown in **Figure C.** 5. These figures clearly demonstrated the correlation between the low values of the coefficient of friction with the wear behavior. All the tests those coefficients of friction were lower than 0.5 are characterized with a fine wear track appearing with a clear color in **Figure C.** 5a) et 5b). In contrary, all the tests presenting a sharp increase of the coefficient of friction displayed a wide wear track corresponding to an important wear loss that will be detailed in the following paragraph.

C3-2 Effect of hydrogen on the friction behavior of β-21S

Figure C. 6 show the friction behavior of un-hydrogenated and hydrogenated β-21S on a sliding distance inferior to 1 m. The initial value of the coefficient of friction for the un-hydrogenated β-21S is relatively low, then that value increased drastically beyond 1, to then progressively decreased. The hydrogenated β-21S displayed a very different behavior characterized by a progressive increase of the coefficient of friction from 0.15, as it was obtained for the un-hydrogenated β-21S to reach value fluctuating between 0.5 and 0.6. It is important to notice that the coefficient of friction of the hydrogenated β-21S is slightly lower than that of the un-hydrogenated samples.

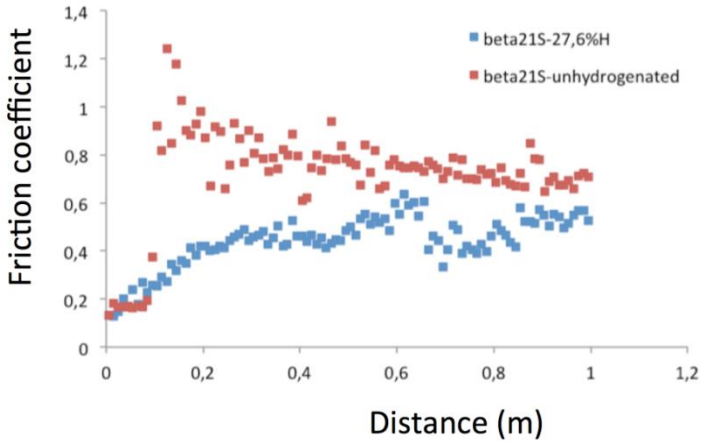

Figure C. 6 Variation of the coefficient of friction for un-hydrogenated and hydrogenated β-21S with 27.6% H on a short sliding distance (up to 1 m).

For tribological tests performed till 2 m (**Figure C.** 7) and 20 m (**Figure C.** 8), the friction behavior for both un-hydrogenated and hydrogenated β-21S is found to be similar to that presented in **Figure C.** 6, i.e., the friction behavior of the hydrogenated β21S was characterized

by a progressive increase of the coefficient of friction with values slightly lower than those of the un-hydrogenated samples. In comparison to the observations made for the Ti50A (**Figure C.** 5), the wear tracks of the hydrogenated β-21S were not significantly different than those of the un-hydrogenated β-21S.

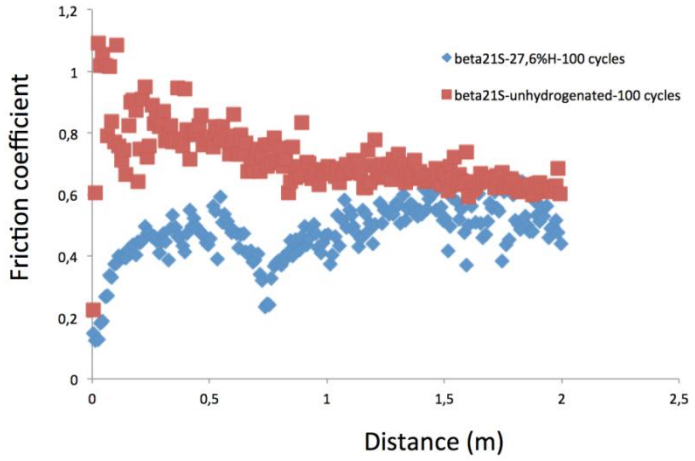

Figure C. 7 Variation of the coefficient of friction for un-hydrogenated and hydrogenated β-21S with 27.6% H on a short sliding distance (up to 2 m).

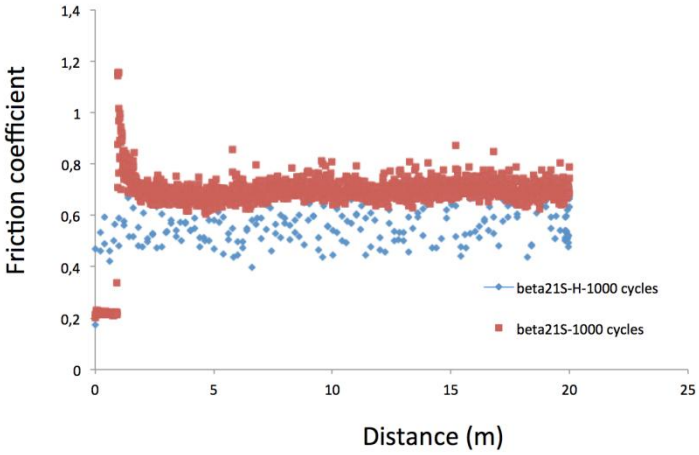

Figure C. 8 Variation of the coefficient of friction for un-hydrogenated and hydrogenated β-21S with 27.6% H on a short sliding distance (up to 20 m).

C3-2 Hydrogen effect on wear property

The wear loss was estimated by measurements of the volume of material removed in the wear track and the results are plotted in **Figure C.** 9 and 10 as a function of the sliding distance for respectively Ti50A and β21S.

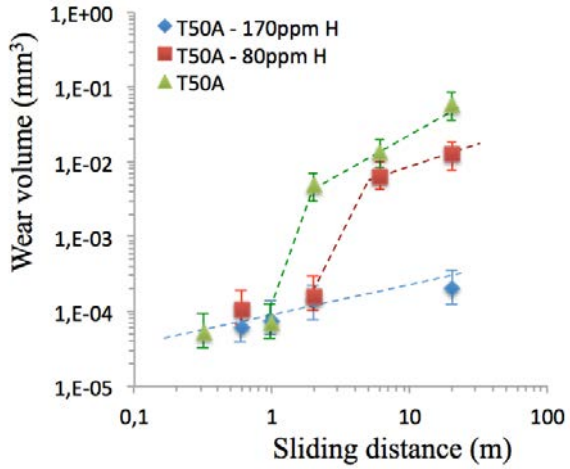

Figure C. 9 : Variation of the wear volume with the sliding distance for un-hydrogenated and hydrogenated Ti50A

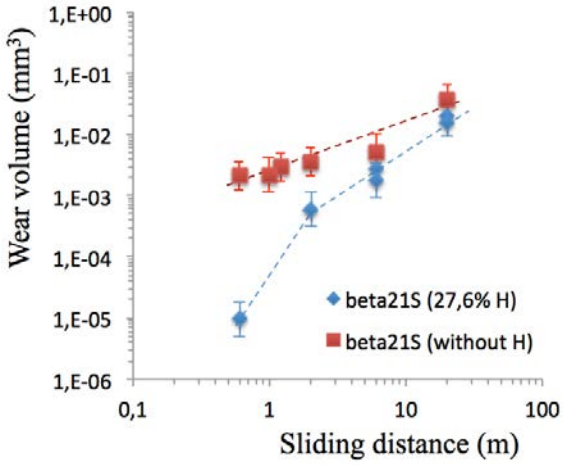

Figure C. 10 : Variation of the wear volume with the sliding distance for un-hydrogenated and hydrogenated β-21S

Figure C. 9 indicates that for short sliding distance, the wear loss data of un-hydrogenated and hydrogenated Ti50A are superimposed on a single line, when displayed in bi-logarithmic diagram. However for sliding distance larger than 1 m, the wear loss of the un-hydrogenated Ti50A increased drastically. Similar trend is observed for sliding distance larger than 2 m for Ti50A+80 ppm H. In contrast, the wear loss in this range of sliding distance remained more of one order magnitude lower for the Ti50A+170 ppm H. These results clearly demonstrated that hydrogenation of the Ti50A reduced both the coefficient of friction and the wear within the sliding distance investigated in this study. Indeed the friction behavior of the Ti50A is characterized by an initially low coefficient of friction. And only after a short distance of 'running-in' the friction showed an abrupt increase. As hydrogen is introduced from the outer surface of the Ti50A, despite a minor increase of the coefficient of friction, the 'running-in distance leading to an sharp increase of coefficient of friction seems to be retarded, and the larger the H concentration the more retarded is the running-in stage. In this preliminary investigation, the sliding distance was limited to 2 m however further tests should be undertaken on a longer sliding distance in order to correlate the running-in distance with the hydrogen concentration. Though the mechanism responsible for the increase of the running-in distance is not explained yet, these results demonstrated a beneficial effect of hydrogen on the friction behavior of the Ti50A.

The effect of hydrogen on the friction and wear properties of the β-21S is wholly different that that of hydrogen in Ti50A. As shown in **Figure C.10**, the friction of the un-hydrogenated β-21S alloy also displays a short running-in stage followed but a marked increase of the coefficient of friction to value beyond 1 and then by a progressive decrease to stabilized around 0.7. The charging of hydrogen does not lead to an increase of the running-in stage as it was for the Ti50A but to a progressive increase of the coefficient of friction toward values moderately lower than those of the un-hydrogenated β-21S alloy. For the β-21S alloy, the charging of hydrogen enabled the reduction of both the coefficient of friction and wear loss. Further investigations would be worth pursuing in order to comprehend the role of hydrogen on the tribological properties.

Conclusion

These preliminary tribological tests revealed a significantly improved friction behavior and wear resistance of Ti50A owing to H charging for concentration larger than 70 ppm under testing conditions defined with a load of 2N, an reciprocal motion at a frequency of 0.5 Hz against 100Cr6 ball and a sliding distance up to 20 m. A moderate effect of hydrogen on the friction and wear behavior was recorded for the β21S. A systematic investigation should be performed to get a better understanding on the effect of hydrogen on the friction behavior of both α- and β-phase Ti alloys.

References

[BW02] C.L. Briant, Z.F. Wang and N. Chollocoop, Hydrogen Embrittlement of Commercial Purity Titanium, Corros. Sci. 44 (**2002**) 1875-1888.

[CD00] H.J. Christ, M. Decker, S. Zeitler, Metall. Mater. Trans. A 31 (**2000**) 1507-1517.

[SW00] P.A. Sundaram, E. Wessel, H. Clemens, et al., Determination of the diffusion coefficient of hydrogen in gamma titanium aluminides during electrolytic charging, Acta mater. 48 **(2000)** 1005-1019.

[WH81] C.J. Wen, C.Ho, et al., Int. Met. Rev., 5 **(1981)** 253.

[L02] Y.J. Liu, Friction at Strip-roll interface in cold rolling, PhD thesis, University of Wollongong, 2002

[G88] R. Grzeskiewicz, Master thesis, Virginia Polytechnic Institute, 1988.

[OT12] K. Oshima, Y. Tokuta, R. Tsuboi, S. Sasaki, M. Kawaguchi, Effect of surrounding hydrogen gas on friction and wear characteristics of DLC films in 15th International Conference on Experimental Mechanics, Porto/Portugal, 22-27 July 2012.

[ZL10] Q.J. Zhou, J.X. Li, W.Y. Chu, International Journal of Minerals, Metallurgy and Materials, 17 (2) **(2010)** 241.

1 Introduction

Avec l'épuisement des ressources naturelles, l'humanité est à la recherche d'autres sources d'énergie. L'hydrogène est considéré comme une des futures sources futures et il est très possible que l'économie de l'hydrogène se réalise au cours des 50 prochaines années. Dans un tel scénario, la production, le stockage, le transport et l'utilisation de l'hydrogène nécessiteront des développements à plus grande échelle.

Le titane a une forte affinité avec l'hydrogène, et de nombreux travaux ont étudié les aspects de stockage et de dégradation des propriétés mécaniques liée à l'hydrogène. Heureusement, la réaction de l'hydrogène avec du titane est réversible en raison d'une enthalpie positive de la solution en titane [W97, M51] permettant la désorption de l'hydrogène durant un traitement sous vide à haute température. Par conséquent, l'hydrogène comme élément d'alliage temporaire a été utilisé pour améliorer la mise en forme des alliages de titane, ces traitements conduisant à une modification de la microstructure et des propriétés mécaniques [FS04, ZZ97]. Récemment, un nouveau concept introduit par Kirchheim [K09] et désigné par le terme anglais « defactant » (*un DEFect ACTing AgeNT étant défini comme atome de soluté se plaçant autour des défauts des structures cristallines jouant un rôle similaire à celui d'un agent tensioactif sur les surfaces*) a permis d'expliquer les mécanismes de fragilisation par une réduction de l'énergie de formation de défauts par addition d'hydrogène [BV10].

Par conséquent, si un atome d'hydrogène, d'abord dissous en tant que defactant dans la structure d'un matériau métallique permettant faciliter la formation de lacunes, des dislocations et des défauts d'empilement lors d'une déformation à froid est ensuite éliminé, il est connu que la densité de dislocation est augmentée et que les propriétés de façon concomitante par exemple comme la dureté et résistance mécanique sont améliorées. Cependant, peu études se sont intéressées à l'effet de l'hydrogène sur le comportement de déformation en laminage à froid et la recristallisation des alliages de titane. Par conséquent, nous avons entrepris ce travail dans le but d'étudier l'évolution de la microstructure induite par l'introduction d'hydrogène et ses effets sur les propriétés mécaniques, la déformation en laminage à froid et la recristallisation de deux alliages de titane de structures cristallographiques différentes. Cette étude a été réalisée en combinant les techniques expérimentales d'analyses de diffraction des rayons-X, d'observations

au microscope électronique à balayage (MEB) équipé de la technique EBSD (Electron BackScattered Diffraction) et de microscope électronique à transmission (MET).

2 Materials and Experiments

Dans le présent travail, les deux alliages de titane utilisés sont le titane commercialement pur Ti50A (ASTM 2) de structure cristallographique hexagonale et l'alliage de titane β-métastable connu par la désignation β-21S, de composition Ti-15Mo-3Nb-3Al-0.2Si et de structure cristallographique cubique à face centrée. La **Figure 1** résume la procédure expérimentale.

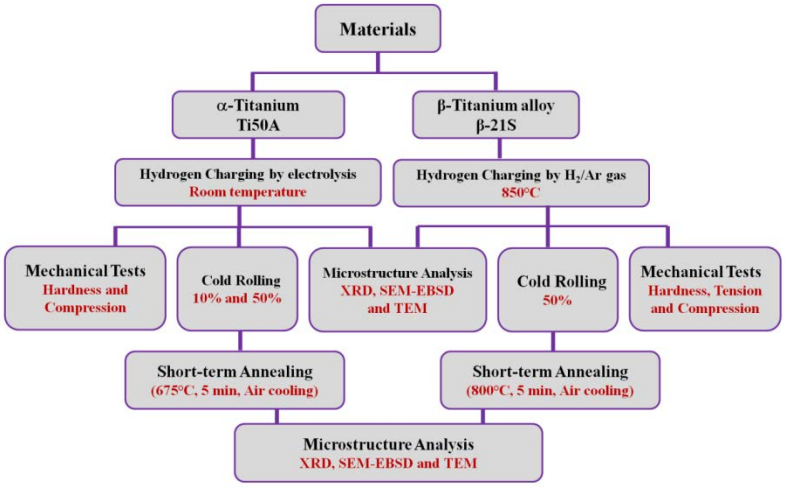

Figure 1 Illustration de la procédure expérimentale utilisée dans cette étude

L'hydrogène a été introduit dans les échantillons par deux méthodes différentes : une méthode électrolytique pour le Ti50A (**Figure 2**) et sous atmosphère de gaz d'hydrogène pour le β-21S. Pour des chargements induisant différentes concentrations en hydrogène, des analyses microstructurales et des essais mécaniques (microdureté, nanoindentation, traction et compression) ont été effectués dans le but d'élucider l'effet de l'hydrogène sur les microstructures et propriétés mécaniques du Ti50A et du β-21S.

Des essais de laminage symétrique à froid ont également été réalisés sur les échantillons pré-hydrogénés. Des traitements de recuit de courte durée ont été appliqués après laminage à froid, pour étudier la recristallisation du Ti50A et de l'alliage β-21S. L'interdépendance entre hydrogène, microstructure et propriétés a pu être révélée grâce aux outils de caractérisation microstructurale de diffraction des rayons-X, microscope électronique à balayage de haute résolution équipé de la technique EBSD et microscope électronique à transmission).

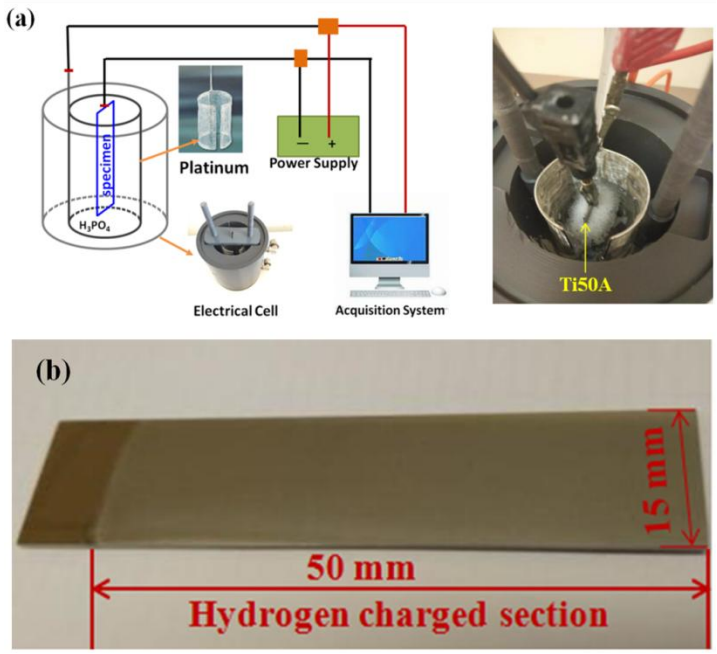

Figure 2 (a) Schéma du système de chargement en hydrogène, (b) photographie d'un échantillon Ti50A hydrogéné

3 Évolutions microstructurales induites par l'hydrogène et leurs effets sur les propriétés mécanique

3.1 Évolutions microstructurales induites par l'hydrogène et leurs effets sur les propriétés mécanique du Ti50A

Comme il est montré sur la **Figure 3**, la courbe de diffraction des rayons X obtenu sur un échantillon après 72 heures de chargement en hydrogène et correspondant à une concentration d'environ 60 ppm, met en évidence la présence de deux types d'hydrures, à savoir le δ-TiH_x et le ε-TiH_2. Ces hydrures ont été détectés sous la surface des échantillons dans une région dont l'épaisseur était approximativement de 20 ± 2 µm. L'hydrure δ-TiH_x ($1,5 \leq x \leq 1,99$) a un structure cristallographique cubique face centrée (structure CaF_2, de paramètre de maille a = 0,4445 nm) avec des atomes d'hydrogène occupant les sites interstitiels tétraédriques, tandis que l'hydrure ε-TiH_2 a une structure quadratique à base centrée (de paramètres de maille a = 0,312 nm et c = 0,418 nm, JCPDS-PDF 9-371) [WE02, LX13].

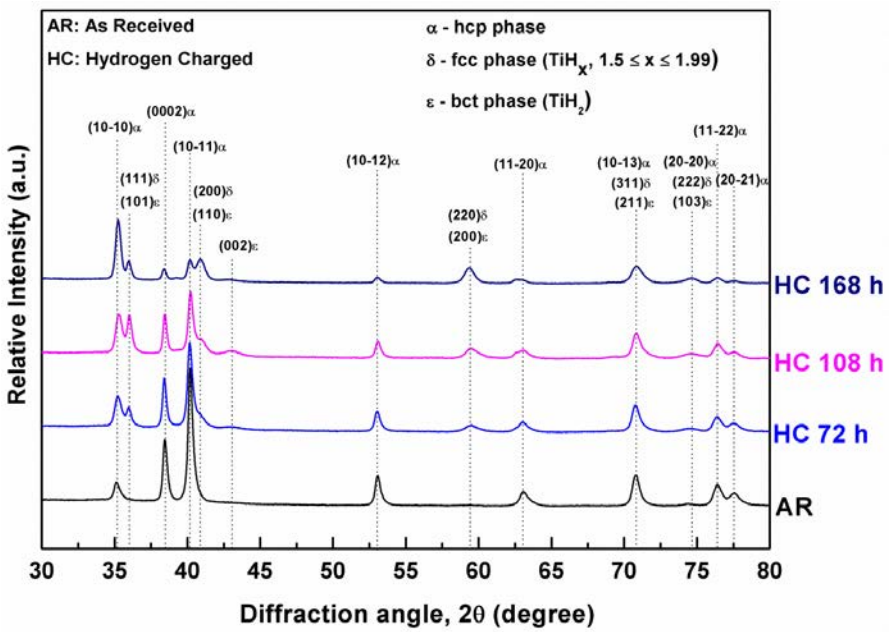

Figure 3 Courbes de diffraction des rayons X du Ti50A à l'état de réception (AR) et après différents chargement en hydrogène (HC).

Comme observé dans les courbes de diffraction des rayons X, l'intensité des pics de diffraction correspondant aux hydrures augmentait avec la durée de chargement en hydrogène, ce qui suggère une augmentation de la fraction volumique de ces hydrures formés en sous-couche des échantillons. En outre, on peut remarquer que les pics de diffraction des rayons X correspondant à la matrice de phase α (structure hexagonale) s'élargissent lors que la durée du temps de chargement en hydrogène augmente. L'observation de l'élargissement des pics de la phase α peut être attribuée à l'apparition d'une déformation locale induite par la formation de hydrures.

Pour étudier quantitativement l'effet de l'hydrogène, les microstructures des échantillons Ti50A après 72, 108 et 168 h de chargement en hydrogène ont été caractérisées par la technique EBSD. La **Figure 4** montre les cartes de phase EBSD du Ti50A avant et après hydrogénation avec les hydrures ε-TiH_2 et δ-TiH_x ainsi que la phase alpha étant respectivement représentées dans les couleurs rouge, bleu et gris. Une petite quantité d'hydrures en forme d'aiguille a pu être détectée au niveau des joints de grains comme le montre la carte de phase de l'échantillon après 72 h de chargement électrolytique (**Figure 4b**). Lorsque la durée de chargement atteint 108 h (**Figure 4**c), la fraction volumique d'hydrure a augmenté mais ceux-ci sont essentiellement situés à l'intérieur des grains d'alpha. Pour des durées de chargement en hydrogène de 168 heures (7 jours), une quantité considérable d'hydrures δ-TiH_x, d'épaisseur moyenne inférieure à 1,0 μm et de longueur

environ 7,0 µm s'est formée aux joints de grains ainsi qu'à l'intérieur des grains de phase α (**Figure 4d**). Les valeurs de la fraction surfacique d'hydrures δ-TiH_x et ε-TiH_2 calculées par le logiciel Channel 5 étaient, respectivement, de 12,5 ± 0,3% et 4,9 ± 0,5% (valeurs moyennées à partir des résultats de 5 analyses).

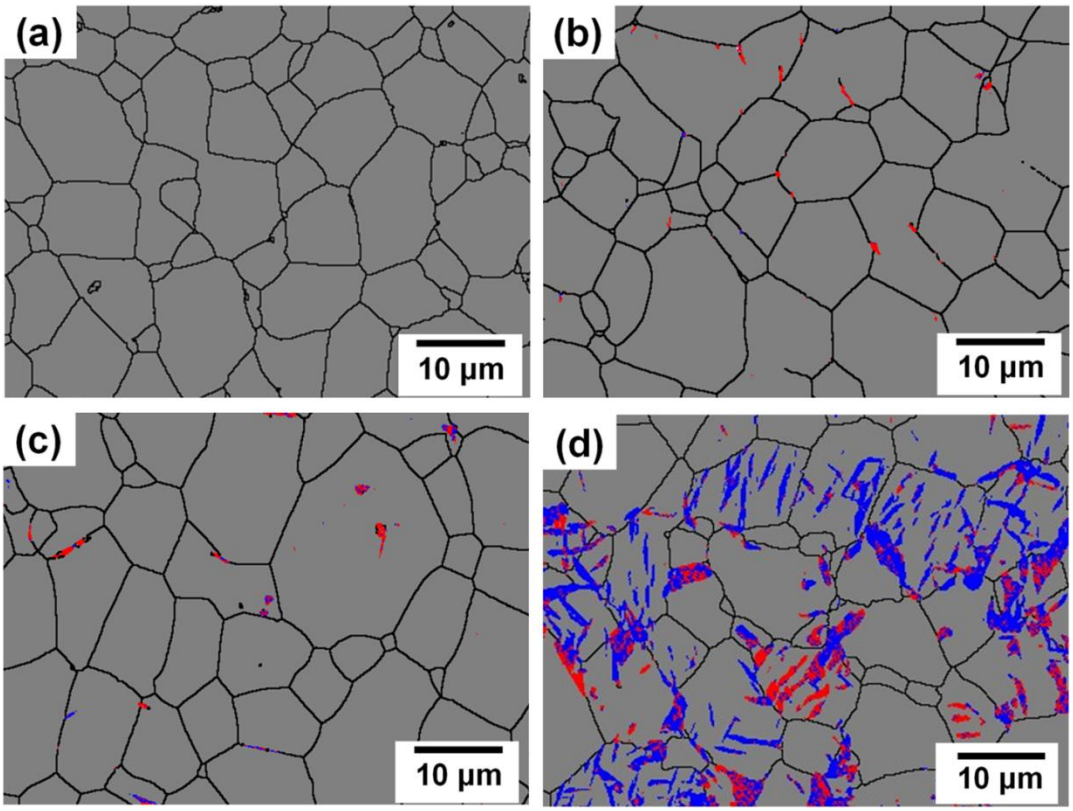

Figure 4 Cartes de phase par analyses EBSD du Ti50A à l'état de réception (a), échantillons de Ti50A après 72 h (b), 108 h (c) and 168 h (d) de chargement électrolytique; (les couleurs rouge, blue et grise correspondent, respectivement, aux hydrures ε-TiH_2, δ-TiH_x et à la matrice α)

Les relations d'orientations (OR) entre l'hydrure stable δ de structure cfc et la matrice α pseudo-hcp ont pu être déterminées par l'analyse des projections stéréographiques correspondantes aux plans et directions des deux phases, comme représenté sur la **Figure 5**. Par exemple, sur la figure 5a, un plan $\{001\}_\delta$ de l'hydrure δ est parallèle à un plan $\{0001\}_\alpha$ de la matrice α. Aussi la projection d'une direction $<110>_\delta$ de l'hydrure δ superpose celle de la projection correspondant à une direction $<11\bar{2}0>_a$ de la matrice α. Par conséquent, l'analyse des projections stéréographiques nous a permis de mettre en évidence cinq relations d'orientations spécifiques entre l'hydrure δ-TiH_x et la matrice α, tel qu'il est présenté dans le tableau 1 (données à partir de 5 cartes). Des études antérieures par le biais de caractérisation MET avaient elles révélé deux

relations d'orientations épitaxiales particulières (OR1 et OR2) [CG17] entre l'hydrure δ et la phase α dans des alliages de Ti et Zr.

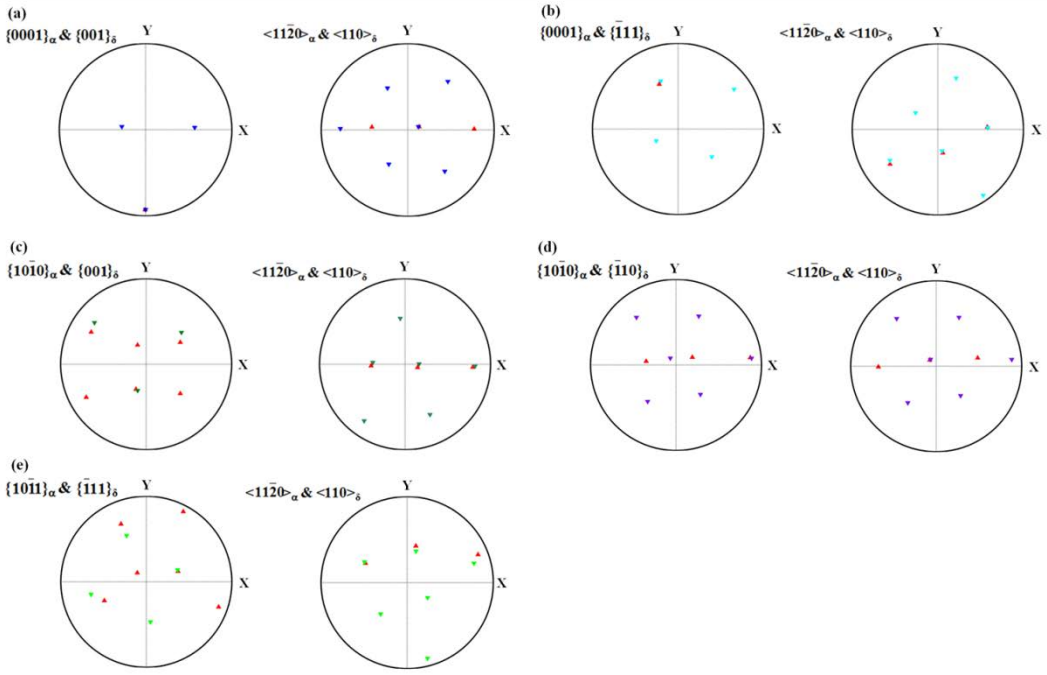

Figure 5 Projections stéréographiques de la matrice α (hexagonale) et des hydrures δ-TiHx (cfc) montrant les relations d'orientations (OR) correspondant aux plans and directions.

Des analyses au microscope électronique à transmission ont été réalisées pour confirmer la structure cristallographique des hydrures. Pour préparer cette caractérisation, les hydrures ont d'abord été localisés par MEB, comme le montre la **Figure 6**a, et une lame mince (**Figure 6**b) a été extraite par Focused Ion Beam. La **Figure 6**c montre la micrographie MET de l'échantillon hydrogéné prise à partir de la lame mince confirme la présence des deux types d'hydrures observés au sein d'un grain α. Les images MET en champ clair prises dans différentes zones de la matrice (correspondants aux régions sélectionnées A et B sur la **Figure 6**c) sont présentées dans la **Figures 6**d et 6e. On peut remarquer que les deux hydrures ont des morphologies totalement différentes, ce qui est conforme aux observations MEB-EBSD décrites ci-dessus. La figure 6f montre le cliché de diffraction d'électrons de la région sélectionnée (SAED) correspond à la zone encerclée dans la **Figure 6**e. Comme l'indique ce cliché, l'axe de la zone <-112> de l'hydrure δ-TiH_x de structure cubique face centrée coïncide avec l'axe de la zone <000-1> de la phase α de symétrie hexagonale. Les micrographies MET en champ sombre on été réalisés en sélectionnant deux réflexions correspondant à la fois à l'hydrure δ-TiH_x et à la matrice α (encerclée sur le

diagramme SAED, figure 6f). En revanche, l'hydrure ε-TiH_2 avec la structure de phase quadratique à base centrée (correspondant à la **Figure 6**d) présente une intensité de diffraction électronique faible. Il convient de rappeler que la phase ε-TiHx est thermodynamiquement stable jusqu'à une température maximale d'environ 25°C. Ceci est en accord avec les résultats présentés ci-dessus EBSD, et qui indique que la structure de l'hydrure ε-TiHx est instable sous l'irradiation de faisceaux d'électrons des équipements FIB et MET [WE02, LX13].

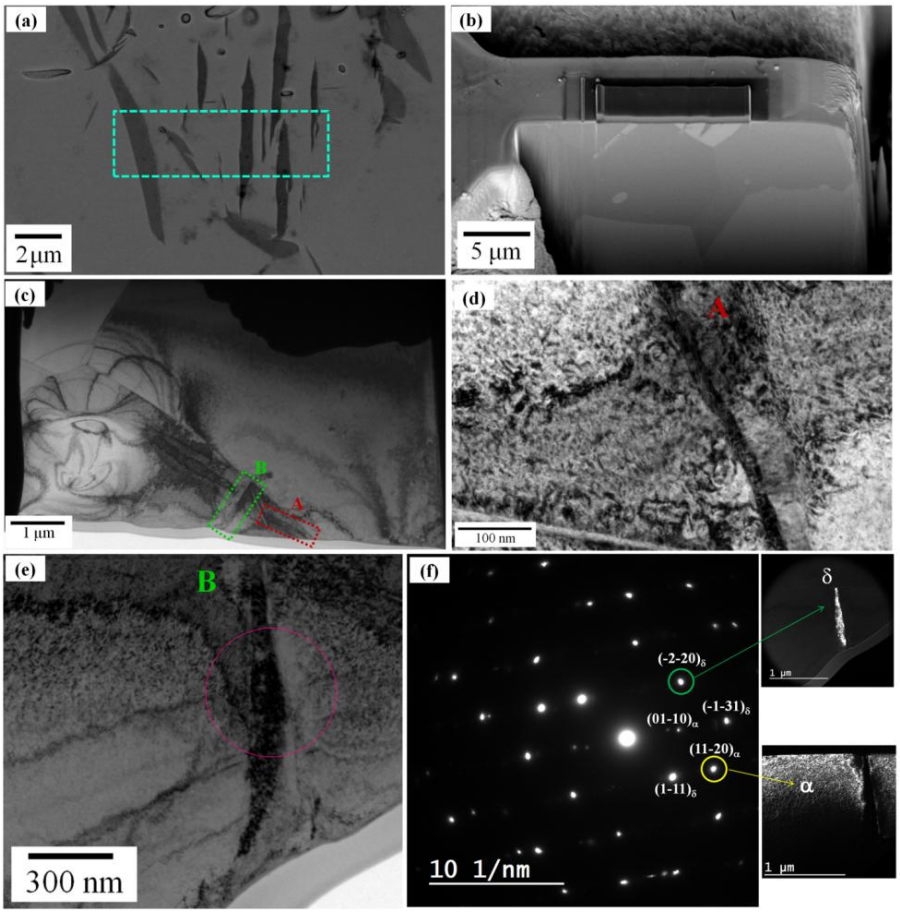

Figure 6 Analyses MEB et MET réalisées sur des spécimens hydrogénés; (a) image MEB (détecteur en électron secondaire); (b) détail de la zone sélectionnée de l'image (a) extraite par FIB); (c) Micrographie MET de la même zone; (d) et (e) images MET en champ clair de la matrice prise de, respectivement, la zone A et B comme indiquée en (c); (f) cliché SAED correspondant à la zone encerclée dans (e) et en insert les images en champ sombre correspondant aux taches de diffraction encerclées dans le cliché SAED et pointées par les flèche.

Des mesures de microdureté ont été effectuées sur la section transversale des alliages de Ti50A hydrogénées. La **Figure 7** montre les profils de microdureté de Ti50A hydrogéné sous différents temps de chargement en hydrogène. Ces échantillons de Ti50A hydrogénés présente un fort gradient de dureté au travers de la section. Par exemple, après un chargement en hydrogène de

168 h, la valeur de la dureté décroît rapidement de 2240 MPa depuis la surface jusqu'à 1700 MPa atteinte à une distance de 75 µm sous la surface. La valeur de dureté décroissante peut être interprétée par le gradient de concentration en hydrogène au travers de la section et de la fraction de volume des hydrures décroissante lorsque l'on se rapproche du centre de l'échantillon où l'hydrogène n'a pas diffusé. Afin de faciliter d'autres analyses, le Ti50A hydrogéné a été recuit pendant 2 heures à 400 ° C sous gaz Ar. Le graphique inséré dans la **Figure 7** montre le profil de microdureté du Ti50A hydrogéné après le traitement de recuit. En supposant un mécanisme de diffusion de Fick, un tel recuit devrait permettre la diffusion de l'hydrogène vers le centre de l'échantillon, fournissant ainsi une répartition uniforme de l'hydrogène sans générer de croissance des grains.

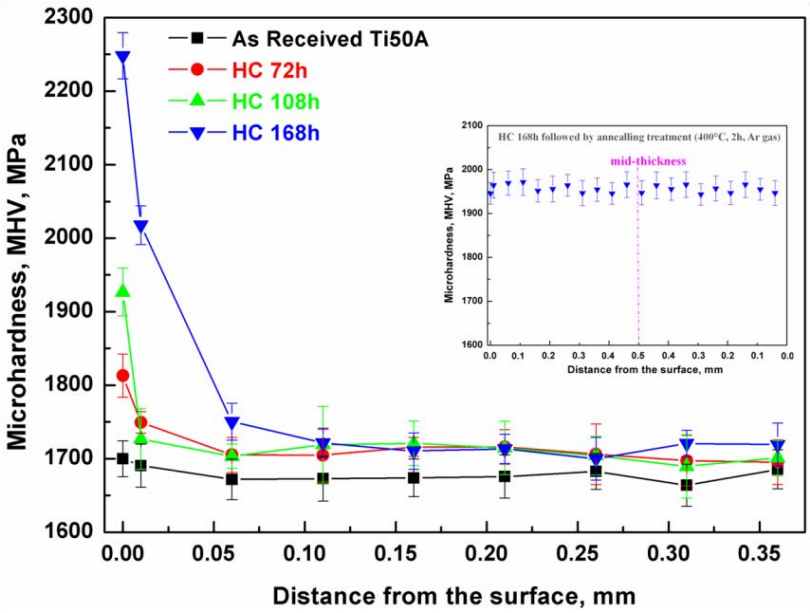

Figure 7 Profiles de microdureté mesurés dans le Ti50A avant et après chargement en hydrogène

3.2 Évolutions microstructurales induites par l'hydrogène et leurs effets sur les propriétés mécanique du β-21S alloy

Les diagrammes de diffraction des rayons-X pour les alliages β-21S hydrogénés sont présentés dans la figure 9 avec leurs concentrations en hydrogène respective. Les courbes ne révèlent que les pics de fraction correspondant à la phase β; aucune indication de la phase α, d'hydrures ou d'autre phase ne peuvent être détectés. Il est important de souligner que les pics de diffraction de cette phase β se déplacent vers des valeurs d'angles 2θ plus faible, indiquant une expansion du réseau cristallin de la phase β résultant du chargement en hydrogène. L'introduction de l'hydrogène dans les sites interstitiels tétraédriques de petites dimensions conduit à une

expansion non négligeable du réseau cristallin, ainsi qu'à des distorsions de réseau [K01, SC01]. La variation du paramètre de maille déterminé par la relation de Bragg a été reportée dans le **Tableau 1** en fonction de la concentration en hydrogène. Ces variations sont en accord avec celles rapportées par Robertson [TR01].

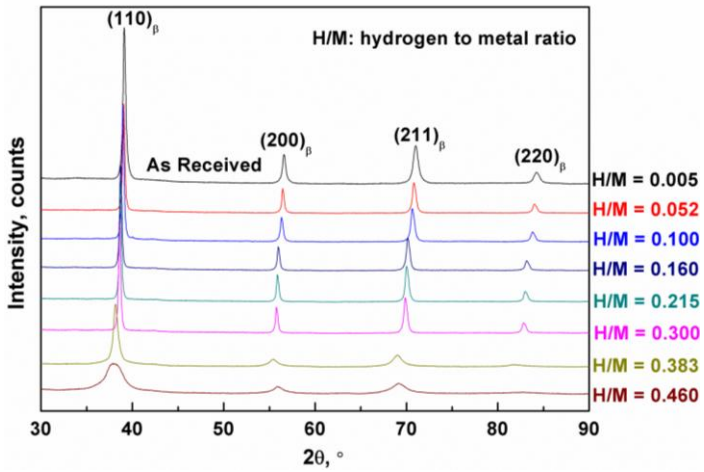

Figure 8 Profiles de diffraction des rayons-X pour le β-21S préparés avec différentes concentrations en hydrogène (exprimées en rapport H/M)

Table 1 Variation du paramètre de maille du titane -21S en fonction de la concentration en hydrogène

Sample series	H_2 charging pressure (kPa)	Lattice parameter (Å)	Relative volume change of BCC lattice, %	Hydrogen concentration	
				(at. %)	(H/M)
As received	N/A	3.247	/	0.500	0.005
1123-1	1	3.256	0.834	4.940	0.052
1123-2	5	3.259	1.113	9.091	0.100
1123-3	10	3.273	2.421	13.793	0.160
1123-4	25	3.285	3.552	17.695	0.215
1123-5	35	3.294	4.405	23.077	0.300
1123-6	50	3.311	6.030	27.660	0.383
1123-7	100	3.317	6.607	31.530	0.460

Etant donné que l'hydrogène diminue la température de la transformation allotropique (température du transus β) [SC01], celui-ci améliore la stabilité de la phase β lors du refroidissement. Il est également important de préciser l'évolution de la microstructure induite par l'hydrogène et de comprendre l'origine de la baisse d'intensité diffractée accompagnée d'un

élargissement des pics tel que l'on peut le constater dans la **Figure 8**. Les micrographies MEB prises sur la section transversale des alliages β-21S hydrogénés contenant différentes concentrations en hydrogène sont montrées dans la figure 10. Les **Figures 9**a et 9b montrent les images MEB de l'alliage de titane β-21S hydrogéné avec une concentration d'hydrogène H/M = 0,215. Cette concentration en hydrogène a été sélectionnée car elle correspond à la concentration critique pour laquelle une transition ductile-fragile brusque a été rapportée par Teter et al. [TR01]. La microstructure est composée uniquement de grains équiaxes de la phase β; aucune autre phase α ou hydrure n'est détectée sur ces images. Toutefois, lorsque la concentration en hydrogène est augmentée jusqu'à un rapport H/M = 0,380, des structures en forme de plaque sont observées dans les grains de la phase β, comme cela peut être observé dans les **Figures 10**c et 10d. Lorsque la concentration en hydrogène atteint un rapport H/M = 0,460, un nombre croissant de structures analogues à des plaques est formé dans les échantillons, comme il est représenté dans les **Figures 9e et 9**f. Cette morphologie en forme de plaque est identique à la structure martensite couramment observée dans les alliages de titane β-métastable déformés ou trempés [CW87, MT04 et CZ16]. L'apparition des micro-fissures, comme indiqué par les flèches, suggère une importante concentration de contrainte locale notamment aux joints de grains des alliages β-21S hydrogénés.

Dans le but d'examiner plus en détail la structure de la martensite, des analyses EBSD ont été effectuées sur la section transverse de l'échantillon hydrogéné avec un rapport H/M = 0,460. La **Figure 10**a montre la micrographie MEB en électron secondaire de la région analysée. Les grains β observées sont marqués avec les indices A, B, C, D, E, F et G. La **Figure 10**b montre la micrographie en électron rétrodiffusé du grain A prise avec un grossissement plus élevé. Sur cette Figure on peut observer quatre plaquettes de phase martensite α'' d'orientations cristallographiques différentes coexistant au sein d'un même grain β et repérées par des chiffres arabes en jaune dans la **Figure 11**b. Les plaquettes de martensite repérées 1 et 2 ayant les directions communes sont distribuées de façon alternative dans le grain β. Pour avoir une valeur précise de l'angle d'Euler de chacune des plaquettes de martensite, nous avons mesuré les orientations qu'elles forment avec la phase β. Par exemple, dans le grain A, quatre variantes de martensite orientées, α_1", α_2", α_3" et α_4", peuvent être détectées. Cette martensite α" phase a une structure orthorhombique c'est-à-dire la même phase martensitique que la phase α" induite par contrainte mécanique [CW87, LX98 et MT04].

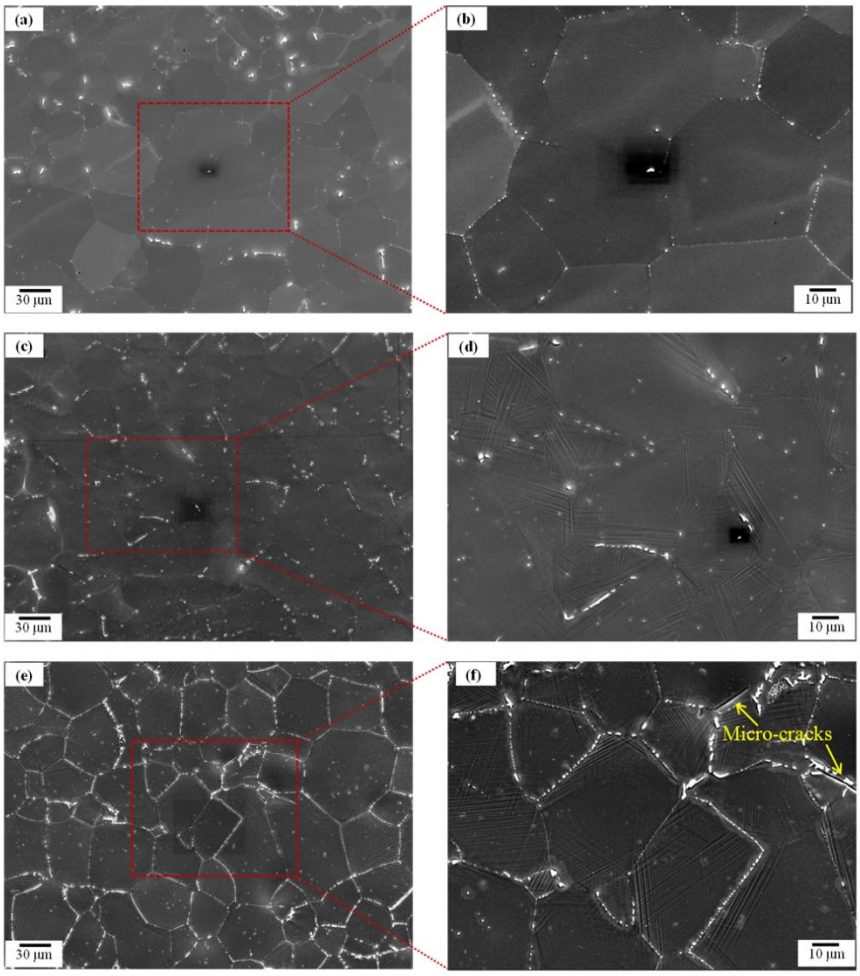

Figure 9 Microscopies MEB montrant la section d'échantillons β-21S hydrogenés; (a), (b) H/M = 0.215; (c), (d) H/M = 0.383 et (e), (f) H/M = 0.460.

Les relations d'orientations (OR) {112} β // (110) α " et $\langle \bar{1}10 \rangle \beta$ // [001] α" ont été décrites dans des études antérieures portant sur les alliages de titane β-métastable [CW87, MT04 et CZ16]. Dans le présent alliage, ces OR ont été confirmée par l'analyse des projections stéréographiques des plans et directions des deux phases sur les **Figures 10**c et 10d. À partir des projections stéréographiques, on peut constater que pour chaque variante de martensite possède un plan {110}α'' parallèles à un plan {112} de la phase β. La projection de la direction <001> α" pour chaque variante de martensite coïncide avec une direction $\langle \bar{1}10 \rangle$ de la phase β. Par conséquent, les résultats décrits ci-dessus confirment la formation d'un réseau constitué de quatre variantes de la phase martensitique α'' respectant les relations d'orientations classiques entre les phases α'' et β détectée sous la surface des échantillons c'est-à-dire jusqu'à une épaisseur de l'ordre de 250 à 400 nm.

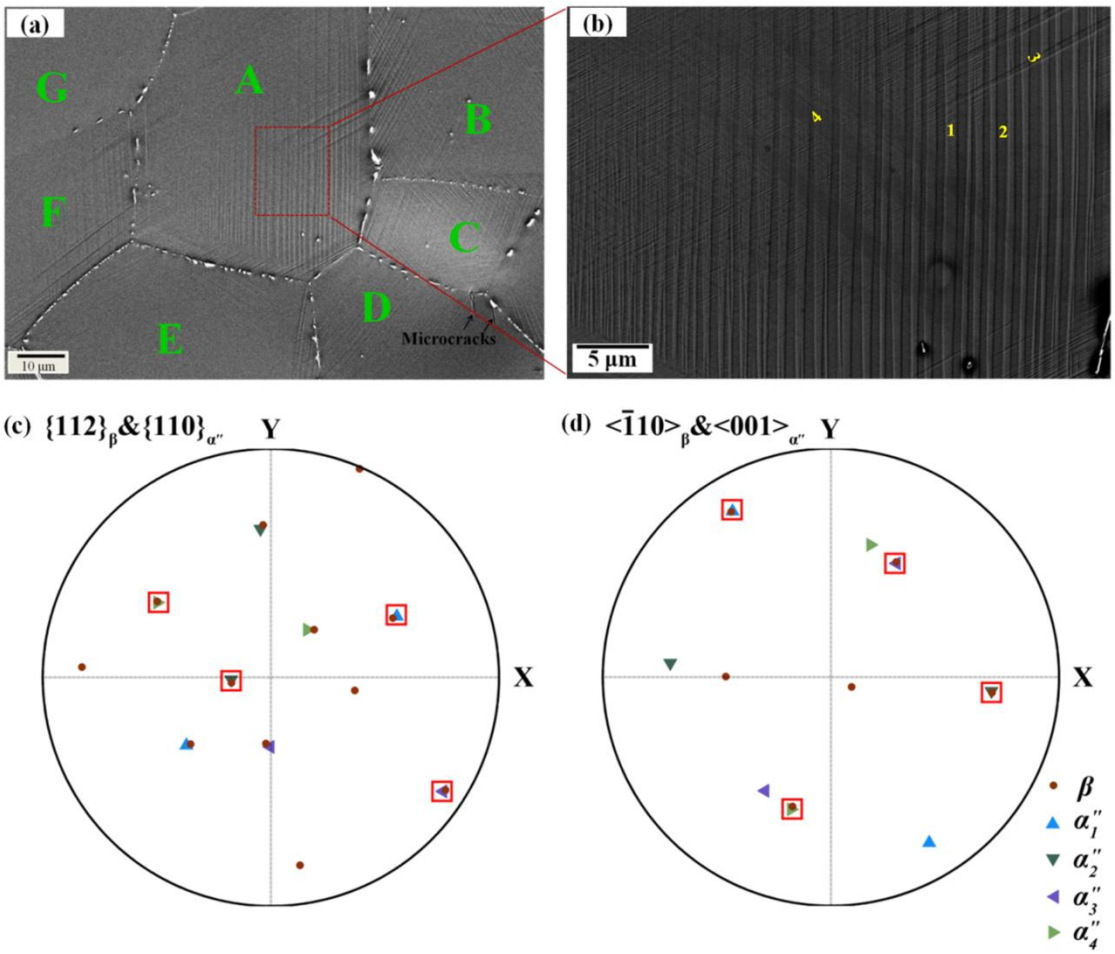

Figure 10 Analyse des variants de martensite par EBSD : (a) micrographie MEB montrant les variants de martensite α'' dans des grains β; (b) micrographie obtenue en mode électrons rétrodiffusés de la zone analysée par EBSD; (c) projections stéréographiques des plans$_{\alpha}$ {112}$_{\beta}$ and {110}$_{\alpha''}$, et (d) projections stéréographiques des directions $<\bar{1}10>_{\beta}$ et <001>$_{\alpha''}$ (les projections surperposées des phases β et α'' sont entourées par les carrés de couleur rouge).

La microstructure locale dans des échantillons d'alliage β-21S hydrogéné et non-hydrogéné a été observée par MET. La **Figure 11**a montre l'image MEB de cet échantillon après préparation par micro-usinage ionique (comme indiqué par la flèche).The insert micrograph is magnification of the selected grain, no internal structure can be observed.

La **Figure 11**b montre l'image en champ clair (BF) de la lame mince extraite d'un échantillon de l'alliage β-21S non-hydrogéné. Le cliché de diffraction des électrons de la région sélectionnée (SAED) correspondante est donnée dans la **Figure 11**c. Les stries diffuses dans ce diagramme de diffraction des électrons sont typiques de la présence de la phase de ω athermique telle qu'il a été rapporté par Teter et al. dans un échantillon de l'alliage β-21S trempé à l'air [TR01]. Ceci est dû au fait que la formation de la phase de ω athermique ne peut être évitée dans les alliages titanes β,

quelque soit la vitesse de refroidissement. Cependant, la fraction volumique de cette phase ω athermique est très faible. Les tentatives de détection de cette phase ω à partir des stries ont échoué.

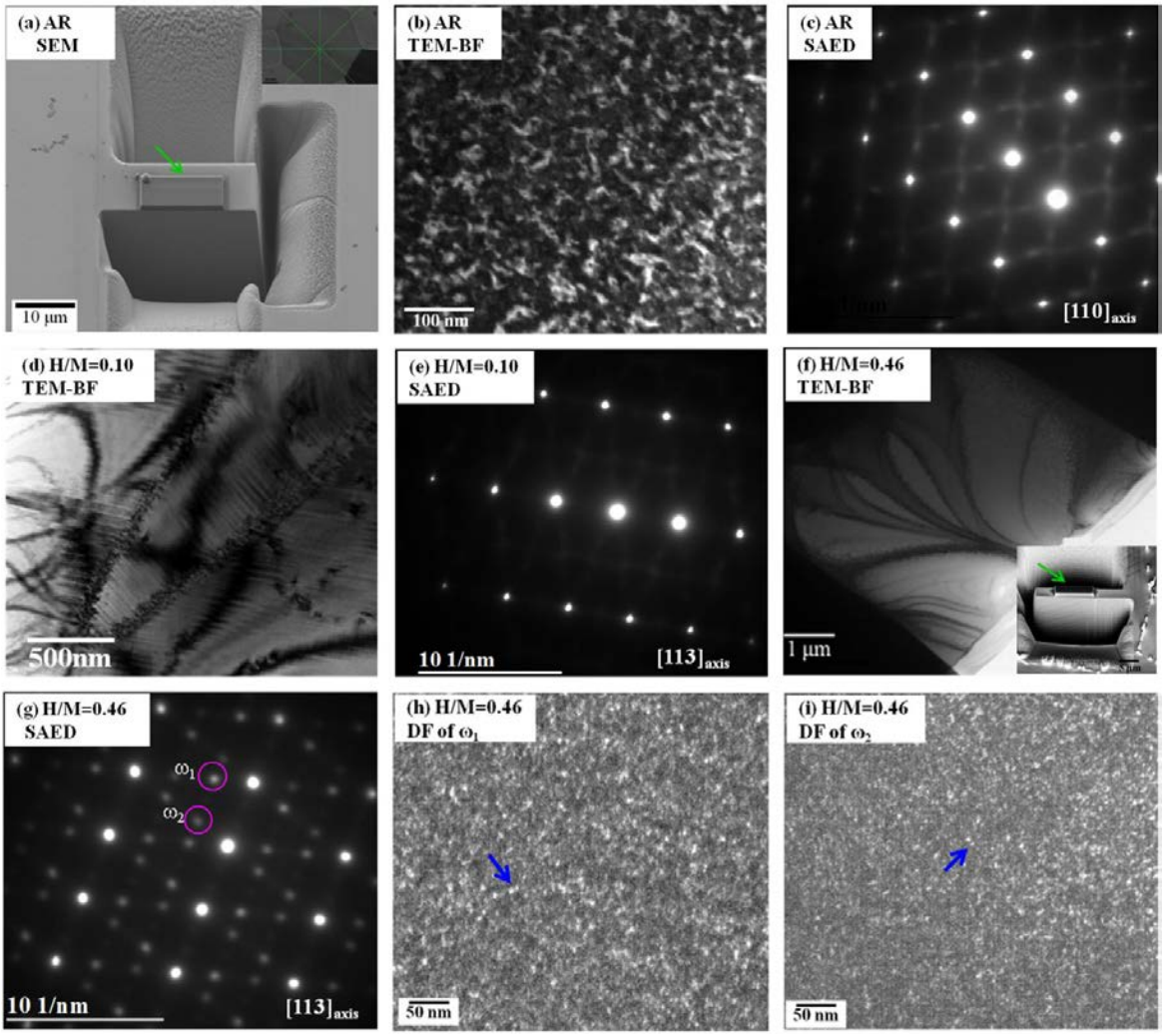

Figure 11 Caractérisation métallographique des alliages β -21S hydrogénés et non-hydrogénés. (a) image MEB de l'alliage β-21S non-hydrogéné après préparation par micromachining ionique (FIB); (b) micrographie MET-BF de l'alliage β-21S non-hydrogéné; (c) cliché SAED de l'alliage β-21S non-hydrogéné; (d) micrographie MET-BF de l'alliage β-21S chargé en hydrogène avec un rapport H/M = 0,10; (e) cliché SAED de l'alliage β-21S hydrogéné correspondant; (f) micrographie MET-BF de l'alliage β-21S chargé en hydrogène avec un rapport H/M = 0,46, et l'image en insertion montrant la préparation de l'échantillon par micromachinage ionique; (g) cliché SAED de l'alliage β-21S hydrogéné correspondant; et (h), (i) images en champ sombre de deux variantes ω_1 et ω_2, respectivement.

La **Figure 11d** représente l'image en champ sombre de l'alliage β-21S hydrogéné avec un rapport H/M = 0,10. Des joints de faibles désorientations et des défauts d'empilement ont été observés à l'intérieur des grains de la phase β. La **Figure 11**e montre le cliché de diffraction SAED

correspondant. Par rapport à l'alliage β-21S non-hydrogéné, l'intensité des raies diffuses associées à la présence de la phase ω athermique a diminué, ce qui indique que la phase ω athermique devient moins stable après addition d'hydrogène. Cette observation est cohérente avec des études antérieures [I87, TW87, I94 et TR01] et confirme que l'hydrogène stabilise la phase β et supprime la formation de la phase ω athermique dans des alliages de titane β-métastable.

L'échantillon contenant une concentration élevée en hydrogène, c'est-à-dire un rapport H/M = 0,46, étant trop fragile, une lame mince n'a pas pu être préparée par les méthodes traditionnelles. Par conséquent, la lame mince a été extraite de l'échantillon hydrogéné (auparavant localisés par SEM-EBSD représentées sur la **Figure 10**b) par micro-usinage ionique FIB. L'image MET en champ clair de la feuille mince est montrée dans la **Figure 11**f, et la micrographie prise lors de la préparation de la feuille mince (comme indiqué par la flèche) par le micro-usinage ionique en a été insérée à cette **Figure 11**f.

Le cliché SAED correspondant est présenté dans la **Figure 11**g. Malheureusement aucune phase martensite α'' n'a pu être détectée par MET, par contre une nouvelle phase de structure hexagonale correspondant à la phase ω a été observée. Deux variantes, ω_1 et ω_2, comme indiqué par les cercles roses ont notamment pu être détectées. Les images en champ sombre (DF) correspondant à ces deux variantes ω_1 et ω_2 sont montrées dans les **Figures 11**h et 11i, respectivement. Il peut être observé que, ces deux variantes de la phase ω ont la même morphologie et se trouvent sous la forme de particules de taille nanométrique distribuées aléatoirement dans la phase de matrice β, quelque unes étant repérées par les flèches. Cette morphologie correspond à la structure typique de la phase ω-athermique qui est habituellement formée par trempe dans des alliages de titane β-métastable [CWT87, MT04, LN16 et CZ16].

3.3 Effets de l'hydrogène sur le laminage à froid et la recristallisation

3.3.1 Effets de l'hydrogène sur le laminage à froid du Ti50A

Il a été montré précédemment que l'hydrogène conduisait à des modifications microstructurales et du comportement mécanique. Afin de vérifier le rôle de l'hydrogène sur le comportement en laminage à froid, des échantillons pré-hydrogéné (notés Ti50A-H) ont été laminées à froid jusqu'à des réductions d'épaisseur de 10% et 50%. L'évolution des microstructures a été analysée par diffraction des rayons X et MEB à haute résolution équipée de la technique EBSD.

3.3.1.1 Effets de l'hydrogène sur le comportement en laminage à froid pour un niveau de déformation faible (εeq = 0.12)

Des réductions successives d'épaisseur par laminage symétrique a été imposée sur des échantillons de Ti50A pré-hydrogéné. La réduction d'épaisseur totale était d'environ 10%, ce qui correspond à la déformation équivalente de von Mises $\varepsilon_{eq} = 0{,}12$., Des analyses EBSD ont ensuite été réalisés pour révéler l'effet de l'hydrogène sur la déformation par maclage du titane pur. La **Figure 12** montre les cartes en contraste de bande (BC) avec les joints de jumelles identifiés ; la couleur rouge indique, respectivement, les macles de compression $\left\{11\bar{2}\bar{2}\right\}\left\langle 11\bar{2}3\right\rangle$ référées CT1, alors que la couleur bleue correspond aux macles de tension $\left\{10\bar{1}2\right\}\left\langle \bar{1}011\right\rangle$ référées TT1. On peut observer qu'un nombre croissant de macle de tension de type TT1 ont été générées après augmentation du temps de chargement en hydrogène.

La distribution des angles de désorientation mesurées grain-à-grain dans des échantillons de Ti50A laminés à froid à un niveau de déformation équivalente $\varepsilon_{eq} = 0{,}12$ est représentée dans la **Figure 13**. La ligne verte dans la figure 14a correspond à une distribution aléatoire des angles de désorientation (mesurée grain-à-grain) prédite pour une structure hexagonale sans aucune texture [M04]. La **Figure 13**a indique que les tôles de Ti50A à l'état de réception ne présente pas de distribution aléatoire compte-tenu de la texture subsistante même après traitement de recuit.

Lorsque ces tôles subissent un traitement de laminage avec un niveau de déformation équivalente $\varepsilon_{eq} = 0{,}12$, deux pics importants apparaissent pour des angles de fortes désorientations autour de 65° et 85° (**Figure 13b**). Ces deux pics peuvent être associés à la formation de macles détectés dans les cartes en contraste de bande (**Figure 12**), c'est-à-dire les macles de compression CT1 pour un angle de 65^{o} et les macles de tension TT1 pour l'angle de 85^{o} [BC81]. Comparativement aux toles non chargées en hydrogène, les **Figures 13**c, d et e montrent que la fréquence des macles de tension TT1 augmente proportionnellement à la durée du chargement en hydrogène alors que la fréquence des macles de compression reste approximativement constante

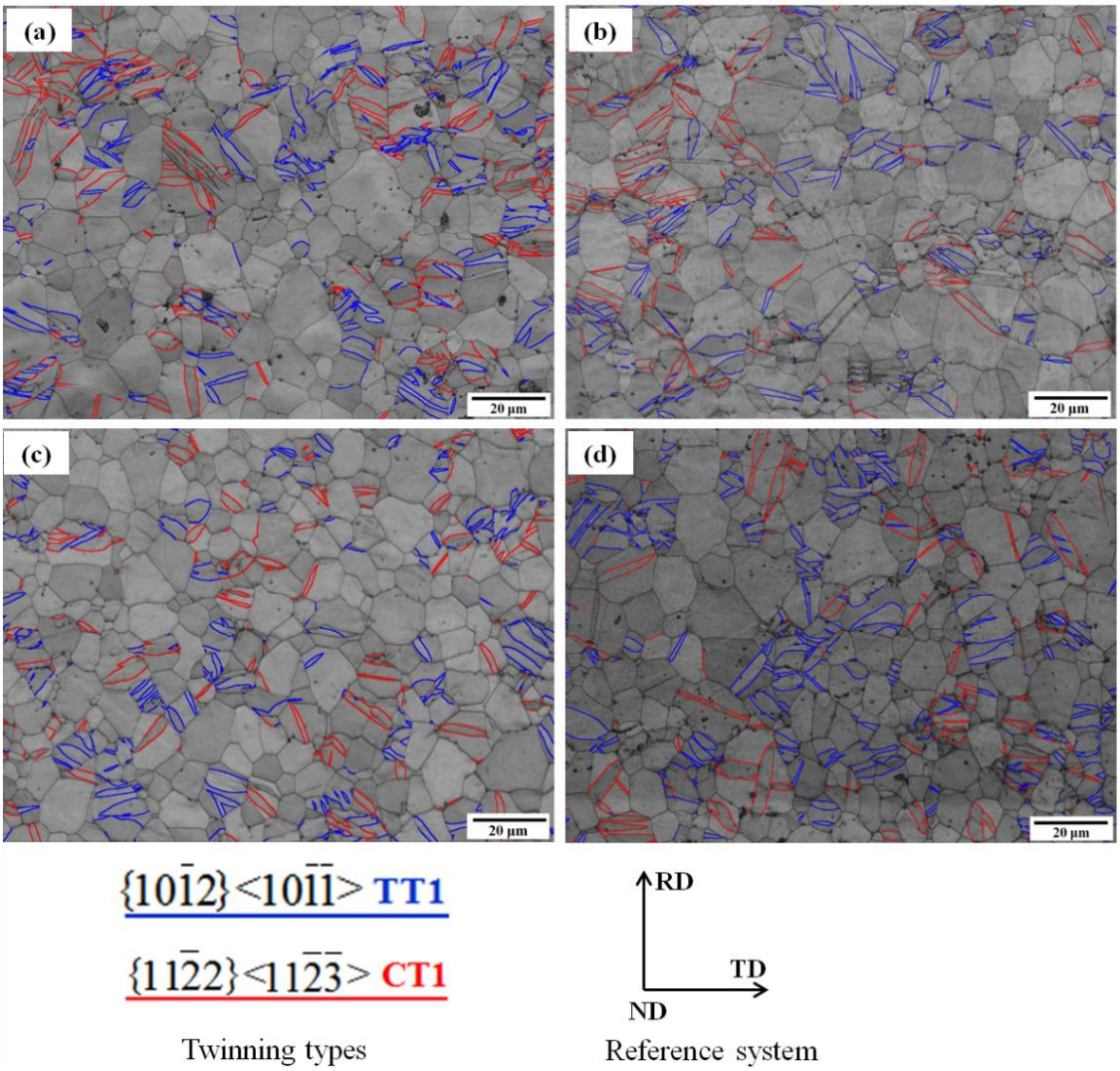

Figure 12 Cartes en contraste de bande du Ti50A laminé à froid après une réduction d'épaisseur de 10%; (a) échantillon Ti50A non hydrogéné; (b), (c) et (d) échantillons Ti50A chargés en hydrogène pendant 72 h, 108 h et 168 h, respectivement. (Les couleurs rouge et bleue correspondent, respectivement, aux joints de macle de compression CT1 et aux macles de tension TT1).

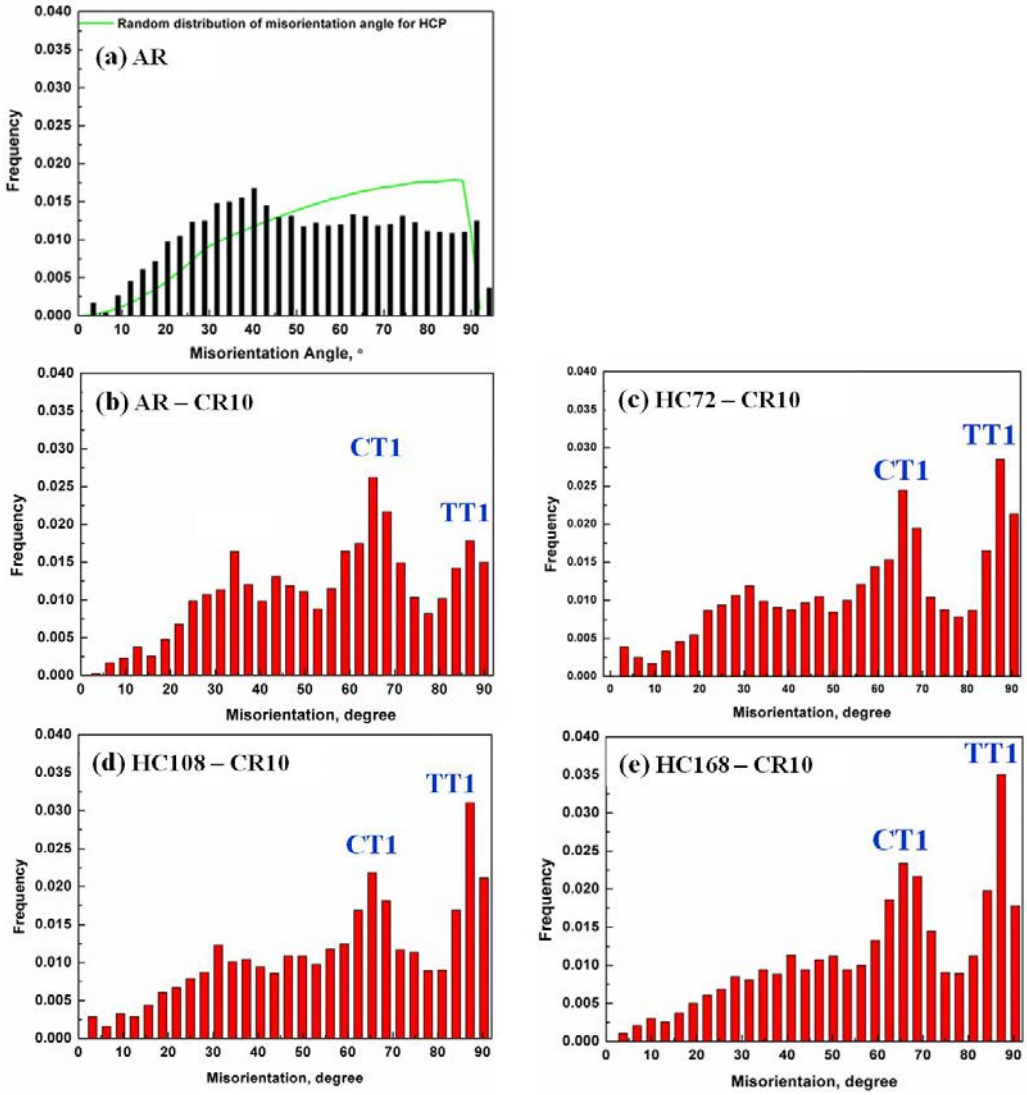

Figure 13 Distributions de angles de désorientation (grain-à-grain) dans différents échantillons de Ti50A; a) échantillon non-chargé en hydrogène, b) à e) échantillons avec différents durée de chargement en hydrogène. (AR: état de réception, CR10: laminage à froid avec réduction d'épaisseur de 10%, HC + CR10: laminé à froid après chargement en hydrogène; TT1 : {10$\bar{1}$2}<$\bar{1}$011> and CT1 : {11$\bar{2}$2}<11$\bar{2}$3>.

3.3.1.2 Effets de l'hydrogène sur le comportement en laminage à froid pour un niveau de déformation moyenne (ε_{eq}=0.80)

Pour étudier l'effet de l'hydrogène sur le comportement du Ti50A en laminage à froid, une réduction d'épaisseur de 50% (ε_{eq} = 0,80) a été appliquée sur des échantillons pré-hydrogénés ainsi que sur des échantillons non-hydrogénés. Les figures de pole inverse (IPF) et cartes en contraste de bandes (BC) obtenues par EBSD dans le plan de laminage après polissage sont montrées dans la **Figure 14**. Le code de couleur correspond à l'orientation de l'axe de la normale au plan (ND) par rapport au système de référence de cristal. Dans les cartes BC, les joints de

faible désorientation (HAB) et forte désorientation (LAB) sont identifiés par des lignes, respectivement, noires et bleues.

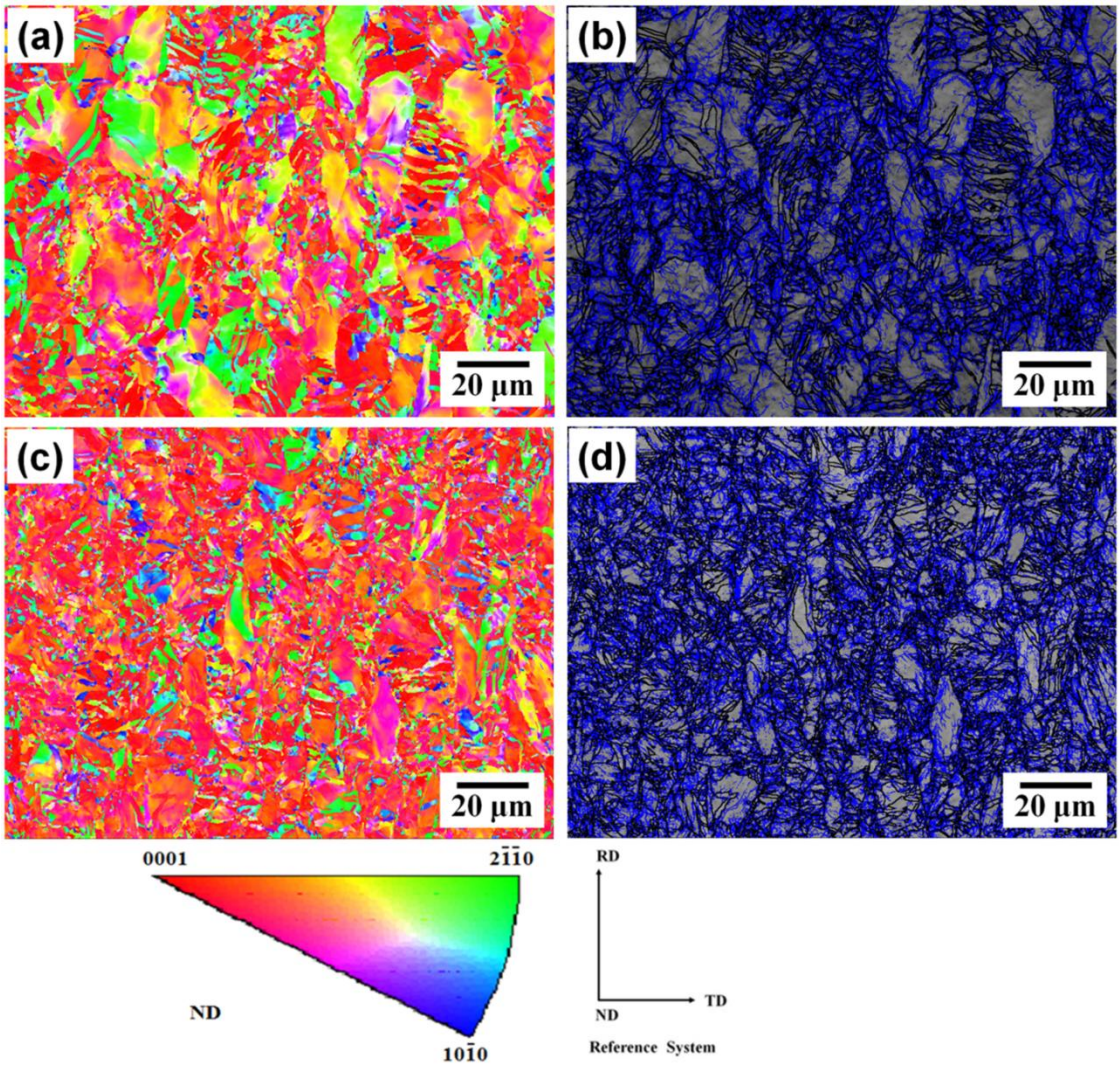

Figure 14 Cartes IPF et BC prises sur la surface d'échantillons de Ti50A laminés à froid avec une réduction d'épaisseur de 50%. (a), (b) Ti50A non hydrogéné et (c), (d) échantillon chargé en hydrogène pendant 168 h; (les lignes bleues soulignent les joints de faible désorientation et les lignes noires les joints de forte désorientation).

Après une réduction d'épaisseur de 50%, la microstructure consiste en un mélange de grains allongés, de macles et de joints de faible désorientation (lignes bleues). Ces résultats indiquent que, comparativement au laminage appliqué à un échantillon non hydrogéné, le laminage des échantillons chargés en hydrogène tend à être favorable à une rotation de l'axe des c <0001> vers la direction normale de laminage (ND). En outre, la **Figure 14**d révèle un raffinement marque de la microstructure dans les échantillons hydrogénés. Le **Tableau 2** donne la taille moyenne des grains pour chacun des échantillons, la taille moyenne étant obtenue par le logiciel ATOM. La

diminution de la taille des grains dans les échantillons hydrogénés peut être attribuée à l'hétérogénéité de la déformation induite par les hydrures.

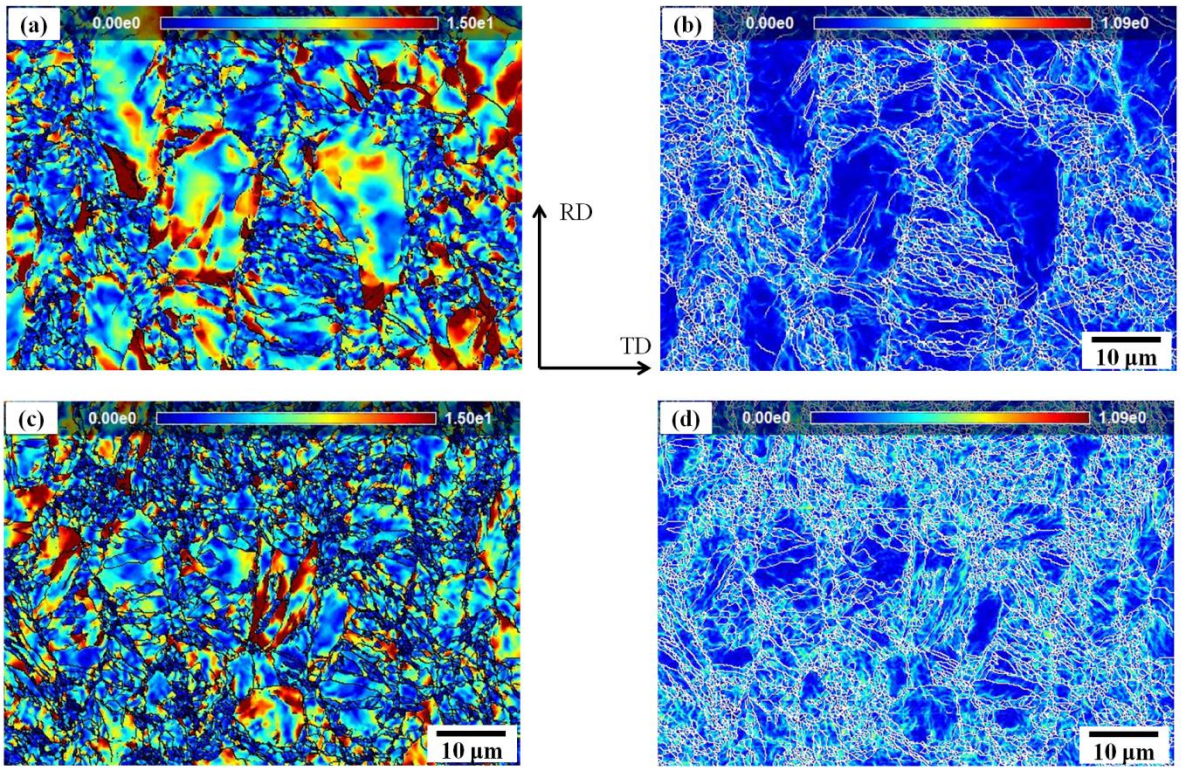

Figure 15 Cartes montrant la désorientation intragranulaire et les GND extraites d'échantillons Ti50A après 50% de réduction d'épaisseur par laminage à froid : (a), (c) échantillon non-hydrogéné et (b), (d) échantillon après 168 h de chargement en hydrogène.

Tableau 2 Taille moyenne des grains et densité normée des dislocations géométriquement nécessaires (GND)

	AR	CR50	HC168 + CR50
Average Grain Size, [µm]	12.0 ± 0.8	2.0 ± 0.2	1.1 ± 0.1
Norm of GND, [µm-1]	0.007 ± 0.002	0.175 ± 0.003	0.224 ± 0.003
Average Internal Misorientation degree, [°]	0.34 ± 0.19	1.50 ± 0.23	2.64 ± 0.20

AR: As-received Ti50A; CR 50: cold rolled to 50% thickness reduction;

HC: hydrogen charged for 168 h

Dans le présent travail, le gradient de déformation local est représenté par la désorientation interne due à la courbure du réseau dans le grain. La **Figure 15**a et c montre les cartes de

désorientation internes mesurées dans 50% d'échantillon laminé à froid, qui correspondent aux cartes IPF de la **Figure 14**a et c. Le schéma de couleurs indique la plage d'angle de désorientation de 0 à 15 °. Comme on l'a observé dans les cartes, il existe un grand gradient de déformation du centre de la limite grain-grain.

Par rapport au Ti50A non chargé (**Figure 15**b), le Ti50A préchargé (**Figure 15d**) montre une augmentation de la teneur en GND après un taux de réduction d'épaisseur de 50% par traitement de laminage à froid. Il convient de mentionner que les cartes ne montrent qu'un sous-ensemble du total des données disponibles; Au total, entre 80 et 150 grains ont été cartographiés pour chaque échantillon. Les données statistiques sur la norme moyenne de GND sont données dans le **tableau 2.**

3.3.2 3.3.2 Effets de l'hydrogène sur le laminage à froid de l'alliage β-21S

La **Figure 16** montre les cartes IPF de l'alliage β-21S laminé à froid, les HAB et les LAB étant identifiés par respectivement des lignes noires et grises. Le code de couleur correspond à l'orientation de l'axe transverse (TD) par rapport au système de référence de cristal. En raison de l'erreur expérimentale dans l'évaluation des orientations mesurées par EBSD [H99], les joints dont les angles de désorientation entre grains étaient inférieurs à 2° ont été exclus de l'analyse. À l'état de réception (après recuit), la microstructure était constituée de grains essentiellement équiaxes avec une taille moyenne de l'ordre de 36,0 ± 0,5 μm (**Figure 16a**). Aucune texture (non représentée ici) et sous-structure interne n'a pu être observée. Après 50% de réduction d'épaisseur par laminage à froid, les grains étaient devenus allongés le long de la direction de laminage et de nombreux joints de faible désorientation peuvent être détectés à l'intérieur des grains déformés.

Dans le domaine de concentration en hydrogène défini tel que 0,052 < H/M <0,160, et comme le montre la **Figure 16**b-d, des nouveaux joints de faible désorientation caractéristique d'une subdivision des grains ont été généré, le nombre de joints augmentant proportionnellement avec la concentration d'hydrogène introduite dans l'alliage. Cependant, pour des concentrations en hydrogène supérieure à H/M = 0,215, le nombre de joints de faible désorientation tend à diminuer et les grains β paraissent moins allongés (**Figure 16**e). Ces résultats suggèrent que l'hydrogène a des effets contradictoires sur le comportement en laminage à froid de l'alliage β-21S selon la concentration en hydrogène, c'est-à-dire un adoucissement lorsqu'une faible concentration en hydrogène (H/M < 0,160) est introduite dans le β-21S, mais un durcissement serait obtenu pour

des concentrations en hydrogène plus élevée (H / M > 0,215). Ces résultats sont en parfait accord avec de nombreuses observations expérimentales sur des alliages à structure cubique et le concept de ‘defactant’ proposée par Kirchheim [K09].

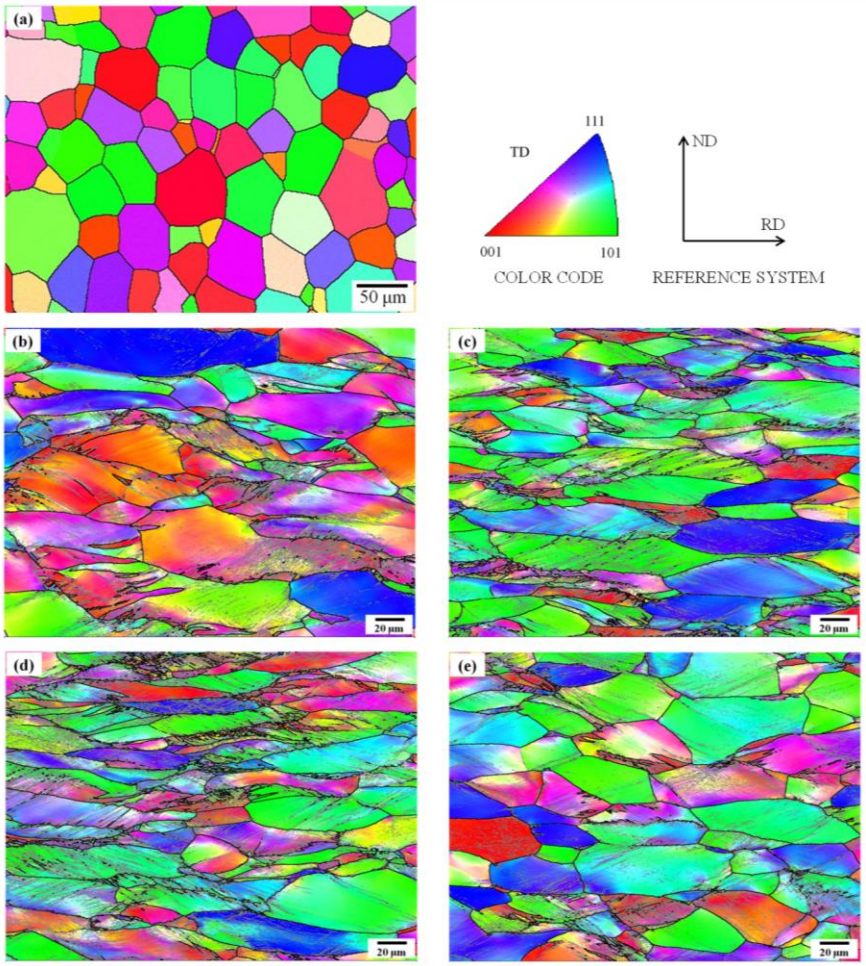

Figure 16 Images EBSD prises sur le plan transverse TD d’échantillons β-21S : (a) à l’état recuit laminé à froid, (b) H / M = 0,052, (c) H / M = 0,100, d) H / M = 0,160 et (e) H / M = 0,215

La **Figure 17**a-d montre les cartes de désorientation intragranulaires mesurées après une réduction en épaisseur de 50% dans des échantillons laminés à froid, ces cartes correspondant aux cartes IPF de la **Figure 16**b-e. Le schéma de couleurs indique la plage d'angle de désorientation variant de 0 à 30°. Un fort gradient de déformation est observé du centre vers les joints de grain dans ces échantillons laminés. L’analyse de la courbure des mailles élémentaires obtenue à partir des mesures EBSD a été utilisée pour estimer la densité et la distribution de dislocation géométriquement nécessaire (GND). Sur la base de la théorie de Nye décrivant la courbure de mailles élémentaires induites par la présence des dislocations [N53], Pantleon [P08] a développé une méthode permettant d’obtenir cinq composants du tenseur de Nye, α, à partir de cartes

d'orientation 2D. À partir de ces cinq composants, une estimation raisonnable de la densité des GND, désignée par la norme de la densité de GND ($r_{GND} = \sqrt{a_{ij}a_{ij}}$), peut être calculée. Dans ce travail, cela a été réalisé à l'aide du logiciel ATOM.

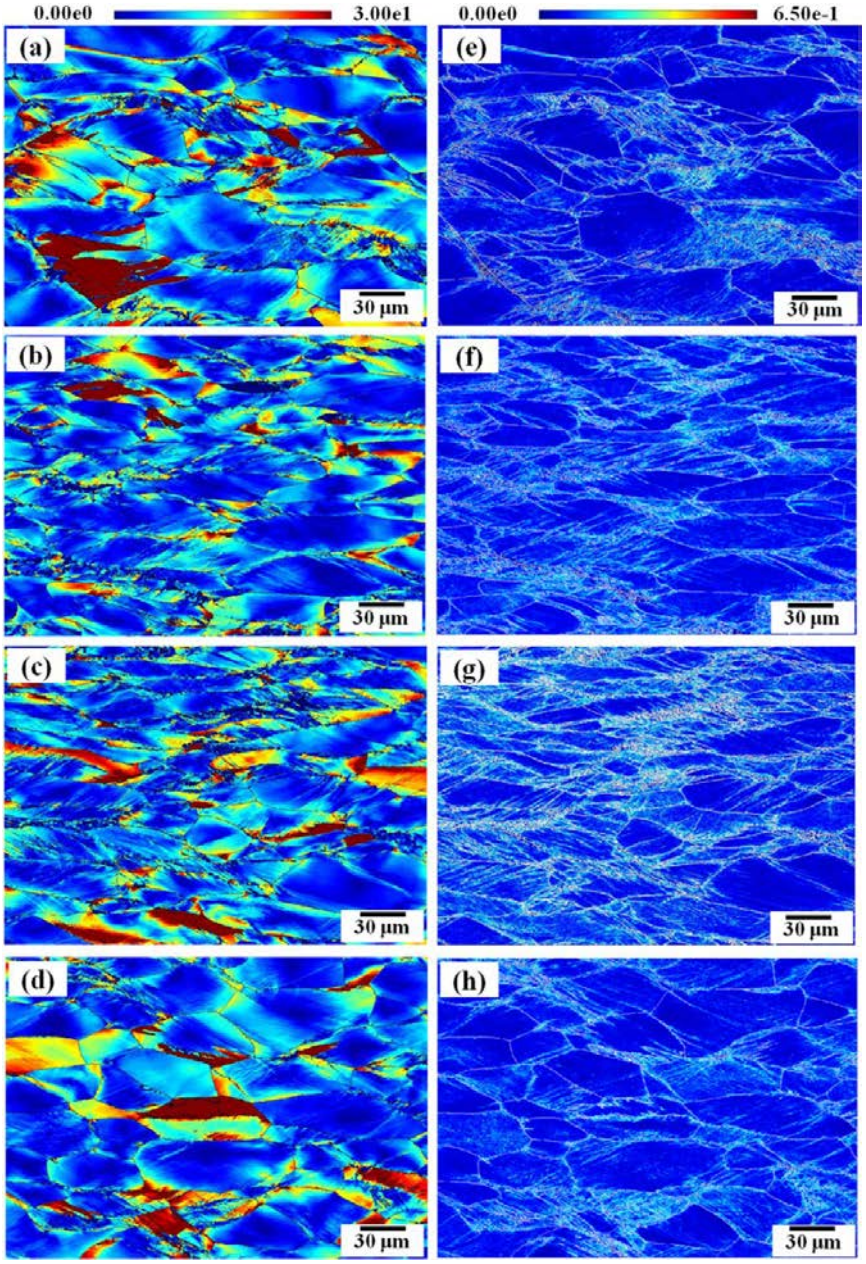

Figure 17 Désorientation intragranulaire (a-d) et cartes GND (e-h) d'alliages β-21S laminés à froid : (a, e) H/M = 0.052; (b, f) H/M = 0.100; (c, g) H/M = 0.160 and (d, h) H/M = 0.215.

Les **Figures 17**e-h montre les cartes GND correspondant aux cartes IPF illustrées dans la **Figure 1**6b-e. Les couleurs correspondent aux valeurs de la norme GND dans la plage variant entre 0 et

$6{,}5 \times 10^{-1}$. Pour chaque carte de GND, certains pixels non pas pu être indexé, car ces pixels étaient soit trop proches d'un joint de grain, ou bien parce que le matériau était trop déformé. On constate que la distribution des GND n'est pas homogène dans l'échantillon et que la plupart des GND sont situées en proximité des joints de grains. Pour les valeurs de concentration en hydrogène comprise dans la plage 052 < H/M <0,160, ces résultats suggèrent que la densité de GND augment avec l'augmentation de la concentration en hydrogène. Comparativement, pour des valeurs de concentration en hydrogène supérieures à H/M = 0,215, la densité de GND montre une légère décroissance. Cela confirme l'effet de l'hydrogène montré ci-dessus décrit par le concept de 'defactant'.

Le **Tableau 3** rassemble les résultats de la taille moyenne des grains et la densité des GND obtenues à l'aide du logiciel ATOM à partir des cartographies EBSD (cartes non représentées ici). Il convient de mentionner que les cartes données dans les figures 16e-h) ne montre qu'un échantillonnage de toutes les données analysées; entre 80 et 150 grains ont été cartographiés pour chaque échantillon. De ces résultats, nous pouvons constater qu'une concentration croissante en hydrogène entraîne une augmentation de la densité des GND ainsi qu'une diminution de la taille des grains.

Tableau 3 Taille moyenne des grains et densité des GND déterminées par EBSD

Hydrogen concentration, (H/M)	Average grain sizes, [um]	GNDs density 10^{14}, $[m^{-2}]$
0.052	12.87 ± 0.20	3.02 ± 0.06
0.100	11.09 ± 0.20	3.76 ± 0.08
0.160	9.32 ± 0.15	4.05 ± 0.05
0.215	10.60 ± 0.10	3.92 ± 0.06

3.3.3 Influence combinée de l'hydrogène et de la déformation à froid sur la recristallisation du Ti50A et de l'alliage β-21S

Dans cette étude, il a été démontré au-dessus, que les échantillons non hydrogénés et hydrogénés présentaient des microstructures différentes après une réduction de l'épaisseur de 50% par laminage à froid. Sachant que le laminage introduit des contraintes internes importantes, il est donc important de suivre l'évolution de la microstructure lors d'un traitement de recuit ultérieur.

Cela repose sur le fait que la libération de l'énergie stockée joue le rôle de force motrice pour les phénomènes de restauration et de recristallisation. Cependant la nature de la microstructure contrôle le développement et la croissance des nuclei, ainsi que l'orientation cristallographique des grains recristallisés.

3.3.3.1 Recrystallisation du Ti50A hydrogené

Pour évaluer l'influence combinée de l'hydrogène / hydrure et de la déformation de laminage à froid sur la recristallisation du titane de pureté commerciale Ti50A, les échantillons avec et sans hydrogène ont été recuits à 675°C pendant 5 min. Les **Figures 18**a et 18c montre les cartes IPF et celles des joints de grain (GB) après traitement de recristallisation pour des échantillons de Ti50A sans hydrogène, alors que les **Figures 18b et 18d** montrent celles obtenues sur des échantillons ayant été chargés 168 h en hydrogène par méthode électrolytique. Dans les cartes GB, les lignes noires et blanches correspondent respectivement aux joints de forte et de faible désorientation. Les couleurs bleues, jaunes et rouges indiquent, respectivement, les grains entièrement recristallisés, les grains présentant encore des sous-structures de dislocation et des grains déformés. Il convient de mentionner que les angles de désorientation minimale séparant les sous-grains et les grains ont été fixés respectivement à 1° et 15°. Comme le montrent les **Figures 18**a et c, un nombre important de nouveaux grains équiaxes sans orientation cristallographique préférentielles a été formé dans cet échantillon Ti50A déformé. La présence de grains contenant des sous-structures indique que la recristallisation avec ce traitement de recuit de 5 min à 675°C n'a pas été complète. Comparativement, ce même traitement réalisé sur des échantillons hydrogénés conduit à une recristallisation d'un plus grand nombre de grains (**Figures 18**b et d). Ce résultat démontre l'effet de la présence d'hydrogène caractérisée par une accélération de la cinétique de recristallisation du Ti50A.

La distribution des angles de désorientation mesurés après traitement de recuit sur des échantillons de Ti50A non-hydrogénés et hydrogénés est donnée respectivement sur les **Figures 19**a et 19b. En plus des joints de forte désorientation, une très petite fraction de joints de faible désorientation (angles de désorientation inférieurs à 15°) a été observée dans l'échantillon sans hydrogénation (**Figure 19**a). Comparativement, l'échantillon hydrogéné (**Figure 19**b) présentait un nombre négligeable de grains de faible désorientation, ce qui suggère que la structure originale a été presqu'entièrement restaurée par ce traitement de recuit. Il est important de noter que,

comme le montrent les **Figures 19c et 19**d, aucune différence significative n'a été observée dans la distribution des tailles de grain entre les spécimens hydrogénés et non-hydrogénés. La distribution de la taille du grain dans les deux cas est décrite par une loi Gaussienne normale, soulignée par les courbes noires. Par rapport au Ti50A non hydrogéné, la distribution de la taille des grains pour l'échantillon de Ti50A hydraté était moins étendue, ce qui indique que, dans ces conditions, la recristallisation et la croissance de nouveaux grains sont bien contrôlées, c'est-à-dire exemptes de croissance anormale des grains.

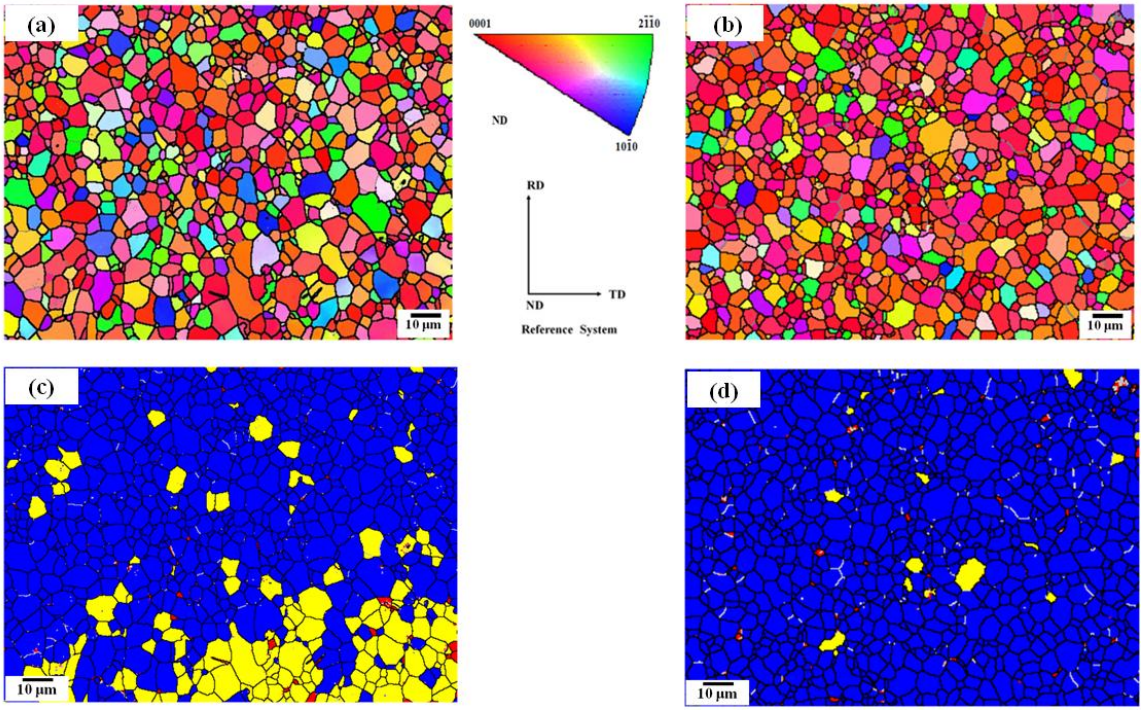

Figure 18 Cartes IPF et GB réalisées sur des échantillons de Ti50A après traitement de recristallisation. (a) et (c) échantillons sans hydrogène, et (b) et (d) échantillons chargés en hydrogène pendant 168 h. (Les lignes en noir et blanc correspondent, respectivement, à des joints de forte et de faible désorientation, les couleurs bleue, jaune et rouge indiquent, respectivement, les grains entièrement recristallisés, les grains dans lesquels subsistent une sous-structure et les grains déformés).

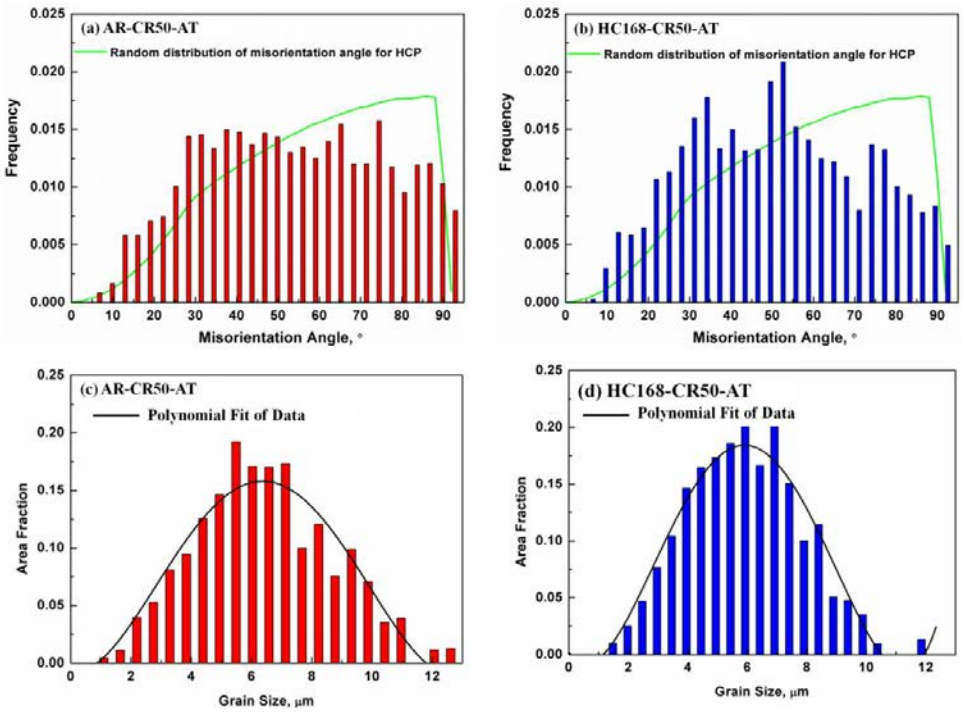

Figure 19 Angle de désorientation et les distributions de la taille des grains du Ti50A recuit : (a), (c) échantillons sans hydrogène et (b), (d) échantillons chargés en hydrogène par méthode électrolytique pendant 168 h.

3.3.3.2 Recristallisation de l'alliage β-21S hydrogéné

Pour étudier l'effet combinée de hydrogène et de la déformation de laminage à froid sur la recristallisation de l'alliage β-21S, des traitements de recuit de courte durée ont été réalisés à 800°C pendant 5 min sur des échantillons laminés contenant différentes concentrations d'hydrogène. La **Figure 20** montre les cartes IPF et GB des spécimens après un traitement de recuit. Dans les cartes GB, les lignes noires et grises correspondent respectivement aux joints de forte et faible désorientation, les couleurs bleu, rouge et jaune indiquent, respectivement, les grains entièrement recristallisés, les grains présentant des sous-structures de dislocation et les grains encore déformés. Comme ci-dessus pour le Ti50A, les angles de désorientation minimale séparant les sous-grains et les grains ont été fixés à, respectivement, 1° et 15°. Pour des valeurs de concentration en hydrogène H/M = 0,052 **(Figures 20a et 20d)**, un grand nombre de grains déformés et de grains présentant sous-structure de dislocation sont observés accompagnés de quelque nouveaux grains recristallisés. L'émergence de nouveaux grains recristallisés suggère que ces conditions de traitement sont propices au début de la recristallisation.

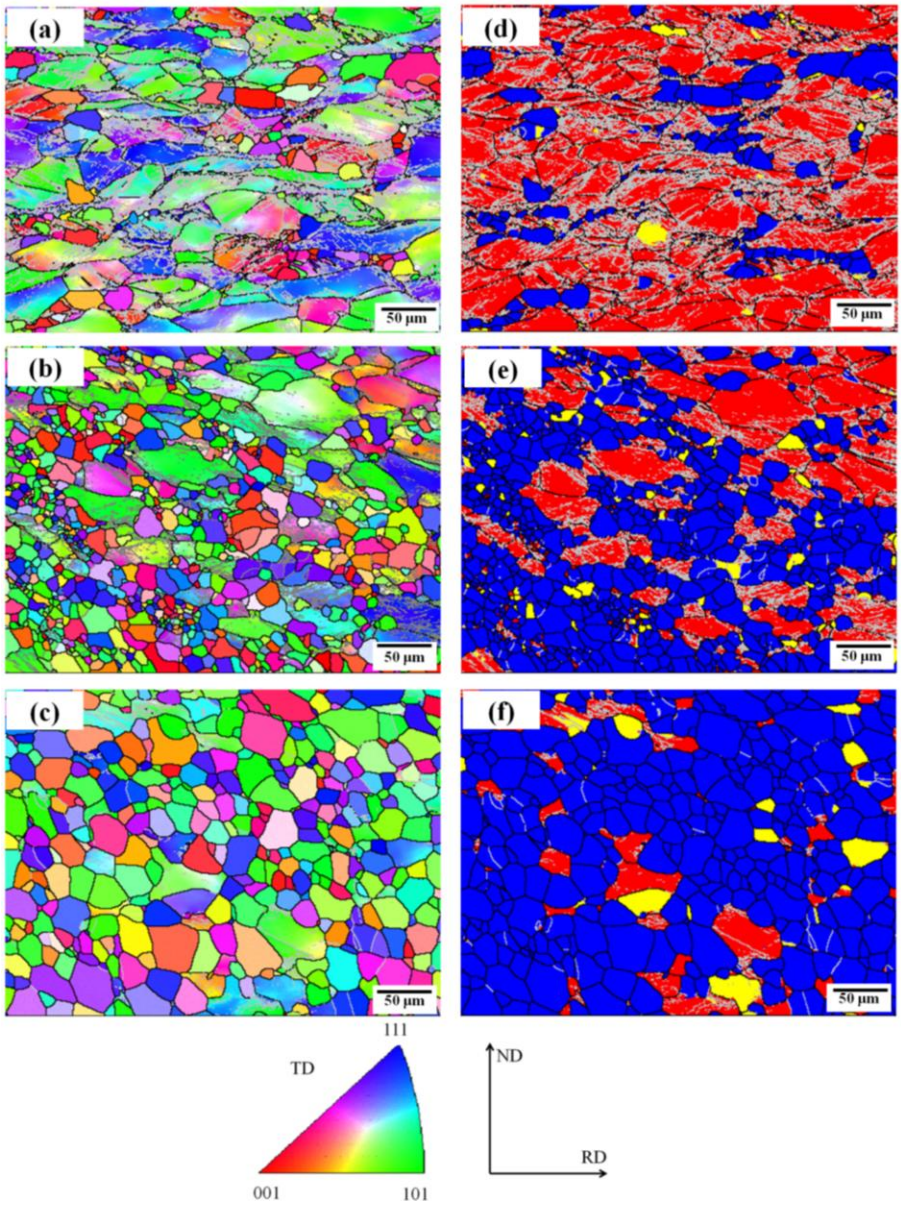

Figure 20 Cartes IPF et GB obtenues pour des échantillons d'alliage β-21S après traitement de recistallisation, (a) et (d) H/M = 0,052; (b) et (e) H/M = 0,100 et (c) et (f) H/M = 0,160. (Les lignes en noir et blanc correspondent respectivement à des joints de forte et de faible désorientation, les couleurs bleue, rouge et jaune indiquent, respectivement, des grains entièrement recristallisés, des grains contenant une sous-structure de dislocation et des grains déformés).

L'observation des **Figures 20b et 20e**) correspondant à des échantillons contenant une concentration d'hydrogène de l'ordre de H/M = 0,100 révèle un plus grand nombre de nouveaux grains recristallisés, ces nouveaux grains représentant approximativement 60% de la fraction surface de dans l'échantillon hydrogéné près traitement de recuit. Lorsque de la concentration en hydrogène est augmenté jusqu'à H/M = 0,160 (**Figures 20c et 20f**), la microstructure recristallisée couvre une fraction surfacique d'environ 88%. Aussi les grains apparaissent avec

une morphologie équiaxe et une croissance de grain minimale. Malgré la présence d'une sous-structure de déformation dans quelques grains déformés, ces résultats indiquent que l'hydrogène favorise la recristallisation de l'alliage β-21S à 800oC. Cependant une optimisation des conditions de traitement de recristallisation est encore nécessaire afin d'éliminer intégralement les grains déformés et ceux présentant encore des sous-structures de dislocation.

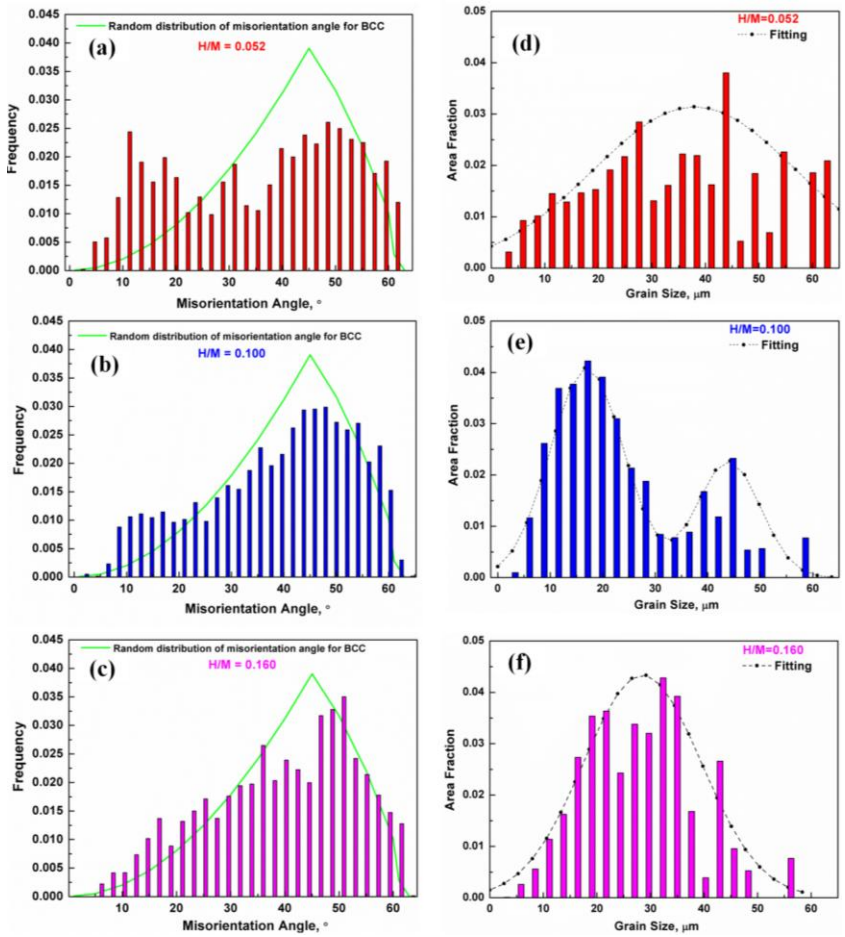

Figure 21 Distributions des angles de désorientation et de la taille des grains après traitement de recristallisation pour les alliages β-21S contenant différentes concentrations en hydrogène, (a), (d) H / M = 0,052; (B), (e) H / M = 0,100 et (c), (f) H / M = 0,160.

Les modifications de la microstructure induite par ce traitement de recuit de courte durée ont également été étudiées en étudiant la distribution des angles de désorientation entre premiers voisins (également appelée distribution de désorientation corrélée de Mackenzie), comme le montrent les **Figures 21a, 21b et 21c**. La ligne verte indique une distribution aléatoire de l'angle de disorientation (grain-à-grain) prévue pour un alliage à structure cubique sans aucune texture cristallographique. Pour une concentration en hydrogène H/M = 0,052 (**Figure 21a**), une fraction élevée de joints de faible désorientation (angle de désorientation inférieur à 15°) est observée,

celle-ci étant aussi importante que la fraction de joints de forte désorientation. Ces joints de faible désorientation sont représentatifs de la microstructure représentée dans les cartes IPF et GB (**Figures 20a et 20d**). Aussi, nos résultats indiquent qu'au fur et à mesure que la concentration en hydrogène augmentait à H/M = 0,100 (**Figure 21**b), celle-ci se traduit par une diminution évidente de la fraction de joints de faible désorientation, qui est le produit direct de la restauration de la microstructure. Lorsque la concentration d'hydrogène est augmentée jusqu'à une valeur H/M = 0,160 (**Figure 21c**), la répartition des joints de faible désorientation dans les échantillons recuits tend se rapproché de la distribution idéale d'un matériau à structure cubique isotrope. Cela indique que les microstructures déformées ont presque été entièrement remplacées par de nouveaux grains exempts de dislocation.

À l'instar du titane de pureté commerciale Ti50A, la distribution de la taille des grains pour les alliages β-21S recuits représentée par la fraction surfacique [U70] est présentée dans les **Figures 21d, 21e et 21f**. L'enveloppe de la distribution de la taille du grain suit une fonction gaussienne, comme l'indiquent les courbes noires. Pour une concentration en hydrogène H/M = 0,052, la dispersion de la taille de grain est relativement important car elle s'étend de 2 à 62 μm, ce qui peut être expliqué par la coexistence de petits grains recristallisés et de grains fortement déformés par laminage. Pour une concentration en hydrogène H/M = 0,100, la dispersion de la taille des grains est comparativement réduite avec une taille de grain moyenne de l'ordre de 12,1 ± 0,2 μm. Lorsque la concentration en hydrogène est augmentée jusqu'à H/M = 0,160, la distribution de la taille de grain suit une répartition gaussienne typique avec une taille moyenne des grains de 14,3 ± 0,3 μm, ce qui correspond à une très légère croissance des grains comparativement à une concentration en hydrogène H/M = 0,100.

4. Conclusions

Sur la base de l'étude de l'évolution microstructurale induite par l'hydrogène et de ses effets sur les propriétés mécaniques, du laminage à froid et de la recristallisation dans l'α-titane Ti50A et l'alliage β-titane β-21S, les principales conclusions sont résumées dans les points suivants:

(1) Dans le titane de pureté commerciale Ti50A de structure cristallographique hexagonale, l'analyse microstructurale combinant les techniques de caractérisation XRD, MEB-EBSD et MET a montré que lors du chargement en hydrogène par méthode électrolytique deux types d'hydrures

(δ-TiHx, ε-TiH_2) précipitaient dans la matrice α et que la fraction de volume de ces hydrures augmentait avec l'augmentation de la durée de chargement. Le présence de contrainte interne résultante de la différence de volume entre les hydrures et la matrice a pu être détectée par l'élargissement des pics de diffraction de la phase α. Cinq relations d'orientation (OR) entre la phase α et l'hydrure stable δ-TiH_x ont été déterminées par l'analyse des projections stéréographiques des plans et directions des deux phases. Les mesures de microdureté en surface ont montré que ces valeurs augmentaient proportionnellement avec la durée de chargement en hydrogène par méthode électrolytique. Ce résultat a été expliqué par l'augmentation de la fraction d'hydrures formée en sous-surface. Aussi le profil de dureté observé de la surface vers le cœur des échantillons qui reflète le gradient de concentration de l'hydrogène à travers la section des échantillons a suggéré une diffusion de l'hydrogène inhibitée par la présence des hydrures en sous-surface.

(2) Dans l'alliage de titane β-21S β-métastables, l'analyse combinée de XRD, MEB-EBSD et MET a montré que l'hydrogène tend à stabiliser la phase β jusqu'à une teneur en hydrogène de l'ordre de H/M < 0,3, mais que la stabilité diminuée pour des concentrations supérieures. Pour une concentration en hydrogène atteignant une valeur H/M = 0,460, l'observation d'une fraction important de phase martensite α". La formation de cette phase martensitique de structure hexagonale a pu être expliquée par le cisaillement induit par la présence d'atomes d'hydrogène en position interstitiel et l'affaiblissement des liaisons interatomiques entre les atomes de la matrice.

(3) L'effet de l'hydrogène a également été étudié sur le laminage à froid de ces deux matériaux. Pour une faible réduction d'épaisseur appliqué au Ti50A correspond à un niveau de déformation équivalente ε_{eq} = 0,12, il a été observé que la formation de macle de tension TT1 $\left\{10\bar{1}2\right\}\left\langle\bar{1}011\right\rangle$ était favorisée ce qui a été attribué à l'augmentation du rapport c/a induite par l'introduction de l'hydrogène et la formation d'hydrures. Pour des niveaux de déformation plus élevées (ε_{eq} = 0,80) (c'est-à-dire une réduction d'épaisseur de 50%), twinning became almost saturated et il est accompagné par un raffinement notable de la microstructure des échantillons pré-hydrogénés de Ti50A comparativement à ce qui a pu être observé pour les échantillons non hydrogénés. L'observation du raffinement microstructural se traduit par une un nombre élevée de joints de forte désorientation (HAB) particulièrement à proximité des hydrures. En outre, les analyses ont révélés la présence d'un grand nombre de dislocations géométriquement nécessaires (GND)

produites pour tenir compte de l'incompatibilité de déformation imposée par laminage particulièrement importante dans le cas échantillons chargé en hydrogène à cause d'hydrures dans la matrice α. L'influence de l'hydrogène sur le laminage à froid de l'alliage β-21S a révélé des effets distincts en fonction de la teneur en hydrogène satisfaisant le concept de 'defactant'. Dans la plage de concentration en hydrogène $0{,}052 < H/M < 0{,}160$, les atomes d'hydrogène dissous dans la solution solide β tendent à faciliter la mobilité et la densité des dislocations, ce qui se caractérise par un affinement de la microstructure proportionnel à la concentration en hydrogène. Pour des concentrations en hydrogène supérieures à $H/M = 0{,}215$, l'observation de grains β moins déformés ainsi que de micro-fissures suggère un mécanisme de durcissement de la solution solide, expliqué par une réduction de la mobilité des dislocations par l'hydrogène.

(4) L'effet combiné de l'hydrogène et de la déformation induite par le laminage à froid permettant la recristallisation a montré que le Ti50A pré-hydrogéné contenait une fraction plus élevée de nouveaux grains recristallisés comparativement au même condition imposée aux échantillons non hydrogénés. L'étude sur l'alliage β-21S a permis de mettre en évidence une fraction croissante de grains recristallisés avec l'augmentation de la concentration en hydrogène. Bien que le rôle exact de l'hydrogène sur la recristallisation n'a pas pu être établi, les résultats observés dans cette étude suggèrent que l'introduction de l'hydrogène dans les alliages de titane peut faciliter la recristallisation ce qui peut se montrer très intéressant pour la réduction des coûts de procédés.

1 Introduction

Avec l'épuisement des ressources naturelles, l'humanité est à la recherche d'autres sources d'énergie. L'hydrogène est considéré comme une des futures sources futures et il est très possible que l'économie de l'hydrogène se réalise au cours des 50 prochaines années. Dans un tel scénario, la production, le stockage, le transport et l'utilisation de l'hydrogène nécessiteront des développements à plus grande échelle.

Le titane a une forte affinité avec l'hydrogène, et de nombreux travaux ont étudié les aspects de stockage et de dégradation des propriétés mécaniques liée à l'hydrogène. Heureusement, la réaction de l'hydrogène avec du titane est réversible en raison d'une enthalpie positive de la solution en titane [W97, M51] permettant la désorption de l'hydrogène durant un traitement sous vide à haute température. Par conséquent, l'hydrogène comme élément d'alliage temporaire a été utilisé pour améliorer la mise en forme des alliages de titane, ces traitements conduisant à une modification de la microstructure et des propriétés mécaniques [FS04, ZZ97]. Récemment, un nouveau concept introduit par Kirchheim [K09] et désigné par le terme anglais « defactant » (*un DEFect ACTing AgeNT étant défini comme atome de soluté se plaçant autour des défauts des structures cristallines jouant un rôle similaire à celui d'un agent tensioactif sur les surfaces*) a permis d'expliquer les mécanismes de fragilisation par une réduction de l'énergie de formation de défauts par addition d'hydrogène [BV10].

Par conséquent, si un atome d'hydrogène, d'abord dissous en tant que defactant dans la structure d'un matériau métallique permettant faciliter la formation de lacunes, des dislocations et des défauts d'empilement lors d'une déformation à froid est ensuite éliminé, il est connu que la densité de dislocation est augmentée et que les propriétés de façon concomitante par exemple comme la dureté et résistance mécanique sont améliorées. Cependant, peu études se sont intéressées à l'effet de l'hydrogène sur le comportement de déformation en laminage à froid et la recristallisation des alliages de titane. Par conséquent, nous avons entrepris ce travail dans le but d'étudier l'évolution de la microstructure induite par l'introduction d'hydrogène et ses effets sur les propriétés mécaniques, la déformation en laminage à froid et la recristallisation de deux alliages de titane de structures cristallographiques différentes. Cette étude a été réalisée en combinant les techniques expérimentales d'analyses de diffraction des rayons-X, d'observations

au microscope électronique à balayage (MEB) équipé de la technique EBSD (Electron BackScattered Diffraction) et de microscope électronique à transmission (MET).

2 Materials and Experiments

Dans le présent travail, les deux alliages de titane utilisés sont le titane commercialement pur Ti50A (ASTM 2) de structure cristallographique hexagonale et l'alliage de titane β-métastable connu par la désignation β-21S, de composition Ti-15Mo-3Nb-3Al-0.2Si et de structure cristallographique cubique à face centrée. La **Figure 1** résume la procédure expérimentale.

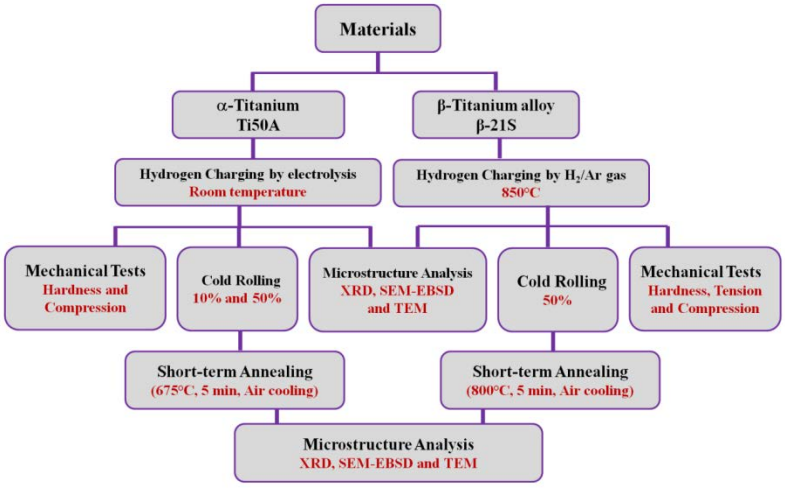

Figure 8 Illustration de la procédure expérimentale utilisée dans cette étude

L'hydrogène a été introduit dans les échantillons par deux méthodes différentes : une méthode électrolytique pour le Ti50A (**Figure 2**) et sous atmosphère de gaz d'hydrogène pour le β-21S. Pour des chargements induisant différentes concentrations en hydrogène, des analyses microstructurales et des essais mécaniques (microdureté, nanoindentation, traction et compression) ont été effectués dans le but d'élucider l'effet de l'hydrogène sur les microstructures et propriétés mécaniques du Ti50A et du β-21S.

Des essais de laminage symétrique à froid ont également été réalisés sur les échantillons pré-hydrogénés. Des traitements de recuit de courte durée ont été appliqués après laminage à froid, pour étudier la recristallisation du Ti50A et de l'alliage β-21S. L'interdépendance entre hydrogène, microstructure et propriétés a pu être révélée grâce aux outils de caractérisation microstructurale de diffraction des rayons-X, microscope électronique à balayage de haute résolution équipé de la technique EBSD et microscope électronique à transmission).

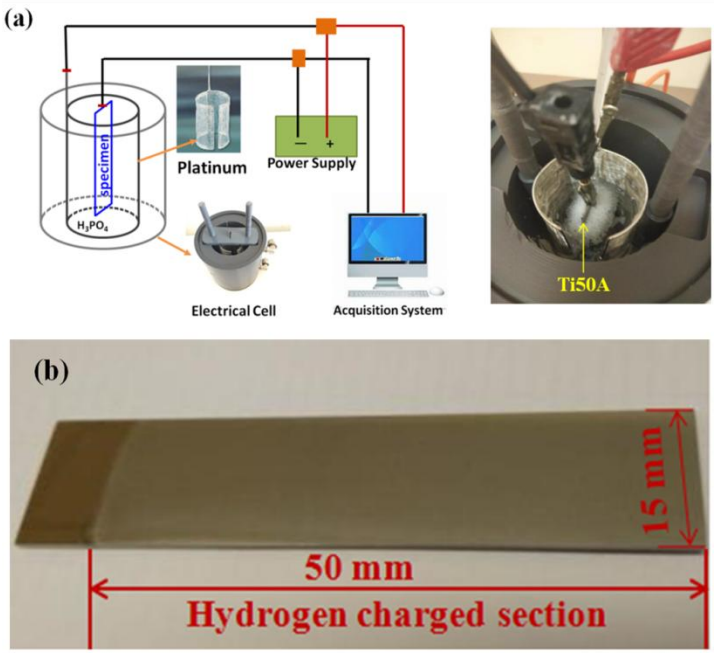

Figure 9 (a) Schéma du système de chargement en hydrogène, (b) photographie d'un échantillon Ti50A hydrogéné

3 Évolutions microstructurales induites par l'hydrogène et leurs effets sur les propriétés mécanique

3.1 Évolutions microstructurales induites par l'hydrogène et leurs effets sur les propriétés mécanique du Ti50A

Comme il est montré sur la **Figure 3**, la courbe de diffraction des rayons X obtenu sur un échantillon après 72 heures de chargement en hydrogène et correspondant à une concentration d'environ 60 ppm, met en évidence la présence de deux types d'hydrures, à savoir le δ-TiH_x et le ε-TiH_2. Ces hydrures ont été détectés sous la surface des échantillons dans une région dont l'épaisseur était approximativement de 20 ± 2 µm. L'hydrure δ-TiH_x ($1,5 \leq x \leq 1,99$) a un structure cristallographique cubique face centrée (structure CaF_2, de paramètre de maille a = 0,4445 nm) avec des atomes d'hydrogène occupant les sites interstitiels tétraédriques, tandis que l'hydrure ε-TiH_2 a une structure quadratique à base centrée (de paramètres de maille a = 0,312 nm et c = 0,418 nm, JCPDS-PDF 9-371) [WE02, LX13].

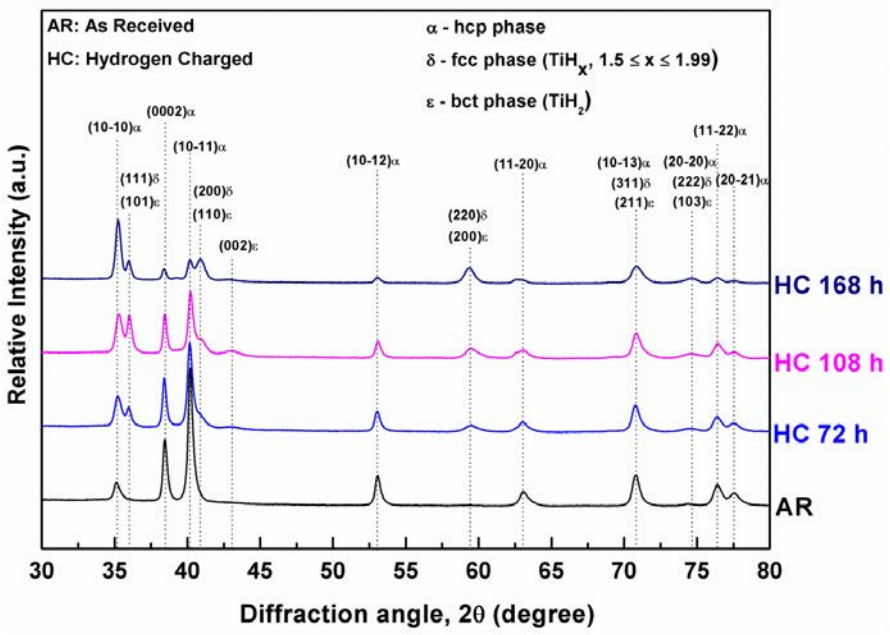

Figure 10 Courbes de diffraction des rayons X du Ti50A à l'état de réception (AR) et après différents chargement en hydrogène (HC).

Comme observé dans les courbes de diffraction des rayons X, l'intensité des pics de diffraction correspondant aux hydrures augmentait avec la durée de chargement en hydrogène, ce qui suggère une augmentation de la fraction volumique de ces hydrures formés en sous-couche des échantillons. En outre, on peut remarquer que les pics de diffraction des rayons X correspondant à la matrice de phase α (structure hexagonale) s'élargissent lors que la durée du temps de chargement en hydrogène augmente. L'observation de l'élargissement des pics de la phase α peut être attribuée à l'apparition d'une déformation locale induite par la formation de hydrures.

Pour étudier quantitativement l'effet de l'hydrogène, les microstructures des échantillons Ti50A après 72, 108 et 168 h de chargement en hydrogène ont été caractérisées par la technique EBSD. La **Figure 4** montre les cartes de phase EBSD du Ti50A avant et après hydrogénation avec les hydrures ε-TiH_2 et δ-TiH_x ainsi que la phase alpha étant respectivement représentées dans les couleurs rouge, bleu et gris. Une petite quantité d'hydrures en forme d'aiguille a pu être détectée au niveau des joints de grains comme le montre la carte de phase de l'échantillon après 72 h de chargement électrolytique (**Figure 4b**). Lorsque la durée de chargement atteint 108 h (**Figure 4**c), la fraction volumique d'hydrure a augmenté mais ceux-ci sont essentiellement situés à l'intérieur des grains d'alpha. Pour des durées de chargement en hydrogène de 168 heures (7 jours), une quantité considérable d'hydrures δ-TiH_x, d'épaisseur moyenne inférieure à 1,0 μm et de longueur

environ 7,0 µm s'est formée aux joints de grains ainsi qu'à l'intérieur des grains de phase α (**Figure 4d**). Les valeurs de la fraction surfacique d'hydrures δ-TiH_x et ε-TiH_2 calculées par le logiciel Channel 5 étaient, respectivement, de 12,5 ± 0,3% et 4,9 ± 0,5% (valeurs moyennées à partir des résultats de 5 analyses).

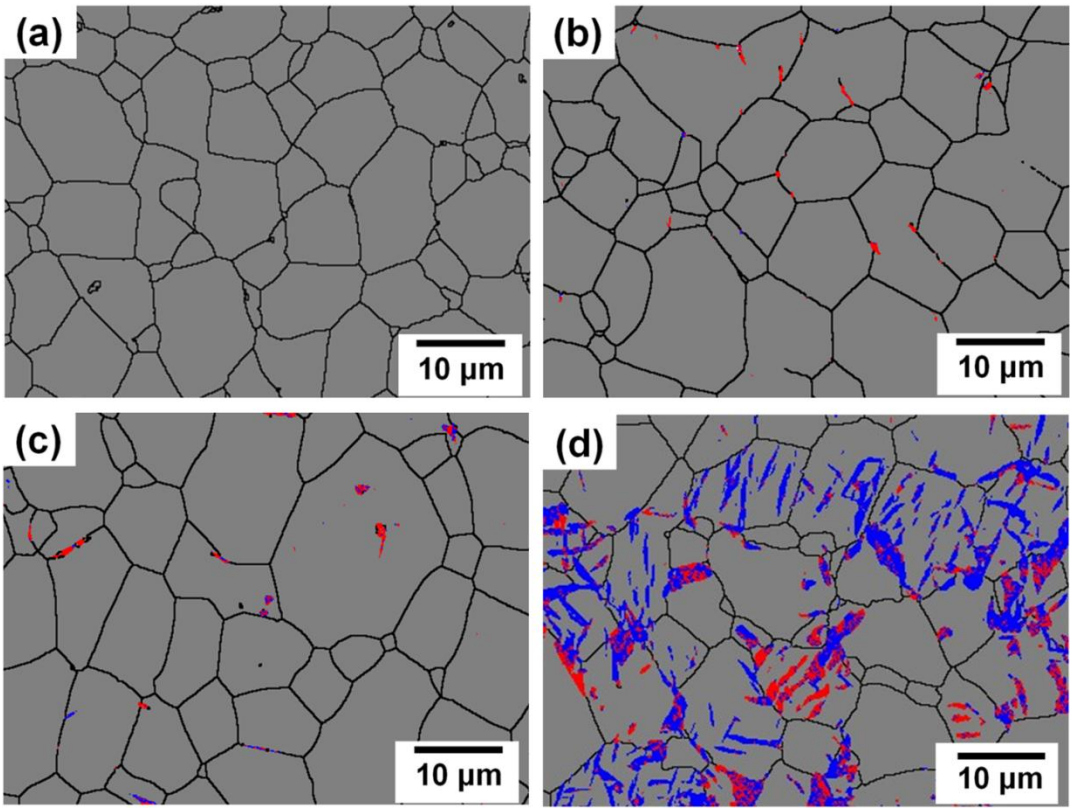

Figure 11 Cartes de phase par analyses EBSD du Ti50A à l'état de réception (a), échantillons de Ti50A après 72 h (b), 108 h (c) and 168 h (d) de chargement électrolytique; (les couleurs rouge, blue et grise correspondent, respectivement, aux hydrures ε-TiH_2, δ-TiH_x et à la matrice α)

Les relations d'orientations (OR) entre l'hydrure stable δ de structure cfc et la matrice α pseudo-hcp ont pu être déterminées par l'analyse des projections stéréographiques correspondantes aux plans et directions des deux phases, comme représenté sur la **Figure 5**. Par exemple, sur la figure 5a, un plan $\{001\}_\delta$ de l'hydrure δ est parallèle à un plan $\{0001\}_\alpha$ de la matrice α. Aussi la projection d'une direction $<110>_\delta$ de l'hydrure δ superpose celle de la projection correspondant à une direction $<11\bar{2}0>_a$ de la matrice α. Par conséquent, l'analyse des projections stéréographiques nous a permis de mettre en évidence cinq relations d'orientations spécifiques entre l'hydrure δ-TiH_x et la matrice α, tel qu'il est présenté dans le tableau 1 (données à partir de 5 cartes). Des études antérieures par le biais de caractérisation MET avaient elles révélé deux

relations d'orientations épitaxiales particulières (OR1 et OR2) [CG17] entre l'hydrure δ et la phase α dans des alliages de Ti et Zr.

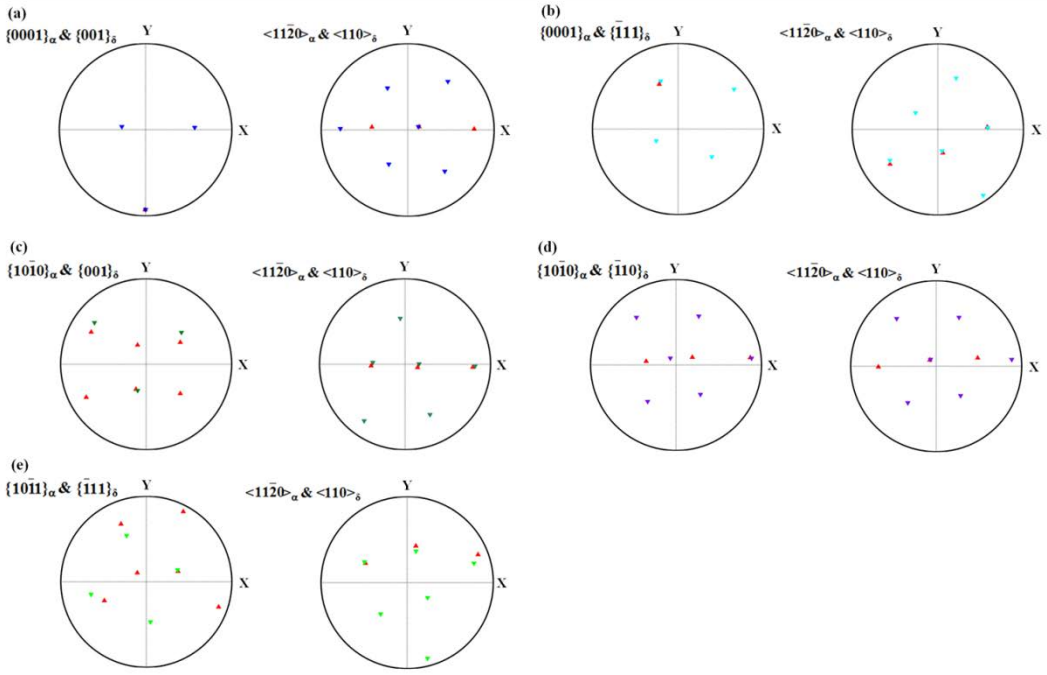

Figure 12 Projections stéréographiques de la matrice α (hexagonale) et des hydrures δ-TiHx (cfc) montrant les relations d'orientations (OR) correspondant aux plans and directions.

Des analyses au microscope électronique à transmission ont été réalisées pour confirmer la structure cristallographique des hydrures. Pour préparer cette caractérisation, les hydrures ont d'abord été localisés par MEB, comme le montre la **Figure 6**a, et une lame mince (**Figure 6**b) a été extraite par Focused Ion Beam. La **Figure 6**c montre la micrographie MET de l'échantillon hydrogéné prise à partir de la lame mince confirme la présence des deux types d'hydrures observés au sein d'un grain α. Les images MET en champ clair prises dans différentes zones de la matrice (correspondants aux régions sélectionnées A et B sur la **Figure 6**c) sont présentées dans la **Figures 6**d et 6e. On peut remarquer que les deux hydrures ont des morphologies totalement différentes, ce qui est conforme aux observations MEB-EBSD décrites ci-dessus. La figure 6f montre le cliché de diffraction d'électrons de la région sélectionnée (SAED) correspond à la zone encerclée dans la **Figure 6**e. Comme l'indique ce cliché, l'axe de la zone <-112> de l'hydrure δ-TiH_x de structure cubique face centrée coïncide avec l'axe de la zone <000-1> de la phase α de symétrie hexagonale. Les micrographies MET en champ sombre on été réalisés en sélectionnant deux réflexions correspondant à la fois à l'hydrure δ-TiH_x et à la matrice α (encerclée sur le

diagramme SAED, figure 6f). En revanche, l'hydrure ε-TiH_2 avec la structure de phase quadratique à base centrée (correspondant à la **Figure 6**d) présente une intensité de diffraction électronique faible. Il convient de rappeler que la phase ε-TiHx est thermodynamiquement stable jusqu'à une température maximale d'environ 25°C. Ceci est en accord avec les résultats présentés ci-dessus EBSD, et qui indique que la structure de l'hydrure ε-TiHx est instable sous l'irradiation de faisceaux d'électrons des équipements FIB et MET [WE02, LX13].

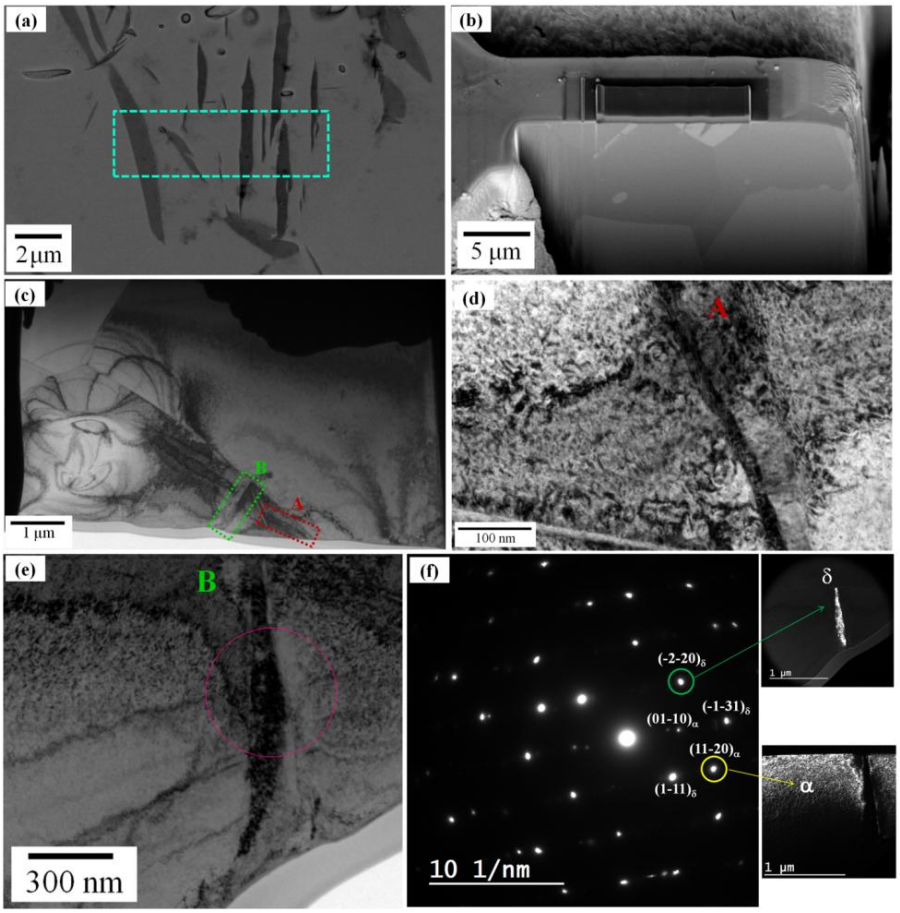

Figure 13 Analyses MEB et MET réalisées sur des spécimens hydrogénés; (a) image MEB (détecteur en électron secondaire); (b) détail de la zone sélectionnée de l'image (a) extraite par FIB); (c) Micrographie MET de la même zone; (d) et (e) images MET en champ clair de la matrice prise de, respectivement, la zone A et B comme indiquée en (c); (f) cliché SAED correspondant à la zone encerclée dans (e) et en insert les images en champ sombre correspondant aux taches de diffraction encerclées dans le cliché SAED et pointées par les flèche.

Des mesures de microdureté ont été effectuées sur la section transversale des alliages de Ti50A hydrogénées. La **Figure 7** montre les profils de microdureté de Ti50A hydrogéné sous différents temps de chargement en hydrogène. Ces échantillons de Ti50A hydrogénés présente un fort gradient de dureté au travers de la section. Par exemple, après un chargement en hydrogène de

168 h, la valeur de la dureté décroît rapidement de 2240 MPa depuis la surface jusqu'à 1700 MPa atteinte à une distance de 75 µm sous la surface. La valeur de dureté décroissante peut être interprétée par le gradient de concentration en hydrogène au travers de la section et de la fraction de volume des hydrures décroissante lorsque l'on se rapproche du centre de l'échantillon où l'hydrogène n'a pas diffusé. Afin de faciliter d'autres analyses, le Ti50A hydrogéné a été recuit pendant 2 heures à 400 ° C sous gaz Ar. Le graphique inséré dans la **Figure 7** montre le profil de microdureté du Ti50A hydrogéné après le traitement de recuit. En supposant un mécanisme de diffusion de Fick, un tel recuit devrait permettre la diffusion de l'hydrogène vers le centre de l'échantillon, fournissant ainsi une répartition uniforme de l'hydrogène sans générer de croissance des grains.

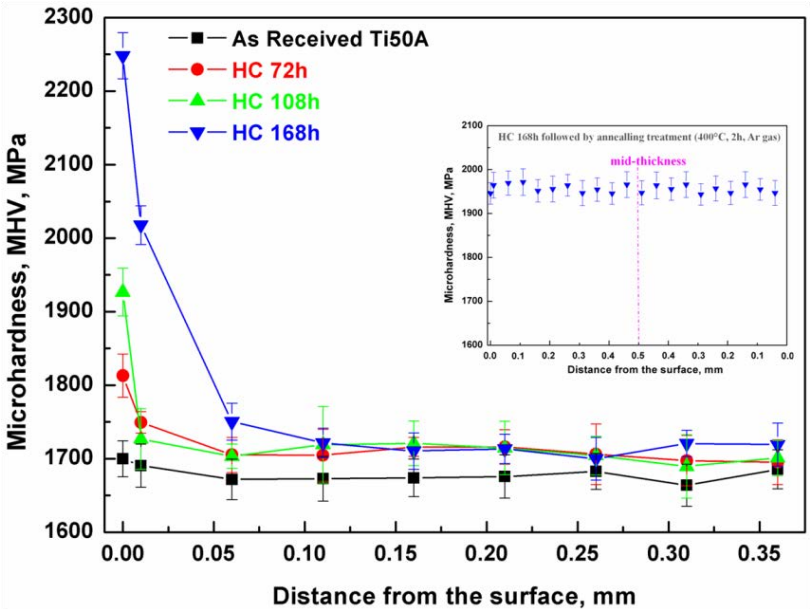

Figure 14 Profiles de microdureté mesurés dans le Ti50A avant et après chargement en hydrogène

3.2 Évolutions microstructurales induites par l'hydrogène et leurs effets sur les propriétés mécanique du β-21S alloy

Les diagrammes de diffraction des rayons-X pour les alliages β-21S hydrogénés sont présentés dans la figure 9 avec leurs concentrations en hydrogène respective. Les courbes ne révèlent que les pics de fraction correspondant à la phase β; aucune indication de la phase α, d'hydrures ou d'autre phase ne peuvent être détectés. Il est important de souligner que les pics de diffraction de cette phase β se déplacent vers des valeurs d'angles 2θ plus faible, indiquant une expansion du réseau cristallin de la phase β résultant du chargement en hydrogène. L'introduction de l'hydrogène dans les sites interstitiels tétraédriques de petites dimensions conduit à une

expansion non négligeable du réseau cristallin, ainsi qu'à des distorsions de réseau [K01, SC01]. La variation du paramètre de maille déterminé par la relation de Bragg a été reportée dans le **Tableau 1** en fonction de la concentration en hydrogène. Ces variations sont en accord avec celles rapportées par Robertson [TR01].

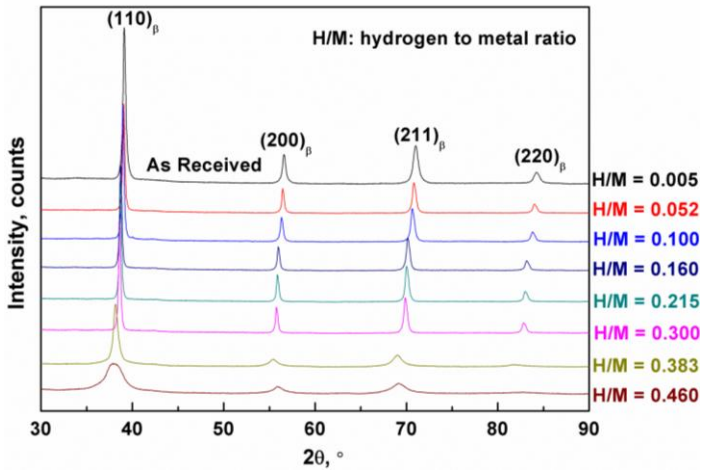

Figure 8 Profiles de diffraction des rayons-X pour le β-21S préparés avec différentes concentrations en hydrogène (exprimées en rapport H/M)

Table 1 Variation du paramètre de maille du titane -21S en fonction de la concentration en hydrogène

Sample series	H_2 charging pressure (kPa)	Lattice parameter (Å)	Relative volume change of BCC lattice, %	Hydrogen concentration	
				(at. %)	(H/M)
As received	N/A	3.247	/	0.500	0.005
1123-1	1	3.256	0.834	4.940	0.052
1123-2	5	3.259	1.113	9.091	0.100
1123-3	10	3.273	2.421	13.793	0.160
1123-4	25	3.285	3.552	17.695	0.215
1123-5	35	3.294	4.405	23.077	0.300
1123-6	50	3.311	6.030	27.660	0.383
1123-7	100	3.317	6.607	31.530	0.460

Etant donné que l'hydrogène diminue la température de la transformation allotropique (température du transus β) [SC01], celui-ci améliore la stabilité de la phase β lors du refroidissement. Il est également important de préciser l'évolution de la microstructure induite par l'hydrogène et de comprendre l'origine de la baisse d'intensité diffractée accompagnée d'un

élargissement des pics tel que l'on peut le constater dans la **Figure 8**. Les micrographies MEB prises sur la section transversale des alliages β-21S hydrogénés contenant différentes concentrations en hydrogène sont montrées dans la figure 10. Les **Figures 9**a et 9b montrent les images MEB de l'alliage de titane β-21S hydrogéné avec une concentration d'hydrogène H/M = 0,215. Cette concentration en hydrogène a été sélectionnée car elle correspond à la concentration critique pour laquelle une transition ductile-fragile brusque a été rapportée par Teter et al. [TR01]. La microstructure est composée uniquement de grains équiaxes de la phase β; aucune autre phase α ou hydrure n'est détectée sur ces images. Toutefois, lorsque la concentration en hydrogène est augmentée jusqu'à un rapport H/M = 0,380, des structures en forme de plaque sont observées dans les grains de la phase β, comme cela peut être observé dans les **Figures 10**c et 10d. Lorsque la concentration en hydrogène atteint un rapport H/M = 0,460, un nombre croissant de structures analogues à des plaques est formé dans les échantillons, comme il est représenté dans les **Figures 9e et 9**f. Cette morphologie en forme de plaque est identique à la structure martensite couramment observée dans les alliages de titane β-métastable déformés ou trempés [CW87, MT04 et CZ16]. L'apparition des micro-fissures, comme indiqué par les flèches, suggère une importante concentration de contrainte locale notamment aux joints de grains des alliages β-21S hydrogénés.

Dans le but d'examiner plus en détail la structure de la martensite, des analyses EBSD ont été effectuées sur la section transverse de l'échantillon hydrogéné avec un rapport H/M = 0,460. La **Figure 10**a montre la micrographie MEB en électron secondaire de la région analysée. Les grains β observées sont marqués avec les indices A, B, C, D, E, F et G. La **Figure 10**b montre la micrographie en électron rétrodiffusé du grain A prise avec un grossissement plus élevé. Sur cette Figure on peut observer quatre plaquettes de phase martensite α'' d'orientations cristallographiques différentes coexistant au sein d'un même grain β et repérées par des chiffres arabes en jaune dans la **Figure 11**b. Les plaquettes de martensite repérées 1 et 2 ayant les directions communes sont distribuées de façon alternative dans le grain β. Pour avoir une valeur précise de l'angle d'Euler de chacune des plaquettes de martensite, nous avons mesuré les orientations qu'elles forment avec la phase β. Par exemple, dans le grain A, quatre variantes de martensite orientées, α_1", α_2", α_3" et α_4", peuvent être détectées. Cette martensite α" phase a une structure orthorhombique c'est-à-dire la même phase martensitique que la phase α" induite par contrainte mécanique [CW87, LX98 et MT04].

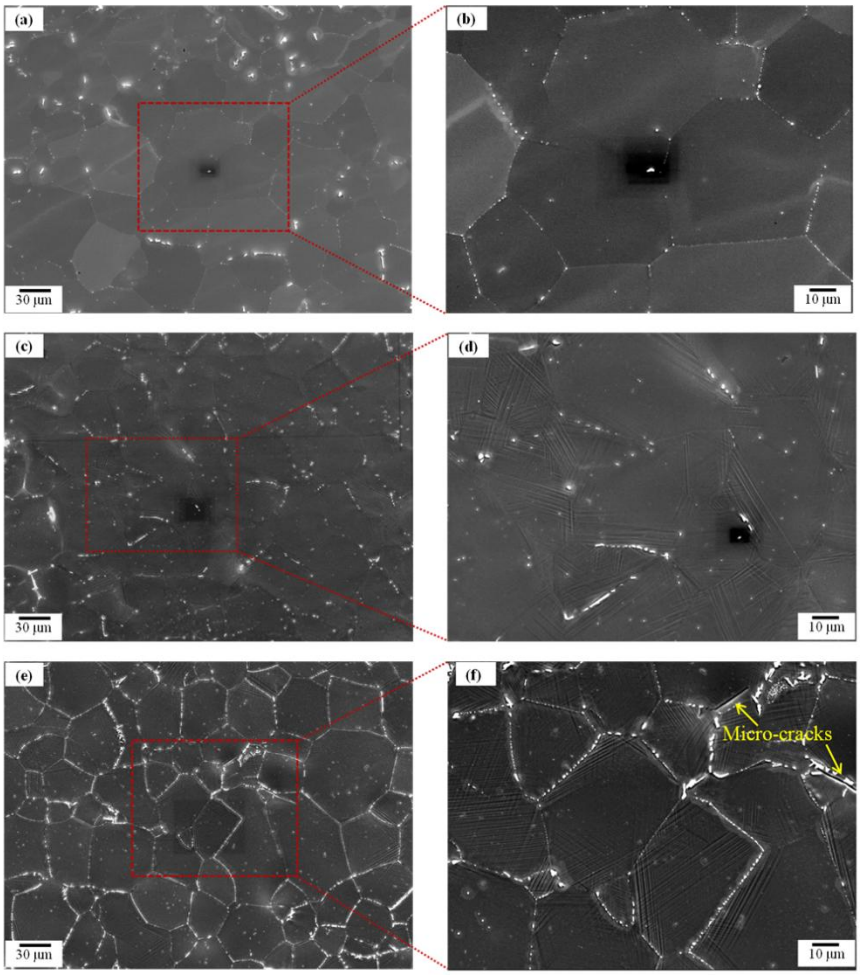

Figure 9 Microscopies MEB montrant la section d'échantillons β-21S hydrogenés; (a), (b) H/M = 0.215; (c), (d) H/M = 0.383 et (e), (f) H/M = 0.460.

Les relations d'orientations (OR) {112} β // (110) α " et $\langle \bar{1}10 \rangle$β // [001] α" ont été décrites dans des études antérieures portant sur les alliages de titane β-métastable [CW87, MT04 et CZ16]. Dans le présent alliage, ces OR ont été confirmée par l'analyse des projections stéréographiques des plans et directions des deux phases sur les **Figures 10**c et 10d. À partir des projections stéréographiques, on peut constater que pour chaque variante de martensite possède un plan {110}α'' parallèles à un plan {112} de la phase β. La projection de la direction <001> α" pour chaque variante de martensite coïncide avec une direction $\langle \bar{1}10 \rangle$ de la phase β. Par conséquent, les résultats décrits ci-dessus confirment la formation d'un réseau constitué de quatre variantes de la phase martensitique α'' respectant les relations d'orientations classiques entre les phases α'' et β détectée sous la surface des échantillons c'est-à-dire jusqu'à une épaisseur de l'ordre de 250 à 400 nm.

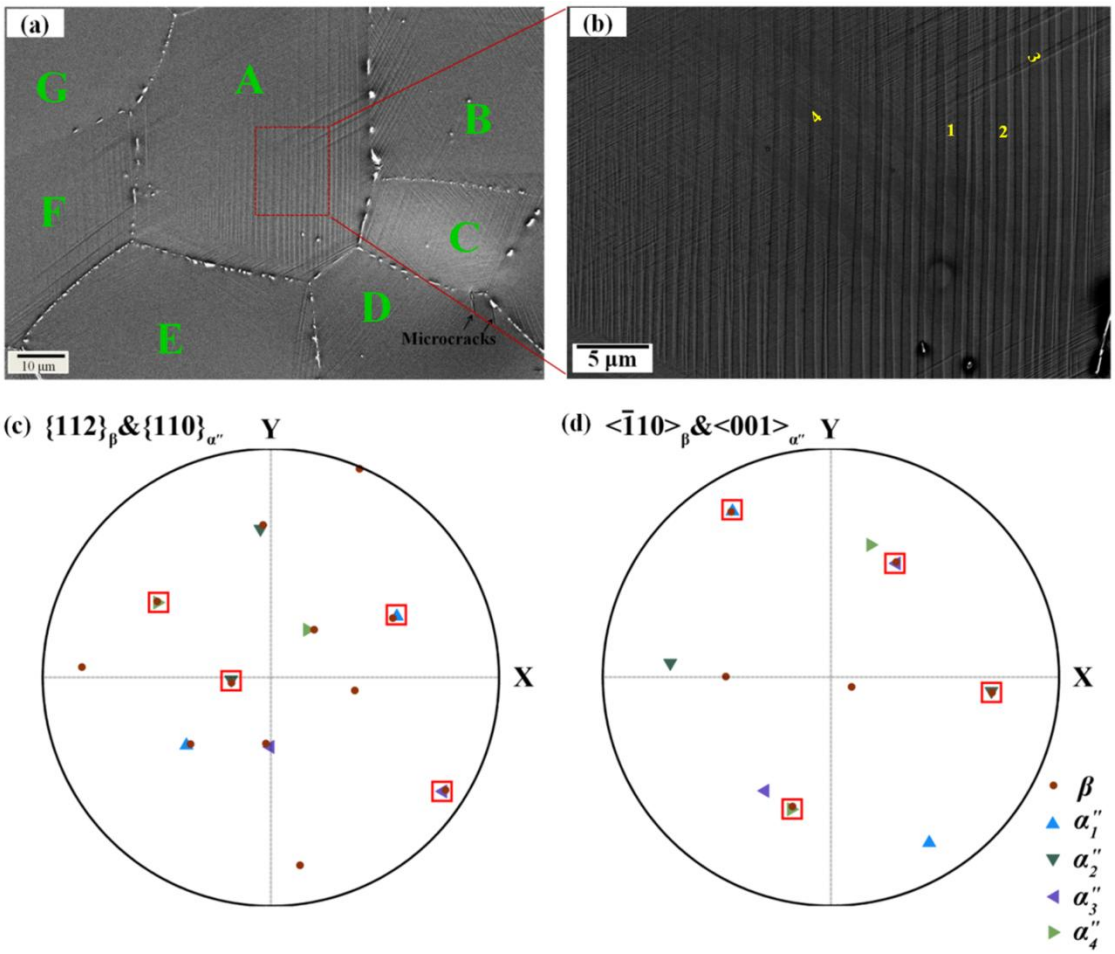

Figure 10 Analyse des variants de martensite par EBSD : (a) micrographie MEB montrant les variants de martensite α'' dans des grains β; (b) micrographie obtenue en mode électrons rétrodiffusés de la zone analysée par EBSD; (c) projections stéréographiques des plans$_{\alpha}$ {112}$_{\beta}$ and {110}$_{\alpha''}$, et (d) projections stéréographiques des directions $<\bar{1}10>_{\beta}$ et <001>$_{\alpha''}$ (les projections surperposées des phases β et α'' sont entourées par les carrés de couleur rouge).

La microstructure locale dans des échantillons d'alliage β-21S hydrogéné et non-hydrogéné a été observée par MET. La **Figure 11**a montre l'image MEB de cet échantillon après préparation par micro-usinage ionique (comme indiqué par la flèche).The insert micrograph is magnification of the selected grain, no internal structure can be observed.

La **Figure 11**b montre l'image en champ clair (BF) de la lame mince extraite d'un échantillon de l'alliage β-21S non-hydrogéné. Le cliché de diffraction des électrons de la région sélectionnée (SAED) correspondante est donnée dans la **Figure 11**c. Les stries diffuses dans ce diagramme de diffraction des électrons sont typiques de la présence de la phase de ω athermique telle qu'il a été rapporté par Teter et al. dans un échantillon de l'alliage β-21S trempé à l'air [TR01]. Ceci est dû au fait que la formation de la phase de ω athermique ne peut être évitée dans les alliages titanes β,

quelque soit la vitesse de refroidissement. Cependant, la fraction volumique de cette phase ω athermique est très faible. Les tentatives de détection de cette phase ω à partir des stries ont échoué.

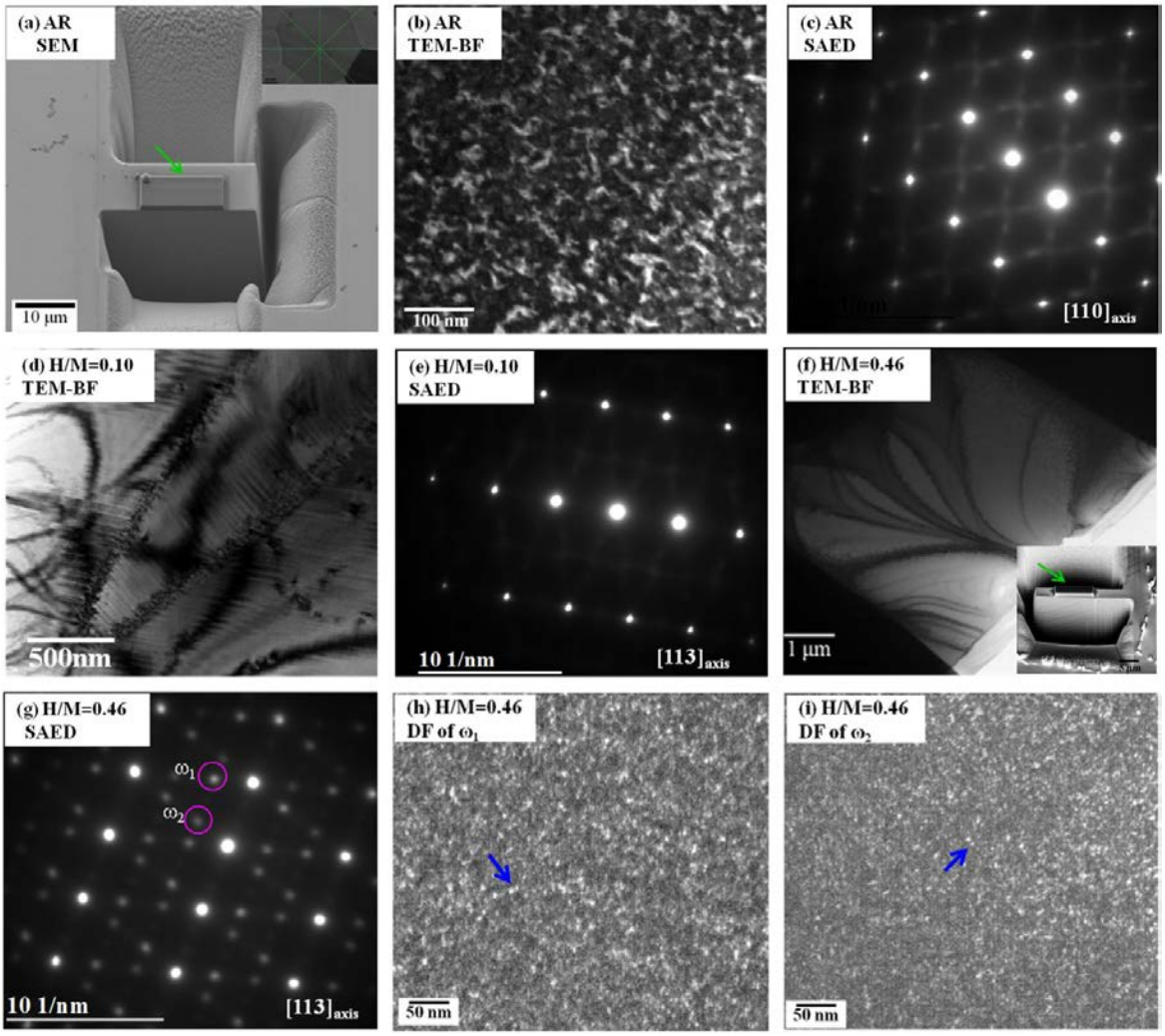

Figure 11 Caractérisation métallographique des alliages β -21S hydrogénés et non-hydrogénés. (a) image MEB de l'alliage β-21S non-hydrogéné après préparation par micromachining ionique (FIB); (b) micrographie MET-BF de l'alliage β-21S non-hydrogéné; (c) cliché SAED de l'alliage β-21S non-hydrogéné; (d) micrographie MET-BF de l'alliage β-21S chargé en hydrogène avec un rapport H/M = 0,10; (e) cliché SAED de l'alliage β-21S hydrogéné correspondant; (f) micrographie MET-BF de l'alliage β-21S chargé en hydrogène avec un rapport H/M = 0,46, et l'image en insertion montrant la préparation de l'échantillon par micromachinage ionique; (g) cliché SAED de l'alliage β-21S hydrogéné correspondant; et (h), (i) images en champ sombre de deux variantes ω_1 et ω_2, respectivement.

La **Figure 11d** représente l'image en champ sombre de l'alliage β-21S hydrogéné avec un rapport H/M = 0,10. Des joints de faibles désorientations et des défauts d'empilement ont été observés à l'intérieur des grains de la phase β. La **Figure 11**e montre le cliché de diffraction SAED

correspondant. Par rapport à l'alliage β-21S non-hydrogéné, l'intensité des raies diffuses associées à la présence de la phase ω athermique a diminué, ce qui indique que la phase ω athermique devient moins stable après addition d'hydrogène. Cette observation est cohérente avec des études antérieures [I87, TW87, I94 et TR01] et confirme que l'hydrogène stabilise la phase β et supprime la formation de la phase ω athermique dans des alliages de titane β-métastable.

L'échantillon contenant une concentration élevée en hydrogène, c'est-à-dire un rapport H/M = 0,46, étant trop fragile, une lame mince n'a pas pu être préparée par les méthodes traditionnelles. Par conséquent, la lame mince a été extraite de l'échantillon hydrogéné (auparavant localisés par SEM-EBSD représentées sur la **Figure 10**b) par micro-usinage ionique FIB. L'image MET en champ clair de la feuille mince est montrée dans la **Figure 11**f, et la micrographie prise lors de la préparation de la feuille mince (comme indiqué par la flèche) par le micro-usinage ionique en a été insérée à cette **Figure 11**f.

Le cliché SAED correspondant est présenté dans la **Figure 11**g. Malheureusement aucune phase martensite α'' n'a pu être détectée par MET, par contre une nouvelle phase de structure hexagonale correspondant à la phase ω a été observée. Deux variantes, ω_1 et ω_2, comme indiqué par les cercles roses ont notamment pu être détectées. Les images en champ sombre (DF) correspondant à ces deux variantes ω_1 et ω_2 sont montrées dans les **Figures 11**h et 11i, respectivement. Il peut être observé que, ces deux variantes de la phase ω ont la même morphologie et se trouvent sous la forme de particules de taille nanométrique distribuées aléatoirement dans la phase de matrice β, quelque unes étant repérées par les flèches. Cette morphologie correspond à la structure typique de la phase ω-athermique qui est habituellement formée par trempe dans des alliages de titane β-métastable [CWT87, MT04, LN16 et CZ16].

3.3 Effets de l'hydrogène sur le laminage à froid et la recristallisation

3.3.1 Effets de l'hydrogène sur le laminage à froid du Ti50A

Il a été montré précédemment que l'hydrogène conduisait à des modifications microstructurales et du comportement mécanique. Afin de vérifier le rôle de l'hydrogène sur le comportement en laminage à froid, des échantillons pré-hydrogéné (notés Ti50A-H) ont été laminées à froid jusqu'à des réductions d'épaisseur de 10% et 50%. L'évolution des microstructures a été analysée par diffraction des rayons X et MEB à haute résolution équipée de la technique EBSD.

3.3.1.1 Effets de l'hydrogène sur le comportement en laminage à froid pour un niveau de déformation faible (εeq = 0.12)

Des réductions successives d'épaisseur par laminage symétrique a été imposée sur des échantillons de Ti50A pré-hydrogéné. La réduction d'épaisseur totale était d'environ 10%, ce qui correspond à la déformation équivalente de von Mises $\varepsilon_{eq} = 0{,}12$., Des analyses EBSD ont ensuite été réalisés pour révéler l'effet de l'hydrogène sur la déformation par maclage du titane pur. La **Figure 12** montre les cartes en contraste de bande (BC) avec les joints de jumelles identifiés ; la couleur rouge indique, respectivement, les macles de compression $\left\{11\bar{2}\bar{2}\right\}\left\langle 11\bar{2}3\right\rangle$ référées CT1, alors que la couleur bleue correspond aux macles de tension $\left\{10\bar{1}2\right\}\left\langle \bar{1}011\right\rangle$ référées TT1. On peut observer qu'un nombre croissant de macle de tension de type TT1 ont été générées après augmentation du temps de chargement en hydrogène.

La distribution des angles de désorientation mesurées grain-à-grain dans des échantillons de Ti50A laminés à froid à un niveau de déformation équivalente $\varepsilon_{eq} = 0{,}12$ est représentée dans la **Figure 13**. La ligne verte dans la figure 14a correspond à une distribution aléatoire des angles de désorientation (mesurée grain-à-grain) prédite pour une structure hexagonale sans aucune texture [M04]. La **Figure 13**a indique que les tôles de Ti50A à l'état de réception ne présente pas de distribution aléatoire compte-tenu de la texture subsistante même après traitement de recuit.

Lorsque ces tôles subissent un traitement de laminage avec un niveau de déformation équivalente $\varepsilon_{eq} = 0{,}12$, deux pics importants apparaissent pour des angles de fortes désorientations autour de 65° et 85° (**Figure 13b**). Ces deux pics peuvent être associés à la formation de macles détectés dans les cartes en contraste de bande (**Figure 12**), c'est-à-dire les macles de compression CT1 pour un angle de 65^{o} et les macles de tension TT1 pour l'angle de 85^{o} [BC81]. Comparativement aux toles non chargées en hydrogène, les **Figures 13**c, d et e montrent que la fréquence des macles de tension TT1 augmente proportionnellement à la durée du chargement en hydrogène alors que la fréquence des macles de compression reste approximativement constante

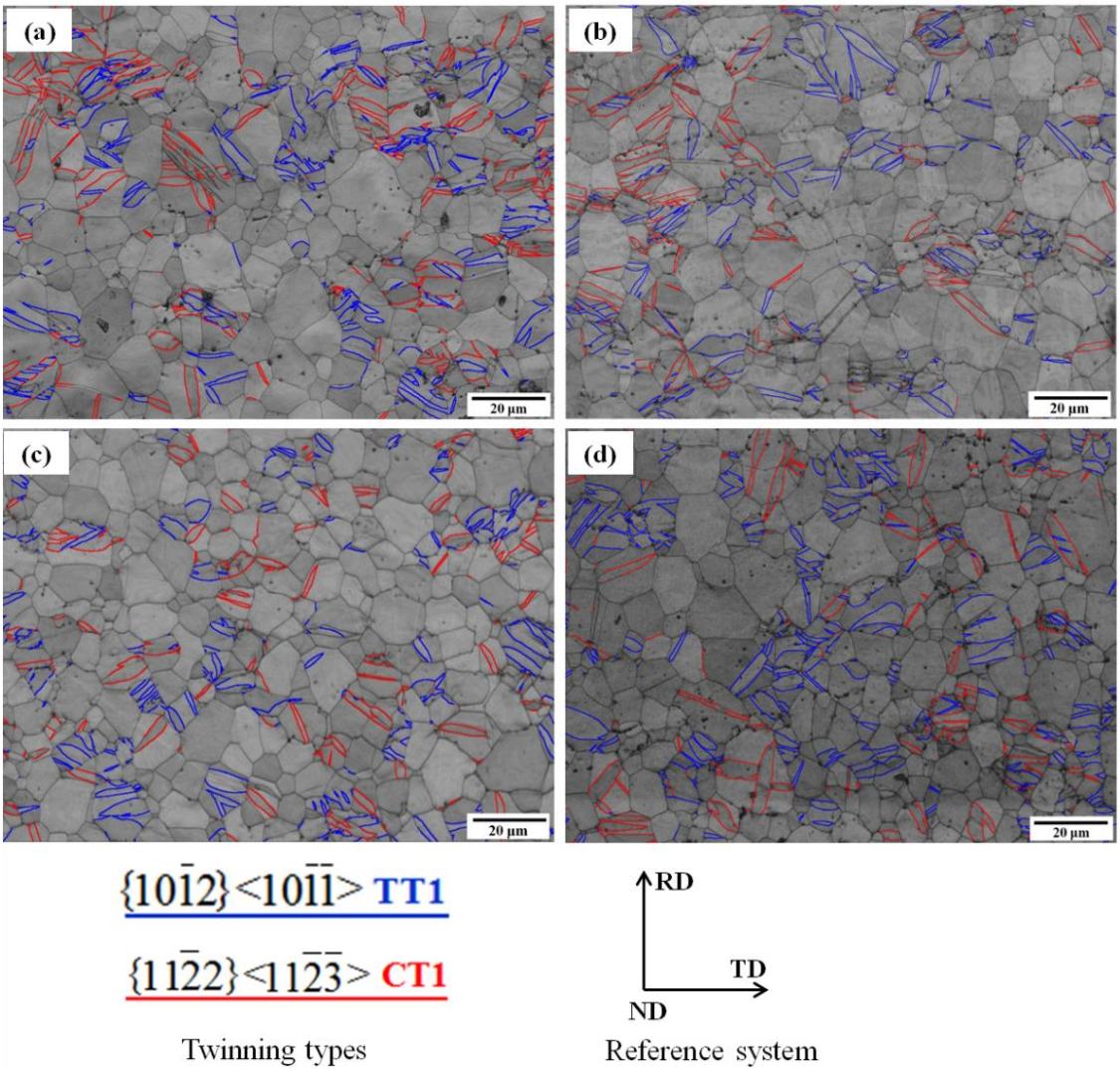

Figure 12 Cartes en contraste de bande du Ti50A laminé à froid après une réduction d'épaisseur de 10%; (a) échantillon Ti50A non hydrogéné; (b), (c) et (d) échantillons Ti50A chargés en hydrogène pendant 72 h, 108 h et 168 h, respectivement. (Les couleurs rouge et bleue correspondent, respectivement, aux joints de macle de compression CT1 et aux macles de tension TT1).

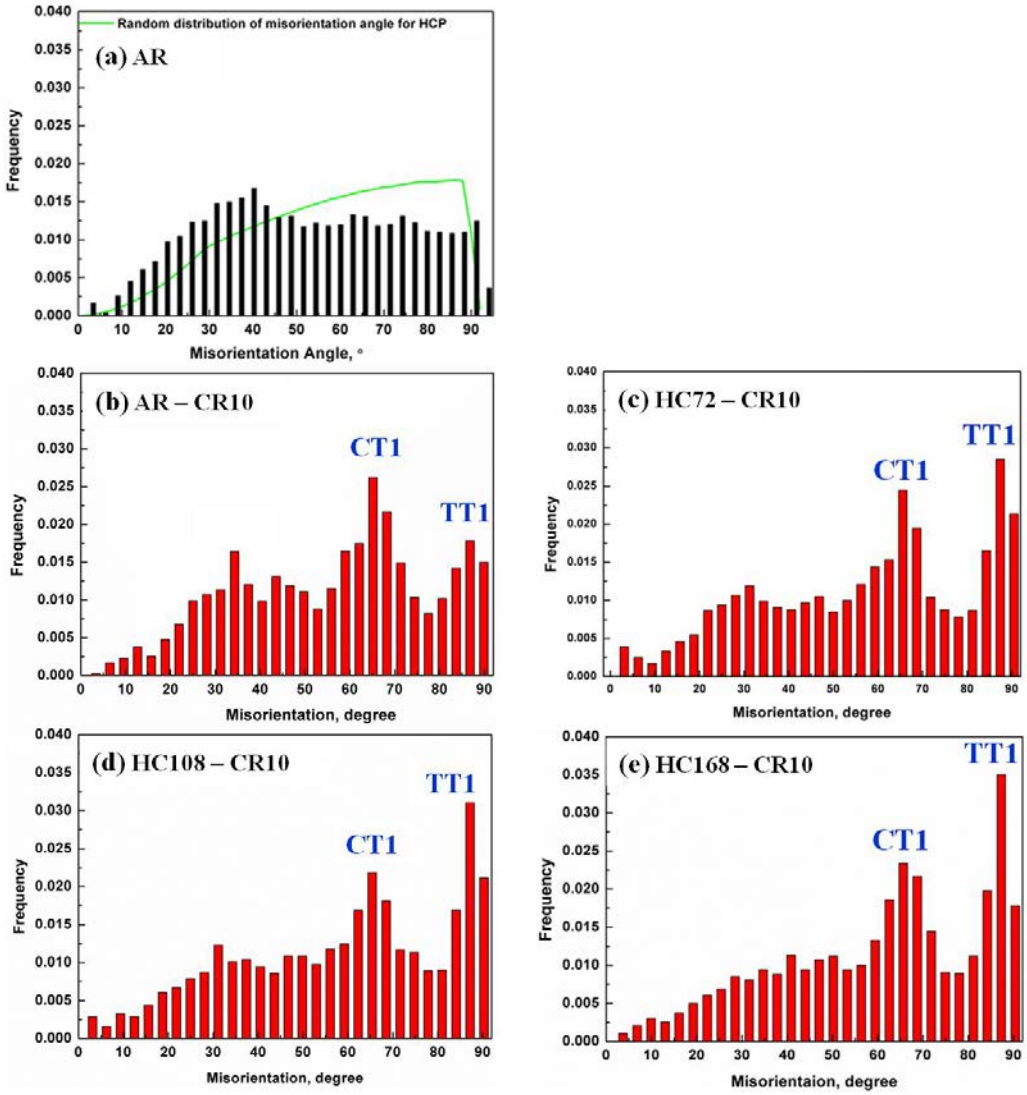

Figure 13 Distributions de angles de désorientation (grain-à-grain) dans différents échantillons de Ti50A; a) échantillon non-chargé en hydrogène, b) à e) échantillons avec différents durée de chargement en hydrogène. (AR: état de réception, CR10: laminage à froid avec réduction d'épaisseur de 10%, HC + CR10: laminé à froid après chargement en hydrogène; TT1 : {10$\bar{1}$2}<$\bar{1}$011> and CT1 : {11$\bar{2}$2}<11$\bar{2}$3>.

3.3.1.2 Effets de l'hydrogène sur le comportement en laminage à froid pour un niveau de déformation moyenne (ε_{eq}=0.80)

Pour étudier l'effet de l'hydrogène sur le comportement du Ti50A en laminage à froid, une réduction d'épaisseur de 50% (ε_{eq} = 0,80) a été appliquée sur des échantillons pré-hydrogénés ainsi que sur des échantillons non-hydrogénés. Les figures de pole inverse (IPF) et cartes en contraste de bandes (BC) obtenues par EBSD dans le plan de laminage après polissage sont montrées dans la **Figure 14**. Le code de couleur correspond à l'orientation de l'axe de la normale au plan (ND) par rapport au système de référence de cristal. Dans les cartes BC, les joints de

faible désorientation (HAB) et forte désorientation (LAB) sont identifiés par des lignes, respectivement, noires et bleues.

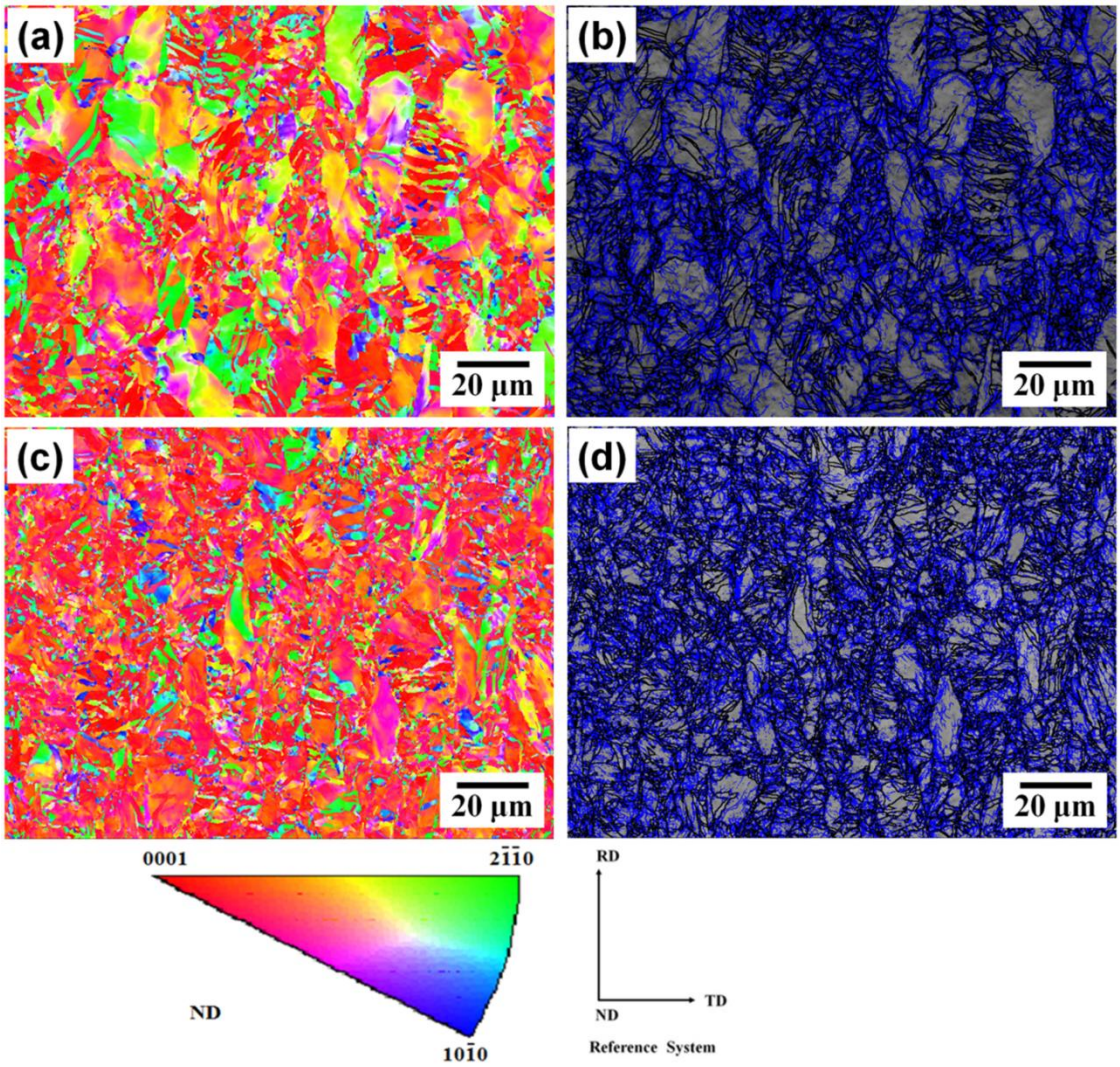

Figure 14 Cartes IPF et BC prises sur la surface d'échantillons de Ti50A laminés à froid avec une réduction d'épaisseur de 50%. (a), (b) Ti50A non hydrogéné et (c), (d) échantillon chargé en hydrogène pendant 168 h; (les lignes bleues soulignent les joints de faible désorientation et les lignes noires les joints de forte désorientation).

Après une réduction d'épaisseur de 50%, la microstructure consiste en un mélange de grains allongés, de macles et de joints de faible désorientation (lignes bleues). Ces résultats indiquent que, comparativement au laminage appliqué à un échantillon non hydrogéné, le laminage des échantillons chargés en hydrogène tend à être favorable à une rotation de l'axe des c <0001> vers la direction normale de laminage (ND). En outre, la **Figure 14**d révèle un raffinement marque de la microstructure dans les échantillons hydrogénés. Le **Tableau 2** donne la taille moyenne des grains pour chacun des échantillons, la taille moyenne étant obtenue par le logiciel ATOM. La

diminution de la taille des grains dans les échantillons hydrogénés peut être attribuée à l'hétérogénéité de la déformation induite par les hydrures.

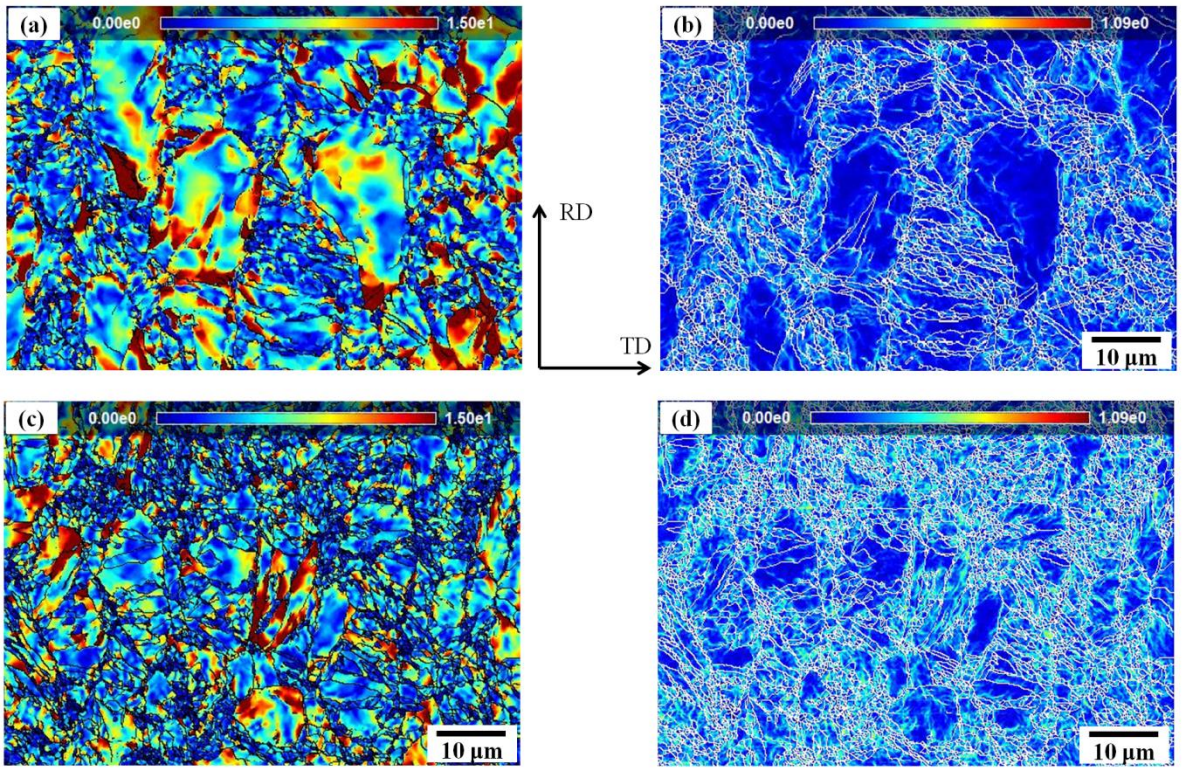

Figure 15 Cartes montrant la désorientation intragranulaire et les GND extraites d'échantillons Ti50A après 50% de réduction d'épaisseur par laminage à froid : (a), (c) échantillon non-hydrogéné et (b), (d) échantillon après 168 h de chargement en hydrogène.

Tableau 2 Taille moyenne des grains et densité normée des dislocations géométriquement nécessaires (GND)

	AR	CR50	HC168 + CR50
Average Grain Size, [µm]	12.0 ± 0.8	2.0 ± 0.2	1.1 ± 0.1
Norm of GND, [µm-1]	0.007 ± 0.002	0.175 ± 0.003	0.224 ± 0.003
Average Internal Misorientation degree, [°]	0.34 ± 0.19	1.50 ± 0.23	2.64 ± 0.20

AR: As-received Ti50A; CR 50: cold rolled to 50% thickness reduction;

HC: hydrogen charged for 168 h

Dans le présent travail, le gradient de déformation local est représenté par la désorientation interne due à la courbure du réseau dans le grain. La **Figure 15**a et c montre les cartes de

désorientation internes mesurées dans 50% d'échantillon laminé à froid, qui correspondent aux cartes IPF de la **Figure 14**a et c. Le schéma de couleurs indique la plage d'angle de désorientation de 0 à 15 °. Comme on l'a observé dans les cartes, il existe un grand gradient de déformation du centre de la limite grain-grain.

Par rapport au Ti50A non chargé (**Figure 15**b), le Ti50A préchargé (**Figure 15d**) montre une augmentation de la teneur en GND après un taux de réduction d'épaisseur de 50% par traitement de laminage à froid. Il convient de mentionner que les cartes ne montrent qu'un sous-ensemble du total des données disponibles; Au total, entre 80 et 150 grains ont été cartographiés pour chaque échantillon. Les données statistiques sur la norme moyenne de GND sont données dans le **tableau 2.**

3.3.2 3.3.2 Effets de l'hydrogène sur le laminage à froid de l'alliage β-21S

La **Figure 16** montre les cartes IPF de l'alliage β-21S laminé à froid, les HAB et les LAB étant identifiés par respectivement des lignes noires et grises. Le code de couleur correspond à l'orientation de l'axe transverse (TD) par rapport au système de référence de cristal. En raison de l'erreur expérimentale dans l'évaluation des orientations mesurées par EBSD [H99], les joints dont les angles de désorientation entre grains étaient inférieurs à 2° ont été exclus de l'analyse. À l'état de réception (après recuit), la microstructure était constituée de grains essentiellement équiaxes avec une taille moyenne de l'ordre de 36,0 ± 0,5 μm (**Figure 16a**). Aucune texture (non représentée ici) et sous-structure interne n'a pu être observée. Après 50% de réduction d'épaisseur par laminage à froid, les grains étaient devenus allongés le long de la direction de laminage et de nombreux joints de faible désorientation peuvent être détectés à l'intérieur des grains déformés.

Dans le domaine de concentration en hydrogène défini tel que 0,052 < H/M <0,160, et comme le montre la **Figure 16**b-d, des nouveaux joints de faible désorientation caractéristique d'une subdivision des grains ont été généré, le nombre de joints augmentant proportionnellement avec la concentration d'hydrogène introduite dans l'alliage. Cependant, pour des concentrations en hydrogène supérieure à H/M = 0,215, le nombre de joints de faible désorientation tend à diminuer et les grains β paraissent moins allongés (**Figure 16**e). Ces résultats suggèrent que l'hydrogène a des effets contradictoires sur le comportement en laminage à froid de l'alliage β-21S selon la concentration en hydrogène, c'est-à-dire un adoucissement lorsqu'une faible concentration en hydrogène (H/M < 0,160) est introduite dans le β-21S, mais un durcissement serait obtenu pour

des concentrations en hydrogène plus élevée (H / M > 0,215). Ces résultats sont en parfait accord avec de nombreuses observations expérimentales sur des alliages à structure cubique et le concept de ‘defactant’ proposée par Kirchheim [K09].

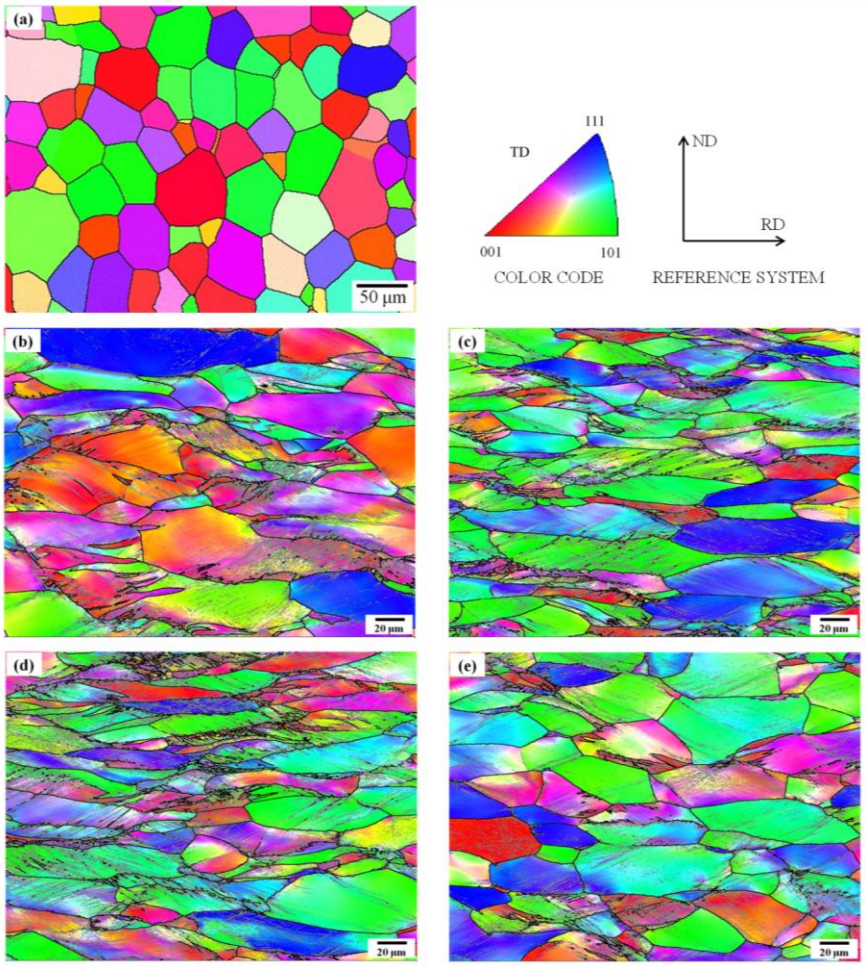

Figure 16 Images EBSD prises sur le plan transverse TD d’échantillons β-21S : (a) à l’état recuit laminé à froid, (b) H / M = 0,052, (c) H / M = 0,100, d) H / M = 0,160 et (e) H / M = 0,215

La **Figure 17**a-d montre les cartes de désorientation intragranulaires mesurées après une réduction en épaisseur de 50% dans des échantillons laminés à froid, ces cartes correspondant aux cartes IPF de la **Figure 16**b-e. Le schéma de couleurs indique la plage d'angle de désorientation variant de 0 à 30°. Un fort gradient de déformation est observé du centre vers les joints de grain dans ces échantillons laminés. L’analyse de la courbure des mailles élémentaires obtenue à partir des mesures EBSD a été utilisée pour estimer la densité et la distribution de dislocation géométriquement nécessaire (GND). Sur la base de la théorie de Nye décrivant la courbure de mailles élémentaires induites par la présence des dislocations [N53], Pantleon [P08] a développé une méthode permettant d’obtenir cinq composants du tenseur de Nye, α, à partir de cartes

d'orientation 2D. À partir de ces cinq composants, une estimation raisonnable de la densité des GND, désignée par la norme de la densité de GND ($r_{GND} = \sqrt{a_{ij}a_{ij}}$), peut être calculée. Dans ce travail, cela a été réalisé à l'aide du logiciel ATOM.

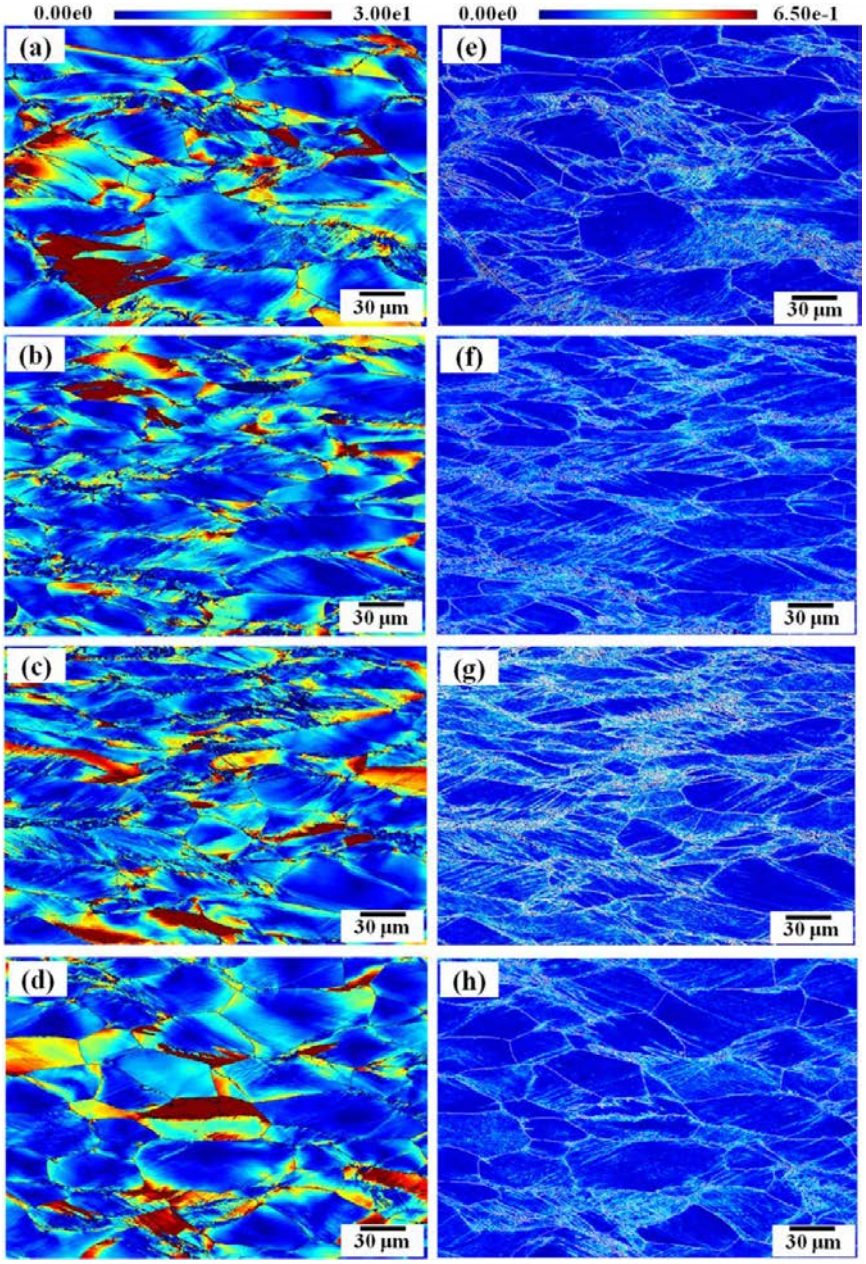

Figure 17 Désorientation intragranulaire (a-d) et cartes GND (e-h) d'alliages β-21S laminés à froid : (a, e) H/M = 0.052; (b, f) H/M = 0.100; (c, g) H/M = 0.160 and (d, h) H/M = 0.215.

Les **Figures 17**e-h montre les cartes GND correspondant aux cartes IPF illustrées dans la **Figure 1**6b-e. Les couleurs correspondent aux valeurs de la norme GND dans la plage variant entre 0 et

$6{,}5 \times 10^{-1}$. Pour chaque carte de GND, certains pixels non pas pu être indexé, car ces pixels étaient soit trop proches d'un joint de grain, ou bien parce que le matériau était trop déformé. On constate que la distribution des GND n'est pas homogène dans l'échantillon et que la plupart des GND sont situées en proximité des joints de grains. Pour les valeurs de concentration en hydrogène comprise dans la plage 052 < H/M <0,160, ces résultats suggèrent que la densité de GND augment avec l'augmentation de la concentration en hydrogène. Comparativement, pour des valeurs de concentration en hydrogène supérieures à H/M = 0,215, la densité de GND montre une légère décroissance. Cela confirme l'effet de l'hydrogène montré ci-dessus décrit par le concept de 'defactant'.

Le **Tableau 3** rassemble les résultats de la taille moyenne des grains et la densité des GND obtenues à l'aide du logiciel ATOM à partir des cartographies EBSD (cartes non représentées ici). Il convient de mentionner que les cartes données dans les figures 16e-h) ne montre qu'un échantillonnage de toutes les données analysées; entre 80 et 150 grains ont été cartographiés pour chaque échantillon. De ces résultats, nous pouvons constater qu'une concentration croissante en hydrogène entraîne une augmentation de la densité des GND ainsi qu'une diminution de la taille des grains.

Tableau 3 Taille moyenne des grains et densité des GND déterminées par EBSD

Hydrogen concentration, (H/M)	Average grain sizes, [um]	GNDs density 10^{14}, $[m^{-2}]$
0.052	12.87 ± 0.20	3.02 ± 0.06
0.100	11.09 ± 0.20	3.76 ± 0.08
0.160	9.32 ± 0.15	4.05 ± 0.05
0.215	10.60 ± 0.10	3.92 ± 0.06

3.3.3 Influence combinée de l'hydrogène et de la déformation à froid sur la recristallisation du Ti50A et de l'alliage β-21S

Dans cette étude, il a été démontré au-dessus, que les échantillons non hydrogénés et hydrogénés présentaient des microstructures différentes après une réduction de l'épaisseur de 50% par laminage à froid. Sachant que le laminage introduit des contraintes internes importantes, il est donc important de suivre l'évolution de la microstructure lors d'un traitement de recuit ultérieur.

Cela repose sur le fait que la libération de l'énergie stockée joue le rôle de force motrice pour les phénomènes de restauration et de recristallisation. Cependant la nature de la microstructure contrôle le développement et la croissance des nuclei, ainsi que l'orientation cristallographique des grains recristallisés.

3.3.3.1 Recrystallisation du Ti50A hydrogené

Pour évaluer l'influence combinée de l'hydrogène / hydrure et de la déformation de laminage à froid sur la recristallisation du titane de pureté commerciale Ti50A, les échantillons avec et sans hydrogène ont été recuits à 675°C pendant 5 min. Les **Figures 18**a et 18c montre les cartes IPF et celles des joints de grain (GB) après traitement de recristallisation pour des échantillons de Ti50A sans hydrogène, alors que les **Figures 18b et 18d** montrent celles obtenues sur des échantillons ayant été chargés 168 h en hydrogène par méthode électrolytique. Dans les cartes GB, les lignes noires et blanches correspondent respectivement aux joints de forte et de faible désorientation. Les couleurs bleues, jaunes et rouges indiquent, respectivement, les grains entièrement recristallisés, les grains présentant encore des sous-structures de dislocation et des grains déformés. Il convient de mentionner que les angles de désorientation minimale séparant les sous-grains et les grains ont été fixés respectivement à 1° et 15°. Comme le montrent les **Figures 18**a et c, un nombre important de nouveaux grains équiaxes sans orientation cristallographique préférentielles a été formé dans cet échantillon Ti50A déformé. La présence de grains contenant des sous-structures indique que la recristallisation avec ce traitement de recuit de 5 min à 675°C n'a pas été complète. Comparativement, ce même traitement réalisé sur des échantillons hydrogénés conduit à une recristallisation d'un plus grand nombre de grains (**Figures 18**b et d). Ce résultat démontre l'effet de la présence d'hydrogène caractérisée par une accélération de la cinétique de recristallisation du Ti50A.

La distribution des angles de désorientation mesurés après traitement de recuit sur des échantillons de Ti50A non-hydrogénés et hydrogénés est donnée respectivement sur les **Figures 19**a et 19b. En plus des joints de forte désorientation, une très petite fraction de joints de faible désorientation (angles de désorientation inférieurs à 15°) a été observée dans l'échantillon sans hydrogénation (**Figure 19**a). Comparativement, l'échantillon hydrogéné (**Figure 19**b) présentait un nombre négligeable de grains de faible désorientation, ce qui suggère que la structure originale a été presqu'entièrement restaurée par ce traitement de recuit. Il est important de noter que,

comme le montrent les **Figures 19c et 19**d, aucune différence significative n'a été observée dans la distribution des tailles de grain entre les spécimens hydrogénés et non-hydrogénés. La distribution de la taille du grain dans les deux cas est décrite par une loi Gaussienne normale, soulignée par les courbes noires. Par rapport au Ti50A non hydrogéné, la distribution de la taille des grains pour l'échantillon de Ti50A hydraté était moins étendue, ce qui indique que, dans ces conditions, la recristallisation et la croissance de nouveaux grains sont bien contrôlées, c'est-à-dire exemptes de croissance anormale des grains.

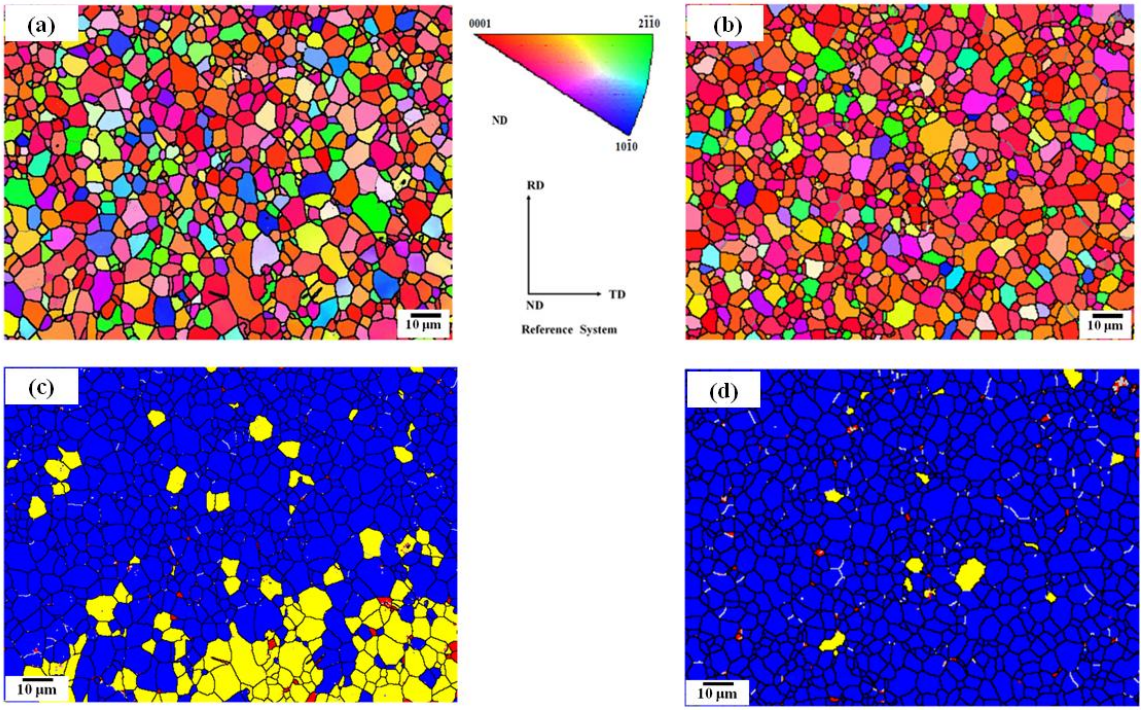

Figure 18 Cartes IPF et GB réalisées sur des échantillons de Ti50A après traitement de recristallisation. (a) et (c) échantillons sans hydrogène, et (b) et (d) échantillons chargés en hydrogène pendant 168 h. (Les lignes en noir et blanc correspondent, respectivement, à des joints de forte et de faible désorientation, les couleurs bleue, jaune et rouge indiquent, respectivement, les grains entièrement recristallisés, les grains dans lesquels subsistent une sous-structure et les grains déformés).

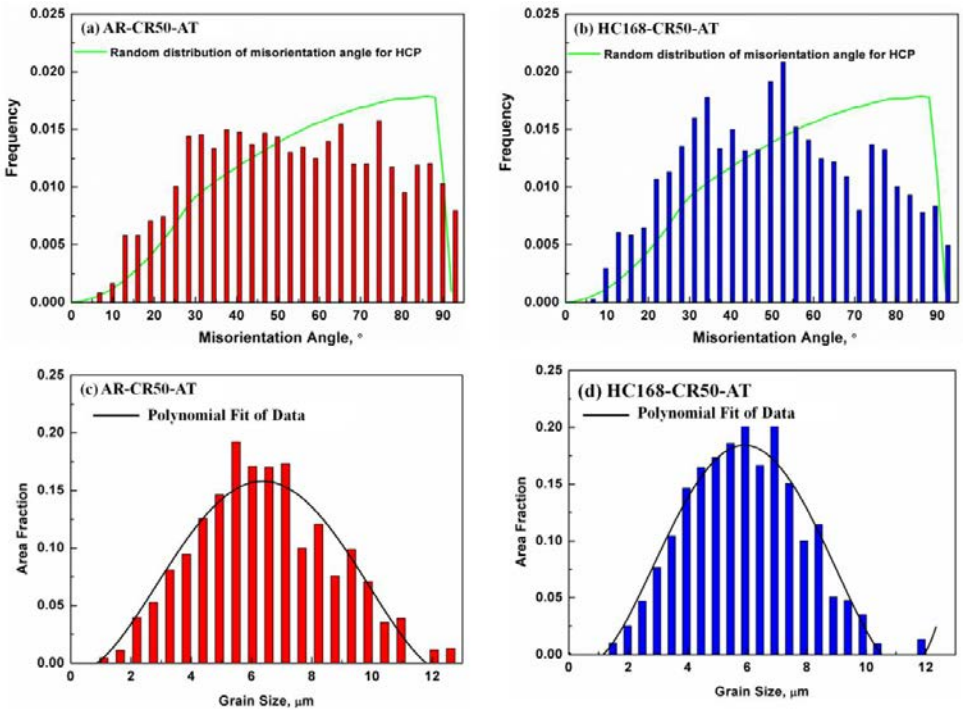

Figure 19 Angle de désorientation et les distributions de la taille des grains du Ti50A recuit : (a), (c) échantillons sans hydrogène et (b), (d) échantillons chargés en hydrogène par méthode électrolytique pendant 168 h.

3.3.3.2 Recristallisation de l'alliage β-21S hydrogéné

Pour étudier l'effet combinée de hydrogène et de la déformation de laminage à froid sur la recristallisation de l'alliage β-21S, des traitements de recuit de courte durée ont été réalisés à 800°C pendant 5 min sur des échantillons laminés contenant différentes concentrations d'hydrogène. La **Figure 20** montre les cartes IPF et GB des spécimens après un traitement de recuit. Dans les cartes GB, les lignes noires et grises correspondent respectivement aux joints de forte et faible désorientation, les couleurs bleu, rouge et jaune indiquent, respectivement, les grains entièrement recristallisés, les grains présentant des sous-structures de dislocation et les grains encore déformés. Comme ci-dessus pour le Ti50A, les angles de désorientation minimale séparant les sous-grains et les grains ont été fixés à, respectivement, 1° et 15°. Pour des valeurs de concentration en hydrogène H/M = 0,052 **(Figures 20a et 20d)**, un grand nombre de grains déformés et de grains présentant sous-structure de dislocation sont observés accompagnés de quelque nouveaux grains recristallisés. L'émergence de nouveaux grains recristallisés suggère que ces conditions de traitement sont propices au début de la recristallisation.

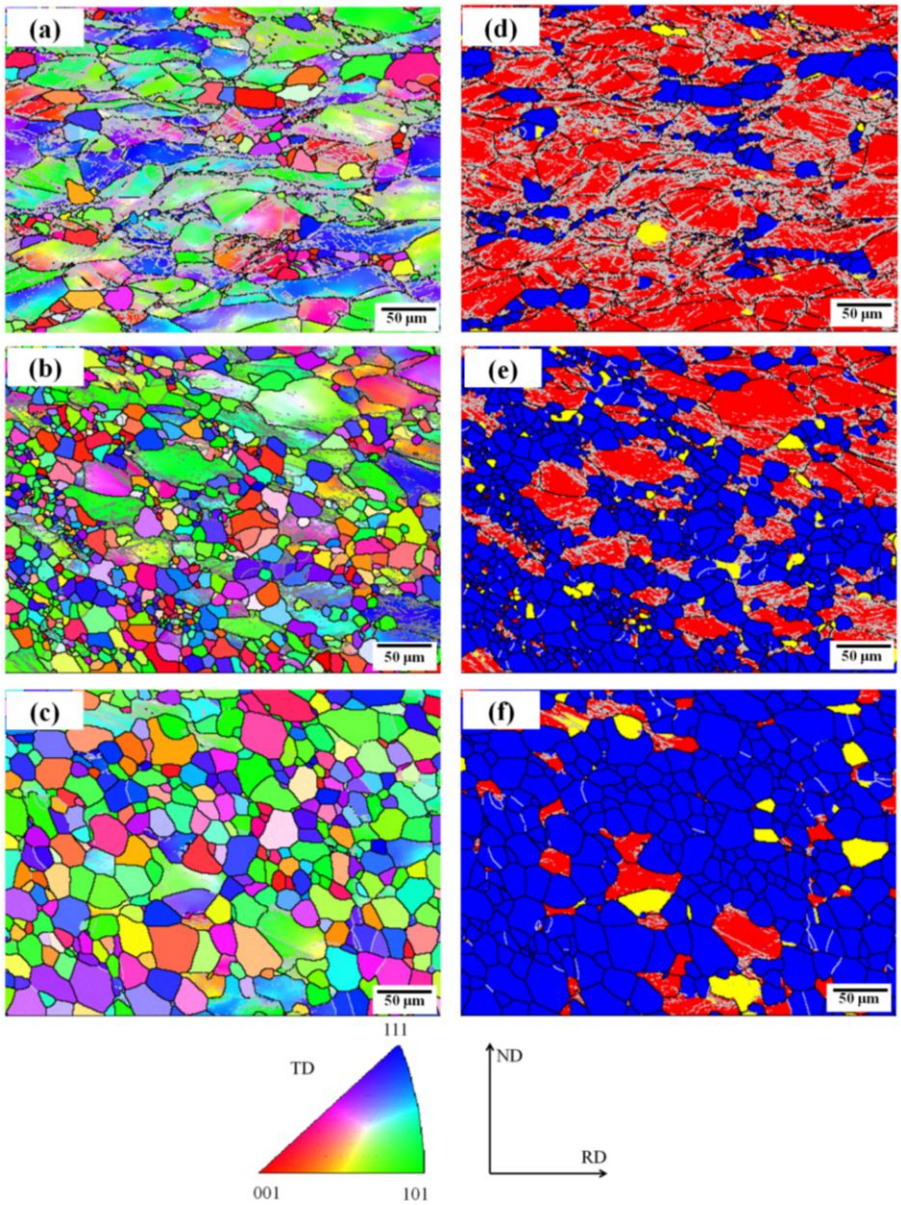

Figure 20 Cartes IPF et GB obtenues pour des échantillons d'alliage β-21S après traitement de recistallisation, (a) et (d) H/M = 0,052; (b) et (e) H/M = 0,100 et (c) et (f) H/M = 0,160. (Les lignes en noir et blanc correspondent respectivement à des joints de forte et de faible désorientation, les couleurs bleue, rouge et jaune indiquent, respectivement, des grains entièrement recristallisés, des grains contenant une sous-structure de dislocation et des grains déformés).

L'observation des **Figures 20b et 20e**) correspondant à des échantillons contenant une concentration d'hydrogène de l'ordre de H/M = 0,100 révèle un plus grand nombre de nouveaux grains recristallisés, ces nouveaux grains représentant approximativement 60% de la fraction surface de dans l'échantillon hydrogéné près traitement de recuit. Lorsque de la concentration en hydrogène est augmenté jusqu'à H/M = 0,160 (**Figures 20c et 20f**), la microstructure recristallisée couvre une fraction surfacique d'environ 88%. Aussi les grains apparaissent avec

une morphologie équiaxe et une croissance de grain minimale. Malgré la présence d'une sous-structure de déformation dans quelques grains déformés, ces résultats indiquent que l'hydrogène favorise la recristallisation de l'alliage β-21S à 800oC. Cependant une optimisation des conditions de traitement de recristallisation est encore nécessaire afin d'éliminer intégralement les grains déformés et ceux présentant encore des sous-structures de dislocation.

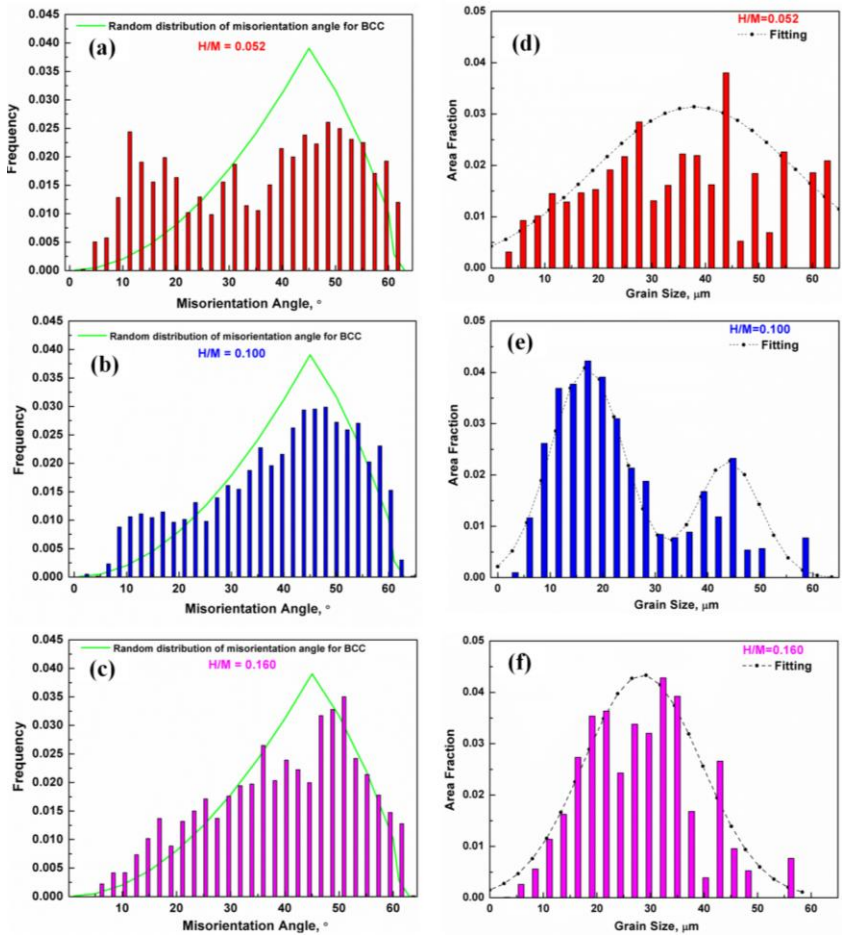

Figure 21 Distributions des angles de désorientation et de la taille des grains après traitement de recristallisation pour les alliages β-21S contenant différentes concentrations en hydrogène, (a), (d) H / M = 0,052; (B), (e) H / M = 0,100 et (c), (f) H / M = 0,160.

Les modifications de la microstructure induite par ce traitement de recuit de courte durée ont également été étudiées en étudiant la distribution des angles de désorientation entre premiers voisins (également appelée distribution de désorientation corrélée de Mackenzie), comme le montrent les **Figures 21a, 21b et 21c**. La ligne verte indique une distribution aléatoire de l'angle de disorientation (grain-à-grain) prévue pour un alliage à structure cubique sans aucune texture cristallographique. Pour une concentration en hydrogène H/M = 0,052 (**Figure 21a**), une fraction élevée de joints de faible désorientation (angle de désorientation inférieur à 15°) est observée,

celle-ci étant aussi importante que la fraction de joints de forte désorientation. Ces joints de faible désorientation sont représentatifs de la microstructure représentée dans les cartes IPF et GB (**Figures 20a et 20d**). Aussi, nos résultats indiquent qu'au fur et à mesure que la concentration en hydrogène augmentait à H/M = 0,100 (**Figure 21**b), celle-ci se traduit par une diminution évidente de la fraction de joints de faible désorientation, qui est le produit direct de la restauration de la microstructure. Lorsque la concentration d'hydrogène est augmentée jusqu'à une valeur H/M = 0,160 (**Figure 21c**), la répartition des joints de faible désorientation dans les échantillons recuits tend se rapproché de la distribution idéale d'un matériau à structure cubique isotrope. Cela indique que les microstructures déformées ont presque été entièrement remplacées par de nouveaux grains exempts de dislocation.

À l'instar du titane de pureté commerciale Ti50A, la distribution de la taille des grains pour les alliages β-21S recuits représentée par la fraction surfacique [U70] est présentée dans les **Figures 21d, 21e et 21f**. L'enveloppe de la distribution de la taille du grain suit une fonction gaussienne, comme l'indiquent les courbes noires. Pour une concentration en hydrogène H/M = 0,052, la dispersion de la taille de grain est relativement important car elle s'étend de 2 à 62 μm, ce qui peut être expliqué par la coexistence de petits grains recristallisés et de grains fortement déformés par laminage. Pour une concentration en hydrogène H/M = 0,100, la dispersion de la taille des grains est comparativement réduite avec une taille de grain moyenne de l'ordre de 12,1 ± 0,2 μm. Lorsque la concentration en hydrogène est augmentée jusqu'à H/M = 0,160, la distribution de la taille de grain suit une répartition gaussienne typique avec une taille moyenne des grains de 14,3 ± 0,3 μm, ce qui correspond à une très légère croissance des grains comparativement à une concentration en hydrogène H/M = 0,100.

4. Conclusions

Sur la base de l'étude de l'évolution microstructurale induite par l'hydrogène et de ses effets sur les propriétés mécaniques, du laminage à froid et de la recristallisation dans l'α-titane Ti50A et l'alliage β-titane β-21S, les principales conclusions sont résumées dans les points suivants:

(1) Dans le titane de pureté commerciale Ti50A de structure cristallographique hexagonale, l'analyse microstructurale combinant les techniques de caractérisation XRD, MEB-EBSD et MET a montré que lors du chargement en hydrogène par méthode électrolytique deux types d'hydrures

(δ-TiHx, ε-TiH_2) précipitaient dans la matrice α et que la fraction de volume de ces hydrures augmentait avec l'augmentation de la durée de chargement. Le présence de contrainte interne résultante de la différence de volume entre les hydrures et la matrice a pu être détectée par l'élargissement des pics de diffraction de la phase α. Cinq relations d'orientation (OR) entre la phase α et l'hydrure stable δ-TiH_x ont été déterminées par l'analyse des projections stéréographiques des plans et directions des deux phases. Les mesures de microdureté en surface ont montré que ces valeurs augmentaient proportionnellement avec la durée de chargement en hydrogène par méthode électrolytique. Ce résultat a été expliqué par l'augmentation de la fraction d'hydrures formée en sous-surface. Aussi le profil de dureté observé de la surface vers le cœur des échantillons qui reflète le gradient de concentration de l'hydrogène à travers la section des échantillons a suggéré une diffusion de l'hydrogène inhibitée par la présence des hydrures en sous-surface.

(2) Dans l'alliage de titane β-21S β-métastables, l'analyse combinée de XRD, MEB-EBSD et MET a montré que l'hydrogène tend à stabiliser la phase β jusqu'à une teneur en hydrogène de l'ordre de H/M < 0,3, mais que la stabilité diminuée pour des concentrations supérieures. Pour une concentration en hydrogène atteignant une valeur H/M = 0,460, l'observation d'une fraction important de phase martensite α". La formation de cette phase martensitique de structure hexagonale a pu être expliquée par le cisaillement induit par la présence d'atomes d'hydrogène en position interstitiel et l'affaiblissement des liaisons interatomiques entre les atomes de la matrice.

(3) L'effet de l'hydrogène a également été étudié sur le laminage à froid de ces deux matériaux. Pour une faible réduction d'épaisseur appliqué au Ti50A correspond à un niveau de déformation équivalente ε_{eq} = 0,12, il a été observé que la formation de macle de tension TT1 $\left\{10\bar{1}2\right\}\left\langle\bar{1}011\right\rangle$ était favorisée ce qui a été attribué à l'augmentation du rapport c/a induite par l'introduction de l'hydrogène et la formation d'hydrures. Pour des niveaux de déformation plus élevées (ε_{eq} = 0,80) (c'est-à-dire une réduction d'épaisseur de 50%), twinning became almost saturated et il est accompagné par un raffinement notable de la microstructure des échantillons pré-hydrogénés de Ti50A comparativement à ce qui a pu être observé pour les échantillons non hydrogénés. L'observation du raffinement microstructural se traduit par une un nombre élevée de joints de forte désorientation (HAB) particulièrement à proximité des hydrures. En outre, les analyses ont révélés la présence d'un grand nombre de dislocations géométriquement nécessaires (GND)

produites pour tenir compte de l'incompatibilité de déformation imposée par laminage particulièrement importante dans le cas échantillons chargé en hydrogène à cause d'hydrures dans la matrice α. L'influence de l'hydrogène sur le laminage à froid de l'alliage β-21S a révélé des effets distincts en fonction de la teneur en hydrogène satisfaisant le concept de 'defactant'. Dans la plage de concentration en hydrogène $0,052 < H/M < 0,160$, les atomes d'hydrogène dissous dans la solution solide β tendent à faciliter la mobilité et la densité des dislocations, ce qui se caractérise par un affinement de la microstructure proportionnel à la concentration en hydrogène. Pour des concentrations en hydrogène supérieures à $H/M = 0,215$, l'observation de grains β moins déformés ainsi que de micro-fissures suggère un mécanisme de durcissement de la solution solide, expliqué par une réduction de la mobilité des dislocations par l'hydrogène.

(4) L'effet combiné de l'hydrogène et de la déformation induite par le laminage à froid permettant la recristallisation a montré que le Ti50A pré-hydrogéné contenait une fraction plus élevée de nouveaux grains recristallisés comparativement au même condition imposée aux échantillons non hydrogénés. L'étude sur l'alliage β-21S a permis de mettre en évidence une fraction croissante de grains recristallisés avec l'augmentation de la concentration en hydrogène. Bien que le rôle exact de l'hydrogène sur la recristallisation n'a pas pu être établi, les résultats observés dans cette étude suggèrent que l'introduction de l'hydrogène dans les alliages de titane peut faciliter la recristallisation ce qui peut se montrer très intéressant pour la réduction des coûts de procédés.